M85010336

DOE/ET/37240--109-PR

DE85 010336

COOLANT MIXING IN LMFBR ROD BUNDLES AND OUTLET PLENUM MIXING TRANSIENTS

NEIL E. TODREAS, Principal Investigator

Shih Kuei Cheng

Kerry Basehore

FINAL REPORT

Report No. DOE/ET/37240 - 109 FR

August 1984

DISCLAIMER

DISCLAIMER

N O T I C E

This report was prepared as an account of work sponsored by the United States Government. Neither the United States nor the Department of Energy, nor any of their employees, nor any of their contractors, subcontractors, or their employees, makes any warranty, express or implied, or assumes any legal liability or responsibility for the accuracy, completeness, or usefulness of any information, apparatus, product or process disclosed or represents that its use would not infringe privately-owned rights.

Abstract

This project principally undertook the investigation of the thermal hydraulic performance of wire wrapped fuel bundles of LMFBR configuration. Results obtained included phenomenological models for friction factors, flow split and mixing characteristics; correlations for predicting these characteristics suitable for insertion in design codes; numerical codes for analyzing bundle behavior both of the lumped subchannel and distributed parameter categories and experimental techniques for pressure velocity, flow split, salt conductivity and temperature measurement in water cooled mockups of bundles and subchannels. Flow regimes investigated included laminar, transition and turbulent flow under forced convection and mixed convection conditions. Forced convections conditions were emphasized. Continuing efforts are underway at MIT to complete the investigation of the mixed convection regime initiated here.

A number of investigations on outlet plenum behavior were also made. The reports of these investigations are identified.

REPORTS AND PAPERS PUBLISHED UNDER MIT COOLANT MIXING IN LMFBR ROD BUNDLES PROJECT

A. Quarterly Progress Reports (Available from:
National Technical Information Service
U. S. Department of Commerce
Springfield, Virginia 22151)

COO-2245-1	Period June 1, 1972 - November 30, 1972
COO-2245-2	Period December 1, 1972 - February 28, 1973
COO-2245-3	Period March 1, 1973 - May 31, 1973
COO-2245-6	Period June 1, 1973 - August 31, 1973
COO-2245-7	Period September 1, 1973 - November 30, 1973
COO-2245-8	Period December 1, 1973 - February 28, 1974
COO-2245-10	Period March 1, 1974 - May 31, 1974
COO-2245-13	Period June 1, 1974 - August 31, 1974
COO-2245-14	Period September 1, 1974 - November 30, 1974
COO-2245-15	Period December 1, 1974 - February 28, 1975
COO-2245-23	Period March 1, 1975 - May 31, 1975
COO-2245-25	Period June 1, 1975 - August 31, 1975
COO-2245-26	Period September 1, 1975 - November 30, 1975
COO-2245-28	Period December 1, 1975 - February 29, 1976
COO-2245-30	Period March 1, 1976 - May 31, 1976
COO-2245-31	Period June 1, 1976 - August 31, 1976
COO-2245-34	Period September 1, 1976 - November 30, 1976
COO-2245-38	Period December 1, 1976 - February 28, 1977
COO-2245-50	Period March 1, 1977 - May 31, 1977
COO-2245-53	Period June 1, 1977 - August 31, 1977
COO-2245-60	Period September 1, 1977 - November 30, 1977
COO-2245-63	Period December 1, 1977 - February 28, 1978
COO-2245-64	Period March 1, 1978 - May 31, 1978
COO-2245-65	Period June 1, 1978 - August 31, 1978
COO-2245-66	Period September 1, 1978 - November 30, 1978

COO-2245-69 Period December 1, 1978-February 28, 1979

COO-2245-70 Period March 1, 1979-May 31, 1979

COO-2245-71 Period June 1, 1979-August 31, 1979

COO-2245-72 Period September 1, 1979-November 30, 1979

DOE/ET/37240-75 Period December 1, 1979-February 29, 1980

DOE/ET/37240-76 Period March 1, 1980-May 31, 1980

DOE/ET/37240-85 Period June 1, 1980-August 31, 1980

DOE/ET/37240-89 Period September 1, 1980-November 30, 1980

DOE/ET/37240-90 Period December 1, 1980-February 28, 1981

DOE/ET/37240-91 Period March 1, 1981 - May 31, 1981

DOE/ET/37240-93 Period June 1, 1981 - August 31, 1981

DOE/ET/37240-94 Period September 1, 1981-November 30, 1981

DOE/ET/37240-95 Period December 1, 1981 - February 28, 1982

DOE/ET/37240-99 Period March 1, 1982 - May 31, 1982

DOE/ET/37240-100 Period June 1, 1982 - August 31, 1982

DOE/ET/37240-103 Period September 1, 1982 - November 30, 1982

DOE/ET/37240-106 Period December 1, 1982 - February 28, 1983

DOE/ET/37240-107 Period March 1, 1983 - May 31, 1983

Reports Issued Under This Contract

B.1 Original Topical Reports (Available from National Technical Information Service, U.S. Department of Commerce, Springfield, VA 22151)

E. Khan and N. Todreas, "A Review of Recent Analytical and Experimental Studies Applicable to LMFBR Fuel and Blanket Assembly Design", COO-2245-4TR, MIT, September 1973.

E. Khan, W. Rohsenow, A. Sonin and N. Todreas, "A Simplified Approach for Predicting Temperature Distribution in Wire Wrapped Assemblies", COO-2245-5TR, MIT, September 1973.

T. Eaton and N. Todreas, "Instrumentation Methods for Interchannel Coolant Mixing Studies in Wire-Wrap Spaced Nuclear Fuel Assemblies", COO-2245-9TR, MIT, June 1974.

Y. B. Chen, K. Ip, N. E. Todreas, "Velocity Measurements in Edge Subchannels of Wire Wrapped LMFBR Fuel Assemblies", COO-2245-11TR, MIT, September 1974.

E. Khan, N. Todreas, W. Rohsenow, A. A. Sonin, "Analysis of Mixing Data Relevant to Wire-Wrapped Fuel Assembly Thermal-Hydraulic Design", COO-2245-12TR, MIT, September 1974.

E. Khan, W. Rohsenow, A. Sonin, N. Todreas, "A Porous Body Model for Predicting Temperature Distributions in Wire Wrapped Fuel and Blanket Assemblies of an LMFBR", COO-2245-16TR, MIT, June 1975.

* E. Khan, W. M. Rohsenow, A. Sonin, N. Todreas, "Input Parameters to the ENERGY Code (To be used with the ENERGY Codes Manual), COO-2245-17TR, MIT, May 1975.

* E. Khan, W. Rohsenow, A. Sonin, N. Todreas, "Manual for ENERGY Codes I, II, III", COO-2245-18TR, MIT, May 1975.

P. Carajilescov and N. Todreas, "Experimental and Analytical Study of Axial Turbulent Flows in an Interion Subchannel of a Bare Rod Bundle", COO-2245-19TR, MIT.

* B. Chen and N. Todreas, "Prediction of Coolant Temperature Field in a Breeder Reactor Including Interassembly Heat Transfer", COO-2245-20TR, MIT, May 1975.

* Revised - See Section B.2

F. Carre and N. Todreas, "Development of Input Data to ENERGY Code for Analysis of Reactor Fuel Bundles", COO-2245-21TR, MIT, May 1975.

H. Ninokata and N. E. Todreas, "Turbulent Momentum Exchange Coefficients for Reactor Fuel Bundle Analysis", COO-2245-22TR, MIT, June 1975.

R. Anoba and N. Todreas, "Coolant Mixing in LMFBR Rod Buncles and Outlet Plenum Mixing Transients, COO-2245-24TR, MIT, August 1975.

* B. Bosy, "Fabrication Details for Wire Wrapped Fuel Assembly Components", COO-2245-27TR, MIT, November 1975.

Ralph G. Bennett and Michael W. Golay, "Interferometric Investigation of Turbulently Fluctuating Temperature in an LMFBR Outlet Plenum Geometry", COO-2245-29TR, MIT, June 1976.

N. E. Todreas, "Thermal Analysis Methods for LMFBR Wire Wrapped Bundles", COO-2245-32TR, MIT, November 1976.

K. L. Basehore and N. E. Todreas, "Development of Stability Criteria and an Interassembly Conduction Model for the Thermal-Hydraulics Code SUPERENERGY", COO-2245-33TR, MIT, December 1976.

Robert Masterson and Neil E. Todreas, "Analysis of the Feasibility of Implementing an Implicit Temporal Differencing Scheme in the SUPERENERGY Code", COO-2245-35TR, MIT, February 1977.

S. Glazer, C. Chiu and N. Todreas, "Collection and Evaluation of Salt Mixing Data with the Real Time Data Acquisition System", COO-2245-36TR, MIT, April 1977.

B. Mikic, E. U. Khan and N. E. Todreas, "An Approximate Method for Predicting Temperature Distribution in Wire Wrapped Fuel Assemblies of an LMFBR", COO-2245-37TR, MIT, April 1977.

J. T. Hawley, C. Chiu and N. Todreas, "Development of a Technique for Subchannel Flow Rate Measurements in LMFBR Wire Wrapped Assemblies", to be issued as COO-2245-39TR 6/80. Never issued. Replaced by DOE/ET/37240-80TR.

* Revised - See Section B.2

B.1 Original Topical Reports (Continued)

* C. Chiu and N. Todreas, "WARD Blanket Assembly Pre-Test Predictions by SUPERENERGY", COO-2245-40TR, MIT, May 1977.

C. Chiu, N. Todreas, W. M. Rohsenow, "Flow Split Measurements in LMFBR Blanket Assemblies", COO-2245-41TR, MIT, April 1978.

C. Chiu, J. Hawley, W. M. Rohsenow and N. Todreas, "Pressure Drop Measurements in Wire Wrapped Blanket Assemblies", COO-2245-42TR, July 1977.

C. Chiu, W. M. Rohsenow and N. Todreas, "Mixing Experiments in LMFBR Wire Wrapped Blanket Assemblies", COO-2245-43TR, April 1978.

Yi Ben Chen and Michael W. Golay, "Coolant Mixing in the LMFBR Outlet Plenum", COO-2245-44TR, June 1977.

J. Kelly and N. Todreas, "Turbulent Interchange in Triangular Array Bare Rod Bundles", COO-2245-45TR, July 1977.

K. L. Basehore and N. E. Todreas, "Assessment of the Need to Incorporate a Variable Swirl Flow Model into the ENERGY Code", COO-2245-46TR, July 1977.

K. L. Basehore and N. Todreas, "Analysis of the Thermal-Hydraulic Behavior in the CRBR Secondary Control Assembly, Including Interassembly Heat Transfer Effects", COO-2245-47TR, July 1977.

J. G. Bartzis and N. E. Todreas, "Hydrodynamic Behavior of a Bare Rod Bundle", COO-2245-48TR, MIT, June 1977.

M. R. Fakori-Monazah and N. E. Todreas, "Measurement and Analysis of Flow Wall Shear Stress in an Interior Subchannel of Triangular Array Rods", COO-2245-49TR, MIT, August 1977.

* A. S. Hanson and N. E. Todreas, "Fluid Mixing Studies in an Hexagonal 61-Pin, Wire-Wrapped Rod Bundle", COO-2245-51TR, MIT, August 1977.

S. Glazer, N. Todreas, W. Rohsenow, and A. Sonin, "TRANSENERGY S - Computer Codes for Coolant Temperature Prediction in LMFBR Cores During Transient Events", COO-2245-52TR, MIT, February 1981.

C. Chiu, W. M. Rohsenow, and N. E. Todreas, "Mixing Experiments in an Alternating Wire Wrapped Assembly", COO-2245-54TR, MIT, December 1977.

* Revised - See Section B.2

B.1 Original Topical Reports (Continued)

* C. Chiu, W. M. Rohsenow and N. E. Todreas, "Turbulent Sweeping Flow Mixing Model for Wire Wrapped LMFBR Assemblies", COO-2245-55TR, MIT, April 1978.

* C. Chiu, W. M. Rohsenow and N. E. Todreas, "Flow Split Model for LMFBR Wire Wrapped Assemblies", COO-2245-56TR, MIT, April 1978.

K. Basehore and N. E. Todreas, "SUPERENERGY: Multiassembly Thermal-Hydraulic LMFBR Code", to be issued as Topical Report COO-2245-57TR, MIT, NED

C-N. Wong and L. Wolf, "A 3-D Slug Flow Heat Transfer Analysis of Coupled Coolant Cells in Finite LMFBR Bundles", COO-2245-58TR, MIT, February 1978.

Roohollah Karimi and L. Wolf, "Two Dimensional Structural Analysis of Reactor Fuel Element Claddings Due to Local Effects", COO-2245-59TR, MIT, April 1978.

Vincent Manno and Michael Golay, "Measurement of Heat and Momentum Eddy Diffusivities in Recirculating LMFBR Outlet Plenum Flows", COO-2245-61TR, MIT, June 1978.

* Hafeez Khan, Chong Chiu and Neil Todreas, "Laboratory Manual for Salt Mixing Test in Rod Bundles", COO-2245-62TR, MIT, October 1978.

J. Y. Kim and L. Wolf, "Fully-Developed Mixed Convection Heat Transfer and Pressure Drop in Characteristic Coolant Cells of Finite Hexagonal Bare Bundles", COO-2245-67TR, MIT, Dec. 1978.

M. K. Yeung and L. Wolf, "A Multicell Slug Flow Heat Transfer Analysis of Finite LMFBR Bundles", COO-2245-68TR, MIT, December 1978.

S. F. Wang, W. M. Rohsenow, N. E. Todreas, "Steady, Laminar, Fully-Developed Mixed Convection in Finite Rod Arrays", COO-2245-73TR, MIT, Feb. 1981.

P. D. Symolon, N. E. Todreas, "A Manual for Use with the Computer Code Superenergy-Data Reduction Version", COO-2245-74TR, MIT, February 1980.

K. J. Burns, N. E. Todreas, "Laboratory Manual for Static Pressure Drop Experiments in LMFBR Wire Wrapped Rod Bundles," DOE/ET/37240-77TR, July 1980.

K. J. Burns, N. E. Todreas, "A Comparison Between the SIMPLE and ENERGY Code Mixing Models," DOE/ET/37240-78TR, July 1980.

* Revised - See Section B.2

B.1 Original Topical Reports (Continued)

J. T. Hawley, C. Chiu, W. M. Rohsenow, N. E. Todreas, "Correlations for Subchannel and Bundle Friction Factors and Flowsplit Parameters for Laminar, Transition, and Turbulent Longitudinal Flows in Wire Wrap Spaced Hexagonal Arrays", DOE/ET/37240-79TR, Dec. 1980.

J. T. Hawley, C. Chiu, N. E. Todreas, "M.I.T. Extraction Method for Measuring Average Subchannel Axial Velocities in Reactor Assemblies", DOE/ET/37240-80TR, July 1980.

* K. J. Burns, W. M. Rohsenow, N. E. Todreas, "Laminar/Transition Sweeping Flow Mixing Model for Wire Wrapped LMFBR Assemblies", DOE/ET/37240-81TR, July 1980.

T.E. Greene, N. E. Todreas, "Criteria for Onset of Mixed Convection in Wire Wrap Spaced Hexagonal Arrays", Report DOE/ET/37240-82TR, to be issued.

D. R. Boyle and M. W. Golay, "Transient Effects in Turbulence Modelling", DOE/ET/37240-83TR, Feb. 1980.

P. D. Symolon and N. E. Todreas, "Fluid Mixing Studies in a Hexagonal 217 Pin Wire Wrapped Rod Bundle," DOE/ET/37240-84TR, Feb. 1981.

* S. F. Wang, W. M. Rohsenow, and N. E. Todreas, "Flow Split, Pressure Drop, and Mixing Experiments in a 61 Pin Shaved-Wire Blanket Assembly, DOE/ET/37240-86TR, Feb. 1981.

S. F. Wang, N. E. Todreas, "Computer Model for M.I.T. Correlations for Friction Factors, Flow Split, and Mixing Parameters in LMFBR Wire-Wrapped Rod Assemblies, DOE/ET/37240-87TR, Feb. 1981.

S. F. Wang and N. E. Todreas, "Experimental Investigations of Laminar Mixed Convection in a Square Array of Bare Rods," Report No. DOE/ET/37240-88TR, Feb. 1981.

* Y. N. Chan and N. E. Todreas, "A Simple LMFBR Axial Flow Friction Factor Correlation," DOE/ET/37240-92TR, Sept. 1981.

S-K. Cheng and N. E. Todreas, "Fluid Mixing Studies in a Hexagonal 37 Pin Wire-Wrapped Rod Bundle," DOE/ET-37240-96TR, Feb. 1982.

C-N. C. Wong and N. E. Todreas, "Wire-Wrapped Rod Bundle Heat Transfer Analysis for LMFBR," DOE/ET/37240-97TR, July 1982.

C-N. C. Wong, S-K. Cheng and N. E. Todreas, "User's Guide to HEATRAN, A computer Program for Three Dimensional Transient Fluid Flow and Heat Transfer Analysis," DOE/ET/37240-98TR, January 1982.

B.1 Original Topical Reports (continued)

P.D. Symolon and N. E. Todreas, "Criteria for Onset of Mixed Convection and Onset of Flow Recirculation in Vertical and Rod Bundles, "DOE/ET/37240-101TR, September

S.-K. Cheng and N. E. Todreas, "Directions for Further Development of the HEATRAN Code; Definition of a New Computational Code,"DOE/ET/37240-102TR, December 1982.

Tsing T. Huang and N.E. Todreas, "Application of the MIT Two Channel Model to Predict Flow Recirculation in WARD 61 Pin Blanket Tests, "DOE/ET/37240-104TR, January 1983.

S.K. Cheng, "Trip Report: A Visit to West Germany," DOE/ET/37240-105TR, February 1983.

S.K. Cheng and N.E. Todreas, "Constitutive Correlations for Wire-Wrapped Subchannel Analysis under Forced and Mixed Convection Condition, "DOE/ET/37240-108TR, July 1984

N.E. Todreas, S.K. Cheng, K. Basehore,"Final Project Report: Coolant Mixing in LMFBR Rod Bundles and Outlet Plenum Mixing Transients", DOE/ET/37240-109TR, August 1984.

Reports Issued Under This Contract

B.2 Revised Topical Reports (Available from National Technical Information Service, U.S. Department of Commerce, Springfield, VA 22151)

Topical Report 17TR

S.F. Wang and N.E. Todreas, "Input Parameters to Codes Which Analyze LMFBR Wire-Wrapped Bundles," COO-2245-17TR, (Revision I), MIT, May 1979

J.T. Hawley, Y.N. Chan and N.E. Todreas, "Input Parameters to Codes which Analyze LMFBR Wire-Wrapped Bundles," COO-2245-17TR, (Revision II), December 1980.

** Chapters 4 and 6 of S.K. Cheng and N.E. Todreas, DOE/ET/37240-108TR Supercede Revision II of COO-2245-17TR

Topical Report 18TR

E. Khan, W. Rohsenow, A. Sonin, N. Todreas, "Manual for ENERGY Codes I, II, III Computer Programs", COO-2245-18TR, Revision I, MIT, July 1976.

** Chapter 7 and Appendix D of S.K. Cheng and N.E. Todreas, DOE/ET/37240-108TR supercede Revision I of COO-2245-18TR.

Topical Report 20TR

** B. C. Chen and N. E. Todreas, "Prediction of Coolant Temperature Field in a Breeder Reactor Including Interassembly Heat Transfer," COO-2245-20TR, (Revision 1), MIT, December, 1976.

Topical Report 27TR

H. Khan, "Fabrication Details for Wire-Wrapped Fuel Assembly Components," COO-2245-27TR, (Revision I), MIT, September, 1978.

**K.W. Chiu, "Fabrication Details for Wire-Wrapped Fuel Assembly Components," COO-2245-27TR, (Revision II), MIT, September, 1979.

Topical Report 51TR

**P.D. Symolon and N.E. Todreas, "Fluid Mixing Studies in a Hexagonal 61 Pin Wire Wrapped Rod Bundle," COO-2245-51TR, (Revision I), February 1981.

Topical Report 55TR

C. Chiu, W.M. Rohsenow and N.E. Todreas, "Turbulent Sweeping Flow Mixing Model for Wire Wrapped LMFBR Assemblies", COO-2245-55TR, Rev. 1, MIT 1978.

** identifies latest version.

Reports Issued Under This Contract

Y.N. Chan and N.E. Todreas, "Turbulent Sweeping Flow Mixing Model for Wire Wrapped LMFBR Assemblies," COO-2245-55TR, (Revision II), December 1980.

** Chapter 6 of S.K. Cheng and N.E. Todreas, DOE/ET/37240-108TR supercedes Revision II of COO-2245-55TR

Topical Report 56TR

Y.N. Chan and N.E. Todreas, "Turbulent Flow Split Model and Supporting Experiments for Wire Wrapped Core Assemblies," COO-2245-56TR, (Revision I), December 1980.

**Chapter 4 of S.K. Cheng and N.E. Todreas, DOE/ET/37240-108TR supercedes Revision I of COO-2245-56TR

Topical Report 62TR

**Y.N. Chan and N.E. Todreas, "Laboratory Manual for Salt Mixing Test in 37- and 217-Pin Bundles," COO-2245-62TR, (Revision I), August 1980.

Topical Report 74TR

P.D. Symolon, N.E. Todreas, "A Manual for Use with the Computer Code Superenergy-Data Reduction Version", COO-2245-74TR, MIT, February 1980.

** Chapter 5 of S.K. Cheng and N.E. Todreas, DOE/ET/37240-108TR supercedes COO-2245-74TR, Feb. 1980

Topical Report 81TR

K.J. Burns, W.M. Rohsenow, N.E. Todreas, "Laminar/Transition Sweeping Flow Mixing Model for Wire Wrapped LMFBR Assemblies", DOE/ET/37240-81TR, July 1980.

** Chapter 6 of S.K. Cheng and N.E. Todreas, DOE/ET/37240-108TR supercede COO-2245-81TR, July 1980.

Topical Report 87TR

S.F. Wang, N.E. Todreas, "Computer Model for M.I.T. Correlations for Friction Factors, Flow Split, and Mixing Parameters in LMFBR Wire-Wrapped Rod Assemblies, DOE/ET/37240-87TR, Feb. 1981.

** Chapters 4 and 6 of S.K. Cheng and N.E. Todreas, DOE/ET/37240-108TR supercede COO-2245-87TR, Feb. 1981

Topical Report 92TR

Y.N. Chan and N.E. Todreas, "A Simple LMFBR Axial Flow Friction Factor Correlation," DOE/ET/37240-92TR, Sept. 1981. A revised version incorporating the latest correlations of DOE/ET/37240-108 TR has not been written.

Reports Issued Under This Contract

C. Papers and Summaries

Y. B. Chen, K. L. Ip, and N. E. Todreas, "Velocity Measurements in Edge Channels of Wire-Wrapped LMFBR Fuel Assemblies," American Nuclear Society Transactions, Vol. 19, 1974, pp. 323-324.

P. Carajilescov and N. Todreas, "Experimental and Analytical Study of Axial Turbulent Flows in an Interior Subchannel of a Bare Rod Bundle," J. of Heat Transfer, Vol. 98, No. 2, May 1976, pp. 262-268, (Included as Appendix to Quarterly Progress Report, COO-2245-15).

E. Khan, W. Rohsenow, A. Sonin, and N. Todreas, "A Porous Body Model for Predicting Temperature Distribution in Wire-Wrapped Fuel Rod Assemblies," Nuclear Engineering and Design, 35 (1975), pp. 1-12.

E. Khan, W. Rohsenow, A. Sonin, and N. Todreas, "A Porous Body Model for Predicting Temperature Distribution in Wire-Wrapped Rod Assemblies Operating in Combined Forced and Free Convection," Nuclear Engineering and Design, 35 (1975), pp. 199-211.

R. G. Bennett and M. W. Golay, "Development of An Optical Method for Measurement of Temperature Fluctuation in Turbulent Flows," American Nuclear Society Transactions, Vol. 22, 1975, p. 581.

B. Chen and N. Todreas, "Prediction of the Coolant Temperature Field in a Breeder Reactor Including Interassembly Heat Transfer," Nuclear Engineering and Design, 35, (1975), pp. 423-440, (Included as Appendix to Quarterly Progress Report, COO-2245-23).

R. Bennett and M. W. Golay, "Interferometric Investigation of Turbulently Fluctuating Temperature in an LMFBR Outlet Plenum Geometry," Presented at the ASME Annual Winter Meeting, December, 1976, (Included as Appendix in Quarterly Progress Report, COO-2245-30).

B. B. Mikic, E. U. Khan, and N. E. Todreas, "An Approximate Method for Predicting Temperature Distribution in Wire-Wrapped Fuel Assemblies of a Liquid Metal Fast Breeder Reactor," Mech. Res. Comm., Vol. 3, (1976), pp. 353-360.

L. Wolf, R. Karimi, J. Y. Kim, C. N. Wong, and M. K. Yeung, "2-D Thermoelastic Analysis of LMFBR Fuel Rod Claddings," Paper C4/d, 4th International Conf. Structural Mechanics in Reactor Technology, San Francisco, August 1977.

C. Papers and Summaries (Continued)

M. Yeung, and L. Wolf, "Effective Conduction Mixing Lengths for Subchannel Analysis of Finite Hexagonal LMFBR Bundles," Transactions of the American Nuclear Society, June 1977, Vol. 26, pp 463-464.

C. Chiu and N. Todreas, "Flow Split Measurements in an LMFBR Radial Blanket Assembly," Transactions of the American Nuclear Society, June 1977, Vol. 26, pp 455-456.

J. Y. Kim and L. Wolf, "Laminar Mixed Convection Heat Transfer in Finite Hexagonal Bundles," Transactions of the American Nuclear Society, (1977), Vol. 27, pp 384-385.

J. Kelly and N. Todreas, "Turbulent Interchange in Triangular Array Bare Rod Bundles," Paper NR-3, Presented at Sixth International Heat Transfer Conference, Toronto, August 1978.

C. Chiu, N. E. Todreas, and W. M. Rohsenow, "Turbulent Flow Split Experiment and Model for Wire-Wrapped Assemblies," Transactions of the American Nuclear Society, June, 1978, Vol. 28, TANSAO 28, (1978), pp 536-537, ISSN: 0003-018X.

C. Chiu, N. E. Todreas, and W. M. Rohsenow, "Pressure Drop Measurements in LMFBR Wire-Wrapped Blanket Bundles," Transactions of the American Nuclear Society, Vol. 30, pp 541-543, (1978).

C. Chiu, N. E. Todreas, and W. M. Rohsenow, "Turbulent Mixing Experiment and Model for Wire-Wrapped Assemblies," Trans. of the American Nuclear Society, Vol. 30, pp 547-548 (1978).

M. Fakory and N. Todreas, "Experimental Investigation of Flow Resistance and Wall Shear Stress in the Interior Subchannel of a Triangular Array of Parallel Rods," Jl. Fluids Eng., Vol. 101, pp 429-435 (Dec. 1979).

J. G. Bartzis and N. E. Todreas, "Turbulence Modeling of Axial Flow in a Bare Rod Bundle," Jl. Ht. Trans., Vol. 101, No. 4, pp 628-634 (Nov. 1979).

Reports Issued Under This Contract

C. Papers and Summaries (Continued)

C. Chiu, W. M. Rohsenow, and N. E. Todreas, "Prediction of Temperatures Distribution in Wire-Wrapped Nuclear Fuel Rod Assemblies," Proceedings NATO Mtg., Vol. 1, pp 175-184, published by Hemisphere Pub. Co., Washington, DC (1978)

S. Glazer, T. Greene, N. Todreas, and L. Wolf, "Transient Thermal-Hydraulic Analysis in the Forced-Convection Regime (TRANSENERGY)," TANSOA, Vol. 32, Atlanta, 1979.

C. Chiu, W. M. Rohsenow, and N. E. Todreas, "Turbulent Flow Split Model and Supporting Experiments for Wire-Wrapped Core Assemblies,"Nuclear Technology, Vol. 50, pp 40-52, August 1980

J. T. Hawley, C. Chiu, W. M. Rohsenow and N. E. Todreas, "Subchannel and Bundel Friction Factors and Flow Split - Parameters for Laminar, Transition and Turbulent Longitudinal Flows in Wire Wrap Spaced Hexagonal Arrays, "Proceedings ANS/ASME/NRC Int'l Topical Mtg. on Nuc. Reactor T/H, NUREG/CP-0014, 3, pp 1766-1788, Oct. 1980.

S. F. Wang, W. M. Rohsenow and N. E., "Subchannel Friction Factors for Bare Rod Arrays under Mixed Convection Conditions,"Decay Heat Removal and Natural Convection in Fast Breeder Reactors, A. K. Agrawal and J. G. Guppy, Eds., Hemisphere Publishing Corp., NY pp 95-109, 1981.

Chiu, C., Morris, R., and N. Todreas, "Experimental Techniques for Liquid Metal Cooled Fast Breeder Reactor Fuel Assembly Thermal/Hydraulic Tests,"Invited Paper for Special Issue of Nuclear Engineering and Design, Vol. 62, No 1-3, 253-270, Dec. 1980.

Bishop, A. and N. Todreas, "Hydraulic Characteristics of Wire-Wrapped Rod Bundles," Invited Paper for Special Issue of Nuclear Engineering and Design, Vol. 62, No. 1-3, 271-293, Dec. 1980.

Reports Issued Under This Contract

C. Papers and Summaries (Continued)

Todreas, N.E., "Model Development of LMFBR Core Thermal Hydraulics", Information Meeting of the Core Components Working Group, Richland, WA, May 13-15, 1980.

Efthimiadis, A., Rohsenow, W.M., Todreas, N.E., and Wang, S-F., "Investigation of Developing Vertical Mixed Convection Flow in a Square Array of Cylindrical Rods," VII International Heat Transfer Conference, Munich, Germany, 6-10 September 1982, 82-IHTC-138

Todreas, N.E., "Sodium-Cooled Fast Reactor Thermal-Hydraulics," NUREG/CP-0034, Vol. 1, Proceedings of the Topical Meeting on Advances in Reactor Physics and Core Thermal Hydraulics, pgs. 20-35, September 1982.

Symolon, P.D., Todreas, N.E. and Rohsenow, W.M., "Criteria for Onset of Mixed Convection and Onset of Flow Recirculation in Vertical Rod Bundles," Volume 2, pgs 1391-1402, Second International Topical Meeting on Nuclear Reactor Thermal-Hydraulics held in Santa Barbara, CA, January 1983.

Wong, C.C., and Todreas, N.E., "Local Heat Transfer Analysis for LMFBR Wire Wrapped Rod Bundle" International Conference on Numerical Methods in Nuclear Engineering Montreal pg. 806-828, September 1983.

Wong, C. C., and Todreas, N. E., "Wire Wrapped Rod Bundle Heat Transfer Analysis for LMFBR" First Proceedings of Nuclear Thermal Hydaulics ANS Winter Meeting, San Francisco, pgs 36-43 October 1983.

Symolon, P. D., Todreas, N. E., and Rohsenow, W. M. "Criteria for the Onset of Flow Recirculation and Onset of Mixed Convection in Vertical Rod Bundles." ASME Paper 84-HT-101, August 1984.

TABLE OF CONTENTS

page

LIST OF FIGURES

LIST OF FIGURES (cont'd)

LIST OF FIGURES (cont'd)

LIST OF FIGURES (cont'd)

LIST OF FIGURES (cont'd)

ACKNOWLEDGEMENTS

The continued support of the Department of Energy and its predecessor agencies is gratefully acknowledged. The senior investigator greatly acknowledges the large number of students, laboratory technicians and secretaries who contributed throughout the project tenure with so much dedication and skill. The help of Kerry Basehore and Shih Kuei Cheng in preparing this final report was keenly appreciated.

The students who worked on this project are noted below:
E. Khan, T. Eaton, Y. B. Chen, P. Carajilescov, B. Chen, F. Carre, H. Ninokata, R. Anoba, B. Bosy, R. G. Bennett, K. L. Basehore, R. Masterson, S. Glazer, J. T. Hawley, C. Chiu, J. Kelly, J. G. Bartzis, M. R. Fakori-Monazeh, A. S. Hanson, C-N Wong, R. Karimi, V. Manno, H. Khan, J. Y. Kim, M. K. Yeung, S. F. Wang, P. D. Symolon, K. J. Burns, T. E. Greene, D. R. Boyle, Y. N. Chan, S. K. Cheng

The professors who participated are Profs. L. Wolf, M. Golay, and W. Rohsenow.

LIST OF TABLES

LIST OF TABLES (Cont'd)

Chapter 1

Project Scope and Research Strategy

The objective of this project has been to develop the capability to predict temperature fields in LMFBR fuel and blanket rod assemblies under forced and mixed convection conditions. Two practical considerations dictated the strategy adopted to achieve this goal:

(1) Subchannel temperature at or near the exit of the assemblies were most needed. Duct axial temperature distributions were also of interest.

(2) A range of bundle characteristic parameters representing "normal" bundle geometries were considered in this mixing project. It is only recently that distorted geometries have been of interest.

These considerations lead to the adoption of the model described in Chapter 2 based on the energy equation to describe bundle performance. This model was formulated to be dependent only on input parameters which could be accurately obtained from experiment. Since this model is based on lead length averaged parameters its applicability within the first lead length is somewhat limited and it does not map localized fluctuations within a lead length. However, for prediction of temperatures in heated rod bundles cooled by sodium within the bounds outlined above under considerations (1) and (2),

desired design accuracy is achieved. The model when embodied as a numerical computer program i.e., the ENERGY family of codes, yielded the desired fast running temperature field solution.

The ENERGY series codes are therefore empirical tools made accurate by extensive calibration of physically based correlations of the defined and bounded geometric range. Within the broad range that they have been validated which includes sodium operation under forced and mixed convection conditions, ENERGY IV (the final product) predicts results with an accuracy equal to or better than alternate codes. However outside this geometry range such as with distorted bundles, tools such as COBRA which simultaneously solve the coupled set of conservation equations shoul be employed. Project topical report 32TR* further expands on the fundamentals of the comparative capabilities of ENERGY and other computer codes.

In executing this strategy, three general types of activities were carried out in parallel.

1. Computer Tools Development (Chapter 3)
2. Constitutive Relation Development (Chapters 4 and 5)
3. Experimental Technique Development (Chapter 6)
4. Computer Code Validation (Chapter 8)

These are sequentially discussed in Chapters 3 through 8 after the basic model is described in Chapter 2. Two chapters are devoted to constitutive relations; Chapter 4 to friction factor correlations and Chapter 5 to mixing parameter correlations. Chapters 2, 4, 5, 7 and 8 are drawn from the final investigation of this project by Cheng and

---

* The full listing of progress and topical reports, summaries and papers published under this project is presented on pages i through xvii.

Todreas reported in 108 TR. In this effort previous correlations were modified and extended to produce a comprehensive, consistent set of constitutive relations and a validated version of the ENERGY IV code. Chapter 8 includes a valuable set of operating condition maps defining regions of importance for the various energy transfer mechanisms.

Several important areas in LMFBR thermal hydraulics related to the main project objective were also explored in this project. They will only be mentioned briefly and referenced in this report. The interested reader should refer to the list of project reports for this information.

CHAPTER 2

SIMPLE SUBCHANNEL ANALYSIS METHOD: THE ENERGY CODE

2.1 General Equations for Subchannel Analysis

Generally, all thermal analysis methods for rod bundles start from the basic governing equations for mass, momentum and energy balance. These equations are then integrated over control volumes used for the method and simplified by some assumptions. This is the typical so-called lumped parameter method. Two kinds of approaches are currently prevalent, one is the subchannel approach; the other is the porous body approach. The subchannel approach uses control volumes defined by the typical subchannel in rod bundles, as shown in Figure 2.1 for a hexagonal LMFBR subassembly while the porous body approach treats the rod bundles as a porous medium, approximating it as a continuum. Hence the control volumes in the porous body approach can theoretically be any size as long as their porosity and permeability can be calculated.

Major benefit for the porous body approach is that the mesh size can be enlarged to be more than a conventional subchannel, hence reducing the computational time for large bundles. In addition, it might be easier to understand some assumptions by imagining a complicated wire-wrapped rod bundle as a homogeneous continuum. However, the final equations for the porous body approach are essentially the same as the subchannel approach if the control volumes are defined in the same conventional way. Lumping many subchannels into one bigger subchannel can also be done in the subchannel approach.

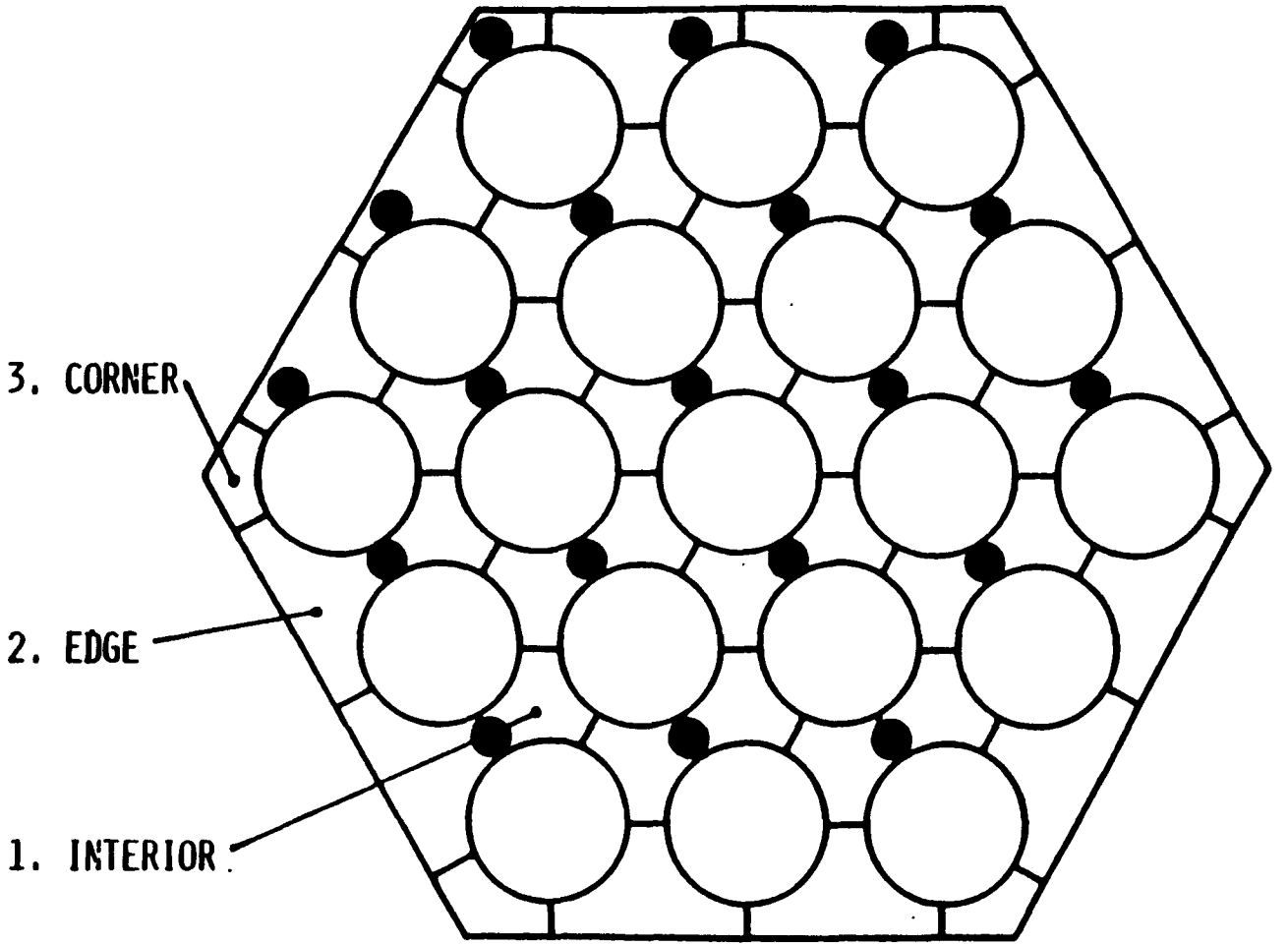

Figure 2.1 Typical Subchannels in LMFBR Wire-Wrapped Bundle

Since all the empirical parameters introduced later in this study are reduced by the subchannel approach, their application to the porous body approach using a different mesh geometry is doubtful. On the other hand, the introduction of porous body representation introduces complexity and confusion in the notation. Therefore, in this study, the subchannel approach will be used.

The general integral equations for the subchannel approach for axially dominant flow have been derived by Todreas (1984). The subchannel equations were presented in the following form.

Continuity

$$A_i \Delta z \frac{\partial}{\partial t} \langle \rho_i \rangle + \Delta \dot{m}_i = - \Delta z \sum_{j=1}^{J} W_{ij} \tag{2.1}$$

Energy

$$A_i \Delta z \frac{\partial}{\partial t} [\langle \rho h \rangle_i] + \Delta [\dot{m}_i \{h_i\}] = A_i \Delta z Q_i$$

$$- \Delta z \sum_{j=1}^{J} W_{ij}^{*H} (h_i - h_j) - \Delta z \sum_{j=1}^{J} W_{ij} \{h^*\} + A_i \Delta z \left\langle \frac{dP_i}{dt} \right\rangle \tag{2.2}$$

Axial Momentum

$$\Delta z \frac{\partial}{\partial t} \langle \dot{m}_i \rangle + \Delta [\dot{m}_i \{v_i\}] = -A_i \Delta z \langle \rho_i \rangle g$$

$$-A_i \Delta \{P\} - \Delta z \sum_{j=1}^{J} W_{ij}^{*M} (v_i - v_j) - \Delta z \sum_{j=1}^{J} W_{ij} \{v^*\} - \{F_{iz}\} \tag{2.3}$$

Transverse Momentum

$$\frac{\partial}{\partial t} \langle W_{ij} \rangle + \frac{\Delta}{\Delta x'} [W_{ij} \{u\}] + \frac{\Delta}{\Delta z} [W_{ij} \{v\}]$$

$$= - \left[s_{ij} \frac{\Delta}{\Delta x'} \{P\} \right] - \left\{ \frac{F_{ix}}{\Delta x' \Delta z} \right\} \tag{2.4}$$

where $\langle\ \rangle$ = indicates volume average over a control volume V_f

$$\langle\Psi\rangle \equiv \frac{1}{V_f}\int_{V_f}\Psi dV$$

$\{\ \}$ = indicates area average over a flow area A_f

$$\{\Psi\} \equiv \frac{1}{A_f}\int_{A_f}\Psi dA$$

$\Delta\Psi \equiv \Psi$ at $z+\Delta z$ - Ψ at z

z = axial direction

x = transverse direction

v = local axial velocity

u = local transverse velocity

h = local enthalpy

ρ = local fluid density

P = static pressure

$\dot{m} = \{\rho vA\}$

A_i = axial subchannel flow area

s_{ij} = gap between subchannel i and j

Δz = axial length of control volume used

$\Delta x'$ = transverse characteristic length

$v_i = \langle v_i \rangle$

$h_i = \langle h_i \rangle$

W_{ij}^{*H} = effective mass exchange rate per unit length between subchannel i and j for energy transfer

W_{ij}^{*M} = effective mass exchange rate per unit length between subchannels i and j for momentum transfer

W_{ij} = transverse mass flow rate per unit length from subchannel i to j = $s_{ij} \{\rho u\}$

$\{h^*\}$ = effective enthalpy transported by transverse flow

$\equiv \{\rho uh\}/\{\rho u\}$

$\{v^*\}$ = effective velocity transported by transverse flow

$\equiv \{\rho uv\}/\{\rho u\}$

F_{ix}, F_{iz} = total force on the fluid at x, z direction due to fluid-solid interaction

Q_i = equivalent dispersed heat source per unit volume

Figures 2.2, 2.3 and 2.4 illustrate the control volume and most of the terms for the continuity, energy and axial momentum equations, respectively. The transverse momentum equation is not used in our model as will be discussed in the next section.

Using this set of equations and some assumptions, a set of subchannel equations was adopted for a simple computer code, ENERGY-IV.

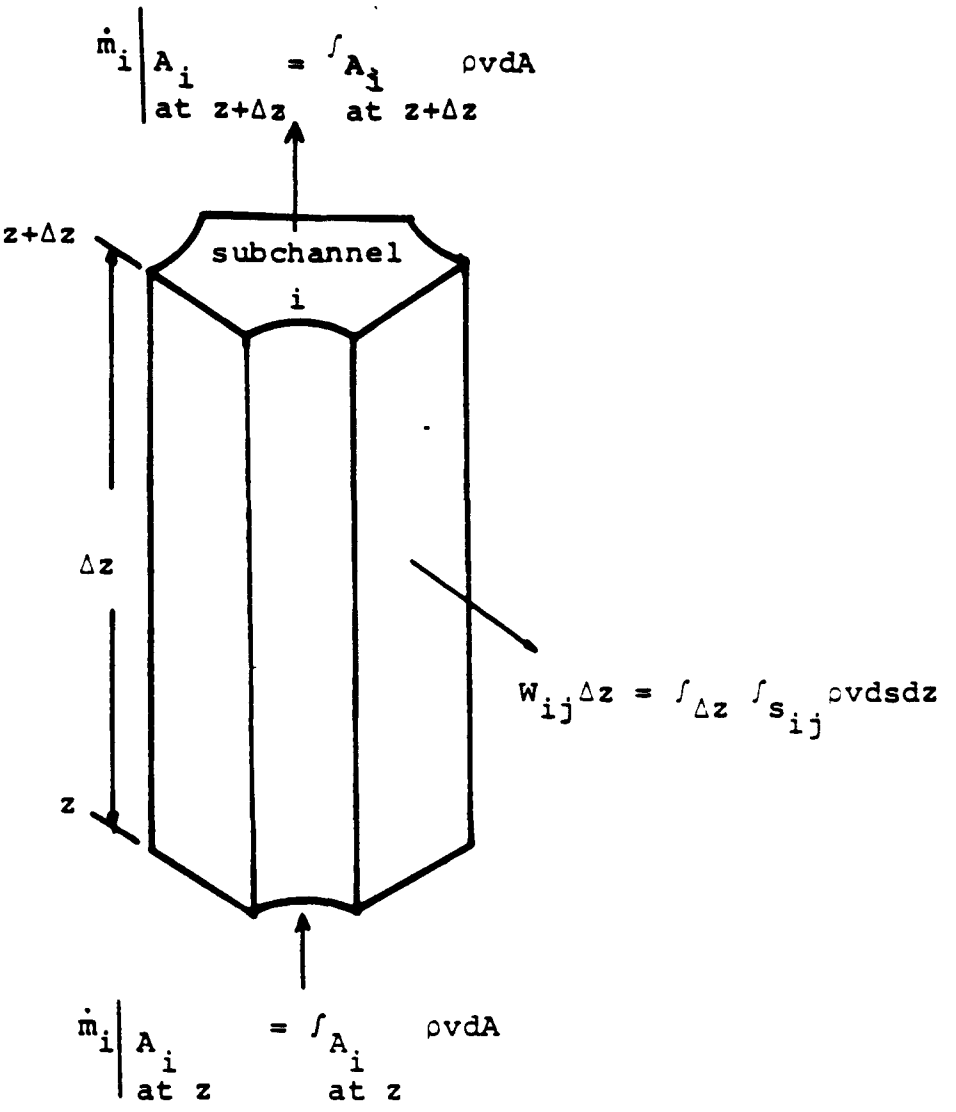

Figure 2.2 Subchannel Control Volume for Continuity Equation

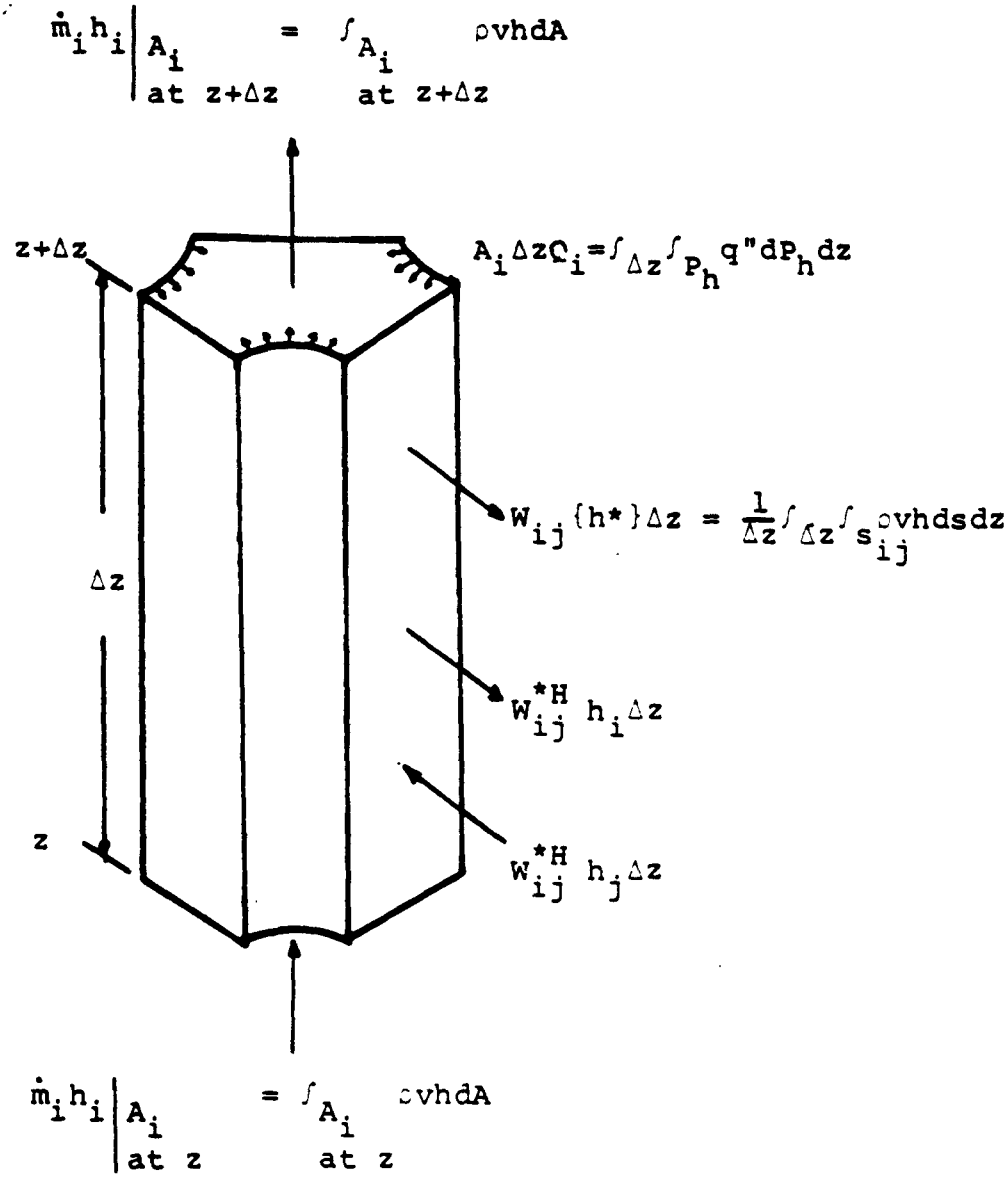

Figure 2.3 Subchannel Control Volume for Energy Equation

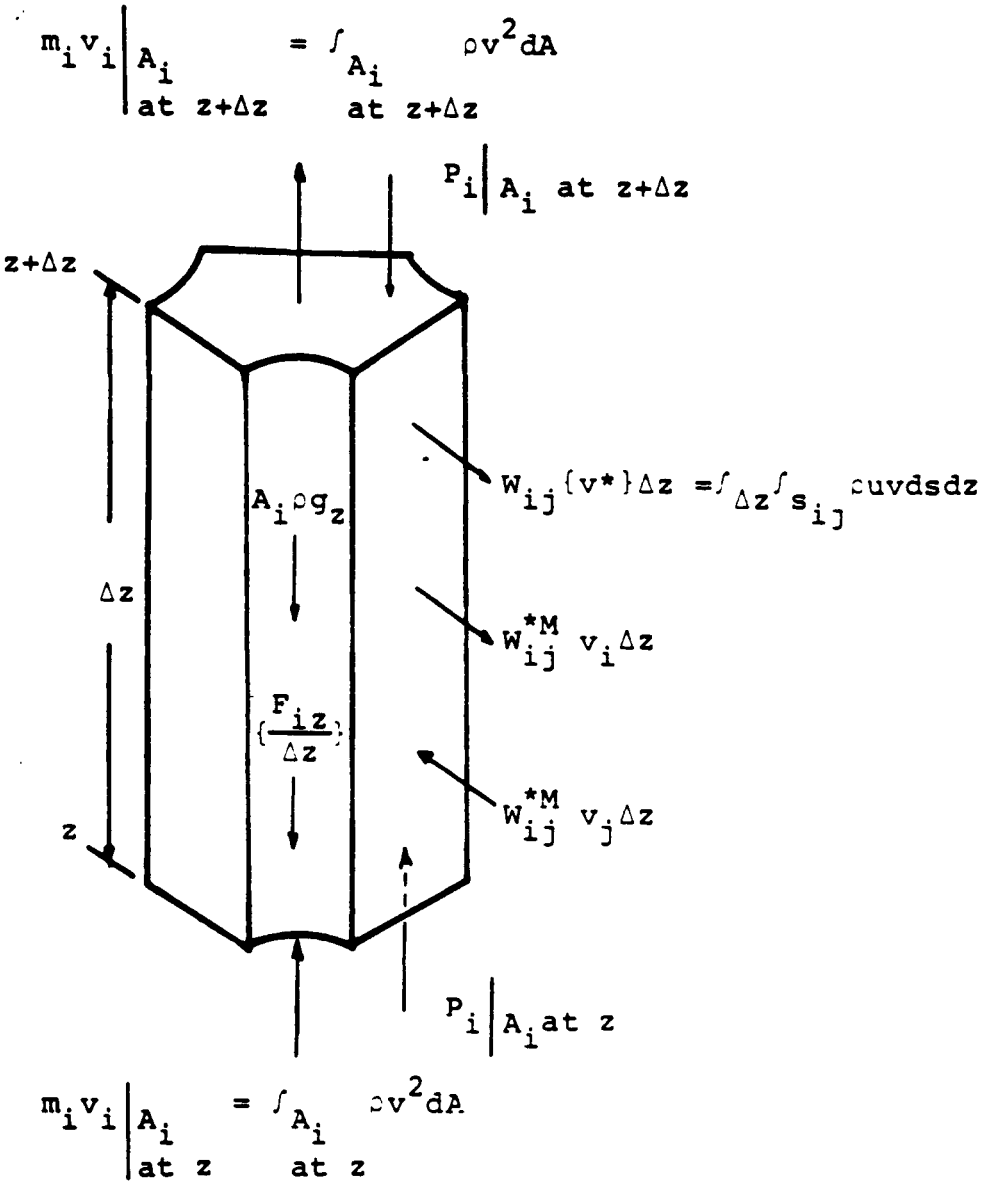

Figure 2.4 Subchannel Control Volume for Axial Momentum Equation

2.2 Simple Subchannel Analysis Model for Wire-Wrapped LMFBR Subassembly

2.2.1 Two Region Approach

In a wire-wrapped LMFBR subassembly, the wire-wrapped rods are packed in an array which is enclosed by a flow duct. As a result there is a region of flow next to the duct wall which is quite different in character from the flow in the interior region. In the interior region the mean flow oscillates around each rod while progressing in an axial direction. This oscillation of flow may be imagined to contribute an effective eddy diffusivity superimposed on the normal eddy diffusivity associated with turbulent interchange. In the outer region near the wall, i.e., the edge region, since the wire wrap is spiralled around each rod in the same direction, the flow progresses with both an axial component and a tangential component parallel to the wall.

Thus, a basis of our simple model is the existence of a uniform lateral effective enhanced (by the wire) eddy diffusivity for the heat transfer in the interior region and a uniform transverse velocity, V_T along the duct wall in the edge region. These two parameters are integral values averaged over a wire lead length. The local wire position effect is therefore not modeled. In our model these two parameters will be empirically determined and treated as input parameters to the code. Figure 2.5 illustrates the two regions and these two parameters.

Regarding conservation equations used in our model, the first simplifying assumption is that the pressure is uniformly distributed across the assembly. This gives constant pressure in each axial plane of the bundle and enables us to discard the transverse momentum

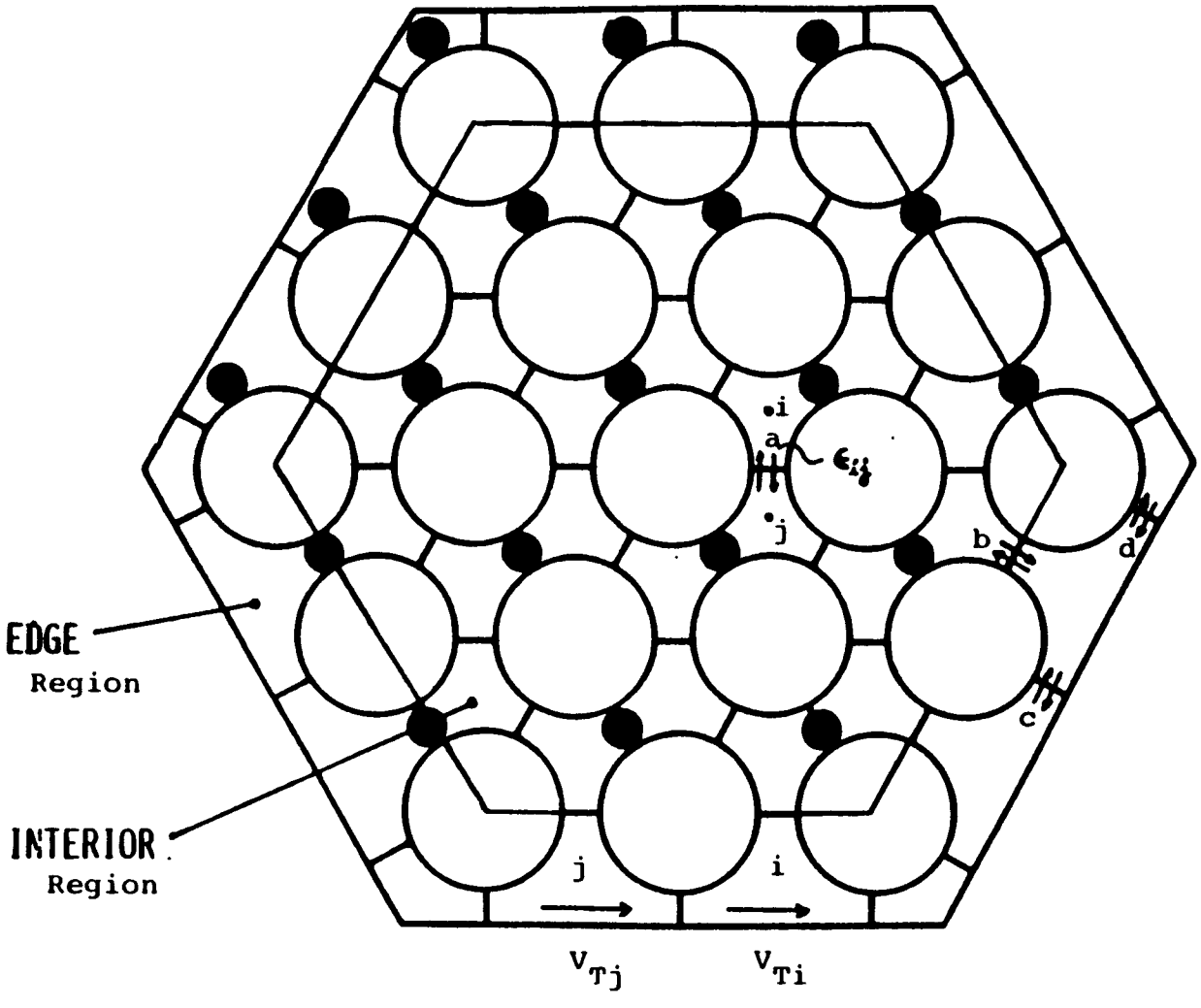

Figure 2.5 Two Region Approach for LMFBR Subchannel Analysis

equation. Because no transverse momentum equation is used, the cross flow can not be calculated at each gap. Only the total cross flow for each subchannel can be calculated by substituting the crossflow terms

$$\sum_{j=1}^{J} W_{ij} \{h^*\} \text{ and } \sum_{j=1}^{J} W_{ij} \{v^*\}$$

into the energy and momentum equations respectively, from the continuity equation.

To compensate for the equal pressure drop assumption the bundle inlet flow distribution must be empirically supplied as an input parameter for the code. In this study, the inlet velocity field is assumed to consist of three constant values for three kinds of subchannels i.e., V_1 for the interior subchannel, V_2 for the edge subchannel, and V_3 for the corner subchannel. Specifically, we define three flow split input parameters X_1, X_2, and X_3 as V_1/V_2, V_2/V_b, and V_3/V_b respectively where V_b is the bundle average velocity.

2.2.2 Treatment of Continuity Equation

Since only the steady state condition is considered in this work, all time dependent terms in the conservation equation are dropped. The continuity equation then becomes:

$$\frac{\Delta \dot{m}_i}{\Delta z} = - \sum_{j=1}^{J} W_{ij} \qquad (2.5)$$

where W_{ij} is the transverse mass flow rate per unit length from subchannel i to j. In the interior region, since the wire sweeping flow is modelled by an effective eddy diffusivity, no net crossflow will be

introduced by wire. However, in the edge region, a uniform transverse velocity is assumed to model the wire sweeping effect. Hence, there is a net cross flow transported by this velocity, in addition to the cross flow caused by the requirement to keep subchannel axial pressue drops equal.

As shown in Figure 2.5, subchannel i in the edge region gains mass at flow rate $\Delta z D_g \rho_j V_{Tj}$ from subchannel j and transports mass at flow rate $\Delta z D_g \rho_i V_{Ti}$ to subchannel k where Dg is the gap between subchannels in the edge region. Hence, the continuity equation for subchannels in the edge region becomes

$$\frac{\Delta \dot{m}_i}{\Delta z} = - \sum_{j=1}^{J} W_{ij} + D_g \left[\rho_j V_{Tj} - \rho_i V_{Ti} \right] \tag{2.6}$$

Note that W_{ij} always denotes the cross flow caused by momentum balance.

2.2.3 Treatment of Energy Equation

For the steady state condition, the subchannel energy conservation equation for an interior subchannel, equation (2.4), becomes

$$\frac{\Delta}{\Delta z} \left[\dot{m}_i \{h_i\} \right] = A_i Q_i - \sum_{j=1}^{J} W_{ij}^{*H} \left[h_i - h_j \right] - \sum_{j=1}^{J} W_{ij} \{h^*\} \tag{2.7}$$

The term $W_{ij}^{*H} (h_i - h_j)$ is the total effective energy exchange rate per unit length contributed by both the effective conduction due to the molecular effects and the effective mixing due to wire sweeping and turbulent interchange which we label "mixing."

$$W_{ij}^{*H}(h_i - h_j) = q''_{ij}\, s_{ij}\Big|_{\text{conduction}} + q''_{ij}\, s_{ij}\Big|_{\text{mixing}} \qquad (2.8)$$

In a hexaganal rod bundle, there are four kinds of subchannel pairs. As also illustrated in Figure 2.5, in which gap a is between interior and interior subchannels; gap b is between interior and edge subchannels; gap c is between edge and edge subchannels; and gap d is between edge and corner subchannels. The s_{ij} in equation (2.8) is the gap between rods for a, b and gap between rod and wall for c, d. In gaps c, d, the wires sweep flow in the same direction which is modelled by a uniform transverse velocity. Hence the wire-sweeping effects are not included in $q''_{ij}\, s_{ij}\Big|_{\text{mixing}}$, and only the natural turbulence interchange is counted. In gaps a, b, the wire sweeping effects are the major contributions to $q''_{ij} s_{ij}\Big|_{\text{mixing}}$.

The effective conduction between subchannels can be formulated as

$$q''_{ij} s_{ij}\Big|_{\text{conduction}} = \int_{s_{ij}} \left[- k \frac{\partial T}{\partial n}\Big|_{\text{gap}}\right] ds$$

$$= k \frac{T_i - T_j}{\ell_{ij}} S_{ij} \qquad (2.9)$$

where ℓ_{ij} is an effective mixing length defined by equation (2.9) which allows the gradient across the gap to be expressed in terms of the available subchannel average temperatures T_i and T_j, i.e.,

$$\ell_{ij} \equiv \frac{k(T_i - T_j)}{\frac{1}{s_{ij}} \int_{s_{ij}} \left[- k \frac{\partial T}{\partial n}\Big|_{\text{gap}}\right] ds} \qquad (2.10)$$

These parameters are shown in Figure 2.6 which illustrates the difference between the subchannel centroid to centroid distance, η_{ij}, and the effective mixing length, ℓ_{ij}. Now a parameter called the conduction shape factor, κ, is defined as

$$\kappa \equiv \frac{\eta_{ij}}{\ell_{ij}} \tag{2.11}$$

The contribution of energy transfer by effective conduction can be then formulated as

$$q_{ij}s_{ij}\Big|_{\text{conduction}} = \kappa k \left(\frac{T_i - T_j}{\eta_{ij}}\right) s_{ij} = \rho s_{ij} \kappa \left(\frac{\alpha}{\eta_{ij}}\right) (h_i - h_j) \tag{2.12}$$

where α = thermal diffusivity $\equiv k/\rho Cp$

The contribution of energy transfer due to wire sweeping and turbulent interchange effects will be combined as one term and modelled by an enhanced eddy diffusivity. Usually, the energy transfer by turbulent interchange only is written as

$$q''_{ij}\, s_{ij}\Big|_{\substack{\text{turbulent} \\ \text{interchange}}} = W'_{ij}\,(h_i - h_j) \tag{2.13a}$$

where W'_{ij} is the effective mass exchange rate between subchannel i and j due to turbulent interchange. Assuming that the sweeping flow caused by wire can also be treated as an uniform bidirectional transverse flowrate just as that of the turbulent interchange, the effective wire effect can be written as

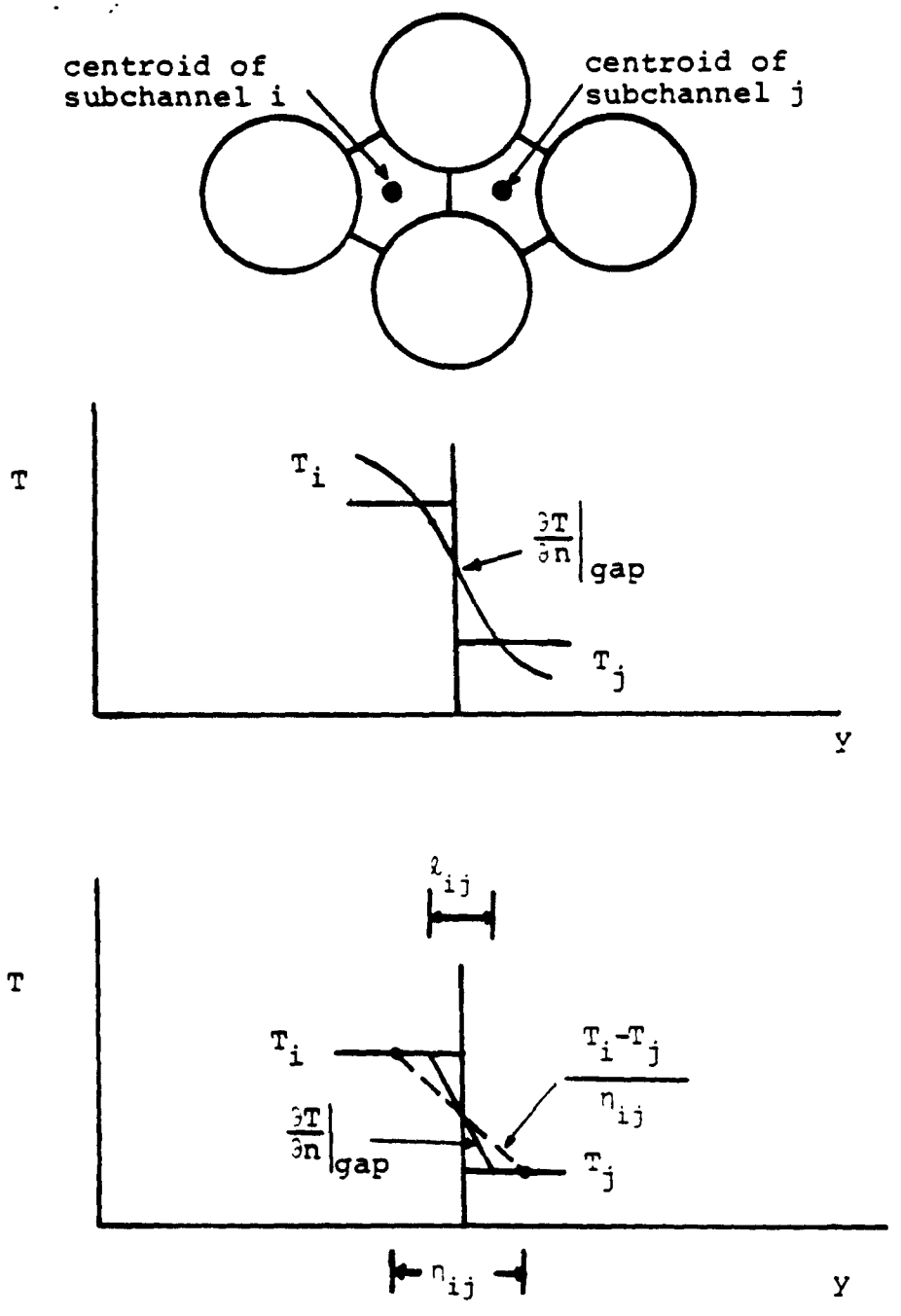

Figure 2.6 Difference between the Subchannel Centroid to Centroid Distance and Laminar Mixing Length

$$q''_{ij}\ s_{ij}\Big|_{\text{wire}} = W'^{W}_{ij}\ (h_i - h_j) \tag{2.13b}$$

where W'^{W}_{ij} represents the effective mass exchange rate due to the effects of wire sweeping. Combining equations (2.13a) and (2.13b) we obtain the total mixing effect as

$$q''_{ij}\ s_{ij}\Big|_{\text{mixing}} = W'^{T}_{ij}\ (h_i - h_j) \tag{2.14}$$

where $W'^{T}_{ij} \equiv W'_{ij} + W'^{W}_{ij}$;

Note that for gaps c and d, $W'^{W}_{ij} = 0$.

Using the eddy diffusivity concept, one can alternatively formulate this total mixing energy transfer as

$$q''_{ij}\ s_{ij}\Big|_{\text{mixing}} = \rho\ s_{ij}\ \varepsilon_{ij}\left(\frac{h_i - h_j}{\eta_{ij}}\right) \tag{2.15}$$

where

ε_{ij} = the effective eddy diffusivity defined by equation (2.15)

η_{ij} = subchannel centroid to centroid distance

ρ = coolant density at the gap

The physical meaning of ε_{ij} can be made clear by comparing equation (2.15) to equation (2.14), i.e.,

$$\rho\frac{\varepsilon_{ij}}{\eta_{ij}} = \frac{W'^{T}_{ij}}{s_{ij}} \tag{2.16}$$

Hence $\rho(\varepsilon_{ij}/\eta_{ij})$ is the mass exchange rate per unit area at the gap, and $(\varepsilon_{ij}/\eta_{ij})$ represents the transverse velocity for this exchange.

From equations (2.12) and (2.15), the total energy transfer between subchannel i and j is finally written as

$$W_{ij}^{*H}(h_i - h_j) = \left[\rho s_{ij}\kappa\left(\frac{\alpha}{\eta_{ij}}\right) + \rho s_{ij}\left(\frac{\varepsilon_{ij}}{\eta_{ij}}\right)\right](h_i - h_j) \qquad (2.17)$$

Similar to the argument for the continuity equation, the transverse flow caused by the wire sweeping effect should be included in W_{ij} in the last term of equation (2.7) for the edge region. Hence for the edge region the last term of equation (2.7) becomes

$$\sum_{j=1}^{J} W_{ij}\{h^*\} + D_g\left[\rho_j V_{Tj} h_j - \rho_i V_{Ti} h_i\right]$$

The term $\sum_{j=1}^{J} W_{ij}\{h^*\}$ will be treated next. The enthalpy carried by cross flow, $\{h^*\}$, should be different for different gaps of a subchannel. However, in the final equations of our work, only the total cross flow rate $\sum_{j=1}^{J} W_{ij}$ will be calculated for each subchannel, and the energy transported by this total cross flow is approximated by multiplying it by a cross flow enthalpy H_i^* i.e.,

$$\sum_{j=1}^{J} W_{ij}\{h^*\} \approx H_i^* \sum_{j=1}^{J} W_{ij} \qquad (2.18)$$

The necessary value of H_i^* is a weighted average value determined from the average enthalpies of each subchannel and its adjacent subchannels.

The defining equation for H_i^* is

$$H_i^* \equiv \frac{\sum_{j=1}^{J} \left[\left| X_{ij} \right| (h_i + h_j) - X_{ij}(h_i - h_j) \right]}{2 \sum_{j=1}^{J} \left| X_{ij} \right|} \tag{2.19}$$

where $X_{ij} \equiv \Delta\dot{m}_i - \Delta\dot{m}_j$

$$\Delta\dot{m}_i \equiv \dot{m}_i \Big|_{z+\Delta z} - \dot{m}_i \Big|_z \qquad (\dot{m}_i \text{ is the mass flow rate of subchannel i})$$

The weighting factor X_{ij} represents the net gain in the rate of mass flow per unit cell between subchannel i and j along the length step Δz. With this definition the value of H_i^* is bounded by the least and greatest values of h for subchannel i and subchannels j.

Finally, the energy equation becomes

$$\frac{\Delta}{\Delta z} \left[\dot{m}_i \{h_i\} \right] = A_i Q_i - \sum_{j=i}^{J} \rho s_{ij} \left[\kappa \left(\frac{\alpha}{\eta_{ij}} \right) + \left(\frac{\varepsilon_{ij}}{\eta_{ij}} \right) \right] (h_i - h_j)$$

$$- H_i^* \sum_{j=1}^{J} W_{ij} + D_g \left[\rho_j V_{Tj} h_j - \rho_i V_{Ti} h_i \right] \tag{2.20}$$

Note that for the interior region, there is no V_{Ti} or V_{Tj}, hence the last term is zero.

2.2.4 Treatment of Axial Momentum Equation

For the steady state condition, the axial momentum equation, equation (2.3), becomes

$$\frac{\Delta}{\Delta z}\left[\dot{m}_i\{v_i\}\right] = A_i\langle\rho_i\rangle g - A_i\frac{\Delta\{p\}}{\Delta z} - \sum_{j=1}^{J} W_{ij}^{*M}(v_i - v_j)$$

$$- \sum_{j=1}^{J} W_{ij}\{v^*\} - \frac{\{F_{iz}\}}{\Delta z} \qquad (2.21)$$

The effective momentum transfer rate per unit axial length $W_{ij}^{*M}(v_i - v_j)$ can be treated similarly to that in the energy equation. We further assume that the molecular contribution, i.e., viscous effect, is negligible compared to the effective mixing contribution. Therefore, this term can be written as

$$\text{Momentum transfer} = \rho\, s_{ij}\, \varepsilon_{ij}^{m}\left(\frac{v_i - v_j}{\eta_{ij}}\right) \qquad (2.22)$$

The effective eddy diffusivity for momentum transfer ε_{ij}^{m} is assumed to be the same as ε_{ij} for energy transfer since both the mass exchange rates for momentum and energy transfer come mainly from the same wire sweeping flow effects.

The term $W_{ij}\{v^*\}$ can also be treated similarly to that in the energy equation. The definition for the velocity transported by cross flow is exactly the same as equation (2.19) except that v is used in place of h. The same weighting factor X_{ij} is used. The momentum transported by cross flow is then

$$- v_i^* \sum_{j=1}^{J} W_{ij} + D_g\left[\rho_j V_{Tj} v_j - \rho_i V_{Ti} v_i\right]$$

The last term in equation (2.21) is the force per unit length on the fluid at x direction due to fluid-solid interaction. If τ is the average shear stress including both rod surface friction loss and wire drag loss, then the force per unit length is $\tau \cdot P_w$, where P_w is the

wetted perimeter for that subchannel. But τ is usually calculated by

$$\tau = \left(\frac{f_i}{4}\right)\left(\frac{\rho_i v_i^2}{2}\right) \tag{2.23}$$

where f_i is the subchannel friction faction, hence

$$\frac{\{F_{iz}\}}{\Delta z} = \tau \cdot P_w = f_i \frac{P_w}{4} \frac{\rho_i v_i^2}{2}$$

$$= A_i f_i \frac{P_w}{4A_i} \frac{s_i v_i^2}{2} = A_i \frac{f_i}{De_i} \frac{\rho_i v_i^2}{2} \tag{2.24}$$

where De_i= subchannel hydraulic equivalent diameter $\equiv P_w/4A_i$

Finally, the axial momentum equation becomes

$$\frac{\Delta}{\Delta z}\left[\dot{m}_i\{v_i\}\right] = -A_i\langle\rho_i\rangle g - A_i \frac{\Delta\{p\}}{\Delta z} - A_i \frac{f_i}{De_i} \frac{\rho_i v_i^2}{2}$$

$$- \sum_{j=1}^{J} s_{ij}\left(\frac{\varepsilon_{ij}}{\eta_{ij}}\right)(v_i - v_j) - V_i^* \sum_{j=1}^{J} W_{ij} + D_g\left[\rho_j V_{Tj} v_j - \rho_i V_{Ti} v_i\right] \tag{2.25}$$

2.3 Finite Difference Equations for the ENERGY-IV Code

2.3.1 Finite Difference Equations for the Forced Convection Condition

In the forced convection regime, the buoyancy-induced cross flow is negligible. The velocity distribution is assumed to be constant throughout the length of the bundle. Thus, only the energy equation needs to be solved to determine the temperature distribution.

In addition to the fixed velocity distribution assumption, the following assumptions are used to simplify the final energy equation for the forced convection condition.

1) constant density and thermal properties throughout the bundles.

By constant density and constant velocity, the cross flow $\sum_{j=1}^{J} W_{ij}$ is forced to be zero since the axial mass flow distribution does not change with position from the prescribed inlet distribution.

2) in calculating the energy transfer, the average enthalpy of each node is approximated by the enthalpy at the exit of the last axial step of that node. Hence no iteration will be needed for calculating the enthalpy at the exit of each step.

3) the transverse velocity is the same for all the subchannels in the edge region.

By the above assumptions, the energy equation, equation (2.20) will be written as finite different equations for different kinds of subchannels. In the following equations, the subscripts 1, 2, 3, refer to interior, edge and corner subchannels, respectively. The subscript ij refers to the quantity relating to subchannel types i and j.

Interior Subchannels

A control volume and noding scheme for an interior subchannel is illustrated in Figure 2.7a. In this case, equation (2.20) becomes

$$\rho A_1 v_1 \frac{\Delta h_1}{\Delta z} = A_1 Q_1 + \rho c \left[\kappa_{11}\left(\frac{\alpha}{\eta_{11}}\right) + \left(\frac{\varepsilon_{11}}{\eta_{11}}\right)\right](h_i + h_j - 2h_1)$$

$$+ \rho c \left[\kappa_{1x}\left(\frac{\alpha}{\eta_{1x}}\right) + \left(\frac{\varepsilon_{1x}}{\eta_{1x}}\right)\right](h_k - h_1) \qquad (2.26)$$

where c = gap between rods, i.e., s_{11} or s_{12} = P - D

x = 1 if the third adjacent subchannel is an interior subchannel

= 2 if the third adjacent subchannel is an edge subchannel

Dividing equation (2.26) by $\rho A_1 v_1$, we have

a. Interior Subchannel

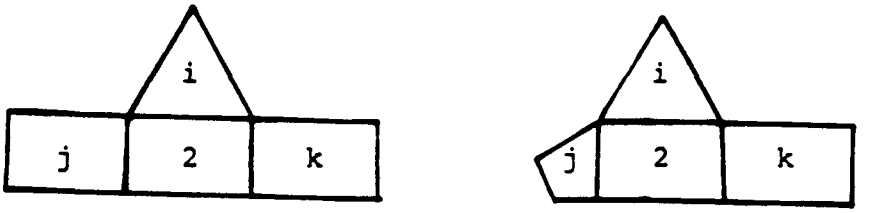

b. Edge Subchannel

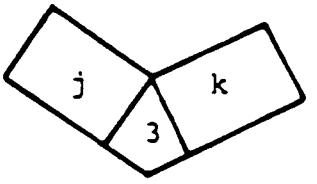

c. Corner Subchannel

Figure 2.7 Control Volumes and Noding Scheme for Different Kinds of Subchannels

$$\frac{\Delta h_1}{\Delta z} = \frac{Q_1}{\rho v_1} + \frac{c}{A_1}\left[\kappa_{11}\left(\frac{\alpha}{v_1 \eta_{11}}\right) + \left(\frac{\varepsilon_{11}}{v_1 \eta_{11}}\right)\right](h_i + h_j - 2h_1)$$

$$+ \frac{c}{A_1}\left[\kappa_{1x}\left(\frac{\alpha}{v_1 \eta_{1x}}\right) + \left(\frac{\varepsilon_{1x}}{v_1 \eta_{1x}}\right)\right](h_k - h_1) \qquad (2.27)$$

Edge Subchannel

A control volume and noding scheme for an edge subchannel is illustrated in Figure 2.7b. An edge subchannel has three neighbors. One is always an interior subchannel, and the other two may be either edge or corner subchannels. In this case, after dividing $\rho A_2 v_2$ equation (2.20) becomes

$$\frac{\Delta h_2}{\Delta z} = \frac{Q_2}{\rho v_2} + \frac{c}{A_2}\left[\kappa_{12}\left(\frac{\alpha}{v_2 \eta_{12}}\right) + \left(\frac{\varepsilon_{12}}{v_2 \eta_{12}}\right)\right](h_i - h_2)$$

$$+ \frac{D_g}{A_2}\left[\kappa_{2x}\left(\frac{\alpha}{v_2 \eta_{2x}}\right) + \left(\frac{\varepsilon_{2x}}{v_2 \eta_{2x}}\right)\right](h_j - h_2)$$

$$+ \frac{D_g}{A_2}\left[\kappa_{2y}\left(\frac{\alpha}{v_2 \eta_{2y}}\right) + \left(\frac{\varepsilon_{2x}}{v_2 \eta_{2y}}\right)\right](h_k - h_2)$$

$$+ \frac{D_g}{A_2}\left(\frac{V_T}{v_2}\right)(h_j - h_2) \qquad (2.28)$$

where

D_g = gap between rod and wall

x (or y) = 2 if node j (or k) is an edge subchannel

= 3 if node j (or k) is a corner subchannel

Corner Subchannel

A control volume and noding scheme for a corner subchannel is illustrated in Figure 2.7c. A corner subchannel is always adjacent to two edge subchannels. In this case, after dividing by $\rho A_3 v_3$, equation (2.20) becomes

$$\frac{\Delta h_3}{\Delta z} = \frac{Q_3}{\rho v_3} + \frac{D_g}{A_3}\left[\kappa_{23}\left(\frac{\alpha}{v_3 \eta_{23}}\right) + \left(\frac{\varepsilon_{23}}{v_3 \eta_{23}}\right)\right](h_j + h_k - h_3)$$

$$+ \frac{D_g}{A_3}\left(\frac{V_T}{v_3}\right)(h_j - h_3) \qquad (2.29)$$

In these different equations, equations (2.27), (2.28), and (2.29), the following nondimensional parameters need to be inputted:

a) Flow split parameters X_1, X_2, X_3 for calculating v_1, v_2, and v_3 at a given bundle flow rate,

b) Conduction shape factors, κ_{11}, κ_{12}, κ_{22}, κ_{23}, for interior to interior subchannel, interior to edge subchannel, edge to edge subchannel and edge to corner subchannel.

c) Mixing parameters, related to eddy diffusivity,

$$\left(\frac{\varepsilon_{11}}{v_1 \eta_{11}}\right),\ \left(\frac{\varepsilon_{12}}{v_1 \eta_{12}}\right),\ \left(\frac{\varepsilon_{12}}{v_2 \eta_{12}}\right),\ \left(\frac{\varepsilon_{22}}{v_2 \eta_{22}}\right),\ \left(\frac{\varepsilon_{23}}{v_2 \eta_{23}}\right),\ \left(\frac{\varepsilon_{23}}{v_3 \eta_{23}}\right)$$

related to transverse velocity,

$$\left(\frac{V_T}{v_2}\right),\ \left(\frac{V_T}{v_3}\right)$$

Note that in our two region approach, ε_{11}, ε_{12} and V_T are related to the wire sweeping effects, while ε_{22} and ε_{23} are only related to the conventional turbulent interchange between subchannels in the edge region.

The forms of above mixing parameters suggest defining the following dimensionless parameters for use in these equations:

Dimensionless effective eddy Diffusivity (DEED), $\varepsilon^*_{1\eta}$ for the interior region

$$\varepsilon^*_{1\eta} \equiv \frac{\varepsilon_{11}}{v_1 \eta_{11}} \tag{2.30}$$

Edge Transverse Velocity Ratio (ETVR), C_{1L}, for the edge region

$$C_{1L} \equiv \frac{V_T}{v_2} \tag{2.31}$$

The physical meaning of $\varepsilon^*_{1\eta}$ is easy to understand if one remembers that $(\varepsilon_{ij}/\eta_{ij})$ represents the transverse velocity at the interior gap from equation (2.16). Therefore,

$$\varepsilon^*_{1\eta} = \frac{W'^T_{ij}/s_{ij}}{\rho v_1} = \frac{\text{Transverse mass flux}}{\text{Axial mass flux}} \tag{2.32}$$

From this physical meaning, $\varepsilon^*_{1\eta}$ actually represents a transverse mass exchange rate. Note that if one enlarges the mesh size, the mass exchange rate per unit area at the mesh boundary should not be changed and no η_{ij} effect should show in the heat transfer by the mixing effect. This is one major merit of using $\varepsilon^*_{1\eta}$ which uses η_{ij} as the characteristic length in its definition, hence, η_{ij} correctly does not appear in the effective mixing term in the final energy equation.

Similar to the definition for DEED, a dimensionless eddy diffusivity, $\varepsilon^*_{2\eta}$ can also be defined for the edge region as

$$\varepsilon^*_{2\eta} \equiv \frac{\varepsilon_{22}}{v_2 \eta_{22}}$$

To simplify those mixing parameters, the following two assumptions will be adopted,

1) The transverse velocity for the effective mixing between interior and edge subchannels $\varepsilon_{12}/\eta_{12}$ is the same as that between interior and interior subchannels, $\varepsilon_{11}/\eta_{11}$.

2) Similarly the transverse velocity between edge and corner is the same as between edge subchannels, $\varepsilon_{23}/\eta_{23} = \varepsilon_{22}/\eta_{22}$

By the above definitions and assumptions, these mixing parameters become

$$\frac{\varepsilon_{11}}{v_1\eta_{11}} = \varepsilon^*_{1\eta}, \quad \frac{\varepsilon_{12}}{v_1\eta_{12}} = \varepsilon^*_{1\eta}, \quad \frac{\varepsilon_{12}}{v_2\eta_{12}} = \left(\frac{v_1}{v_2}\right)\left(\frac{\varepsilon_{12}}{v_1\eta_{12}}\right) = \left(\frac{X_1}{X_2}\right)\varepsilon^*_{1\eta},$$

$$\frac{\varepsilon_{22}}{v_2\eta_{22}} = \varepsilon^*_{2\eta}, \quad \frac{\varepsilon_{23}}{v_2\eta_{23}} = \varepsilon^*_{2\eta}, \quad \frac{\varepsilon_{23}}{v_3\eta_{23}} = \left(\frac{v_2}{v_3}\right)\left(\frac{\varepsilon_{23}}{v_2\eta_{23}}\right) = \left(\frac{X_2}{X_3}\right)\varepsilon^*_{2\eta},$$

$$\frac{V_T}{v_2} = C_{1L}, \quad \frac{V_T}{v_3} = \left(\frac{v_2}{v_3}\right)\left(\frac{V_T}{v_2}\right) = \left(\frac{X_2}{X_3}\right)C_{1L}$$

The finite different equations for the forced convection condition then become,

Interior subchannel

$$\frac{\Delta h_1}{\Delta z} = \frac{Q_1}{\rho v_1} + \frac{c}{A_1}\left[\kappa_{11}\left(\frac{\alpha}{v_1\eta_{11}}\right) + \varepsilon^*_{1\eta}\right](h_i + h_j - 2h_1)$$

$$+ \frac{c}{A_1}\left[\kappa_{1x}\left(\frac{\alpha}{v_1\eta_{1x}}\right) + \varepsilon^*_{1\eta}\right](h_k - h_1) \qquad (2.34)$$

Edge subchannel

$$\frac{\Delta h_2}{\Delta z} = \frac{Q_2}{\rho v_2} + \frac{c}{A_2}\left[\kappa_{12}\left(\frac{\alpha}{v_2 \eta_{12}}\right) + \left(\frac{X_1}{X_2}\right)\varepsilon^*_{1\eta}\right](h_i - h_2)$$

$$+ \frac{D_g}{A_2}\left\{\left[\kappa_{2x}\left(\frac{\alpha}{v_2 \eta_{2x}}\right) + \varepsilon^*_{2\eta}\right](h_j - h_2) + \left[\kappa_{2y}\left(\frac{\alpha}{v_2 \eta_{2y}}\right) + \varepsilon^*_{2\eta}\right](h_k - h_2)\right\}$$

$$+ \frac{D_g}{A_2} C_{1L}(h_j - h_2) \qquad (2.35)$$

Corner Subchannel

$$\frac{\Delta h_3}{\Delta z} = \frac{Q_3}{\rho v_3} + \frac{D_g}{A_3}\left[\kappa_{23}\left(\frac{\alpha}{v_3 \eta_{23}}\right) + \left(\frac{X_2}{X_3}\right)\varepsilon^*_{2\eta}\right](h_j + h_k - 2h_3)$$

$$+ \frac{D_g}{A_3}\left(\frac{X_2}{X_3}\right) C_{1L}(h_j - h_3) \qquad (2.36)$$

The empirical parameters which need to be determined are then:

- Flow split parameters: X_1, X_2, X_3
- Conduction shape factor: κ_{11}, κ_{12}, κ_{22}, κ_{23}
- Mixing parameters: $\varepsilon^*_{1\eta}$, $\varepsilon^*_{2\eta}$, C_{1L}

2.3.2 Finite Different Equations for the Mixed Convection Condition

At low flow rate, the net crossflow driven from the hot region to the cold region due to the buoyancy effect may be significant. This crossflow not only carries cold fluid to the hot region but also increases (decreases) the flow rate in the hot (cold) region. Therefore, the temperature distribution in the mixed convection

condition will be flatter than that in the forced convection condition in which this crossflow is negligible. Criteria for determining when the flow is in mixed convection have been proposed by Engel et al. (1982) and Symolon and Todreas (101TR).

To model this crossflow, the continuity, energy and momentum equations, equations (2.6), (2.20) and (2.25) must be simultaneously solved. However, the continuity equation is only used to obtain the net cross flow rate $\sum_{j=1}^{J} W_{ij}$ in terms of other quantities for each subchannel which are then utilized in the energy and momentum equations. These two conservation equations are coupled with one total mass balance equation

$$\sum_{i=1}^{I} \Delta \dot{m}_i = 0 \tag{2.37}$$

where I = total number of subchannels, and solved numerically.

From equation (2.6),

$$\Delta z \sum_{j=1}^{J} W_{ij} = -\Delta \dot{m}_i + D_g\left[\rho_j V_{Tj} - \rho_i V_{Ti}\right] \tag{2.38}$$

where for the interior subchannels the term in [] is zero. Substituting equation (2.38) and the following identities,

$$\Delta \dot{m}_i = (\rho_i v_i A_i)_{z+\Delta z} - (\rho_i v_i A_i)_z \tag{2.39}$$

$$\Delta[\dot{m}_i\{h_i\}] = (\rho_i v_i A_i h_i)_{z+\Delta z} - (\rho_i v_i A_i h_i)_z \tag{2.40}$$

where $z+\Delta z$ and z are the axial positions at inlet and exit of each node, into equation (2.20), the energy equation becomes,

$$\left[(\rho_i v_i A_i h_i)_{z+\Delta z} - (\rho_i v_i A_i h_i)_z\right] - H_i^* \left[(\rho_i v_i A_i)_{z+\Delta z} - (\rho_i v_i A_i)_z\right] =$$

$$A_i \Delta z Q_i - \Delta z \sum_{j=1}^{J} \rho s_{ij} \left[\kappa\left(\frac{\alpha}{\eta_{ij}}\right) + \left(\frac{\varepsilon_{ij}}{\eta_{ij}}\right)\right](h_i - h_j) +$$

$$D_g \Delta z \left[\rho_j V_{Tj}(h_j - H_i^*) - \rho_i V_{Ti}(h_i - H_i^*)\right] \tag{2.41}$$

Similarly, substituting equations (2.38), (2.39) and the following identities

$$\Delta[m_i\{v_i\}] = (\rho_i A_i v_i^2)_{z+\Delta z} - (\rho_i A_i v_i^2)_z \tag{2.42}$$

$$\Delta\{P\} = P_{z+\Delta z} - P_z \equiv \Delta P \tag{2.43}$$

into equation (2.25), the momentum equation becomes,

$$\left[(\rho_i A_i v_i^2)_{z+\Delta z} - (\rho_i A_i v_i^2)_z\right] - V_i^* \left[(\rho_i v_i A_i)_{z+\Delta z} - (\rho_i v_i A_i)_z\right] =$$

$$- A_i \Delta z \rho_i g - A_i \Delta z \frac{f_i}{De_i} \frac{\rho_i v_i^2}{2} - A_i \Delta P - \Delta z \sum_{j=1}^{J} \rho s_{ij} \left(\frac{\varepsilon_{ij}}{\eta_{ij}}\right)(v_i - v_j)$$

$$+ Dg \Delta z \left[\rho_j V_{Tj}(v_j - V_i^*) - \rho_i V_{Ti}(v_i - V_i^*)\right] \tag{2.44}$$

Now the following definitions and approximations are introduced

$$\Delta\rho = \rho_{z+\Delta z} - \rho_z, \text{ i.e., } \rho_{z+\Delta z} = \rho_z + \Delta\rho \tag{2.45a}$$

$$\Delta v = v_{z+\Delta z} - v_z, \text{ i.e., } v_{z+\Delta z} = v_z + \Delta v \tag{2.45b}$$

$$\Delta h = h_{z+\Delta z} - h_z, \text{ i.e., } h_{z+\Delta z} = h_z + \Delta h \tag{2.45c}$$

and

$$\Delta h \simeq R\Delta\rho, \text{ where } R \equiv \left(\frac{\partial h}{\partial \rho}\right)_p \text{ (at constant pressure)} \tag{2.45d}$$

$$\rho_i = \rho_{z+\Delta z/2} \simeq \rho_{iz} + \frac{\Delta\rho_i}{2} \tag{2.46a}$$

$$v_i = v_{z+\Delta z/2} \simeq v_{iz} + \frac{\Delta v_i}{2} \tag{2.46b}$$

The terms in the left hand side of equations (2.41) and (2.44) are expanded using equations (2.45a, b, c, d). The parameters ρ_i and v_i in the first two terms of the right hand side of equation (2.44) are substituted by equations (2.46a, b). After these arrangements and dividing by A_i , equations (2.41) and (2.44) become,

Energy equation

$$S_i \Delta\rho_i + T_i \Delta v_i = Q_i \Delta z + EEX_i \tag{2.47}$$

where

$$S_i = (v_{iz} + \Delta v_i)\left[R_i(\rho_{iz} + \Delta\rho_i) + h_{iz} - H_i^*\right] \tag{2.47a}$$

$$T_i = \rho_{iz}(h_{iz} - H_i^*) \tag{2.47b}$$

$$EEX_i = -\frac{\Delta z}{A_i} \sum_{j=1}^{J} \rho s_{ij}\left[\kappa\left(\frac{\alpha}{\eta_{ij}}\right) + \left(\frac{\varepsilon_{ij}}{\eta_{ij}}\right)\right](h_i - h_j)$$

$$+ \frac{Dg\,\Delta z}{A_i}\left[\rho_j V_{Tj}(h_j - H_i^*) - \rho_i V_{Ti}(h_i - H_i^*)\right] \tag{2.47c}$$

and Momentum Equation

$$E_i \Delta\rho_i + F_i \Delta v_i + \Delta P = G_i + MEX_i \tag{2.48}$$

where

$$E_i = (v_{iz} + \Delta v_i)(v_{iz} + \Delta v_i - V_i^*) + \frac{f_i \Delta z}{16De_i}(2v_{iz} + \Delta v_i)^2 + \frac{g\Delta z}{2} \tag{2.48a}$$

$$F_i = \rho_{iz}\left[\left(2 + \frac{f_i \Delta z}{2De_i}\right) v_{iz} + \left(1 + \frac{f_i \Delta z}{8De_i}\right) \Delta v_i - V_i^*\right] \tag{2.48b}$$

$$G_i = -\rho_{iz}\left(g\Delta z + \frac{f_i \Delta z}{2De_i} v_{iz}^2\right)$$

$$MEX_i = -\frac{\Delta z}{A_i} \sum_{j=1}^{J} \rho s_{ij} \left(\frac{\varepsilon_{ij}}{\eta_{ij}}\right)(v_i - v_j)$$

$$+ \frac{Dg\Delta z}{A_i}\left[\rho_j V_{Tj}(v_j - V_i^*) - \rho_i V_{Ti}(v_i - V_i^*)\right] \qquad (2.48d)$$

The total mass balance equation, equation (2.37) can be written in a similar form,

$$\sum_{i=1}^{I} A_i (v_{iz} + \Delta v_i)\Delta\rho_i + \sum_{i=1}^{I} A_i \rho_{iz} \Delta v_i = 0 \qquad (2.49)$$

Equations (2.47) and (2.48) when written for each subchannel and equation (2.49) form a system of 2I + 1 equations (I being the number of subchannels) in the 2I + 1 unknown $\Delta\rho_i$, Δv_i and Δp.

We now consider the empirical parameters for the mixed convection condition. In addition to the inlet flow distribution which is provided as three constant velocitites, v_1, v_2, v_2 as in the forced convection condition, the subchannel friction factor f_i, interior transverse mass flux $\rho(\varepsilon_{ij}/\eta_{ij})$ and edge transverse velocity V_{Ti} are the parameters required in equations (2.47) and (2.48).

From the definition of $\varepsilon_{l\eta}^*$, equation (2.32), $\rho(\varepsilon_{ij}/\eta_{ij})$ can be written as

$$\rho \frac{\varepsilon_{ij}}{\eta_{ij}} = \rho v \varepsilon_{l\eta}^* \qquad (2.50)$$

Since now ρ and v are not same values between subchannel i and j, average values of these two subchannel should be used to evaluate this parameter. As for the edge transverse velocity, V_{Ti}, it can be

calculated by

$$V_{Ti} = v_i C_{1L} \tag{2.51}$$

The parameters $\varepsilon^*_{1\eta}$ and C_{1L} are assumed to be constant values for the subchannels in the interior regions and the subchannels in the edge region at one operation condition, respectively. These parameters are reduced from the forced convection data. The validation of their application in the mixed convection condition will be discussed in chapter 8.

2.4 Empirical Parameters for the ENERGY Code

In summary, the following empirical parameters are required for our model,

a) Flow slip parameters: X_1, X_2, X_3

b) Subchannel friction factors: f_1, f_2, f_3

c) Dimensionless Effective Eddy Diffusivity (DEED): $\varepsilon^*_{1\eta}$

d) Dimensionless eddy diffusivity for the edge region : $\varepsilon^*_{2\eta}$

e) Edge Transverse Velocity Ratio (ETVR): C_{1L}

f) Conduction shape factor: κ_{11}, κ_{12}, κ_{22}, κ_{23}

These parameters are functions of bundle geometry and operation conditions. The major work of this study will be developing models and correlations for these parameters. After implementing these correlations into ENERGY code, recent temperature data will be used to validate our subchannel analysis method.

CHAPTER 3 - Computer Tools Developed

3.1 Introduction

Analytical method of development associated with the Project has concentrated on two general areas: (1) lumped parameter assembly and core analysis techniques using a Porous Body formulation called the ENERGY approach and (2) distributed parameter analysis methods and comupter codes developed during the course of this Project and discuss their importance to the nuclear industry. Due to the large number of topical reports published by the project dealing with this specific area (see the preface of this document for a listing), the specific details of each report cannot be discussed here. Only the significant highlights of each will be summarized.

3.2 Porous Body Models

Using the lumped parameter approach, an assembly is partitioned into a finite number of control volumes. The temperature and velocity distributions within these control volumes are represented as uniform profiles. These control volumes interact with each other both thermally and hydraulically. By using this lumped approach, the number of spatially dependent unknowns is greatly reduced, facilitating the simultaneous solution of large segments of the reactor core. Most existing calculational lumped parameter methods are based on the subchannel analysis approach, i.e., the assembly is broken radially

into control volumes coincident with the individual subchannels. The radial mixing or crossflow between subchannels is calculated by solving a transverse momentum equation along with the continuity, energy and axial momentum equations. In the case of an LMFBR assembly, the wire-wrap induced flow sweeping is generally modeled as "forced diversion" crossflow between subchannels. A wire wrap mixing model is required to determine the magnitude and duration of the crossflow forced through the gap with every sweep of the wire wrap.

The porous body model developed under this contract differs from the subchannel approach in that the LMFBR assembly is radially characterized by two distinct regions: the interior or central region and the peripheral region. These regions are treated as a continuum by viewing the entire wire-wrapped bundle as a porous body. These regions are shown in Figure 3.1. In the interior region of the assembly, the lateral flowfield is characterized by wire-wrap induced flow sweeping. Any given coolant subchannel feels the effect of the continuously changing flow oscillations induced by the superimposing sweeping of the wire wraps on the three neighboring rods. Because of this ever-changing flow sweeping in the interior region, the radial mixing is modeled by an enhanced effective eddy diffusivity, $\varepsilon^{*}_{1\eta}$. On the other hand, the peripherial region is characterized by a unidirectional sweeping of the wire wraps on the outer ring of rods along the duct wall. This directional lateral flowfield is modeled by an average circumferential swirl flow ratio , C_{1L}. These parameters have been

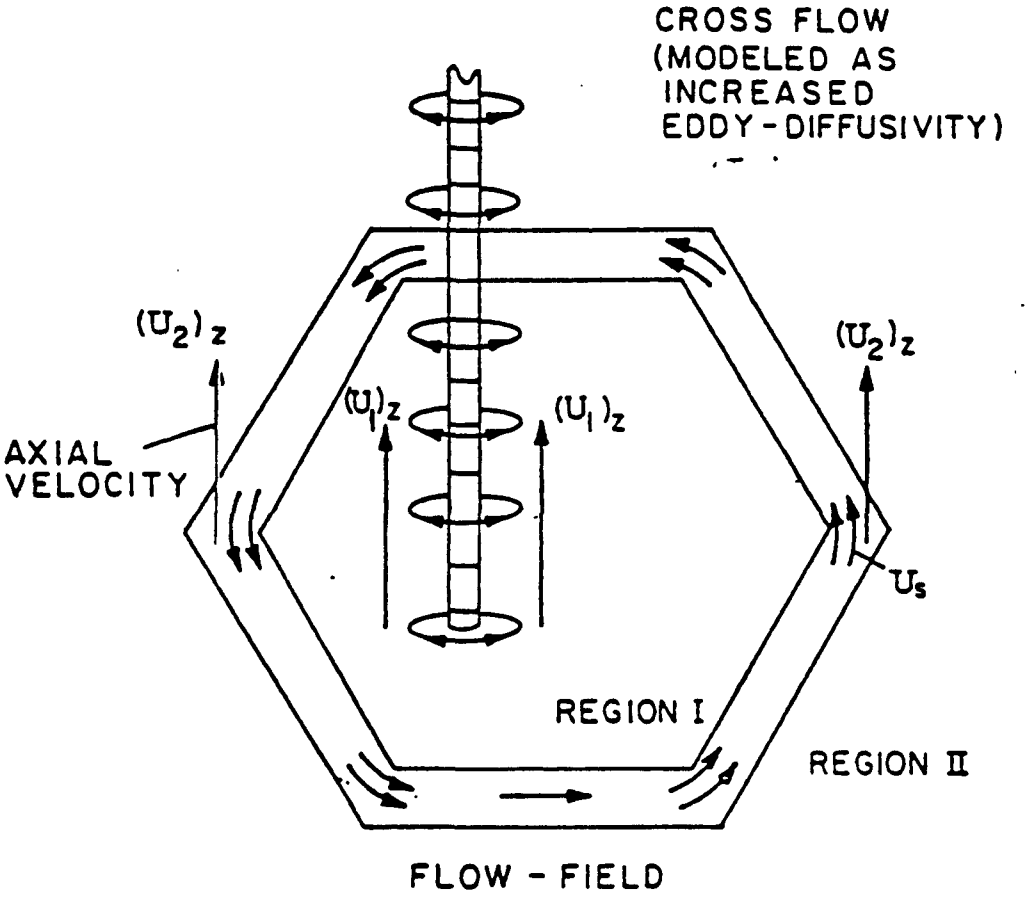

Figure 3.1 Flow regions in wire wraped hexagonal bundles

correlated based on the available experimental data, as will be discussed in the next two chapters, and form the basis for the ENERGY porous body model. Note that although porous body approach is used as discussed above for the ENERGY-IV, the control volumes used in the ENERGY-IV are similar to the conventional subchannel modeling scheme.

3.2.1 Numerical Formulation of the ENERGY Model

The difference equations used in the ENERGY-IV code have been derived in Chapter 2. The code structure and numerical methods will be discussed in Chapter 7.

3.2.2 Strengths and Limitations of the ENERGY Model

Strengths of ENERGY Model

As a result of its simple final form, the ENERGY model is very efficient in terms of both computer storage and required computation time. Since lateral mixing is modeled by the correlated enhanced eddy diffusivity $\varepsilon^{*}_{l\eta}$ and the swirl flow parameter C_{lL}, there is not transverse momentum equation to solve. In the case of forced convection with the inlet flowsplit specified, both momentum equations can be eliminated. This forced convection ENERGY model lends itself quite nicely to fast running explicit solution schemes. Several codes were developed under this project to solve problems in this flow regime. These are described in Section 3.2.3.

The ENERGY method can also yield substantial savings in computer time and storage by virtue of its ability to represent larger control volumes than those used in classical subchannel approaches. Typical subchannel lumped-parameter techniques require wire-wrap mixing models in order to model the magnitude and duration of the "forced diversion" crossflow moving periodically through the subchannel gaps. The use of this type of wire-wrap model generally restricts the size of the control volumes to subchannels. The computer time and storage required in the solution of the coupled momentum, continuity, and energy equations for large LMFBR bundles using these classic methods can be excessive.* Since the physical model from which the ENERGY method was derived is based on region averaged mixing parameters, however, the subchannel-sized control volumes can be aggregated into larger control volumes as desired. The resulting temperatures predicted for the larger lumped volume are in fact the average temperatures for the volume.

The ENERGY model has been extensively documented throughout the project. The bases for the model, the empirical input parameters required, and the method of solution are readily available to the would-be code user. In particular, the ENERGY code input summary (originally 17TR, now 108TR) has been kept up-to-date with the latest

---

* Successful efforts have been made with the COBRA-WC code to remove this restriction by using an increased turbulence parameter to model the effect of the wire wrap. This is similar in principle to the enhanced eddy diffusivity, but lacks the physical basis and peripheral swirl effects of the ENERGY model.

empirical correlations, important user information and the necessary descriptions to aid in understanding the different forms of the ENERGY model and its input parameters. A substantial amount of effort was spent to ensure the later versions of the ENERGY codes (see next Section 3.2.3) are user oriented, including features to give them modeling flexibility as well as reduce the amount of user input required.

Section 3.2.1 showed the two forms of the ENERGY model: the simplified form applicable to the forced convection flow regime, and the form incorporating an axial momentum equation that is applicable to the mixed convection flow regime. In order to provide a clear indication when the more complex (and expensive) mixed convection form of the ENERGY model is required, a criterion for the onset of mixed convection has been developed by Symolon, Todreas and Rohsenow (101TR). For the purposes of the criterion, the onset of mixed convection was defined as the point at which 1% of the cold region inlet axial flow is being redistributed to the hot region. The criterion is presented in terms of dominant dimensionless parameters and input parameters for conduction, coolant mixing, and friction. Symolon's criterion can be applied to both wire wrap and bare rod bundles of various P/D and H/D, provided correlations are available for the input parameters. The criterion has also been extended to predict the onset of flow recirculation, the point at which the ENERGY mixed convection model is also invalid.

Limitations of the ENERGY Model

The ENEGY model is not recommended for use outside of the range of data used to correlate $\varepsilon^*_{1\eta}$ and C_{1L}. While the physical basis for these two empirical constants appear to offer the opportunity to predict their behavior with these geometric parameters, this has not been done to date. The range of these constants, in terms of H/D, P/D and Re is highlighted along with other important user information in the ENERGY code input summary (108TR).

The ENERGY model is applicable to ducted LMFBR bundles with one wire wrap per rod starting at the same relative location. Using the code to perform calculations for off-normal geometry (such as ductless bundles or gridded bundles) will provide questionable results. For such problems the ENERGY method can only be used when calibrated for the stipulated configurations. The method is not a "benchmark" tool and should not be used as such.

For very low flows and high radial power skews, flow reversal may occur in the low power regions of an assembly, requiring the use of a code with a full transverse momentum equation, an implicit solution scheme and a recirculation model, such as COBRA-WC. In such flow situations, the assumptions behind the ENERGY approach break down and the method is not applicable.

Model predictions within the developing flow of the first wire wrap lead length may be less accurate than predictions further downstream. The wire wrap geometry sets up a flow field which can be characterized by an effective eddy diffusivity only when a sufficient

number of wire passes have been made through a subchannel. In addition, the ENERGY model assumes a fully developed flow split as an input parameter.

The steady state ENERGY codes do not contain a fuel rod model, but rather transfer the specified input power directly to the proper coolant control volumes via a local volumetric heat generation rate. This is not a fundamental limitation and could easily be relaxed when desired. A fuel model has been included in the transient TRANSENERGY-S code.

3.2.3 Description of ENERGY Related Codes Developed

The ENERGY model related computer codes developed under this project fall into several different categories: 1) Single bundle steady state codes, 2) Multiple bundle steady state codes, 3) Transient codes and 4) Speciality or auxiliary codes used to support of enhance the capabilities of the other ENERGY codes. The subsections that follow give an overview of the various codes developed. These codes are compared in Table 3-1.

3.2.3.1 Single Bundle Steady State Codes

Khan, Rohensow, Sonin and Todreas (16TR, 18TR) developed three computer codes which determine the steady state coolant temperature field in a single LMFBR assembly with adiabatic boundary conditions on the duct wall. The codes, designated as ENERGY-I, ENERGY-II, and

Table 3-1 Comparison of ENERGY based Codes*

CODE	DOCUMENT	FLOW REGIME	RADIAL B.C.	TRANSIENT	NODING GEOMETRY	COMMENTS
ENERGY I	18TR	Forced	Adiabatic	SS	Single Bundle Variable Radial Mesh	
ENERGY II	18TR	Mixed	Adiabatic	SS		
ENERGY III	18TR	Mixed	Adiabatic	SS		
ENERGY IV	108TR	Forced & Mixed	Adiabatic	SS		Latest of Its Typ
SUPERENERGY	20TR	Forced	Multibundle or Adiabatic	SS	Multiple Bundle Subchannel Mesh	
SUPERENERGY-2	57TR	Forced	Multibundle or Generalized H.T.	SS	Multiple Bundle Variable Radial Mesh	Latest of Its Typ
SUPERENERGY-6		Forced	Generalized H.T.	Transient	Single Bundle Variable Radial Mesh	Latest of Its Typ

* All LMFBR Codes were compared in July 1983 in report "Assessment Development; and Application of LMFBR Thermal-Hydraulic Analysis Tool," EPRI NP-3167

ENERGY-III, were intended primarily as research tools to investigate the validity of the ENERGY approach. ENERGY-I predicts the coolant temperature field for the forced convection flow regime. The pre-determined radial velocity fiels (flow split) was assumed unaltered by buoyancy effects, allowing the temperature and velocity fields to be numerically decoupled. The forced convection equations for this model were presented in Section 2.3.1 above. ENERGY-II and ENERGY-III predict the coolant temperature field for LMFBR bundles in the mixed convection flow regime. In these cases, the radial temperature gradient is so severe that the original velocity field is altered. The temperature and velocity fields are no longer decoupled. The mixed convection equations were presented in section 2.3.2 above. The latter two codes differ only in the specific terms included in the finite difference formulations of the axial momentum equation. Khan developed a critical modified Grashof number criteria, G_r^*, to determine when buoyance effects are important, and when the more expensive ENERGY-II or III solutions are required. (This criteria has been superceded by Symolon's work). Khan used the three ENERGY codes to assess the available experimental data and determined preliminary correlations for the two model empirical parameters, C_{1L} and ε_{1L}^*. These codes were not intended to be fast running production type codes. Further refinement in program input and output formats, streamlining of the coding, and additional documentation would generally have been required.

Cheng and Todreas (108TR) built on previous work by Greene (SM thesis) and Kim (SM thesis) to create the ENERGY-IV code. ENERGY-IV contains all the features of the previous versions of ENERGY and supercedes them. At the users option, either of the forced (ENERGY-IV-FC) of mixed (ENERGY-IV-MC) convection solutions schemes can be used. These solution options replace the ENERGY-I and the ENERGY-III codes, respectively. Improved numerical efficiency in ENERGY-IV effectively eliminated the need for an option comparable to ENERGY-II. In addition, at the user's option the code can internally calculate the bundle geometry and noding, using the SUPERENERGY noding subroutines.

3.2.3.2 Multiple Bundle Steady State Codes

Chen and Todreas (20TR) extended the ENERGY-I model to create the first multiassembly code, SUPERENERGY. The code can predict the steady state coolant temperature distribution for thermally coupled assemblies in the forced convection flow regime. The option for multiassembly coupling and interassembly heat transfer is particularly important for LMFBR assemblies in the periphery of the core, where radial power skews can be severe. SUPERENERGY can handle up to 19 coupled assemblies including two different bundle types, simultaneously. By fixing the radial mesh to a standard subchannel noding, the code input was greatly simplified, allowing the assembly geometry and noding to be internally calculated based on a few critical bundle dimensions. Because of its spacially explicit finite differencing scheme and the

method used in assembly coupling, the code had stability limitations when low interassembly gap flows were specified. This problem was examined and resolved by Basehore and Todreas (33TR) using a resistance coupling between assemblies. Because of its many user convenience features, modeling flexibility and fast execution times, SUPERENERGY was suitable for production calculations.

Basehore and Todreas (57TR) extended the desirable features of ENERGY-I and SUPERENERGY with the development of the multiassembly steady-state forced convection code, SUPERENERGY-2. The development emphasized the addition of user-convenience features, modeling versatility, calculational speed, machine independent coding and reduced memory requirements. The code automatically generates noding and geometry for any number of single or double-ducted assembly types based on a few critical dimensions. Optional generalized heat transfer boundary conditions for the bundle faces, including duct wall gamma heating and interassembly heat transfer, have been incorporated. The code contains default property correlations, mixing parameter correlations, flowsplit correlations and heat transfer correlations. These can all be overridden by input. In addition, a critical modified G_r^* check (Khan's criteria - 16TR), an option for stability criteria (33TR) controlled axial noding, and a detailed energy balance summary printout have been included. SUPERENERGY-2 has been used as a production code and is available at the National Energy Software Center.

3.2.3.3 Transient Codes

Glazer et. al. (52TR) extended the steady state ENERGY-I model to form TRANSENERGY-S, a transient subchannel-based single assemly version of ENERGY that is capable of analyzing fuel or blanket bundles operating in the forced convection flow regime. TRANSENERGY-S has similar user convience features as SUPERENERGY-2, such as internally generated geometry and noding, internal default property correlations, flow split correlations, and generalized radial heat transfer boundary conditions. A transient fuel pin model and transient solution logic was developed. After a study of the available alternatives (35TR), the TRANSENERGY finite difference equations for the coolant were formulated as temporally implicit, spacially explicit, in an attempt to optimize storage requirements and running time. While not overly-constaining, the forced convection flow assumption does limit the application of the code to certain classes of LMFBR transients. The code cannot, for example, handle prolonged loss-of-flow transients. The extensive code verification runs and sample problems, performed as part of the development process, confirmed the applicability of the ENERGY approach to transient problems.

After the development of the TRANSENERGY-S code, further adaption of the ENERGY approach to transient code development at MIT, such as the planned development of the sister code, TRANSENERGY-M (for Multibundle), was canceled in favor of the ongoing CORTRAN (based on the ENERGY approach) and COBRA-WC transien LMFBR code development at Battelle Northwest Laboratories.

3.2.3.4 Speciality Codes

Basehore and Todreas (47TR) developed a lumped parameter method for analyzing the thermal-hydraulic behavior of the Clinch River Secondary Control Assembly (SCA), which was being developed at the time by General Electric. The model included counterflow paths, volumetric heating and interassembly heat transfer. In order to account for the important interassembly heat transfer effects, the model could be run using specified radial boundary conditions, or be interactively coupled to the multiassembly SUPERENERGY code. The model was delivered to General Electric for use in the development of the SCA.

Symolon, Todreas and Rohsenow (101TR) created a two channel lumped parameter analytical model of a rod bundle for the expressed purpose of developing a criterion in terms of the dominant dimensionless parameters that is applicable to both bare and wire-wrapped vertical rod bundles of various P/D and H/D ratios. This criterion improves upon and replaces the previous modified Grashof criteria, G_r^*, developed by Khan et. al (16TR). An important second criterion for the onset of recirculation was also developed. This replacees the recirculation criterion developed by Wang (73TR) based on distributed parameter techniques (see Section 3.3.3).

3.2.4 ENERGY Model Applications

The ENERGY model computer programs developed during the course of

this project have several potential industrial application to LMFBR core thermal hydraulics. The code ENERGY-IV (which supercedes its predecessors ENERGY-I, II and III) offers the capability to perform either forced or mixed convection analyses of a single LMFBR assembly. When coupled with Symolon's criterion for the onset of mixed convection, this is a useful tool in predicting temperature profiles in bundles for a wide variety of operating conditions, such as required in the design of test assemblies.

The SUPERENERGY-2 (57TR) code's flexible multiassembly modeling capabilities make it a useful tool for predicting the coolant temperature distribution in the various bundle types found in LMFBR cores, including the effects of interassembly heat transfer. It is for this reason that SUPERENERGY-2 was chosen as the core thermal hydraulic design code for the Fast Flux Test Facility (FFTF) in Hanford, Washington (REF: ANS Transactions Summer 1981 meeting). The FFTF core is highly non-symmetrical and contains a many different bundle types including a large number of cooler assemblies, where as much as half of the temperature rise may be the result of interassembly heat transfer. The code is used to predict the temperature distribution in as many as 100 coupled assemblies simultaneously. The code output has been modified to provide temperatures from this calculation for use as boundary conditions to core restraint and core assembly structural analyses. The capability has also been added to model the specialized reflector assemblies of the FFTF.

One of the primary reasons that the ENERGY series of codes are attractive to industry, is their calculational speed and sparing use of computer memory. In one production run SUPERENERGY-2 was used to calculate the temperature distributions in the first 6 rows of the FFTF core, including 73 fuel assemblies, 12 absorber assemblies, 7 in-core shims and one test assembly. The calculation included over 6 million coupled calculational cells. It used only 210K words of core memory and required approximately 11 minutes to run on a UNIVAC-1100 computer.

3.3 Distributed Parameter Techniques

Distributed parameter techniques are used to predict the local flow and temperature fields within a subchannel or grouping of subchannels. The pointwise velocity and temperature distributions can be calculated analytically or numerically from the governing continuity, momentum and energy equations. For turbulent flow calculations, a turbulent mixing model is required, in addition. The detailed field solutions resulting from these analyses can be used as input to other detailed local structural, mechanical, material or heat transfer analyses. The detailed field solutions can provide friction factors, heat transfer coefficients and radial heat conduction shape factors. These can be used directly as constitutive relations for lumped parameter (subchannel) codes or be used to interpret (or extend) the experimental data which may be the basis of the existing lumped parameter code input. The distributed parameter analysis techniques

may yield information that can be used as modeling guidelines for formation lumped parameter input, e.g. guidelines for control volume size selection in lumped parameter models.

By its very nature, distributed parameter analysis can provide local solutions only to a limited set of problems. The mathematical equations are very complex, and become nearly unmanageable for the irregular geometry associated with rod bundles. In addition, distributed parameter analyses require large amounts of computer storage and computation time, even for those cases where a general analytical solution has been predetermined and the computer is only being used to apply the point-wise boundary conditions. It is not possible, for example, to solve all the possible thermal and flow conditions for a given geometry concurrently, or even to solve all possible geometries for a given flow and thermal condition. Figure 3.2 indicates the potential choices that exist when a distributed parameter analysis is performed. For any proposed distributed parameter analysis, the selection between various subsets of these conditions have a major impact on the complexity of the analysis.

Each distributed parameter analyses performed under this contract was performed only after an extensive literature review of existing work in the distributed parameter area (Each topical report contains a summary of existing work). The analyses that were performed under this contract were selected to augment previous work in areas of specific interest to the LMFBR industrial community. Emphasis was placed both on uderstanding the local phenomenon uncovered by parallel experimental program (see chapter 6) and providing valuable lumped parameter code

Figure 3.2
Potential Choices for Distributed Parameter Analysis

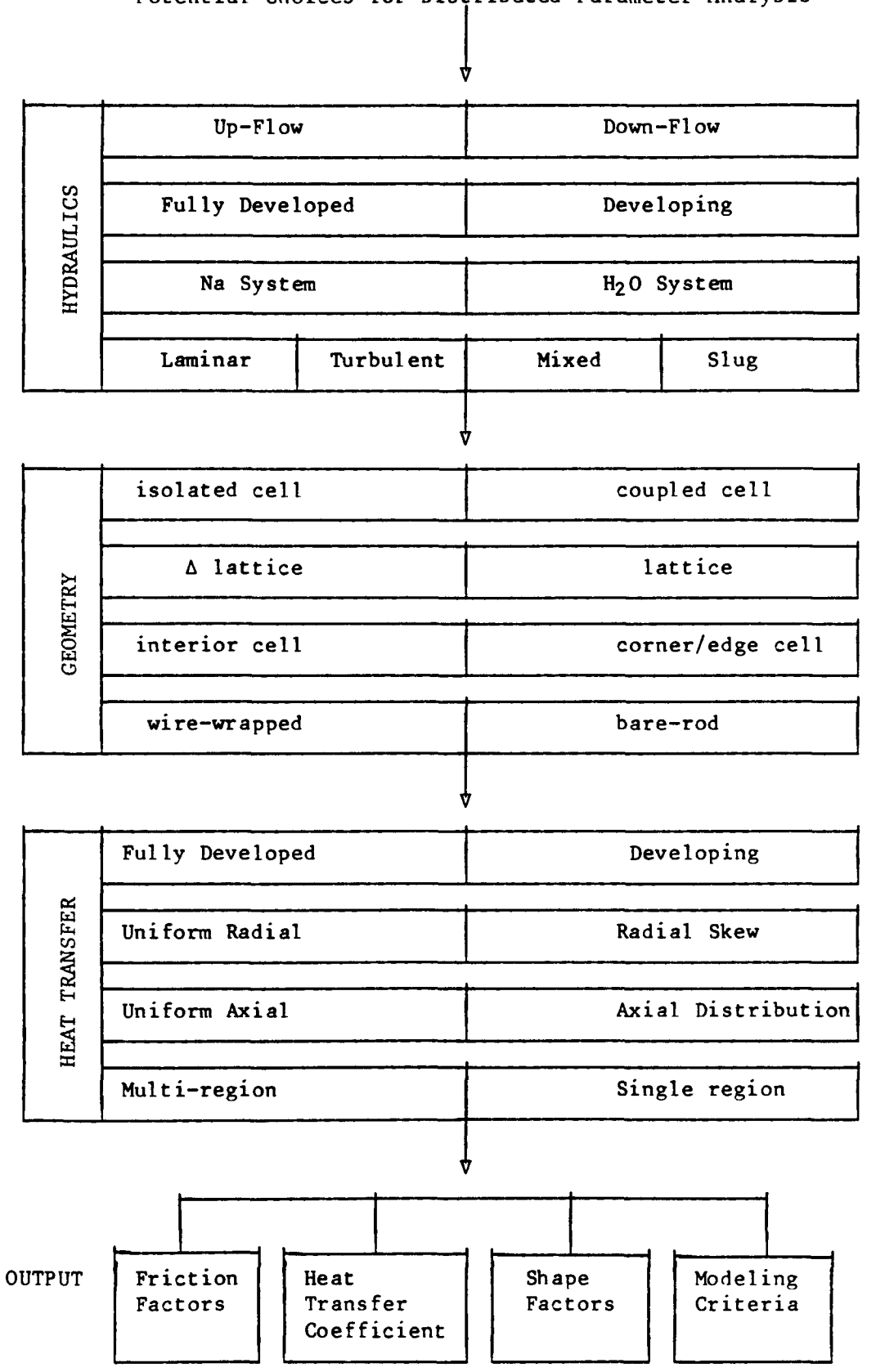

input guidelines and correlations. The various analyses performed under the contract can be lummped into five general categories: (1) turbulent velocity field solutions, (2) slug flow heat transfer analyses, (3) mixed convection heat transfer analyses that solve both the energy and momentum equations, (4) solutions specifically treating wire-wrapped bundles and (5) structural anaalyses of cladding incorporating local effects. Table 3-2 gives a comparison summary of the MIT distributed parameter analyses. By comparing this table with Figure 3.2, it is possible to see the extent of the work performed.

3.3.1 Turbulent Velocity Field Solutions

The project's first distributed parameter analysis was performed by Carajilescov and Todreas (19TR) in 1976. They performed an anal ical study of fully developed isothermal axial turbulent flows in an isolated interior subchannel of a bare rod LMFBR bundle. The study numerically predicted isothermal wall shear stress distributions, friction factors, eddy diffusivities, and secondary flow fields using a single equation turbulence model for mathematical closure. These results were compared against experimental data, including the author's own laser doppler anemometer data. The study verified the validity of the distributed parameter approach.

Bartzis and Todreas (48TR) extended Carajilescov's work using a two-equation turbulence model. The study showed that the use of a non-isotropic eddy viscosity considerably improves the prediction of the isothermal flow field in a rod bare bundle. In addition, the

Table 3-2 Comparison of DP Analyses Performed during the Project

Name	Flow			Thermal		Geometry					Solution	
	Up/ Down Flow	F D Devel- oping	Slug Mixed Laminar Turbulent	Power Dist.	F.D Devel- oping	Bare Wire/ Wrap	Lattice	Cell	Region	P/D	Coupled Isolated	technique
arajilescov 8TR	UP	FD	Turb. (one eq.)	none	N/A	Bare	Triang.	Inter.	Coolant	1.1-1.22	Isolated	numeric.
artzis 8TR	UP	FD	Turb. (two eq.)	none	N/A	Bare	Triang.	Inter.	Coolant	1.1-1.22	Isolated	numeric.
ong 8TR	UP	FD	Slug	radial skew axial skew	Devel.	Bare	Triang.	Inter. Edge Corner	Coolant	1.08-1.30	Isolated Coupled	analyt.
eung 8TR	UP	FD	Slug	rad. skew	F.D.	Bare	Triang.	Inter. Edge Corner	fuel clad coolant	1.0-1.5	Isolated Coupled	analyt.
im 7TR	UP	FD	Laminar Mixed	uniform	F.D.	Bare	Triang.	Inter. Edge	clad coolant	1.05-2.0	Isolated	analyt.
ang 3TR	UP &Down	FD	Laminar Mixed	uniform	F.D.	Bare	Triang. Square	Inter. Edge	clad coolant	1.05-1.55	Isolated	analyt.
ong 7TR	UP	Devel.	Laminar Turb. (Simple)	axial skew radial skew*	Devel.	Bare Wire- wrap	Triang.	Inter.	coolant	1.07,1.24	Isolated	numeric.

imposed through boundary conditions
boundary conditions imposed through pointwise watching techniques

authors performed two region (coolant and clad) heat transfer calculations that highlighted the importance of an anisotropic eddy viscosity model on the cladding azimuthal temperature variation in turbulent flows. The two-equation turbulence model formulated was shown to be a satisfactory engineering tool for predicting useful hydrodynamic quanitities (i.e., mean axial velocity, Reynolds stresses, shear stresses) in a bare rod bundle at high Reynolds numbers.

3.3.2 Slug Flow Heat Transfer Analysis

Wong and Wolf (58TR) extended some existing European isolated cell distributed parameter analyses to perform a 3-Dimensional slug flow heat transfer analysis of coupled coolant cells in a finite bare rod LMFBR bundle. This study yielded heat transfer coefficients, thermal entrance lengths, and effective radial thermal mixing lengths for coupled channels with non-uniform radial and axial power distributions. The analysis indicated that the effective thermal mixing length, used as an input parameter to many subchannel codes, is very sensitive to bundle geometry. Another important conclusion was that the corner and edge cells have a much longer thermal entrance length than an internal cell. Thus, those calculations which assume fully-developed heat transfer analysis yield a prediction of the clad temperature variation throughout the core that is far too conservative. This conclusion was confirmed an quantified by Yeung and Wolf (68TR).

Yeung and Wolf (68TR) performed a multi-region, multi-cell slug

flow heat transfer analysis in finite bare rod LMFBR bundles. The coupled energy equations for the fuel, clad and coolant were solved analytically using point matching techniques at the boundaries. Large segments of 7 pin, 19 pin and 37 pin bundle were analyzed. The study provided detailed clad temperature distributions and a correlation for effective thermal mixing lengths as a function of geometry. The impact of using the correct thermal mixing lengths in COBRA-IIIc code calculations was shown to be significant. A method of performing coupled distributed-lumped parameter analysis was demonstrated.

3.3.3 Mixed Convection Heat Transfer/Momentum Solution

Kim and Wolf (67TR) developed an analytical solution for the heat transfer and pressure drop during combined laminar forced and natural convection in characteristic coolant cells of finite bare rod LMFBR bundles. The two-region (clad and coolant) analysis also assessed the effects of heat redistribution within the cladding. The study computed local temperature, velocity, and shear stress distributions as a function of Rayleigh number and geometry. In addition, average Nusselt numbers and friction factors were provided. This report demonstrated the utility of distributed parameter studies in interpreting experimental data and in deriving meaningful integral transport parameters for use in lumped parameter codes.

Wang, Rohsenow and Todreas (73TR) developed a general analytic solution in the mixed convection regime for isolated cells in a bare rod bundle for both triangular and square arrays. The study thoroughly

analyzed and documented buoyancy effects on the fully developed local velocity and temperature profiles, the wall shear stresses, the clad heat fluxes, the subchannel friction factors, and the heat transfer coefficients for both up-flow and down-flow. Some of the key results of the study were a criteria for the onset of local flow recirculation, a criteria for the transition from laminar to turbulent flow, and a flow regime map defining the transition from forced to mixed convection as a function of Rayleigh number and geometry. Important conclusions of this study for bare rod bundles are: (1) buoyancy force effect of subchannel friction factors is only important in blanket assemblies (and not fuel assemblies) of current LMFBR design, and (2) in blanket assemblies flow tends to become turbulent before local flow recirculation occurs, while in fuel assemblies the reverse is true.

3.3.4 Wire-wrapped Bundle Analyses

Wong and Todreas (97TR) developed a computer code, HEATRAN, to analyze the heat transfer characteristics of a wire-wrapped assemble by solving a system of transient three-dimensional mass, momentum and energy transport equations within a local subchannel. Because of the general dominance of wire-wrap induced mixing, a simple Prandtl mixing length turbulence model was assumed. The effect of a wire wrap was incorporated by a unique rotating coordinate system. The HEATRAN code represented a significant advance in the state of the art in distributed parameter analysis tools. The code was extensively verified against the available experimental data. In particular,

HEATRAN compared well with the Westinghouse Isothermal Air Flow experiments. In addition, the HEATRAN developmental assessment included comprehensive sensitivity studies on the Clinch River LMFBR bundle geometry. Important conclusions of the analyses were: (1) The effect of the helical wire wrap on the clad surface temperature is significant and cannot be neglected; (2) the wire effect rather than the turbulent effect is the domain transport mechanism within the subchannel.

3.3.5. Structural Analyses of the Cladding

Karimi and Wolf (59TR) modified and coupled existing fuel performance and structural codes to compute two-dimensional thermoelastic and thermo-inelastic cladding stress and deformation fields for typical LWR and LMFBR geometries. The codes were reviewed and updated to incorporate the most recent models for fuel-cladding interaction, swelling, creep, fission gas release, irradiation-induced growth, gap conductance, variable properties. The study analyzed the effects of clad-coolant heat transfer variation, eccentric fuel pellets, clad ovality, and power tilt across the fuel on cladding stress and deformation, quantifying the impact for various conditions. The study provided some important guidelines as to when elastic analysis is appropriate and when inelastic analysis must be used.

3.4 Summary of Important Results

3.4.1 Porous Body Model

A simplified approach to LMFBR core thermal hydraulic modeling based upon porous body concepts was developed during the course of the Project. This approach, the ENERGY model, was transformed into several computer codes during the course of the project. Significant contributions from the porous body model code development performed during the Project include:

- The ENERGY porous body model was first applied in the ENERGY-I, II, and III codes. The ability of the codes to match LMFBR experimental data was demonstrated.

- ENERGY-IV consolidated the ENERGY-I and ENERGY-III approaches into one code. It supercedes the ENERGY I, II, and III codes.

- A criterion for the onset of mixed convection was developed for use with the ENERGY codes and elsewhere.

- A criterion for the onset of flow recirculation was developed.

- The applicability of the ENERGY model to transient analysis was demonstrated with the single bundle code TRANSENERGY-S.

- SUPERENERGY first applied the ENERGY model to multiple bundles, including the effects of interassembly heat transfer.

- SUPERENERGY-2 extended SUPERENERGY's modeling capabilities and flexibility. It supercedes the SUPERENERGY code.

- A model of the CRBR secondary control assembly was developed which could be coupled to SUPERENERGY.

3.4.2 Distributed Parameter Models

The distributed parameter models developed during the Project augmented the analysis being performed elsewhere and have helped contribute to current the understanding of intra-subchannel phenomena in LMFBR bundles. The techniques used in the solution of these complex sets of equations have advanced the state of the art in thermal-hydraulic methods. In particular, the HEATRAN code offers a general analysis tool from which significant insight may be gained about the current or proposed LMFBR bundle designs. Specific significant sontributions from the distributed parameter analyses performed during the Project include:

- A two-equation turbulence model which was tested and shown to be satisfactory for engineering work.

- The conservatism of the fully developed heat transfer assumption for the corner and edge channels was shown and quantified.

- Several correlations for the thermal mixing lengths were developed foruse in suchannel codes like COBRA-IIIc.

- Friction factors and average Nusselt numbers were developed for a wide range of flow and geometry conditions for use in subchannel lumped parameter codes.

- Criterion for the transition from laminar to turbulent flow was developed.

- Criterion for the onset of localized flow recirculation based on distributed parameter techniques was developed.

- A subchannel flow regime map, based on distributed parameter techniques, defining the transition from forced to mixed convection was developed.

- The significant importance of the wire wrap on clad surface temperatures was quantified.

- Guidelines for the use of thermo-elastic and thermo-inelastic structural analysis techniques were developed.

CHAPTER 4

SUBCHANNEL FRICTION FACTOR CORRELATIONS

4.1 Introduction

The constitutive relations for subchannel friction factors are essential for subchannel analysis codes, either as input to those codes which solve coupled conservation equations (COBRA, COMMIX, THI-3D, and ENERGY-III) or as the means to derive flow split parameters for use as input to those codes which solve only the energy equation (COTEC, ENERGY-I). Several investigators, deStordeur (1961), Sangster (1968), Novendstern (1972), Rehme (1967), Engel et al. (1979), and Hawley et al. (79TR), have suggested empirical models for correlating the bundle average friction factors as functions of the wire-wrapped subassembly geometry. Significantly, none of these investigators except Hawley et al. extended their efforts to correlate subchannel based friction factors.

Although subchannel friction factors models have been developed by Hawley et al., these models can be substantially improved. In this chapter we present new and consistent subchannel friction factor and flow split models which have been fully calibrated utilizing all old and new published data. These correlations will then be used in the ENERGY-IV code as input for flow split parameters and subchannel friction factors.

The objective of this chapter is to develop the models for drag loss in three kinds of subchannels in a typical wire-wrapped LMFBR subassembly. From these models, the equations for the average value of

subchannel friction factors over one lead length are formulated, and expressions for flow split parameters and bundle average friction factors are then derived. The empirical constants in these formulations are calibrated from bundle average friction factor data and flow split data. These subchannel friction factor models will be formulated to be,

a) applicable to both turbulent and laminar flow conditions; the transition flow region will be represented as a superposition of turbulent and laminar values weighted by some intermittency factor,

b) based on simple but sound physical concepts,

c) correctly reducible to bare rod cases, and most importantly,

d) able to satisfactorily correlate the wire-wrapped experimental data.

4.2 Literature Review

The available data for the wire-wrapped rod bundle friction factor and flow split parameter have been reviewed and collected. Appendix B1 lists all these data in addition to bare rod bundle friction factor data.

4.2.1 Bundle Average Friction Factor Data

The first systematic pressure drop experiments for wire-wrapped rod bundles with varied P/D and H/D reported were by Bishop et al. (1962) in 19-pin bundles. Since the center pin of their bundles was not wire-wrapped, their results are not appropriate for our models in which all the rods are wire-wrapped.

Rehme (1967) performed pressure drop experiments for over seventy-four wire-wrapped rod bundles with different combinations of geometrical parameters (N_r = 7, 19, 37, 61; P/D = 1.125, 1.233, 1.275, 1.343, 1.417; and H/D = 8.33, 12.5, 16.67, 25.0, 50.0). Because of their consistent characteristics, Rehme's data have been widely used for calibrating models.

Bauman et al. (1968) measured pressure drop in several hexagonal bundles with different kinds of spacers. Four of them were wire-wrapped bundles, two of which were 61-pin, P/D = 1.167 and H/D = 16.7, 25.0, while the other two were 19-pin, P/D = 1.227 and H/D = 15.1, 22.7.

Reihman (1969) measured pressure drop in fourteen wire-wrapped rod bundles; most of them were 37-pin. The reported geometry of these bundles showed that the tolerances were quite large. Since no value for the looseness factor has been reported, average values calculated by assuming that the tolerance is uniformly distributed are used. This makes the P/D values of these bundles in Appendix B1 different from the reported values which were $(D+D_w)/D$. This may be the reason why Reihman's data are almost consistently higher than Rehme's correlation using the reported P/D.

Okamoto (1970) and Wakasugi (1971) performed pressure drop measurements in their JEFR 91-pin bundles with one P/D (=1.221) combined with four H/D values (=14.3, 20.6, 30.2, 41.3). Davidson (1971) measured pressure drop in a 217-pin bundle with P/D = 1.283 and H/D = 48.0. Hoffmann (1973) measure pressure drop in three 61-pin bundles with P/D =1.317 and H/D = 16.67, 33.33, and 50.0. Sodium was

used as the working fluid in Hoffmann's bundles.

At MIT, Chiu (42TR) measured pressure drop in two 61-pin simulated LMFBR blanket assemblies with P/D = 1.067 and H/D = 4.0 and 8.0. Although Chiu has measured the pressure drop at low flow rate, only two data points were in the laminar region (Re < 400). The f•Re value of 160 for the H/D = 4.0 bundle and 90 for the H/D = 8.0 bundle are believed to be too high based on our comparison, reported here, with the latest Marten (1982) data. After Chiu, S. K. Cheng performed a pressure drop experiment in a 37-pin bundle with P/D = 1.154 and H/D = 13.4 to fill the gap in the available data as described in 108TR. Recently, Efthimiadis (1983) measured pressure drop in a 19-pin bundle with P/D = 1.245 and H/D = 35.2 at very low flow rate (Re = 30 to 800).

Engel et al. (1979) measured pressure drop in four 61-pin blanket bundles, two of which were cooled by sodium and two by water. The averaged geometrical parameters of these four blanket bundles are P/D = 1.082 and H/D = 7.78. The friction factor has been correlated in a simple form. However, the correlated constants were later corrected by the authors. The reported revised form is [Markley (1982)]

$$\text{for } Re \leq 400 \qquad f = \frac{99}{Re} \tag{4.1a}$$

$$400 < Re < 5000 \qquad f = \frac{99}{Re}(1-\psi)^{1/2} + \frac{0.48}{Re^{0.25}}\psi^{1/2} \tag{4.1b}$$

$$\text{where } \psi \equiv \frac{Re-400}{4600}$$

$$5000 \leq Re \leq 4\times10^{4} \qquad f = \frac{0.48}{Re^{0.25}} \tag{4.1c}$$

Spencer (1980) measured the friction factor of several fuel bundles with N_r = 217, P/D = 1.252 and H/D = 51.74, and correlated all the data in a simple form. Carrelli et. al. (1981) measured pressure drop in a 61-pin absorber bundle which has low P/D (=1.05) and medium H/D (= 20.0).

Marten and Yonekawa (1982) recently carried out pressure drop experiments in nine 37-pin low P/D (= 1.041, 1.072, 1.101) and H/D (≈ 8.3, 12.5, 16.7) bundles. Marten's data are very valuable not only because their P/D is very low but also because very low flow rate (down to Re ≈ 50) data were measured. In these experiments, the same bundle housing was used for all nine bundles, hence the rod and wire diameters were changed to obtain the desired P/D. Excellent tolerance control resulted in very tight geometry. To evaluate the influence of the dynamic pressure caused by crossflow in the edge region, Yonekawa (1982) examined five different measuring methods in one bundle. All results were in good agreement within a deviation of only ±2%; therefore, one standard method was confirmed to be sufficient. The method used to measure all nine bundles was that of interconnecting all six pressure taps in each face such that the orientations of the wire spacers at the measuring planes need not be the same.

In addition to all the data above, data from some new test bundles of the Japanese JOYO and MONJU assemblies are also available. [Itoh (1981)].

4.2.2 Flow Split Data

Most of the flow split experiments were only performed in the turbulent flow condition. Davidson (1971) measured these parameters in a 217-pin fuel bundle (P/D = 1.283, H/D = 48.0) by the time of flight technique. Ginsberg (1973) and Lorentz (1977) investigated 7-pin (P/D = 1.2, H/D = 48.0) and 91-pin (P/D = 1.24, H/D = 48.0) bundles respectively by the isokinetic extraction method. Pederson (1974) used the time of flight method to measure flow split in another 91-pin bundle (P/D = 1.21, H/D = 48.0)

At MIT, Chen (11TR) used a laser doppler anemometer to measure edge subchannel transverse and vertical flow velocities in two 61-pin bundles with the same P/D (= 1.25) but different H/D (= 24.0, 48.0). Two flow rates corresponding to Re = 640 and 4500 were performed. Chen's low flow rate data at Re = 640 were the only available laminar flow split data for low flow rate until recent work performed by Efthimiadis. Efthimiadis (1983) measured the velocity distribution in subchannels at very low flow rates with a hot wire anemometer in a 19-pin bundle (P/D = 1.245, H/D = 35.2). The detailed velocity distribution was measured at three Reynolds numbers, 80, 158 and 316, at which the flow is purely laminar.

Also, the isokinetic extraction method (IEM) was used to measure flow split parameters by Chiu (1978a) in two blanket bundles (N_r = 61, P/D = 1.067, H/D = 4.0, 8.0), by Symolon (84TR) in a fuel bundle (N_r = 217, P/D = 1.25, H/D = 51.72) and by S. K. Cheng in a bundle with medium geometry (N_r = 37, P/D = 1.154, H/D = 13.4). The drawback of the IEM is that there is a flow rate below which no flow can be

extracted from interior subchannels while flow can still be extracted from edge subchannels. The Reynolds number corresponding to this limiting flow rate is around 3000.

In addition to these experiments, some investigators, e.g., Ohtake (1976) and Bartholet (1976), used a pitot tube to measure the detailed air flow velocity distribution in large simulated bundles.

These flow split experiments together with their data are also listed in Appendix B1 of report 108TR.

4.2.3 Correlations for Friction Factor and Flow Split Parameter

de Stordeur (1961) investigated the drag coefficient of fuel element spacers. This method correlated data from both square and triangular rod arrays with both spiral wire and grid type spacers. His drag coefficient is around 0.4 at Re = 2×10^4 and is a slightly decreasing function of Re. The pressure drop is calculated by superimposing the drag loss and the conventional rod surface friction loss.

Sangster (1968) proposed an equivalent bundle friction factor calculated by multiplying the smooth tube friction factor from Blasius' equation by two correction factors Y and Z. The Y factor accounts for rod spacing effect and the Z factor is the spiral wire spacer effect. Sangster's method was later improved by Magee and Nilsson (1971) by using Ibragimov's (1967) results for the Y factor and by making the Z factor a function of both H/D and Reynolds number.

Novendstern (1972) developed a semiempirical model to predict pressure losses in wire-wrapped rod bundles. The model theoretically

determines the flow distribution within the fuel array and multiplies the pressure drop for a smooth pipe, using equivalent diameter techniques, by an empirical correlation factor (M) which accounts for wire effects. The M factor is able to correlate the experimental data of Reihman, Rehme and Baumann to an accuracy of ±14%.

The most widely used correlation for calculating bundle friction factor is Rehme's (1973a) model. The correlation of Rehme is based on an effective velocity to take into account the swirl flow velocity around the rods. The square of the ratio of this effective velocity (V_{eff}) to the bundle average axial velocity (V_b), F, was correlated to be

$$F \equiv \left(\frac{V_{eff}}{V_b}\right)^2 = \left(\frac{P}{D}\right)^{0.5} + \left[7.6 \left(\frac{d_m}{H}\right) \left(\frac{P}{D}\right)^2\right]^{2.16} \qquad (4.2)$$

where d_m is the wrapping diameter of spacers; for wire-wrapped bundles, $d_m = D+D_w$.

The pressure drop of a rod bundle was hypothesized by Rheme to be proportional to the square of this effective velocity and a parameter which accounts for the influence of the number of rods, i.e., the ratio of the wetted perimeter of the rod bundles (rods and wires) S_b to the total wetted perimeter S_t,

$$\Delta P = f \frac{L}{De} \frac{\rho V_b^2}{2} = \left(f' \frac{S_b}{S_t}\right) \frac{L}{De} \frac{\rho V_{eff}^2}{2} \qquad (4.3)$$

where $V_{eff} = \sqrt{F}\ V_b$

The modified friction factor f' was then calibrated as a function of the modified Reynolds number Re' using V_{eff} as the characteristic velocity to be

$$f' = \frac{64}{Re'} + \frac{0.0816}{Re'^{0.133}} \tag{4.4}$$

$$\text{where } Re' \equiv \frac{V_{eff} De}{\nu} = \frac{V_b De}{\nu}\sqrt{F} = Re\sqrt{F}$$

Expressing the pressure drop in the conventional form using the bundle average axial velocity as the characteristic velocity yields

$$\Delta p = f\frac{L}{D_e}\frac{\rho V_b^2}{2} \tag{4.5}$$

The bundle friction factor, f, of equation (4.5) can be expressed utilizing equations (4.2) and (4.3) as,

$$f = f'F\frac{S_b}{S_t}$$

$$= \left(\frac{64}{Re}\sqrt{F} + \frac{0.0816}{Re^{0.133}} F^{0.9335}\right)\frac{N_r\pi(D+D_w)}{S_t} \tag{4.6}$$

This correlation is valid for $2x10^3 \leq Re \leq 3x10^5$, $1.1 \leq P/D \leq 1.42$, $8 \leq H/D \leq 50$, $7 \leq N_r \leq 217$ as later confirmed by the author from the available data in Appendix B of Report 108TR. The accuracy of this correlation is around ±8% in the turbulent region.

For $Re > 2x10^4$, a simpler version of the modified friction factor, f', was reported by Hoffmann (1973),

$$f' = 0.1317Re'^{-0.17} \tag{4.6}$$

The above correlations are applicable primarily in the turbulent region, although Rehme's correlation is valid down to Re = $2x10^3$. For the laminar flow condition, Engel et al. (1979) developed a simple correlation based upon the very limited data base available at that time [Chiu(42TR): P/D = 1.067, H/D = 4.0, Engel(1979): P/D =1.082, H/D =7.78, Spencer(1980): P/D = 1.252, H/D =51.74]; the proposed correlation was

$$f \cdot Re = \frac{320}{\sqrt{H}} \; (P/D)^{1.5} \qquad (4.7)$$

where H is in cm.

Note that the application of this correlation appears limited to the two extreme geometry conditions of the data base, and the laminar friction factor constant f•Re is not expressed as a function of the nondimensional parameter H/D.

Hawley, Chiu and Todreas (79TR) are the first investigators to develop friction factor models from the subchannel point of view. The flow split parameters can be calculated from the subchannel friction factors. These are the 1980 MIT correlations, and they have been discussed in detail in the first chapter of 108TR.

Recently, Carajilescov and Fernandez(1982) developed a semi-empirical model for subchannel friction factors and flow split parameters. However, their data base is very limited.

4.3 SUBCHANNEL FRICTION FACTOR FORMULATIONS

4.3.1 Subchannel Friction Factor Models

The definition of the friction factor, f, in our models is in terms of the total loss of mechanical energy per unit volume, $\hat{e}$, caused by the total drag force over a length L. This energy loss $\hat{e}$ is defined as

$$\hat{e} \equiv f \frac{L}{De}\left(\frac{\rho V^2}{2}\right) \tag{4.8}$$

where De (equivalent hydraulic diameter) $\equiv 4A/P_w$. Note that the parameters A and P_w, and hence D_e, include the presence of the wire in the subchannel, axially averaged over one lead length. The subchannel friction factors can then be formulated from equation (4.8), if one can express the total mechanical energy loss, $\hat{e}$, by some models for each type of subchannel.

Since the flow phenomena in a wire-wrapped LMFBR subassembly are very complicated, no simple models such as those we are going to propose can precisely simulate the drag loss. On the other hand, the models themselves must reflect physical reality; otherwise, they may not be able to correlate the experimental data. Therefore, we try to include the most important physical effects by geometrical factors within these models, and incorporate all the other effects of the presence of the wire into the empirical constants.

In our approach for a wire-wrapped subassembly there are two regions with different flow characteristics: an interior region with an

axial velocity for all interior subchannels, and an edge region with a constant swirl velocity along the assembly wall and one axial velocity for all edge subchannels. However, we will not assume that the corner subchannel axial velocity equals the edge subchannel axial velocity. Consequently, three friction factor equations, i.e., interior, edge, and corner, need to be formulated.

4.3.1.1 Interior Subchannel

Figure 4.1 schematically shows an interior subchannel. Although the real flow direction should be slightly inclined to the wire direction, the effective transverse velocity component should not be significant due to the fact that the the wires change direction every one-third of a lead length. Hence, we assume that the axial velocity, V_1, shown in Figure 4.1, can be used as the characteristic velocity in modeling the drag loss.

The total mechanical energy loss in the interior subchannel is comprised of two parts: a) the friction loss caused by the fuel rod surface and b) the drag loss caused by the wire, i.e.,

$\hat{e}_1 = \hat{e}_f + \hat{e}_d$.

The friction loss along the fuel rod surface can be calculated by:

$\hat{e}_f = F_f$(force caused by friction)$/A_1$(average flow area)

$= [\tau$(average shear stress)$\cdot P'_{w1}$(wetted perimeter of fuel rod surface)$\cdot L] / A_1$ (2.2)

where $\tau = (\frac{f'_1}{4})(\frac{\rho V_1^2}{2})$

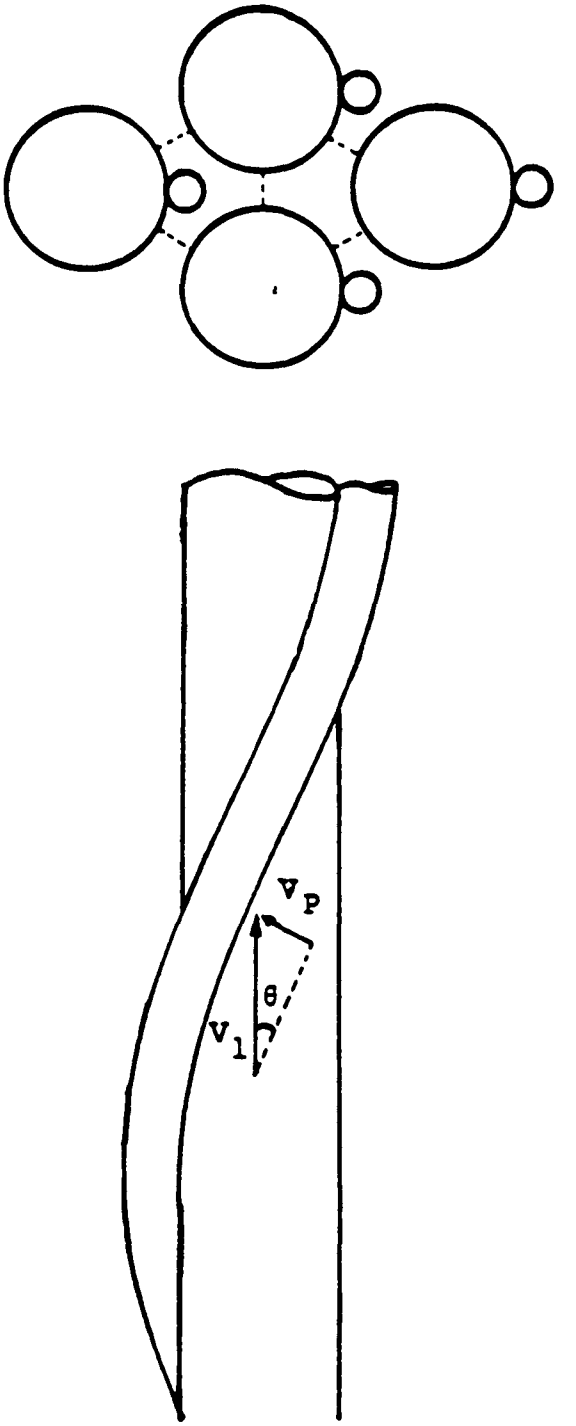

Figure 4.1 Velocity Components and Schematic Configuration of an Interior Subchannel

and $P'_{w1} = \frac{\pi D}{2}$, where the super prime notation refers to the convention that the parameter is calculated based on a bare rod geometry; i.e., the wire presence is not included.

Therefore,

$$\hat{e}_f = (\frac{f'_1}{4})(\frac{\rho V_1^2}{2})P'_{w1}L/A_1 \qquad (4.10)$$

$$= f'_1(\frac{P'_{w1}}{P_{w1}})[\frac{L}{De_1}\frac{\rho V_1^2}{2}]$$

where P_{w1} = wetted perimeter of interior subchannel including the averaged wire surface effect

$$= \frac{\pi D}{2} + \frac{\pi D_w}{2\cos\theta}$$

In calculating the average shear stress around fuel rod surface, τ, we assume that the bare rod friction factor formulation can be used to calculate f'_1, i.e.,

$$f'_1 = K_1 \; / \; Re_1^{\,m} \qquad (4.11)$$

where K_1 is derived from bare rod results.

Re_1 = interior subchannel Reynolds number

$\rho V_1 De_1/\mu$

m = exponent which depends on flow region;

This assumption is made for two reasons: 1) the effect of wire on the spatial distribution of the velocity field, hence the average shear

stress, hence the real friction factor, is not clear; for simplicity, the wire effect is neglected; and 2) equation (4.10) and (4.11) can be easily reduced to the bare rod case as the wire diameter goes to zero.

For the drag loss of the wire, since the wire covers the flow region from the wall to a position near which the velocity is maximum, the average velocity striking the wire can be taken as approximately the same as the average subchannel velocity. Hence the axial average velocity V_1 is used as the characteristic velocity. The drag loss experienced by the fluid slipping over the wire can be represented as

$$\hat{e}_d \propto C_d(\frac{\rho V_1^2}{2}) \tag{4.12}$$

where C_d is a proportional constant; formally a drag coefficient. Note that here we simply use the subchannel average velocity V_1 as the characteristic velocity rather than that of the wall velocity, V_w, as in Chiu's model. The geometrical influence on this flow phenomena will be included in C_d, which is a function of both geometrical parameters and flow regime. Since only fluid encountering the wire experiences this drag loss, the average drag loss for a single crossing of a wire for the total flow in the interior subchannel should be

$$\hat{e}_d = (\frac{A_{r1}}{A_1'})C_d(\frac{\rho V_1^2}{2}) \tag{4.13}$$

where $A_{r1} = \frac{\pi(D+D_w)D_w}{6}$ (projected area of wire wrap)

$A_1' = \frac{\sqrt{3}}{4}P^2 - \frac{\pi D^2}{8}$ (bare subchannel flow area)

Alternatively, one might use the perpendicular velocity, V_p ($=V_1 \sin\theta$) to calculate the drag force exerting on the fluid in the direction perpendicular to the wire wrap,

$$F_D = A_{r1} C_D \left(\frac{\rho V_p^2}{2}\right) \tag{14.14}$$

Projecting this force into the axial direction and dividing by the axial area for flow, we have the mechanical energy loss per unit volume in the axial direction caused by this drag force

$$\hat{e}_d = \frac{F_D \sin\theta}{A_1'} = \frac{A_{r1}}{A_1'} (C_D \sin^3\theta)\left(\frac{\rho V_1^2}{2}\right) \tag{4.15}$$

According to the independence principle, C_D can be taken as the conventional value for a circular cylinder for flow in a inclined (bare) rod bundle [Ebeling-Koning(1983)]. The reason that this argument is not used is that helical wire wrap is much more complicated than a straight circular rod, hence the independence principle and the conventional C_D might not valid in this case. On the other hand, equation (4.15) is similar to equation (4.13) except that $C_D \sin^3\theta$ is combined into one constant C_d. It is later found that C_d is easier to correlate than C_D, not to mention that C_D could be a single constant.

Over length L, the fluid will encounter wire 3(L/H) times; therefore, the total wire drag loss over L is,

$$\hat{e}_d = 3\left(\frac{L}{H}\right)\left(\frac{A_{r1}}{A_1'}\right) C_d \left(\frac{\rho V_1^2}{2}\right)$$

$$= \left[3C_d\left(\frac{A_{r1}}{A_1'}\right)\left(\frac{De_1}{H}\right)\right] \frac{L}{De_1} \frac{\rho V_1^2}{2} \tag{4.16}$$

The total mechanical energy loss for an interior subchannel is

$$\hat{e}_1 = \hat{e}_f + \hat{e}_d$$

$$= \left[f_1'\left(\frac{P_{w1}'}{P_w}\right) + C_d\left(\frac{3A_{r1}}{A_1'}\right)\left(\frac{De_1}{H}\right)\right] \frac{L}{De_1} \frac{\rho V_1^2}{2} \tag{4.17}$$

The interior subchannel friction factor is then formulated as

$$f_1 = f_1'\left(\frac{P_{w1}'}{P_{w1}}\right) + C_d\left(\frac{3A_{r1}}{A_1'}\right)\left(\frac{De_1}{H}\right) \tag{4.18}$$

4.3.1.2 Edge Subchannel

As described earlier, because the wires are in the same direction, the flow in the edge subchannel is assumed to have a constant helical velocity which is more or less following the wire. Figure 4.2 schematically depicts this situation. In this case, it is reasonable to assume that the form drag loss of wire is negligible compared to the skin friction associated with the swirl velocity since only a very small velocity component slips over the wire.

Seban and Hunsbedt (1973) performed water experiments in an annulus in which swirl flow was produced by a single helical vane. They found that the friction force can be predicted by utilizing the helical path length and hydraulic diameter. For an edge subchannel defined as one in the upper part of Figure 4.2, one finds that the flow characteristics in this subchannel are very similar to the annular swirl flow channel. The drag loss in the edge subchannel can then be calculated as

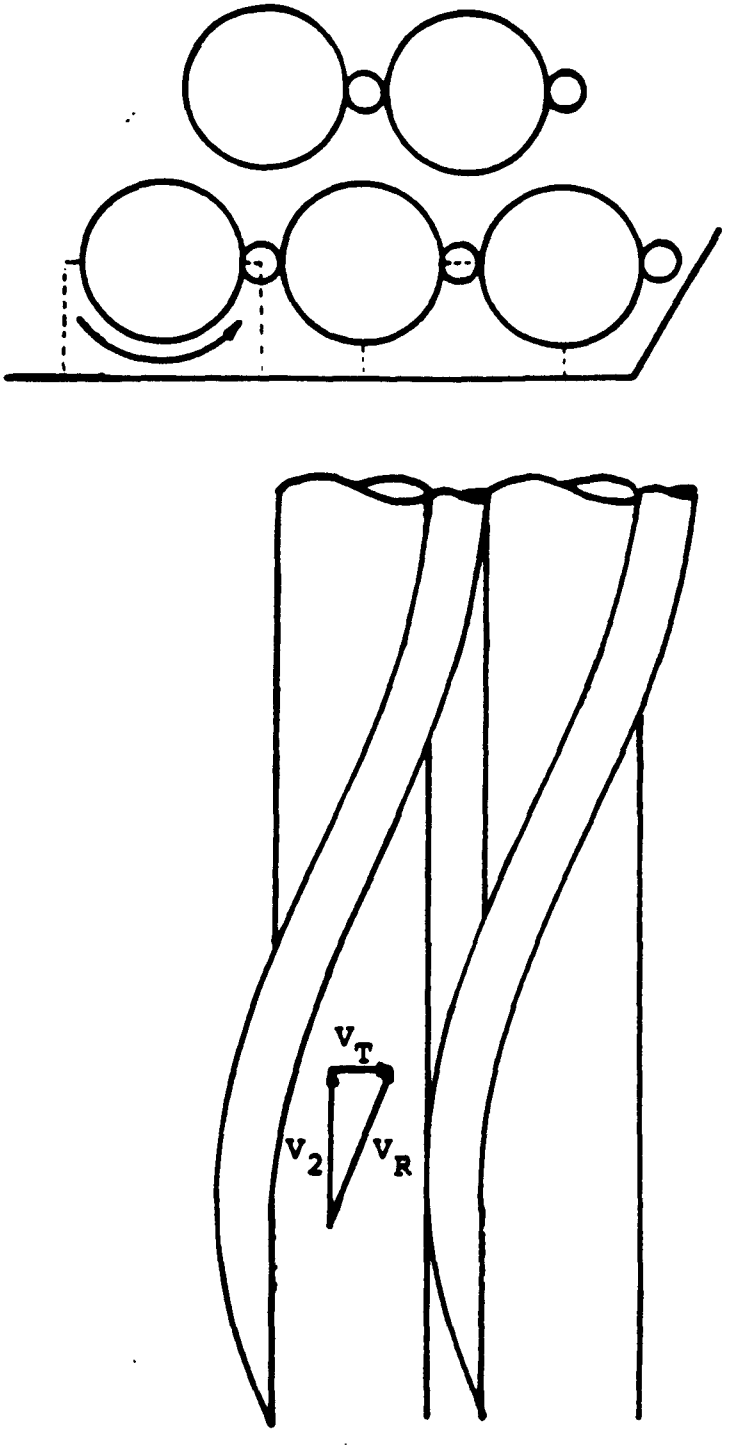

Figure 4.2 Velocity Components and Schematic Configuration of an Edge Subchannel

$$\hat{e}_{friction} = f_R \frac{L_R}{De_R} \frac{\rho V_R^2}{2} \tag{4.19}$$

where R denotes the parameters based on the swirl flow path

L_R = flow path travelled by the swirl flow for an axial length, L

V_R = resultant velocity of the swirl flow

f_R = friction factor corresponding to the swirl flow

De_R = equivalent hydraulic diameter corresponding to the swirl flow

To find V_R and L_R, one needs to know the transverse velocity V_T. If the flow follows the wire exactly, the transverse velocity V_T should be $V_2 \tan\theta$. However, according to some investigators (e.g., Ginsberg and Lorentz(1973)), the flow direction is not exactly following the wire direction, but slightly deviating from it. Nevertheless, it is reasonable to assume that the ratio V_T/V_2 is proportional to $\tan\theta$. Further, the ratio of transverse velocity head to axial velocity head is assumed to be proportional to the ratio of flow area covered by the wire to the total bare subchannel flow area, which reduces to zero when the wire diameter goes to zero. This is discussed in more detailed in Chapter 6 of Report 108 when the model for transverse velocity at the gap is derived. Hence,

$$(\frac{V_T}{V_2})^2 = C_s(\frac{A_{r2}}{A_2'}) \tan^2\theta \tag{4.20}$$

Where C_s = constant of proportionality, a function of geomery

$A_{r_2} = \pi(D + D_w)D_w/4$

$A_2' = P(W-D/2) - \pi D^2/8$

$$\tan\theta = \pi(D+D_w)/H$$

The resultant velocity V_R and the swirl flow path L_R can then be calculated as (refer to Figure 4.2)

$$V_R = V_2 F_R \tag{4.21a}$$

and

$$L_R = L\ F_R \tag{4.21b}$$

where

$$F_R \equiv \left[\ 1 + \left(\frac{V_T}{V_2}\right)^2\ \right]^{\frac{1}{2}}$$

$$= \left[\ 1 + C_s\left(\frac{A_{r2}}{A_2}\right)\tan^2\theta\ \right]^{\frac{1}{2}}$$

The friction factor f_R can be calculated by

$$f_R = \frac{C}{Re_R^{\,m}} \tag{4.22}$$

where C is a function of both geometry and flow regime and m is function of flow regime only. Now we approximate the equivalent hydraulic diameter for the swirl flow, De_R, to be the axial value, De_2. This approximation is close because of the canceling effects of changes in the flow area and wetted perimeter which are both projected to a new plane perpendicular to the swirl flow direction. Hence

$$f_R = \frac{C}{\left(\frac{\rho V_R De_R}{\mu}\right)^m} \approx \frac{C}{Re_2^m F_R^m} \tag{4.23}$$

where $Re_2 = \rho V_2 De_2/\mu$

The constant C is assumed to be the same as that in the bare rod edge subchannel friction factor for the same reasons as described for interior subchannel case. Thus equation (4.23) can be written as

$$f_R = f'_2 / F_R^m \tag{4.24}$$

where $f'_2 = K_2/Re_2^m$, and K_2 is derived from bare rod results.

Substituting V_R, L_R, and f_R into equation (4.19), we have

$$\hat{e}_2 \equiv \hat{e}_{friction}$$

$$= f'_2\left[1 + C_s\left(\frac{A_{r2}}{A'_2}\right)\tan^2\theta\right]^{\frac{3-m}{2}} \frac{L}{De_2} \frac{\rho V_2^2}{2} \tag{4.25}$$

The edge subchannel friction factor is then formulated as

$$f_2 = f'_2\left[1 + C_s\left(\frac{A_{r2}}{A'_2}\right)\tan^2\theta\right]^{\frac{3-m}{2}} \tag{4.26}$$

4.3.1.3 Corner Subchannel

Since the flow characteristics in the corner subchannel are the same as those in the edge subchannel, we assume that equation (4.26) can also be used in this case, except that the bare rod subchannel friction factor constant and geometrical factors should be changed to the corresponding corner subchannel values. Therefore,

$$f_3 = f'_3\left[1 + C_s\left(\frac{A_{r3}}{A'_3}\right)\tan^2\theta\right]^{\frac{3-m}{2}} \tag{4.27}$$

where $A_{r3} = \dfrac{\pi(D + D_w)D_w}{6}$

$$A'_3 = \frac{(W - \frac{D}{2})^2}{\sqrt{3}} - \frac{\pi D^2}{24}$$

4.3.2 Formulations and Empirical Constants for the Laminar and Turbulent Regions

The subchannel friction factor models, equations (4.18), (4.26) and (4.27), are applicable to all flow regimes since no special flow condition restriction has been imposed. The flow regime effect, which is essentially the Reynolds number dependence, appears in the constants f'_1, f'_2, f'_3, m, C_d and C_s. Next formulations for each of these necessary constants are presented.

For the laminar and turbulent regions, the friction factor data show a simple dependence on Reynolds number, i.e., f = constant/Re^m. Hence we will formulate f'_i in this form for laminar and turbulent flow regimes. The exponent m in laminar flow is 1.0, which is obtained from the analytically derived behavior of a simple geometrical flow channel. In turbulent flow for Reynolds numbers higher than 20,000, this exponent is around 0.2 for smooth tubes; however, the bundle average friction factor results derived from pressure drop data show that the average exponent is around 0.18 in this flow regime. The averaged value for m considering the bundle friction factor data for 122 wire-wrapped bundles is 0.1798 as shown in Appendix B of TR108. This low value might be caused by the surface roughness of the simulated rods in the experiments. The bare rod subchannel friction factors can then be expressed as

$$\text{Laminar region:} \quad f'_i = \frac{K_{iL}}{Re_i} \tag{4.28a}$$

$$\text{Turbulent region:} \quad f'_i = \frac{K_{iT}}{Re_i^{0.18}} \tag{4.28b}$$

where K_{iL} and K_{iT} are functions of P/D for the interior subchannel, and W/D for the edge or corner subchannel.

The drag coefficient C_d is not exactly the same as that usually seen in the literature; rather, it is a proportional constant for our models. Rehme (1973a,1980b) did some measurements for the drag coefficient of the grid spacer bundles and found that it was a slightly decreasing function of Reynolds number at high Reynolds number flow conditions. For simplicity, we assume that C_d has the same Reynolds number dependence as f_1' in the turbulent region. In the laminar flow condition, C_d is expected to have (1/Re) dependence from both theoretical derivation and experimental results. Hence

$$\text{Laminar region:} \quad C_d = \frac{W_{dL}}{Re_{D_w}} = \frac{W_{dL}}{Re_1 (\frac{D_w}{De_1})} \tag{4.29a}$$

$$\text{Turbulent region:} \quad C_d = \frac{W_{dT}}{Re_{D_w}^{0.18}} = \frac{W_{dT}}{Re_1^{0.18} (\frac{D_w}{De_1})^{0.18}} \tag{4.29b}$$

where the constants W_{dL} and W_{dT} are directly related to the wire effect which should be influenced by both the wire diameter and wrapping angle; therefore, we expect that the W_d's are functions of both Dw/D and H/D. Note that the Reynolds number calculated by using D_w as the characteristic length is used for this wire drag coefficient.

The constant C_s is the empirical factor which accounts for the assumptions used in deriving the edge subchannel friction factor. In addition to this function, C_s is the proportionality factor between

the real $(V_T/V_2)^2$ and the geometrical factor in equation (4.20). However, one should realize that (V_T/V_2) in equation (4.20) is not exactly the same as the edge transverse velocity ratio C_{1L} reduced from mixing experiments. The edge transverse velocity ratio C_{1L} only accounts for the flow transported from one edge subchannel to the adjacent one rather than the swirl flow along the rod as the formulation leading to equation (4.20) assumed. Nevertheless, the behavior of the edge transverse velocity ratio could indicate the characteristics of C_s, i.e., constant value in the turbulent flow regime but a decreasing function of Reynolds number in the transition region leading to another constant value in the laminar region. Therefore, we expect that C_s's are constants in the turbulent and laminar regions, but they should be different values. On the other hand, the edge transverse velocity ratio is a strong function of H/D, hence we expect that C_s might also be a function of H/D. By analogy with equation (4.29) for C_d, we write C_s in terms of W_s/Re^n where here n = 0 since there is no Re variation in the laminar or turbulent regions, i.e.,

$$\text{Laminar region:} \quad C_s = W_{sL} \tag{4.30a}$$

$$\text{Turbulent region:} \quad C_s = W_{sT} \tag{4.30b}$$

where W_{sL} and W_{sT} are functions of H/D.

Substituting equations (4.28), (4.29), (4.30) into equations (4.18), (4.26) and (4.27), we have the final forms for the subchannel friction factors equations,

$$f_1 = \frac{1}{Re_1^m}\left[K_1\left(\frac{P'_{w1}}{P_{w1}}\right) + W_d\left(\frac{3A_{r1}}{A'_1}\right)\left(\frac{De_1}{H}\right)\left(\frac{De_1}{D_w}\right)^m\right] \quad (4.31)$$

$$= C_{f1}/Re_1^m$$

$$f_2 = \frac{1}{Re_2^m}\left[K_2\left(1 + W_s\left(\frac{A_{r2}}{A'_2}\right)\tan^2\theta\right)^{\frac{3-m}{2}}\right] \quad (4.32)$$

$$= C_{f2}/Re_2^m$$

$$f_3 = \frac{1}{Re_3^m}\left[K_3\left(1 + W_s\left(\frac{A_{r3}}{A'_3}\right)\tan^2\theta\right)^{\frac{3-m}{2}}\right] \quad (4.33)$$

$$= C_{f3}/Re_3^m$$

where m = 1.0 for the laminar flow region

m = 0.18 for the turbulent flow region

K_1 = function of P/D

K_2, K_3 = function of W/D

W_d = function of D_w/D and H/D

W_s = function of H/D

4.3.3 Formulation and Empirical Constants for the Transition Region

4.3.3.1 Reynolds Numbers at Transition Points

Unlike the circular tube case, in which an obvious transition from laminar to turbulent flow conditions occurs around Re = 2,300, the transition within a rod bundle occurs as early as Re_b around 400 to 1000 with only slight deviation from laminar behavior as Re_b

increases. The log-log plot of the friction factor curve gradually changes its slope at a Re_{bL}, which depends on the P/D of the rod bundle, until $Re_b \approx 12000$ to 20000. After this Re_{bT} the slope is nearly a constant. The flow behavior in the transition range can be explained by the assumption that turbulence first appears in the center region of the subchannel and spreads progressively in the radial and circumferential directions with sufficient increase in Reynolds number, until laminar flow eventually disappears [Panknin et al. (1974)]. The Reynolds numbers for laminar-transition, Re^{bL}, and transition-turbulent, Re_{bT}, are required for the application of our model. These two values will be determined next.

Correlations that are assumed to qualitatively estimate the transition Reynolds number at the turbulent-transition and laminar-transition points for infinite bare triangular rod array have been proposed by Ramm et al. (1974) and Yang (1976) respectively. Ramm et al. calculated average value of the eddy diffusivity of momentum along the gap, $(\bar{\varepsilon}_{Mr}/\nu)_{\phi=0}$ and assumed that at $(\bar{\varepsilon}_{Mr}/\nu)_{\phi=0} = 0.2$ onset of laminarization starts at the gap region, i.e., the flow transits from the turbulent to the transition regime. A value of 0.3 for $(\bar{\varepsilon}_{Mr}/\nu)_{\phi=0}$ was later proposed by Johannsen (1981) to improve the correlation. Yang (1976) used a certain average value of the eddy diffusivity of momentum over the whole subchannel, $(\bar{\varepsilon}_{Mr}/\nu)$, as the criterion for the inception of flow transition and applied Ramm's (1975) Model to compute the transition Reynold's number. For the onset of transition from laminar to turbulent flow, he chose a value of 0.5 for the space-averaged eddy diffusivity $(\bar{\varepsilon}_{Mr}/\nu)$ as the qualitative criterion.

Figure 4.3 illustrates the Reynolds numbers from these two correlations as functions of P/D of an infinite triangular rod array.

Figure 4.4 shows the values of bundle Reynolds number for onset of transition from laminar to turbulent flow, Re_{bL}, from the friction factor data obtained by Rehme (1972) for bare rod bundles and other investigators for wire-wrapped rod bundles. The Reynolds number at which friction factor deviates from 1/Re behavior is assumed to be the laminar-transition point as illustrated in Figure 4.5 for bundles with P/D = 1.1. For $P/D \leq 1.1$ the data show that Re_{bL} is nearly a constant around 400. For $P/D > 1.1$, $\log (Re_{bL})$ is proportional to P/D. As shown in Figure 4.3 Yang's correlation for onset of transition can not predict the trend of data. The reasons for this inability might be : 1) the inception of turbulence is a local effect which will occur at $\phi = 30°$ of the characteristic geometry (c.f. Figure 4.3). Hence, chosing the eddy of diffusivity at $\phi = 30°$ would be more appropriate than an average value over whole subchannel, and 2) the application of the adopted eddy diffusivity expressions from Ramm's model far below their stated range of applicability regarding the Reynolds number which is $10^4 \leq Re \leq 2 \times 10^5$ is questionable. Since Yang's model can not predict the data, we develop a purely empirical correlation to calculate Re_{bL} from these data, (c.f. Figure 4.4)

$$\log\left(\frac{Re_{bL}}{300}\right) = 1.7 \left(\frac{P}{D} - 1.0\right) \qquad (4.34a)$$

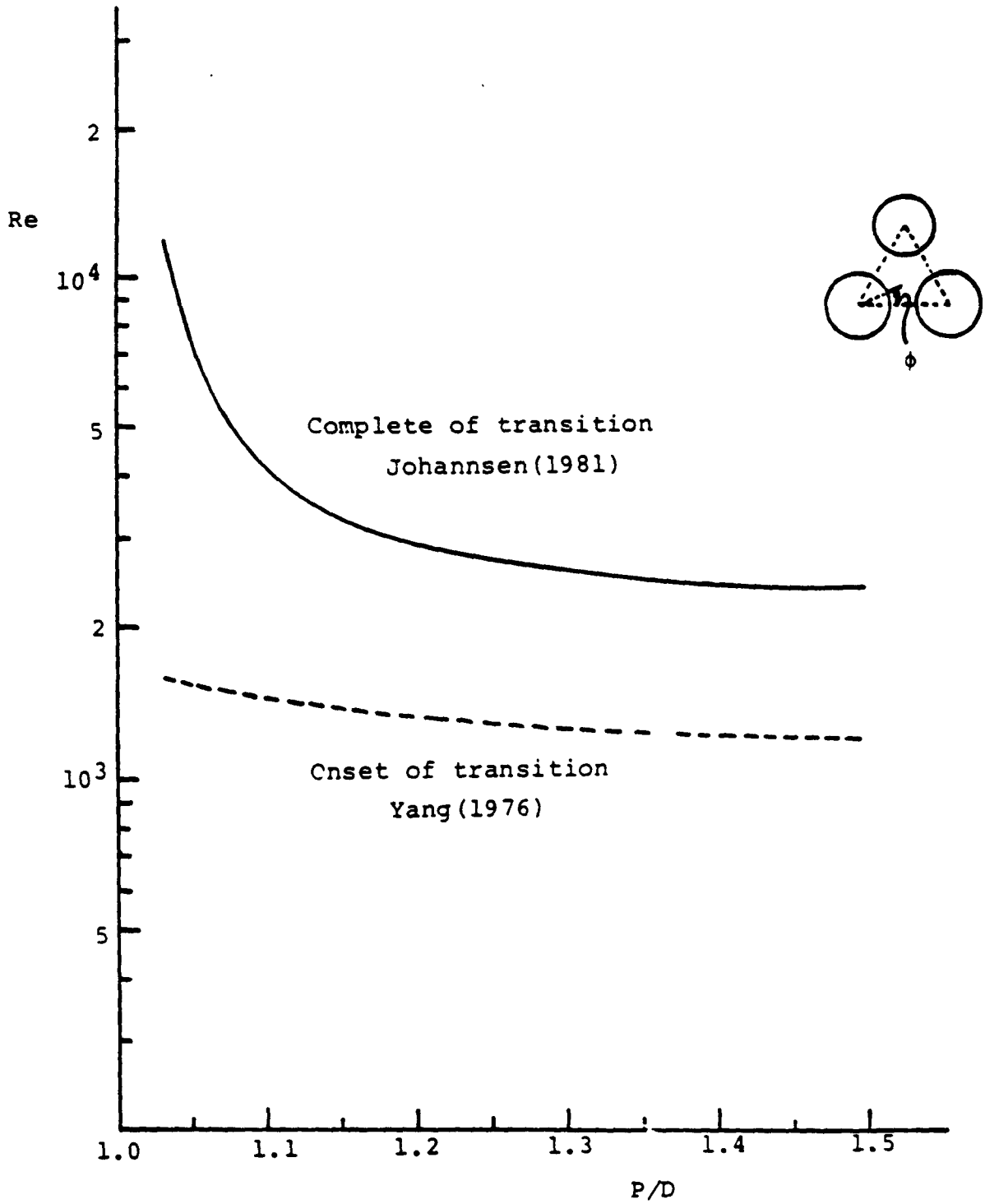

Figure 4.3 Ramm and Johannsen Correlation and Yang Correlation for Reynolds Number at Transition Points

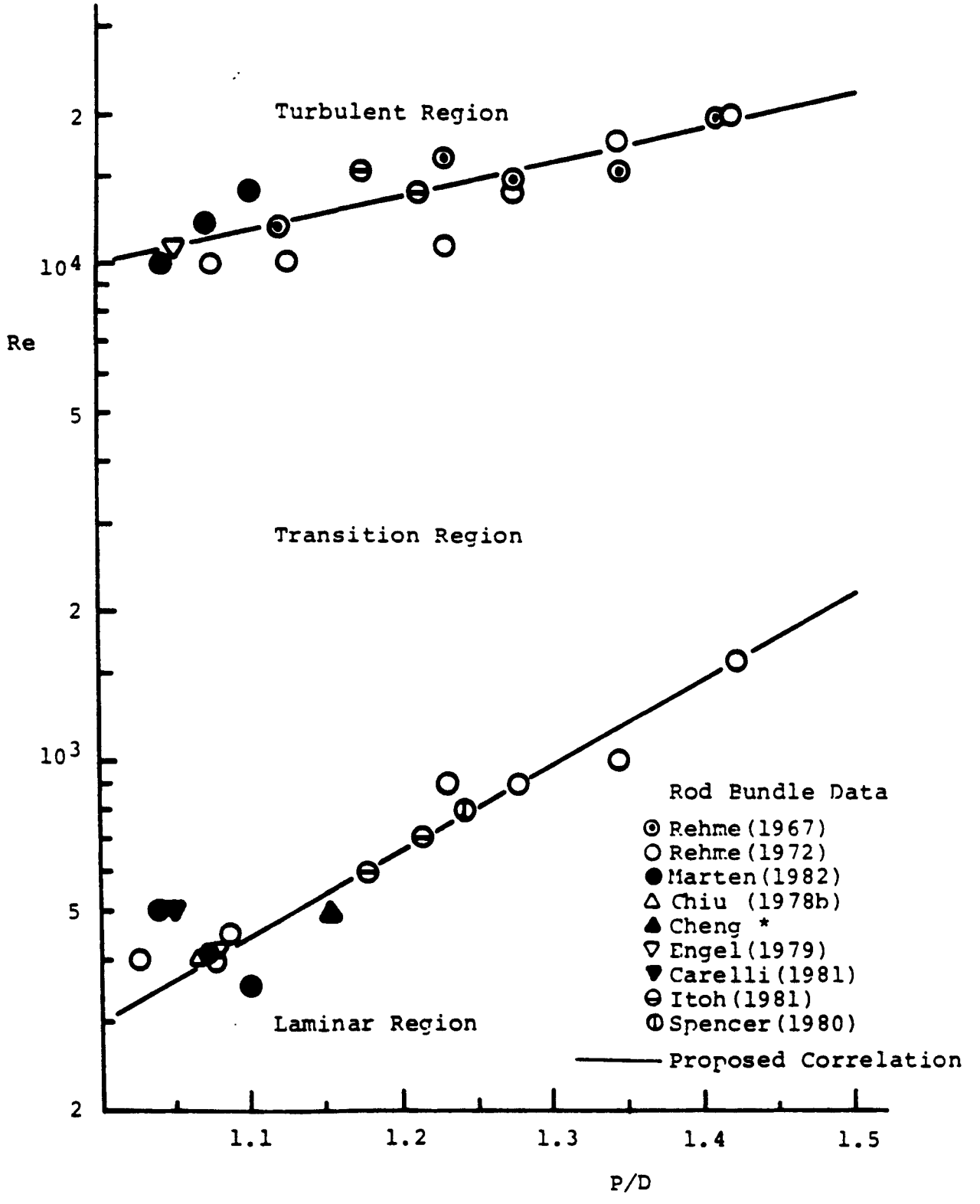

Figure 4.4 Data and Proposed Correlations for the Transition Reynolds Number

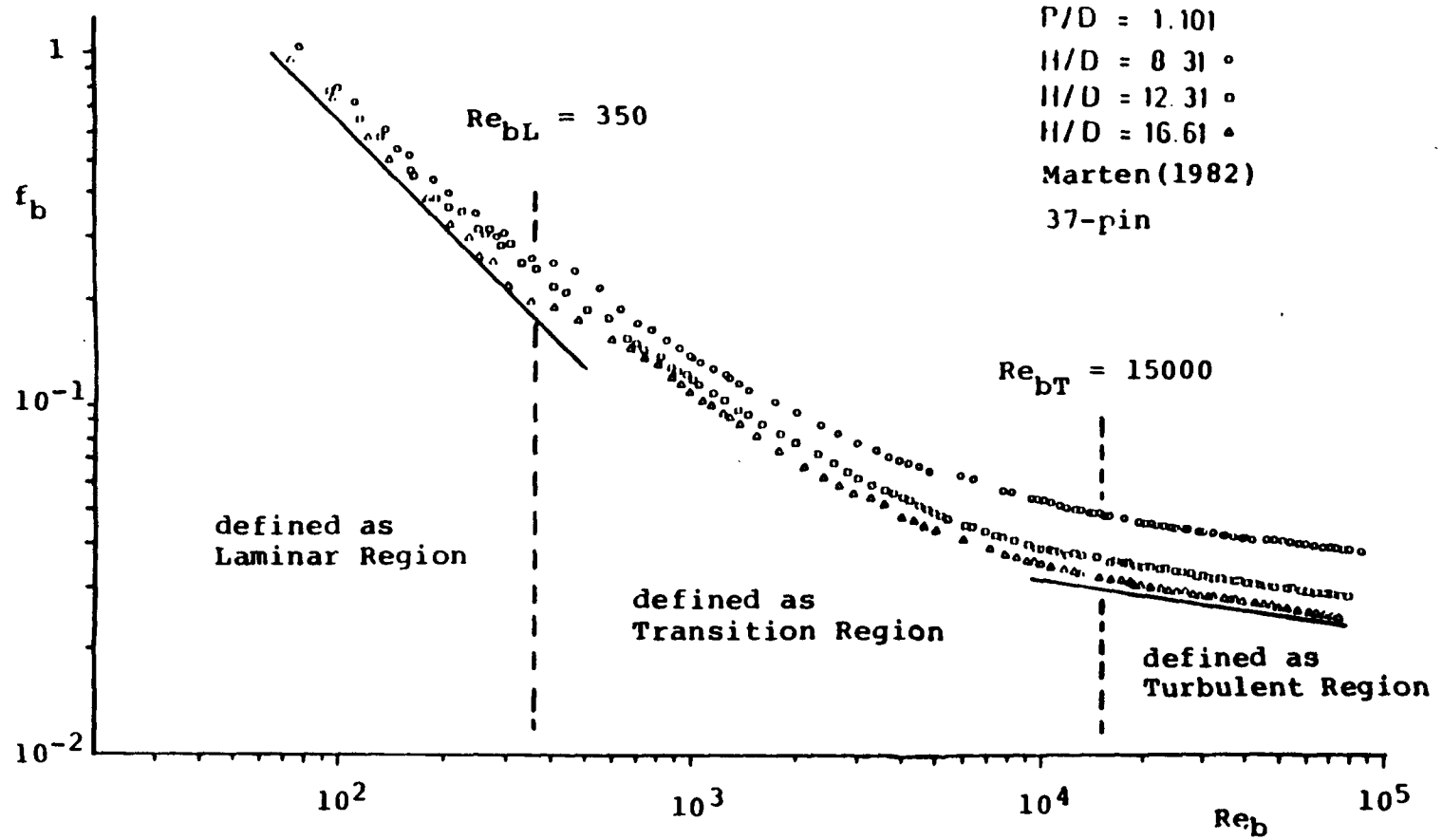

Figure 4.5 Illustration of Re_{bL} and Re_{bT} from Friction Factor Data

Although fully turbulent flow may be achieved much earlier than Re_b = 12000 to 20000 as predicted by Johannsen's model, the slope for log(f) vs. log (Re_b) shows a constant value after a Re_{bT} ≈ 12000 to 20000 from almost all the rod bundles friction factor data. For easy formulation of the correlations, a constant exponent for Reynolds number in the friction factor formulation in the turbulent flow regime is required. Hence a Re_{bT} after which the slope is constant is artifically set to be the point beyond which we call the turbulent flow regime. These Re_{bT}'s are also shown in Figure 4.4. The way to get this Re_{bT} is also illustrated in Figure 4.5. Similar to Re_{bL} a purely empirical correlation is developed to calculate Re_{bT} from these data,

$$\log(\frac{Re_{bT}}{10000}) = 0.7\ (\frac{P}{D} - 1.0) \qquad (4.34b)$$

The subchannel transition region for each kind of subchannel is calculated based on the laminar and turbulent flow split values together withthe Re_{bL} and Re_{bT} criteria. That is we assume that all subchannels start transition at $Re_b = Re_{bL}$ and reach the fully turbulent condition at $Re_b = Re_{bT}$.

4.3.3.2 Formulation and Empirical Constant

For the transition region, we cannot simply formulate the constants m, f'_i, C_d, and C_s, since m and C_s as well as the constants in the numerator of f'_i and C_d are functions of Reynolds number.

Spriggs (1973) successfully used an intermittency factor as a weighting factor to linearly combine the laminar value and the turbulent value for calculating the friction factor for transition flow regime in a circular tube. The intermittency factor, whose value ranges from zero to unity, can be considered to represent that fraction of the flow field which is turbulent in a specified flow subchannel. Based on this argument, we propose the transition subchannel friction factors to be

$$f_{itr} = f_{iL}(1 - \psi_i)^{\gamma} + f_{iT}\psi_i^{\gamma} \qquad (4.35)$$

where $f_{iL} = C_{fiL}/Re_i$

$f_{iT} = C_{fiT}/Re_i^m$

γ = exponent fitted from data

ψ_i = intermittency factor

$$\equiv \frac{\log Re_i - \log Re_{iL}}{\log Re_{iT} - \log Re_{iL}}$$

Re_{iL} = subchannel Reynolds number at which flow starts transition for subchannel i

$= Re_{bL}(De_i/De_b)X_{iL}$

Re_{iT} = subchannel Reynolds number at which flow reaches full turbulence for subchannel i

$= Re_{bT}(De_i/De_b)X_{iT}$

The exponent of ψ_i and $(1 - \psi_i)$, γ, is the empirical constant implemented in the correlation in order to fit the data. Engel et al. (1979) successfully used equation (2.26) with $\gamma = 0.5$ to fit their blanket subassemblies' bundle average friction factor; however, their

definition of intermittency factor is different from our definition. (see equation (4.1)) Differences exist in the criteria for turbulent Reynolds number and the use of a log function in our definition of ψ_i. Note that $\gamma = 1$ means a linear combination of f_{iL} and f_{iT}, while a higher γ value gives a lower f_{itr}; and a lower γ value gives a higher f_{itr}.

4.3.4 Flow Split Parameters and Bundle Average Friction Factor

The subchannel friction factor formulae have been derived in the last two sections. From these equations one can derive the formulae for flow split parameters and bundle average friction factor. For fully developed flow over a length L which is several lead lengths long, the momentum transfer between subchannels can be assumed to be negligible; therefore, the pressure drop along this length for each kind of subchannel can be calculated from the momentum balance:

$$\Delta P_i = f_i \frac{L}{De_i} \frac{\rho V_i^2}{2}$$

By the equal subchannel pressure drop assumption and the mass continuity requirement, one has

$$\frac{f_b}{De_b} = \frac{f_1}{De_1} X_1^2 = \frac{f_2}{De_2} X_2^2 = \frac{f_3}{De_3} X_3^2 \tag{4.36}$$

and

$$S_1 X_1 + S_2 X_2 + S_3 X_3 = 1 \tag{4.37}$$

where $S_1 = \frac{N_1 A_1}{A_b}$, $S_2 = \frac{N_2 A_2}{A_b}$, $S_3 = \frac{N_3 A_3}{A_b}$

These are similar to equations (1.2) and (1.3), except that X_3 is also an unknown rather than assumed to equal X_2. Now we have four equations with seven parameters, f_1, f_2, f_3, X_1, X_2, X_3 and f_b. Since the three parameters, f_1, f_2, and f_3 were given, we can solve equations (4.36) and (4.37) to get the remaining four parameters, X_1, X_2, X_3 and f_b.

4.3.4.1 Turbulent and Laminar Regions

For turbulent and laminar regions, f_i (i = b, 1, 2 or 3) can be simply expressed as (cf. equations (4.31), (4.32), (4.33))

$$f_i = \frac{C_{fi}}{Re_i^m} \tag{4.38}$$

Substituting equation (4.38) into equation (4.36) and assuming that the kinetic viscosity, ν, is constant over the bundle cross section, we have

$$\begin{aligned} \frac{C_{fb}}{De_b}\left[\frac{1}{De_b}\right]^m &= \frac{C_{f1}}{De_1}\left[\frac{1}{De_1 X_1}\right]^m X_1^2 \\ &= \frac{C_{f2}}{De_2}\left[\frac{1}{De_2 X_2}\right]^m X_2^2 \\ &= \frac{C_{f3}}{De_3}\left[\frac{1}{De_3 X_3}\right]^m X_3^2 \end{aligned} \tag{4.39}$$

The ratio between velocities, (X_i/X_j), (X_b = 1.0 by definition), is

$$\frac{X_i}{X_j} = \left[\frac{De_i}{De_j}\right]^{\frac{1+m}{2-m}} \left[\frac{C_{fj}}{C_{fi}}\right]^{\frac{1}{2-m}} \tag{4.40}$$

From the mass continuity equation (4.37), the edge subchannel flow split parameter is

$$X_2 = \frac{1}{S_2 + \left[\frac{X_1}{X_2}\right]S_1 + \left[\frac{X_3}{X_2}\right]S_3} \tag{4.41}$$

where from equation (4.40)

$$\frac{X_1}{X_2} = \left[\frac{De_1}{De_2}\right]^{\frac{1+m}{2-m}}\left[\frac{C_{f2}}{C_{f1}}\right]^{\frac{1}{2-m}} \tag{4.42}$$

$$\frac{X_3}{X_2} = \left[\frac{De_3}{De_2}\right]^{\frac{1+m}{2-m}}\left[\frac{C_{f2}}{C_{f3}}\right]^{\frac{1}{2-m}} \tag{4.43}$$

Equations (4.41), (4.42) and (4.43) are the formulae for flow split parameters in the turbulent and laminar regions. After the constants C_{f1}, C_{f2} and C_{f3} are determined, they can be used to calculate X_i.

For bundle average friction factor, the constant C_{fb} can be derived by substituting X_i/X_b, i = 1, 2, 3, from equation (4.40) into equation (4.37), that is,

$$\sum_{i=1}^{3} S_i \left[\frac{De_i}{De_b}\right]^{\frac{1+m}{2-m}}\left[\frac{C_{fb}}{C_{fi}}\right]^{\frac{1}{2-m}} = 1$$

Hence

$$C_{fb} = De_b\left\{\sum_{i=1}^{3} S_i\left[\frac{De_i}{De_b}\right]^{\frac{m}{2-m}} C_{fi}^{\frac{1}{m-2}}\right\}^{m-2} \qquad (4.44)$$

4.3.4.2 Transition Region

Theoretically, the transition bundle average friction factor and flow split parameters can also be determined from subchannel friction factor equations by substituting equation (4.35) into equation (4.36) together with mass balance equation (4.37). However, the resultant equations are highly nonlinear, hence no simple equation can be derived for those parameters in the transition region. They can only be found by numerical iteration. On the other hand, we would like to have closed form expressions for bundle average friction factor and transition flow split parameters for easy calculation.

Therefore, we assume that an expression for bundle average friction factor in the transition region can take the same form as equation (4.35).

$$f_{btr} = f_{bL}(1-\psi_b)^{\gamma} + f_{bT}\psi_b^{\gamma} \qquad (4.45)$$

where $f_{bL} = C_{fbL}/Re_b$

$f_{bT} = C_{fbT}/Re_b^m$

The constants C_{fbL} and C_{fbT} are determined by equation (4.44).

The transition flow split parameters are considered next. Although the exact solution for flow split parameters from equations (4.36) and (4.37) does not have closed form, we can derive desired expressions as functions of bundle average Reynolds number by some

approximations. The first approximation involves the intermittency factors. Although the intermittency factors ψ_i for different kinds of subchannels at one bundle average Reynolds number are different, they are approximately equal to the bundle value ψ_b, i.e.,

$$\psi_i = \frac{\log(Re_i/Re_{iL})}{\log(Re_{iT}/Re_{iL})} = \frac{\log(Re_b X_i/Re_{bL} X_{iL})}{\log(Re_{bT} X_{iT}/Re_{bL} X_{iL})}$$

$$\simeq \psi_b \equiv \log(Re_b/Re_{bL})/\log(Re_{bL}/Re_{bT}) \qquad (4.46)$$

Note that as $Re_b \to Re_{bL}$ or $Re_b \to Re_{bT}$, $\psi_i \to \psi_b$. Therefore, taking $\psi_i = \psi_b$, equation (4.35) can be written as

$$f_i = \frac{C_{fiL}}{Re_i}(1-\psi_b)^\gamma + \frac{C_{fiT}}{Re_i^m}\psi_b^\gamma$$

$$= \left[\frac{C_{fiL}\left(\frac{De_b}{De_i}\right)}{Re_b}(1-\psi_b)^\gamma\right]\left(\frac{1}{X_i}\right) + \left[\frac{C_{fiT}\left(\frac{De_b}{De_i}\right)^m}{Re^m}\psi_b^\gamma\right]\left(\frac{1}{X_i}\right)^m \qquad (4.47)$$

Substituting equation (4.47) into the portion of equation (4.36), applicable to two subchannels, i and j, we have

$$\left[C_{fiL}\left(\frac{De_b}{De_i}\right)\right]\left[\frac{(1-\psi_b)^\gamma}{Re_b}\right]\left(\frac{X_i}{De_i}\right) + \left[C_{fiT}\left(\frac{De_b}{De_i}\right)^m\right]\left[\frac{\psi_b^\gamma}{Re_b^m}\right]\left[\frac{X_i^{2-m}}{De_i}\right]$$

$$= \left[C_{fjL}\left(\frac{De_b}{De_j}\right)\right]\left[\frac{(1-\psi_b)^\gamma}{Re_b}\right]\left(\frac{X_j}{De_j}\right) + \left[C_{fjT}\left(\frac{De_b}{De_j}\right)^m\right]\left[\frac{\psi_b^\gamma}{Re_b^m}\right]\left[\frac{X_j^{2-m}}{De_j}\right] \qquad (4.48)$$

Equation (4.48) expresses the general relation between X_i and X_j. We next desire to specialize this to yield X_1/X_2 and X_3/X_2. Equation (4.48) can be used to find the approximate equations of these parameters.

Since X_i's are not far away from unity, in the first approximation, let us assume that

$$X_i^{2-m} = X_i^{1.82} \simeq X_i$$

then equation (4.48) becomes

$$\frac{X_j}{X_i} \simeq \frac{\{C_{fiL}[\frac{De_b}{De_i}][\frac{(1-\psi_b)^\gamma}{Re_b}] + C_{fiT}[\frac{De_b}{De_i}]^m[\frac{\psi_b^\gamma}{Re_b^m}]\}\frac{1}{De_i}}{\{C_{fjL}[\frac{De_b}{De_j}][\frac{(1-\psi_b)^\gamma}{Re_b}] + C_{fjT}[\frac{De_b}{De_j}]^m[\frac{\psi_b^\gamma}{Re_b^m}]\}\frac{1}{De_j}} \tag{4.49}$$

On the other hand, if we replace X_i by X_i^{2-m} in equation (4.48), then

$$\frac{X_j}{X_i} \simeq [\text{ right side term of equation (4.49) }]^{\frac{1}{2-m}} \tag{4.50}$$

As $Re_b \to Re_{bL}$, equation (4.49) gives the exact solution since equation (4.49) equals equation (4.48) and $\psi_b \to \psi_i$. On the other hand equation (4.50) does not give the exact solution. Analogously as $Re_b \to Re_{bT}$, equation (4.50) gives the exact solution but equation (4.49) does not. The exact solution in the transition region should not be far away from either equation (4.49) or equation (4.50). To give the correct limiting solutions, a good approximation might be

$$\frac{X_j}{X_i} = \frac{C_{fiL}\left[\frac{De_b}{De_i^2}\right]\left[\frac{(1-\psi_b)^\gamma}{Re_b}\right] + \beta\left\{C_{fiT}\left[\frac{De_b}{De_i}\right]^m \frac{1}{De_i}\left[\frac{\psi_b^\gamma}{Re_b^m}\right]\right\}^{\frac{1}{2-m}}}{C_{fjL}\left[\frac{De_b}{De_j^2}\right]\left[\frac{(1-\psi_b)^\gamma}{Re_b}\right] + \beta\left\{C_{fjT}\left[\frac{De_b}{De_j}\right]^m \frac{1}{De_j}\left[\frac{\psi_b^\gamma}{Re_b^m}\right]\right\}^{\frac{1}{2-m}}} \qquad (4.51)$$

where β is the constant which makes equation (4.51) approach the exact solution or the experimental data, depending on which one we want.

The empirical constants in the transition region are then γ and β. γ is determined from the bundle average friction factor data, while β is determined by the exact solutions or the experimental data of the flow split parameters.

4.3.5 Summary

The formulae for subchannel friction factors and flow split parameters have been derived in this section. In summary,

For the turbulent and laminar regions,

f_1, f_2, f_3 from equations (4.31), (4.32), (4.33), respectively

X_1, X_2, X_3 from equations (4.42), (4.41), (4.43), respectively

f_b from equations (4.38) and (4.44)

For the transition region,

f_1, f_2, f_3 from equation (4.35)

X_1, X_2, X_3 from solving equations (4.36) and (4.37), or from equations (4.41) and (4.51)

f_b from equation (4.45)

The next step will be calibrating the empirical constants K_1, K_2, K_3, W_d, W_s, γ, and β by the available data from bare rod bundles and wire-wrapped rod bundles.

4.4 Empirical Constants for Bare Rod Subchannel Friction Factor

4.4.1 Introduction

Although many investigators have carried out both theoretical and experimental work on the friction factor of bare rod bundles, none have tried to develop subchannel friction factors for use in calculating the average bundle friction factor. The reason may lie in the fact that the bundle pressure drop data can only give us the bundle average friction factor, hence one tends to correlate the data in a bundle sense. However, as we discussed before, subchannel friction factors are essential in subchannel analysis. In this section, the subchannel friction factors for bare rod bundle in both laminar and turbulent flow will be determined.

Since the flow subchannels in an assembly communicate with their neighbors, their flow patterns will be affected by this interaction. Hence the friction factors of these subchannels are not easy to define. We define the interior subchannel friction factor for simplicity to be that of an infinite triangular rod array. The influence of the adjacent duct walls on the flow field in an interior subchannel had been investigated by Schmid (1966). Schmid showed that velocity changes due to the presence of walls was less than 1% for $P/D < 2.5$ if the hydraulic diameter of the individual channels were not markedly different. The friction factor of an interior subchannel inside a rod bundle can then be assumed to be the same as that of an infinite rod array. For edge and corner subchannels with $P/D = W/D$,

the effect of rod number will be assumed to be negligible. Since we are only interested in fast breeder reactor application, the P/D and W/D will be restricted to be within 1.5.

In laminar flow, the bare rod friction factor can be represented as

$$f'_{iL} = \frac{K_{iL}}{Re_i} \tag{4.52}$$

where i = 1 means interior subchannel

= 2 means edge subchannel

= 3 means corner subchannel

= b means bundle average

In turbulent flow, the friction factor can be represented as

$$f'_{iT} = \frac{K_{iT}}{Re_i^m} \tag{4.53}$$

The constants K_{iL} and K_{iT} are functions of P/D or W/D. In order to calculate them easily, simple but accurate equations should be developed. After some tries in determining these equations, we find the best and simplest way is to separate the effect of the P/D (or W/D) into two regions, one of which is in the range of $1.0 \leq P/D \leq 1.1$, while the other is $1.1 < P/D \leq 1.5$. In either region, K_{iL} and K_{iT} are represented by a simple two degree polynomial equation:

$$K_{iL}(\text{or } K_{iT}) = a + b_1(\frac{P}{D} - 1.0) + b_2(\frac{P}{D} - 1.0)^2 \tag{4.54}$$

The objective of this section is to determine the constants a's, b_1's and b_2's.

4.4.2 Laminar Flow Subchannel Friction Factor

4.4.2.1 Interior Subchannel

Sparrow and Loeffler (1959) were the first to publish the velocity field in an infinite triangular rod array. They truncated the series representation of their velocity solution by utilizing a point matching technique (6 points) along the boundary of the triangular sector. By this method, they were able to get the value, fRe_D, as a function of P/D, which is easy to transform to fRe_{De} (i.e., K_{iL}) by

$$fRe_{De} = fRe_D\left[\frac{2\sqrt{3}}{\pi}\left(\frac{P}{D}\right)^2 - 1\right] \tag{4.55}$$

While analyzing the multiregion temperature problem, Axford (1964, 1967) also solved the velocity problem for longitudinal laminar flow over an infinite triangular bundle. He employed a finite Fourier Cosine Transform and a point matching method for the solution. He used 6 to 15 boundary points to obtain the unknown coefficients of the series. Axford's results agree with those of Sparrow and Loeffler.

Rehme (1971,1980) used the so-called method of cyclic reduced block overrelaxation to obtain a finite difference solution to the flow problem in a 7-pin hexaganol bare rod bundle. For the interior subchannel, his results are within 2% with those of the infinite triangular array. This validates our assumption described in the last section, i.e., infinite triangular array results can be used with little error for the interior subchannel of a bundle.

Ullrich (1974) also investigated the finite triangular rod array in laminar flow by a highly sophisticated method. His results are in excellent agreement with Sparrow and Loeffler's results (±2%). Rehme's

fRe factors based on his combination method for the 19-pin and 37-pin bundles are also in excellent agreement (within 1.4%) with the results of Ullrich.

4.4.2.2 Edge and Corner Subchannel

Only Rehme (1971,1980) has solved the flow problem in these two kinds of subchannels in a 7-pin bare rod bundle. According to Rehme's results, K_{iL} will vary with P/D for a fixed value of W/D. However, since we are interested in LMFBR application, at which W/D ≈ P/D, the value at which P/D = W/D will be used for each W/D.

Table 4.1 lists K_{iL}'s in which the interior results are from Axford (1964, 1967), while edge and corner results are from Rehme (1971, 1980). Figure 4.6 compares these three K_{iL} values as a function of P/D.

4.4.2.3 Equation for Determining K_{iL}

The table form of Table 4.1 is not easy to use for determining K_{iL} at one arbitrary P/D (or W/D). As described in section 4.4.1 equation (4.54) is used to fit the values in Table 4.1 in two P/D regions. The results are also depicted in Table 4.1. The values calculated by these coefficients and equation (4.54) are listed in Table 4.1 for comparison. The calculated values (from equation (4.54)) differ from the theoretical values by not more than 1.5%.

4.4.2.4 Comparison between Experimental Data and Correlation

Subchannel friction factor data from only one laminar flow experiment is known to the author. That is Gunn's (1963) edge flow channel with W/D = 1.0. The experimental f•Re is 26.0, which is within 1% of the theoretical value.

Table 4.1
Fitting Results of Laminar KL= f*Re
for Triangular Array
(KL from Axford and Rehme's results)

Calculated KL=a+b(1)*(P/D-1)+b(2)**(P/D-1)**2

Interior subchannel
for 1.0<=P/D<=1.1 the coefficients are
a= 0.2600E+02 b(i)= 0.8882E+03 -0.3334E+04

P/D	KL	cal.KL	%error
1.0000	26.0120	25.9974	-0.1
1.0040	29.4000	29.4970	0.3
1.0100	34.5360	34.5464	0.0
1.0200	42.5160	42.4287	-0.2
1.0300	49.7640	49.6444	-0.2
1.0400	56.2200	56.1932	-0.0
1.0500	61.9120	62.0754	0.3
1.1000	81.5080	81.4854	-0.0

for 1.1<P/D<=1.5 the coefficients are
a= 0.6297E+02 b(i)= 0.2169E+03 -0.1902E+03

P/D	KL	cal.KL	%error
1.1000	81.5080	82.7600	1.5
1.1500	92.5640	91.2299	-1.4
1.2000	99.8000	98.7489	-1.1
1.2500	105.2040	105.3169	0.1
1.3000	109.6680	110.9341	1.2
1.5000	124.1400	123.8941	-0.2

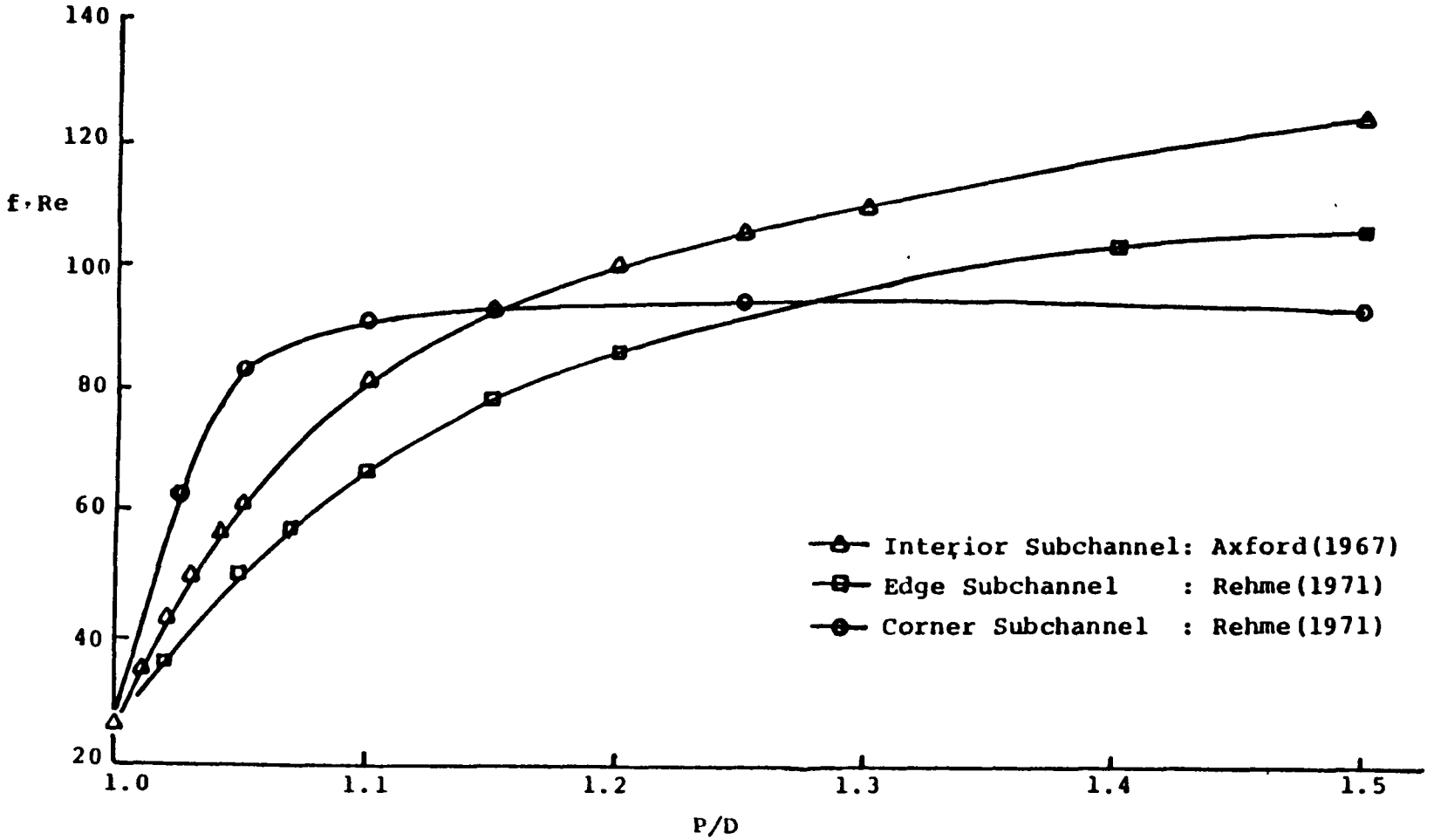

Figure 4.6 Theoretical Results of Laminar f·Re for Different Subchannels

Rehme (1972), and Galloway (1965) have measured the bundle averaged friction factor in their bare rod experiments in laminar flow region. The predicted bundle average friction factors can be calculated from equation (4.44) if one uses the K_{iL} calculated from equation (4.54). Figure 4.7 illustrates this comparison and shows that the correlation can predict the laminar data within 3% except for one point which is still within 10% of the prediction value. Note that the error might be caused by experimental error rather than by theoretical prediction.

4.4.3 Turbulent Flow Sunchannel Friction Factor

The most widely used turbulent flow friction factor for a smooth circular tube is Prandtl's universal law of friction,

$$\frac{1}{\sqrt{f_{ct}}} = 2.0 \log(Re\sqrt{f_{ct}}) - 0.8 \qquad (4.56)$$

Some investigators, e.g., Rehme, however used Maubach's equation to determine the circular tube turbulent friction factor,

$$\frac{1}{\sqrt{f_{ct}}} = 2.035 \log(Re\sqrt{f_{ct}}) - 0.989 \qquad (4.57)$$

For consistency, equation (4.56) will be used to calculate f_{ct} in thiswork.

The turbulent subchannel friction factor investigated below will be represented by the ratio between it and the circular tube value.

4.4.3.1 Theoretical Work on Turbulent Subchannel Friction Factor

The first fundamental theoretical work on the infinite triangular rod array friction factor in turbulent flow was done by Deissler and

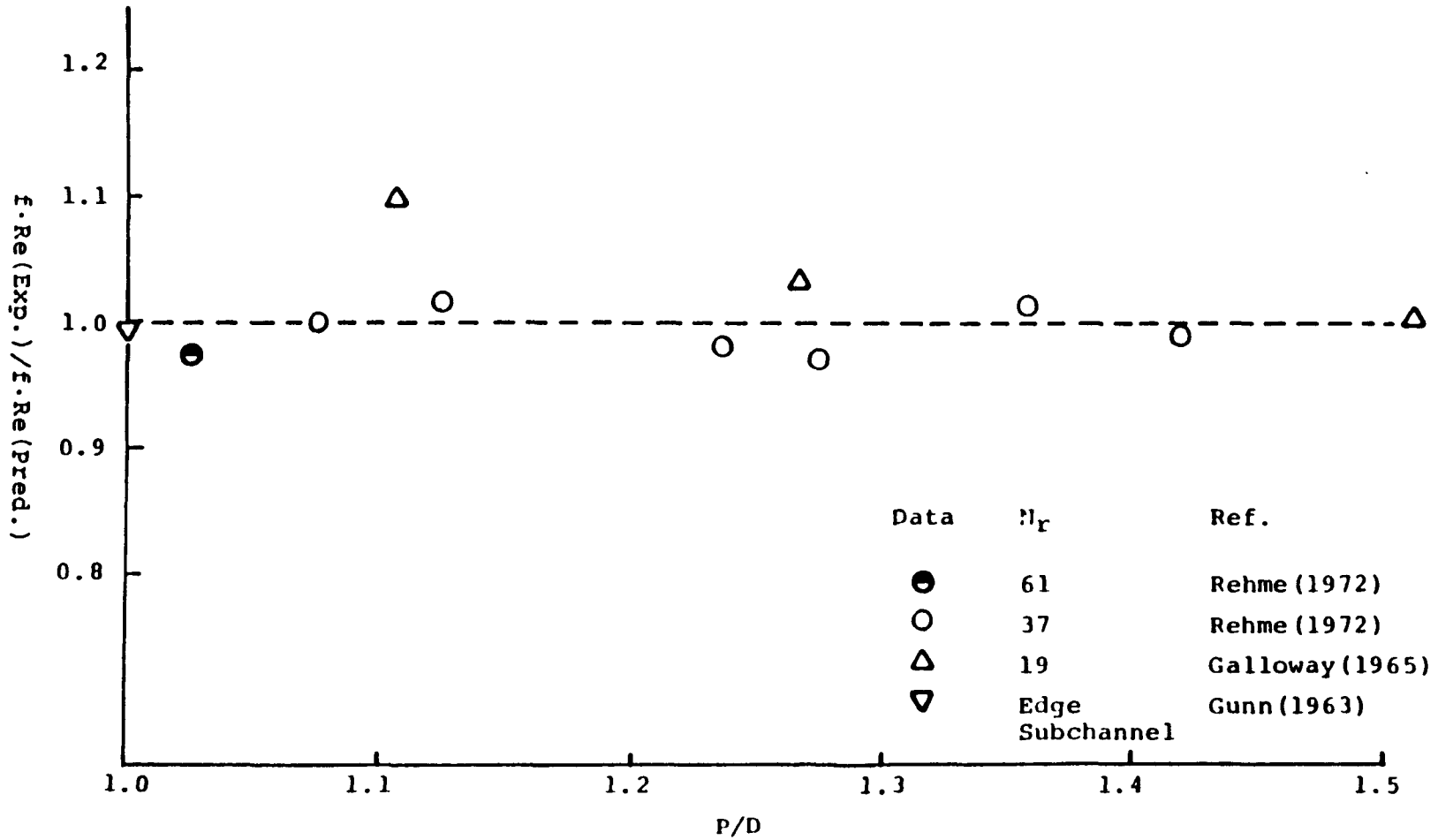

Figure 4.7 Comparison between Experimental and Predicted Bare Rod Bundle Laminar Friction Factor Constant f·Re

Taylor (1957). Deissler's velocity profile, which differs only slightly from Nikuradse's universal velocity profile, was used in their approach.

Ibragimov (1967) developed a fairly complicated method to calculate the friction factor for turbulent flow in channels of non-circular crosssection. His results were used by Magee and Nilsson (1971) as the Y parameter in their bundle friction factor correlation.

Dwyer and Berry (1972) used Nikuradse's universal velocity profile, which has been proved by Eifler (1967) and Levchenko (1967) to describe quite accurately the velocity profile in rod array channels if the local value of wall shear stress $\tau_w(\theta)$ is known, to calculate the friction factor of an interior subchannel in turbulent flow. The friction factor is varied until the average linear velocity calculated from the local velocity distribution equals the average linear velocity corresponding to the Reynolds number on which the local linear velocity was based.

Malak (1975) developed a relation between the turbulent friction factor and a geometrical parameter L* for non-circular flow channels. However, the data used to establish the correlation are restricted. After some arithmetic calculation, the f/f_{ct} for different P/D can be determined from his empirical equation.

Finally and most importantly, Rehme (1972) developed a G*-method to predict the friction factor for turbulent flow through non-circular channels on the basis of the f•Re value for laminar flow. Because of its accuracy, this method will be discussed in some detail in the next section. As for edge and corner subchannel friction factor in turbulent

flow, the only applicable theoretical method known to the author is the G*-method. Although Malak's method can also calculate these values, it is not used because of its restricted data base and difficulty in getting the L* parameter.

The results of the above five investigators for f/f_{ct} at Re = 10^5 are listed in Table 4.2 as a function of P/D. They are also illustrated in Figure 4.8 for comparison.

4.4.3.2 The G*-Method

Maubach (1970) used the "equivalent" annular zone concept for a hexagonal elementary cell around each rod and the universal velocity profile,

$$v^+ = 2.5 \ln y + 5.5$$

where $v^+ \equiv v/v^*$, $y^+ \equiv yv^*/\nu$, $v^* \equiv \sqrt{\tau_w/\rho}$

to obtain a friction factor correlation for an equivalent annular zone:

$$\sqrt{\frac{8}{f}} = 2.5 \ln\left(Re\sqrt{\frac{f}{8}}\right) + 5.5 - \frac{3.966+1.25X}{1+X} - 7.2 \ln 2(1+X) \qquad (4.58)$$

$$\text{where } X \equiv \sqrt{\frac{2\sqrt{3}}{\pi}} \frac{P}{D} \simeq 1.05 \frac{P}{D}$$

This "equivalent" annular zone is a good approximation to rod arrays with large rod distance ratios (P/D > 1.2) for which the wall shear stress is relatively constant around the perimeter of the rod.

Rehme (1972) assumed that the friction factor for non-circular flow channels can be represented in the same form as Maubach's theory to be

$$\sqrt{\frac{8}{f}} = A \left[2.5 \ln\left(Re\sqrt{\frac{f}{8}}\right) + 5.5\right] - G^* \qquad (4.59)$$

TABLE 4.2

f/fct for Bare Rod Interior Subchannel in Turbulent Flow by Different Investigators (at Re = 10^5)

P/D	Deissler (1956)	Ibragimov (1967)	Dwyer (1972)	Malak (1975)	Rehme (1972)
1.00	0.55	—	—	0.693	0.647
1.001	—	0.653	0.630	—	0.657
1.01	—	0.706	0.762	—	0.739
1.02	0.72	0.795	0.841	—	0.816
1.025	—	—	—	0.903	—
1.03	—	0.819	0.895	—	0.884
1.04	—	0.943	0.934	—	0.943
1.05	0.87	0.990	0.964	1.028	0.994
1.06	—	1.023	0.983	—	1.012
1.07	—	—	0.998	—	1.017
1.10	0.98	1.087	1.023	1.133	1.028
1.15	—	1.115	1.047	—	1.038
1.20	1.038	1.129	1.062	1.199	1.046
1.30	1.050	1.149	1.082	1.228	1.059
1.40	1.063	1.166	1.096	1.232	1.067
1.50	—	—	—	—	1.072
1.60	1.070	1.199	1.111	—	—
2.00	1.10	1.268	1.131	—	—

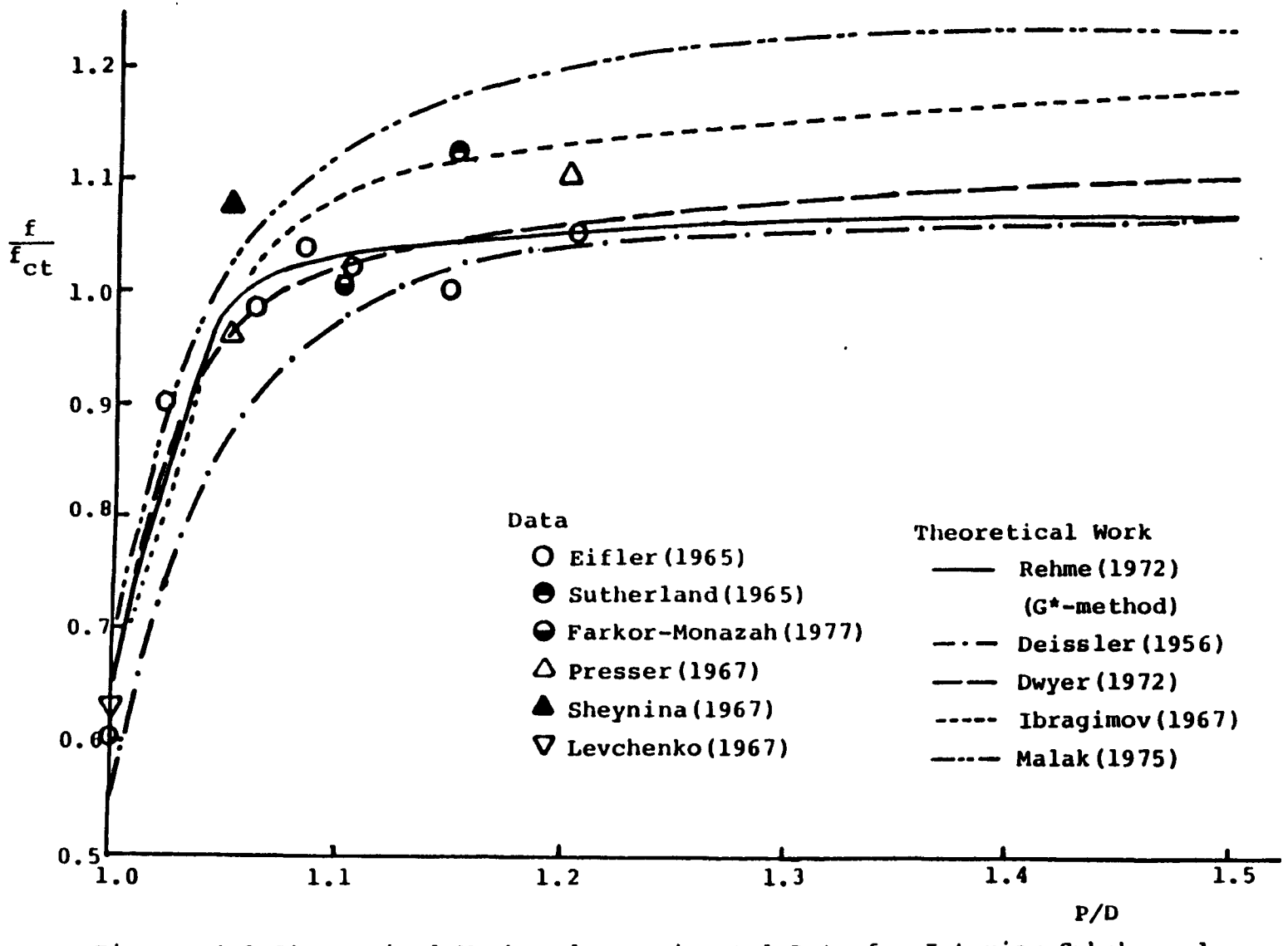

Figure 4.8 Theoretical Work and Experimental Data for Interior Subchannel Friction Factor at $Re=10^5$ as compared to Circular Tube Values

where A and G* are two geometrical constants which are assumed to be only functions of f•Re in laminar flow (i.e.,K_L). This assumption came from the similarity between K_L/K_{Lct} (K_{Lct} = 64) and f/f_{ct} in turbulent flow, which was observed from multiple, parallel tubes by Rehme.

For K_L < 64, the values of A and G* corresponding to each K_L can be calculated from multi-tubes in parallel, at which the total (average) friction factor decreases significantly below the value of the single tube.

For K_L > 64, the relation between A, G* and K_L were determined from the annular zone solution, equation (4.58). Rehme (1971) found the laminar constant f•Re of the equivalent annular zone (AZ) to be

$$(K_L)_{AZ} = \frac{64(X^2-1)^3}{-3X^4 + 4X^2 + 4X^4 \ln X - 1} \tag{4.60}$$

where X is the same as in equation (4.58). Equations (4.58), (4.59) and (4.60) relate A, G* and K_L for the equivalent annular zone (K_L>64).

According to Rehme's results, for $K_L \leq 64$, A can be fitted to be,

$$A = 1.0 + 0.5 \log \left(\frac{64}{K_L}\right) \tag{4.61}$$

For K_L > 64, by comparing equations (4.58) and (4.59), it is clear that A = 1.0 in this case.

Table 4.3 lists the relation between G* and K_L calculated by the method described above. Separating K_L into three regions, G* can almost be exactly fitted as (within 0.5%)

Table 4.3 G*method Fitting Results

Calculated G* = a+b(1)*log(KL)+b(2)*log(KL)**2

for KL <= 64 the coefficients are
a= -.1548E+00 b(i)= 0.5126E+01 -0.1042E+01

KL	G*	cal.G*	%error
25.3800	5.0140	4.9885	-0.5
30.0000	5.1350	5.1427	0.1
30.6300	5.1430	5.1611	0.4
32.9100	5.1980	5.2233	0.5
40.4200	5.3800	5.3902	0.2
42.5100	5.4360	5.4286	-0.1
45.3400	5.4940	5.4763	-0.3
46.9100	5.5270	5.5008	-0.5
47.1600	5.5040	5.5046	0.0
48.0000	5.5210	5.5171	-0.1
48.6500	5.5200	5.5265	0.1
52.2900	5.5750	5.5759	0.0
53.6900	5.5990	5.5935	-0.1
54.4900	5.6030	5.6032	0.0
58.5900	5.6500	5.6497	-0.0
63.4800	5.6940	5.6986	0.1
63.5000	5.6950	5.6988	0.1
63.6600	5.6960	5.7003	0.1
63.7800	5.6970	5.7014	0.1

for $K_L \leq 64$,

$$G^* = -0.1548 + 5.126(\log K_L) - 1.042(\log K_L)^2$$

for $64 < K_L < 125$, (4.62)

$$G^* = 9.430 - 5.976(\log K_L) + 2.159(\log K_L)^2$$

for $K_L \geq 125$

$$G^* = - 0.2344 + 3.151(\log K_L)$$

Now by using equations (4.61) and (4.62), one can calculate any flow channel's turbulent friction factor by equation (4.59), provided that its K_L is given. For the interior subchannel, K_L can be calculated by equation (4.54) and the coefficients in Table 4.1. Hence we can calculate f/f_{ct} for any P/D for turbulent flow. For $Re = 10^5$, these values are listed in Table 4.2 under the G*-method column.

For edge and corner subchannels, K_L can also be calculated by equation (4.54) and the coefficients in Table 4.1. Hence we can also calculate f/f_{ct} in turbulent flow region for edge and corner subchannel by the G*-method. Figure 4.9 illustrates f/f_{ct} for three kinds of subchannel as a function of P/D at $Re = 10^5$.

4.4.3.3 Comparison between Experimental Data and Correlation

Table 4.4 lists the friction factor data for interior subchannel in hexagonal array. The (f/f_{ct}) at $Re = 10^5$ of these data are also plotted in Figure 4.8 for comparison. It can be seen that Dwyer's method and the G*-method give the best predictions. However, selection between these methods will be defered until the bundle friction factor data is examined.

As for edge subchannel, Gunn (1963) measured the pressure drop of an edge flow channel with W/D = 1.0. Rehme (1980) measured the detail

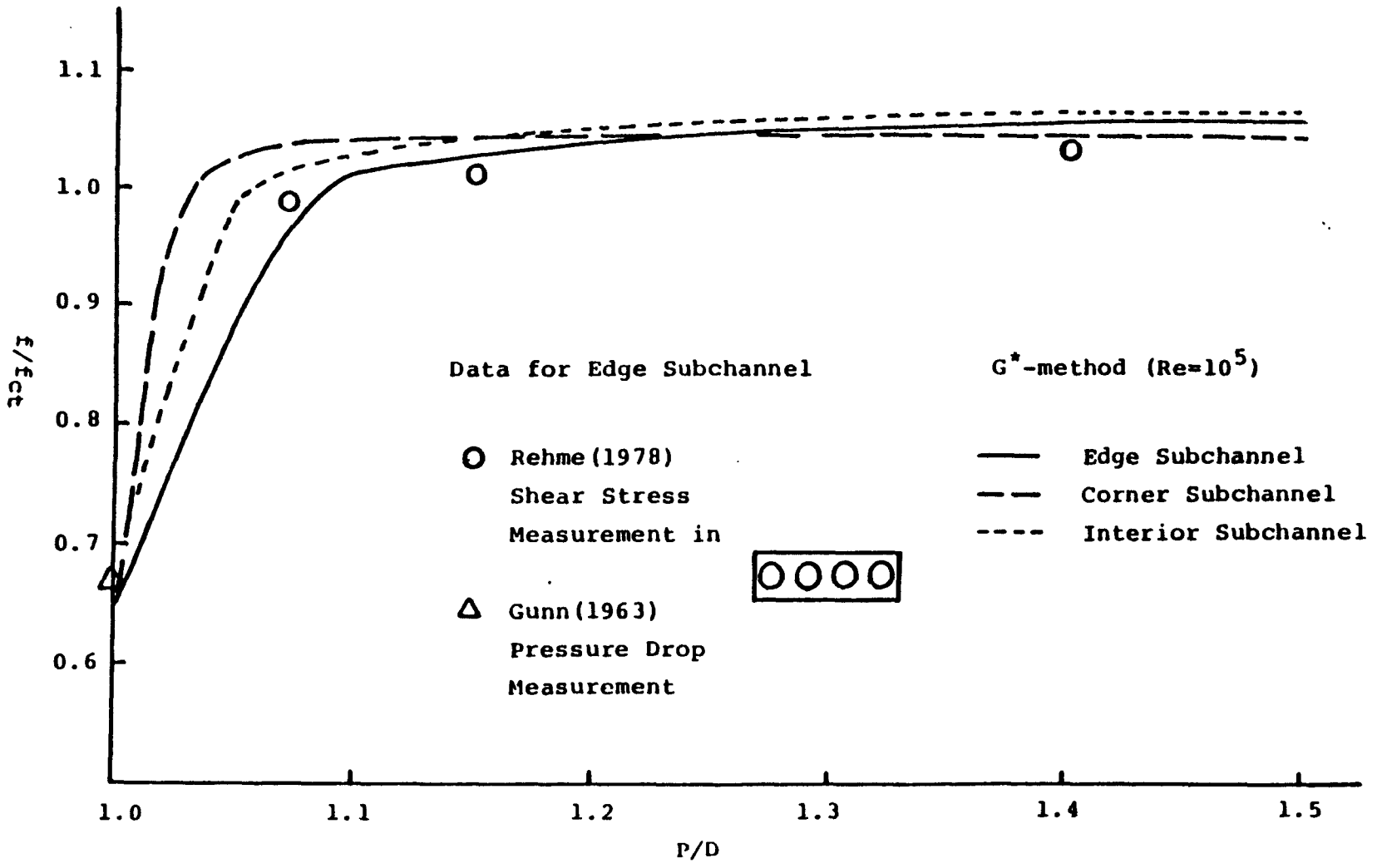

Figure 4.9 G^*-method f/f_{ct} at Re = 10^5 for Interior, Edge, and Corner Subchannel

TABLE 4.4

Data for Bare Rod Interior Subchannel Friction Factor in Turbulent Region

Investigators	Rod Configurations	D(mm)	P/D	f @ 10^4	f @ 10^5
Eifler(1965)	4	40.0	1.00	0.0183	0.0106
"	4	40.0	1.021	0.0281	0.0162
"	4	40.0	1.059	0.0307	0.0177
"	4	40.0	1.102	0.0319	0.0184
"	4	40.0	1.147	0.0313	0.0180
"	4	40.0	1.202	0.0329	0.0189
"	4	40.0	1.08	0.0313	0.0187
Fakori-Monazah(1977)	4	38.1	1.10	0.0350	0.0181
Levchenko(1967)	3	205.0	1.00	0.0215	0.0113
Presser(1967)	1/7	74.0	1.05	0.0266	0.0173
"	7/19	15.0	1.20	0.0320	0.0198
Sheynina(1967)	19/37	14.0	1.05	0.0316	0.0195
Subbotin(1960)	1/7	12.0	1.13	0.0340	0.0225
Sutherland(1965)	7/19	25.4	1.15	0.0364	0.0202

shear stress distribution in the edge subchannel in a four rods rectangular bundle as also shown in Figure 4.9. Three different W/D's have been investigated. Table 4.5 lists these data as well as values calculated by the G*-method. They are also plotted in Figure 4.9 for comparison. Since the data are predicted within 3% accuracy by the G*-method, one can confidently use G*-method for calculating edge subchannel friction factor.

No data are available for corner subchannels. The G*-method is assumed to be valid in this case.

The available bare rod bundle friction factor data were collected and tabulated in Appendix B. These data will be examined to see which one of those five methods for calculating interior subchannel friciton factor predicts them most closely. Since the wire-wrapped bundle friction factor data show that m = 0.18, the same value is used in the bare rod case. For the G*-method, two Reynolds numbers, 5×10^4 and 10^5, are used to get K_{iT}'s. The averaged K_{iT} of these two values for each P/D (or W/D) were used to fit a polynomial equation as equation (4.54). For the other four methods, the values in Table 4.2, i.e., at $Re = 10^5$, were used to get K_{iT} and they were also fitted as equation (4.54). For each of 28 available bare rod bundle geometry for which friction factor data are available, we can calculate C_{fb}'s values utilizing K_{iT} values based on the five methods.

The prediction error of each bundle was squared, then summarized over all 28 bundles. The average square root errors, i.e., total summarized error divided by 28, then square rooted, for these 5 methods are, Malak: 10.2%, Ibragimov: 7.73%, Dwyer: 5.97%, Deissler: 5.63%, and

TABLE 4.5

Data for Bare Rod Edge Subchannel Friction Factor in Turbulent Region

Investigators	W/D	Experimental Type	Re	f	f/fct* at 10^5	Predicted f/fct at 10^5	% Error
Gunn(1963)	1.000	Pressure Drop Measurement	1.0 e5	0.0120	0.667	0.650	-2.6
Rehme(1978a)	1.071	Shear Stress Measurement	8.73e4	0.0182	0.985	0.958	-2.7
Rehme(1978b)	1.148	Shear Stress Measurement	1.23e5	0.0175	1.009	1.024	1.5
Rehme(1978c)	1.402	Shear Stress Measurement	1.94e5	0.0165	1.033	1.056	2.2

* f at Re = 10^5 is extrapolated from the experimental point by using m = 0.18 in equation (3.2).

G*-method: 5.67%.

For considerations of simplicity and consistency, we concluded that Rehme's G*-method is the best choice for calculating the interior subchannel friction factor in turbulent flow. Figure 4.10 compares the prediction results from the G*-method and the experimental data.

Table 4.6 depicts the fitting results together with the original values and fitted values for K_{iT} from the G*-method.

4.4.4 Summary

The theoretical correlations and experimental data base for hexagonal bare rod bundle have been investigated thoroughly. Correlations for bare rod subchannel friction factors have been developed. The constants K_{iL} and K_{iT} defined in equations (4.52) and (4.53), respectively, are calculated by

$$K = a + b_1(P/D - 1) + b_2(P/D - 1)^2$$

where a, b_1, and b_2 are tabulated in Table 4.1 for K_{iL} and Table 4.6 for K_{iT}.

Since square array bundles are also important in the reactor application, we also fit these constants for their three kinds of subchannels. The values used for K_{iL} were from Rehme's (1971) theoretical calculation, and for K_{iT} were also from the G*-method. Tables 4.7 and 4.8 depict the results for the laminar case and the turbulent case, respectively.

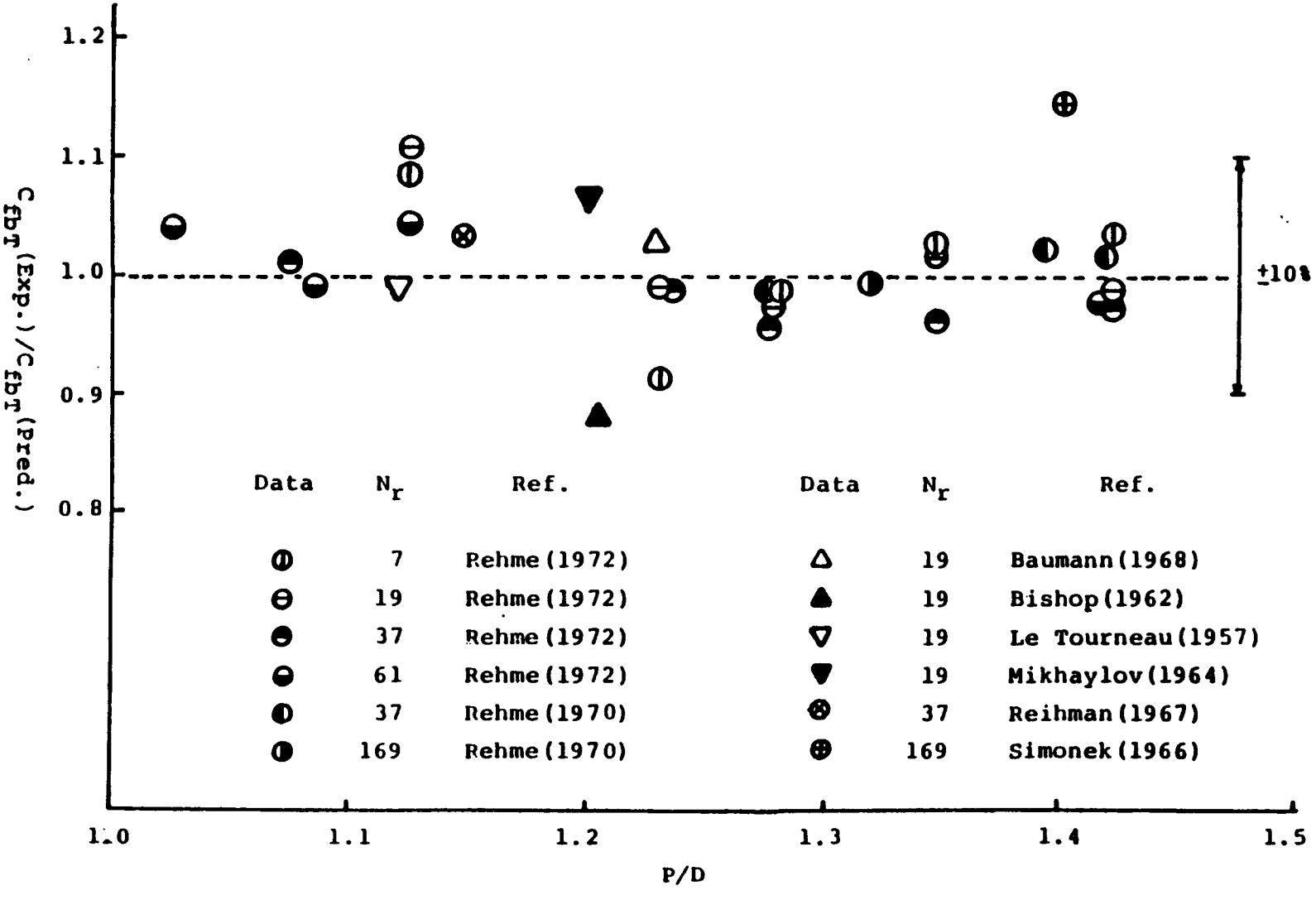

Figure 4.10 Comparison between Experimental and Predicted Bare Rod Bundle Turbulent Friction Factor Constant $C_{fbT}(=f \cdot Re^{0.18})$

Table 4.6
Fitting Results of Turbulent KT=f*Re**0.18
for Triangular Array
(KT from G* method using Re= 5e4 1e5)

Calcualted KT=a+b(1)*(P/D-1)+b(2)*(P/D-1)**2

Interior subchannel
for 1.0<=P/D<=1.1 the coefficients are
a= 0.9378E-01 b(i)= 0.1398E+01 -0.8664E+01

P/D	KT	cal.KT	%error
1.0000	0.0935	0.0938	0.3
1.0010	0.0949	0.0952	0.2
1.0100	0.1068	0.1069	0.1
1.0200	0.1182	0.1183	0.1
1.0300	0.1280	0.1279	-0.1
1.0400	0.1366	0.1358	-0.6
1.0500	0.1441	0.1420	-1.5
1.0600	0.1468	0.1465	-0.2
1.0700	0.1475	0.1492	1.2
1.0800	0.1481	0.1502	1.4
1.0900	0.1486	0.1494	0.5
1.1000	0.1490	0.1470	-1.4

for 1.1<P/D<=1.5 the coefficients are
a= 0.1458E+00 b(i)= 0.3632E-01 -0.3333E-01

P/D	KT	cal.KT	%error
1.1000	0.1490	0.1491	0.1
1.1500	0.1506	0.1505	-0.1
1.2000	0.1518	0.1518	-0.0
1.2500	0.1528	0.1528	-0.0
1.3000	0.1537	0.1537	0.0
1.3500	0.1544	0.1545	0.0
1.4000	0.1550	0.1550	0.0
1.4500	0.1554	0.1554	0.0
1.5000	0.1557	0.1557	-0.0

Table 4.7
Fitting Results of Laminar KL=f*Re
for Square Array
(KL from Rehme's results)

calculated KL=a+b(1)*(P/D-1)+b(2)*(P/D-1)**2

Interior subchannel
for 1.0<=P/D<=1.1 the coefficients are
a= 0.2637E+02 b(i)= 0.3742E+03 -0.4939E+03

P/D	KL	cal.KL	%error
1.0000	26.4000	26.3711	-0.1
1.0200	33.6000	33.6578	0.2
1.0500	43.8800	43.8470	-0.1
1.1200	64.1600	64.1641	0.0

for 1.1<P/D<=1.5 the coefficients are
a= 0.3555E+02 b(i)= 0.2637E+03 -0.1909E+03

P/D	KL	cal.KL	%error
1.1200	64.1600	64.4389	0.4
1.2200	84.7600	84.3166	-0.5
1.3200	100.7200	100.3771	-0.3
1.4200	111.7200	112.6206	0.8
1.5200	121.4400	121.0469	-0.3

Table 4.8
Fitting Results of Turbulent KT=f*Re**0.18
for Square Array
(KT from G* method using Re= 5e4 1e5)

Calculated KT=a+b(1)*(P/D-1)+b(2)*(P/D-1)**2

Interior subchannel
for 1.0<=P/D<=1.1 the coefficients are
a= 0.9423E-01 b(i)= 0.5806E+00 -0.1239E+01

P/D	KT	cal.KT	%error
1.0000	0.0941	0.0942	0.1
1.0010	0.0947	0.0948	0.1
1.0100	0.1000	0.0999	-0.1
1.0200	0.1053	0.1053	-0.1
1.0300	0.1107	0.1105	-0.1
1.0400	0.1155	0.1155	-0.0
1.0500	0.1201	0.1202	0.0
1.0600	0.1245	0.1246	0.1
1.0700	0.1287	0.1288	0.1
1.0800	0.1326	0.1327	0.1
1.0900	0.1364	0.1364	0.0
1.1000	0.1400	0.1399	-0.1

for 1.1<P/D<=1.5 the coefficients are
a= 0.1339E+00 b(i)= 0.9059E-01 -0.9926E-01

P/D	KT	cal.KT	%error
1.1000	0.1400	0.1419	1.3
1.1500	0.1473	0.1452	-1.4
1.2000	0.1489	0.1480	-0.6
1.2500	0.1503	0.1503	-0.0
1.3000	0.1516	0.1521	0.3
1.3500	0.1527	0.1534	0.5
1.4000	0.1536	0.1542	0.4
1.4500	0.1544	0.1545	0.1
1.5000	0.1550	0.1543	-0.5

4.5 Empirical Constants for Wire-Wrapped Subchannel Friction Factor

The empirical constants which need to be determined in wire-wrapped subchannel friction factor correlations are the wire drag constant W_d and swirl flow constant W_s. Since there are no subchannel friction factor data, and only bundle average friction factor and flow split parameters are measurable in wire-wrapped bundles, these two sets of data must be used simutaneously to calibrate these two constants as functions of geometrical parameters. The data reviewed in section 4.2 will be used for calibration. The parameters K_i's are determined from the fitting results of the last section.

The wire drag constant W_d and swirl flow constant W_s are both geometry and flow region dependent. They will be fitted by some functions of geometrical parameters for both laminar or turbulent region. No calibration work is needed for these two constants in the transition region since the formulation in the transition region simply combines laminar and turbulent equations weighted by a intermittency factor to a power of γ. γ is assumed to be a single value, and it is the empirical constant which needs to be calibrated in the transition region.

Since the data base in the turbulent region is vast enough for both bundle friction factor and flow split parameter, W_d and W_s can be calibrated directly from the data. However, in the laminar region, friction factor data are available for only a few bundles, and almost no flow split data are available except the three bundles of Chen

(11TR) and Efthimiadis (1983). Therefore, some assumptions have to be adopted to relate these constants in the laminar region to their values in the turbulent region.

4.5.1 Empirical Constants for the Turbulent Region: W_{dT}, W_{sT}

Since there are two sets of data, i.e., around one hundred bundle friction factor data sets and around ten flow split data sets, with two constants W_{dT} and W_{sT} to be determined, a two stage iterative procedure was developed to calibrate these constants.

For hexagonal rod bundles with 19 pins or more, the number of interior subchannels is considerably more than that of edge subchannels. Hence the wire drag constant W_{dT} is more important than the swirl flow constant W_{sT} in calculating the bundle pressure loss. On the other hand, since the flow split parameter is sensitive to the edge subchannel friction factor value, W_{sT} is more important than W_{dT} in calculating the flow split parameter. For these reasons, W_{dT} is first calculated from the bundle friction factor data for each bundle with a guessed W_{sT}. These W_{dT}'s are then fitted as functions of geometrical parameters. Using this W_{dT} equation, W_{sT} is calculated from the flow split data and then fitted as another function of geometrical parameters. This new W_{sT} equation can then be used together with the friction factor data to calculate W_{dT} again. This iterative procedure is continued until a satisfactory prediction is obtained. Figure 4.11 depicts this procedure. The 'prediction O.K.?' in this figure means that if further iteration can not improve the prediction, the final results are obtained.

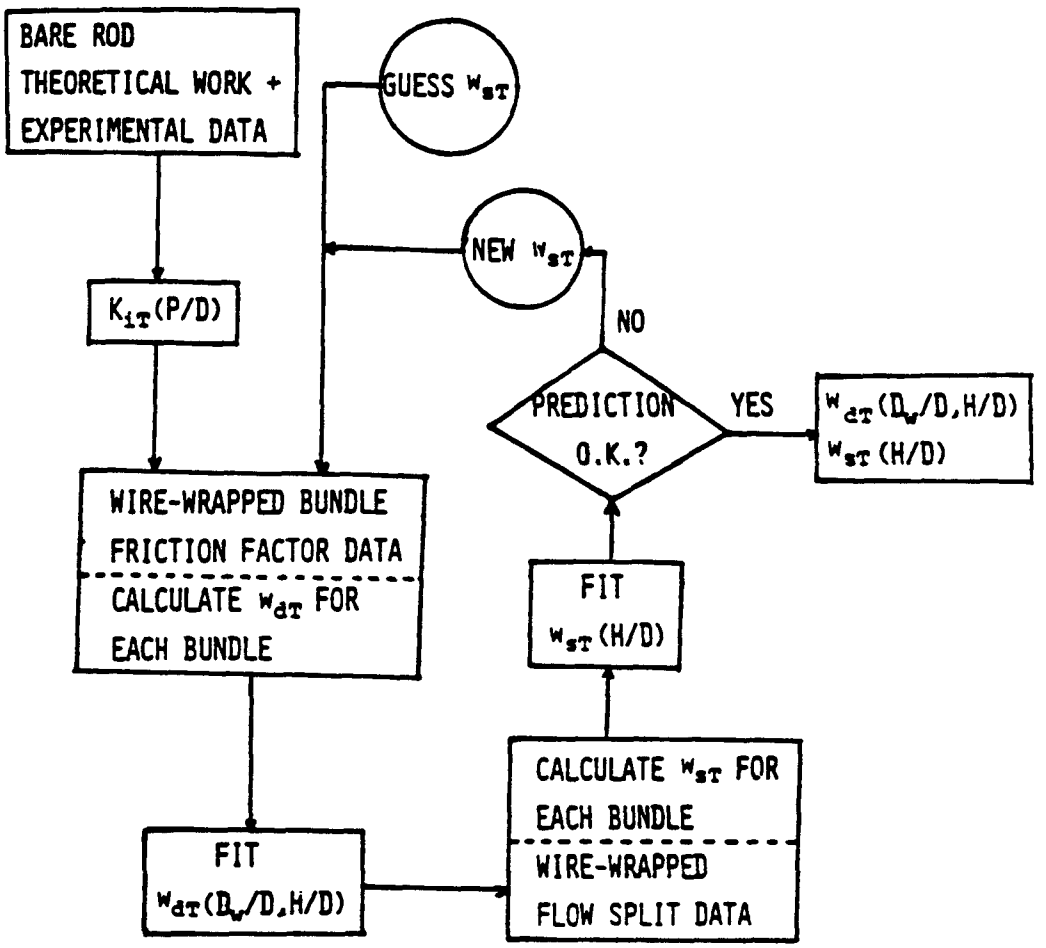

Figure 4.11 Calibration Procedure for Empirical Constants W_{dT} and W_{sT} in Turbulent Region

Since W_{dT} is essentially a wire drag coefficient, it is expected to be a function of D_w, H, and D. Several dimensionless combinations of these three geometrical parameters have been investigated, and the best two were found to be D_w/D and H/D. Since W_{sT} is related to swirl flow, which is strongly dependent on H/D, it is assumed to be function of this parameter only.

Although there are many possible fitting equations for either W_{dT}'s or W_{sT}'s, the following forms and constants were found to be satisfactory:

$$W_{dT} = [\ 29.5 - 140.0(\frac{D_w}{D}) + 401.0(\frac{D_w}{D})^2\ ](\frac{H}{D})^{-0.85} \qquad (4.63)$$

and

$$W_{sT} = 20.0\ \log(\frac{H}{D}) - 7.0 \qquad (4.64)$$

Figure 4.12 illustrates W_{dT} as functions of D_w/D and H/D. Note that the nominal value of W_{dT} is around 3.0. The drag coefficient C_D of a single elliptical shaped rod in turbulent flow is about 0.5 [Morris(1963)]. From the model, $C_d = W_{dT}/Re^{0.18}$ at $Re = 2x10^4$, taking $C_d = 0.5$, one finds that W_{dT} is 3.0. This confirms the soundness of our model.

As shown in figure 4.12, W_{dT} decreases as H/D increases as one expects; however, the dependence of D_w/D is parabolic with a minimum value around $D_w/D = 0.18$. The characteristic of the flow field apparently changes at this point. Geometrically one observes that for an interior subchannel, as D_w/D increases, the projected area of the

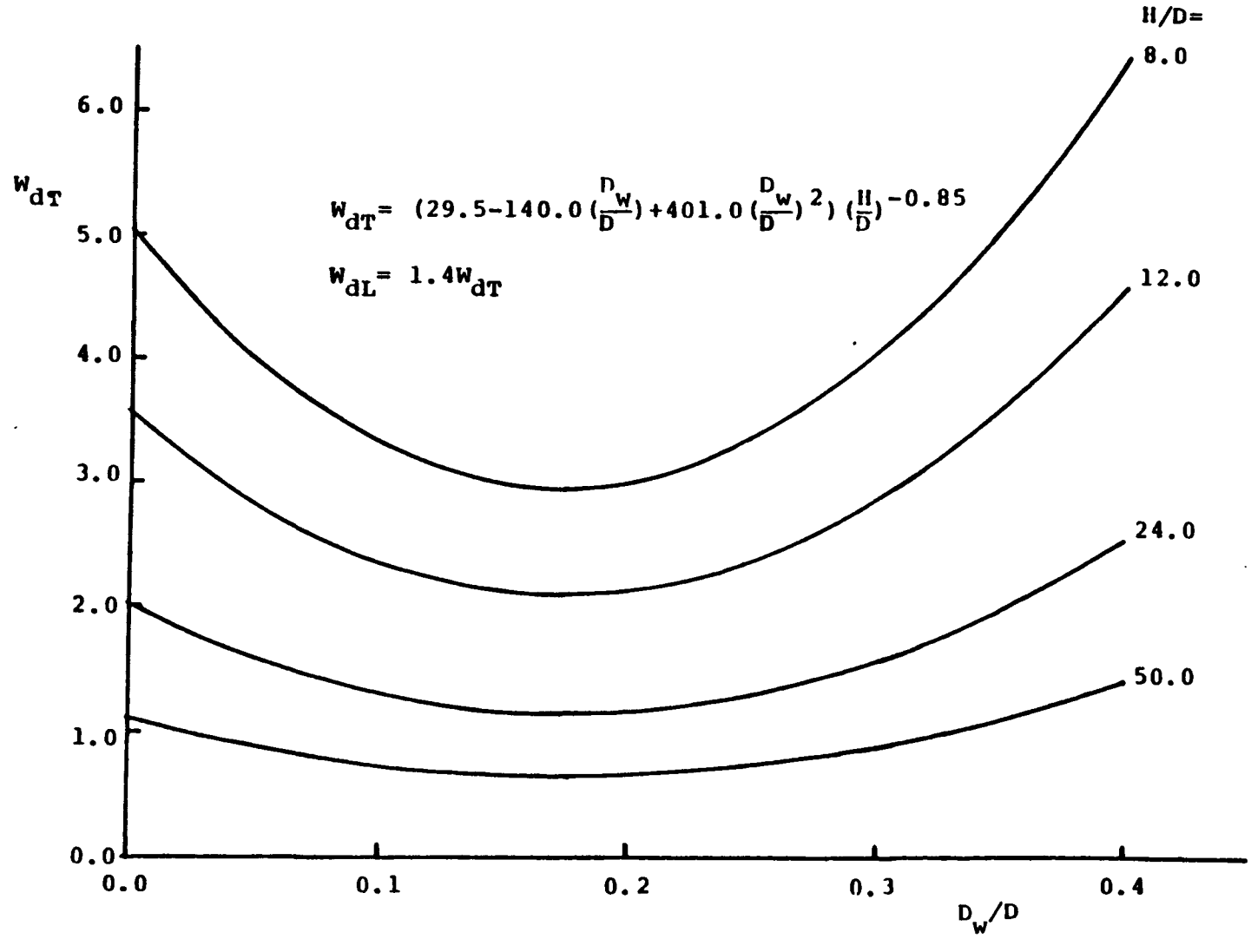

Figure 4.12 Wire Drag Constant W_{dT}

wires traversing the subchannel taken over one axial lead becomes an increasing larger fraction of the total subchannel area. Above a specific value of D_w/D (=0.183) the fraction is greater than unity. This difference in geometrical character may be the reason causing this behavior of W_{dT}.

Figure 4.13 illustrates W_{sT} as a function of H/D. W_{sT} increases as H/D increases, with a value from 5.0 to 26.6 for H/D from 4.0 to 48.0. This is consistent with the swirl flow ratio reduced from mixing experiments in which the transvese velocity in the gap is more than $V_2 \tan\theta$ for high H/D and less than $V_2 \tan\theta$ for low H/D. The trend of this constant is confirmed to be correct.

To check the accuracy of this model and calibration, Figure 4.14 shows the prediction error for overall bundle wire-wrapped turbulent friction factor constants C_{fbT} ($\equiv f_b \cdot Re_b^{0.18}$) from this correlation. The histogram in the right side of this figure is the error distribution for each 2% interval of the 101 bundle data base. Note that all data can be predicted within ±18% error. The standard deviation of this distribution is 8%. If the correlation models the subchannel friction factor accurately enough, the prediction errors for the data only come from the experimental error, which should have a normal distribution as shown by the dashed line in Figure 4.4. For a normal distribution with a standard deviation of 8%, a 92% confidence interval for prediction can be obtained with ±14% (i.e. ±1.75σ) accuracy.

As for the turbulent flow split prediction, Figure 4.15 shows the comparison between wire-wrapped edge subchannel flow split data and the

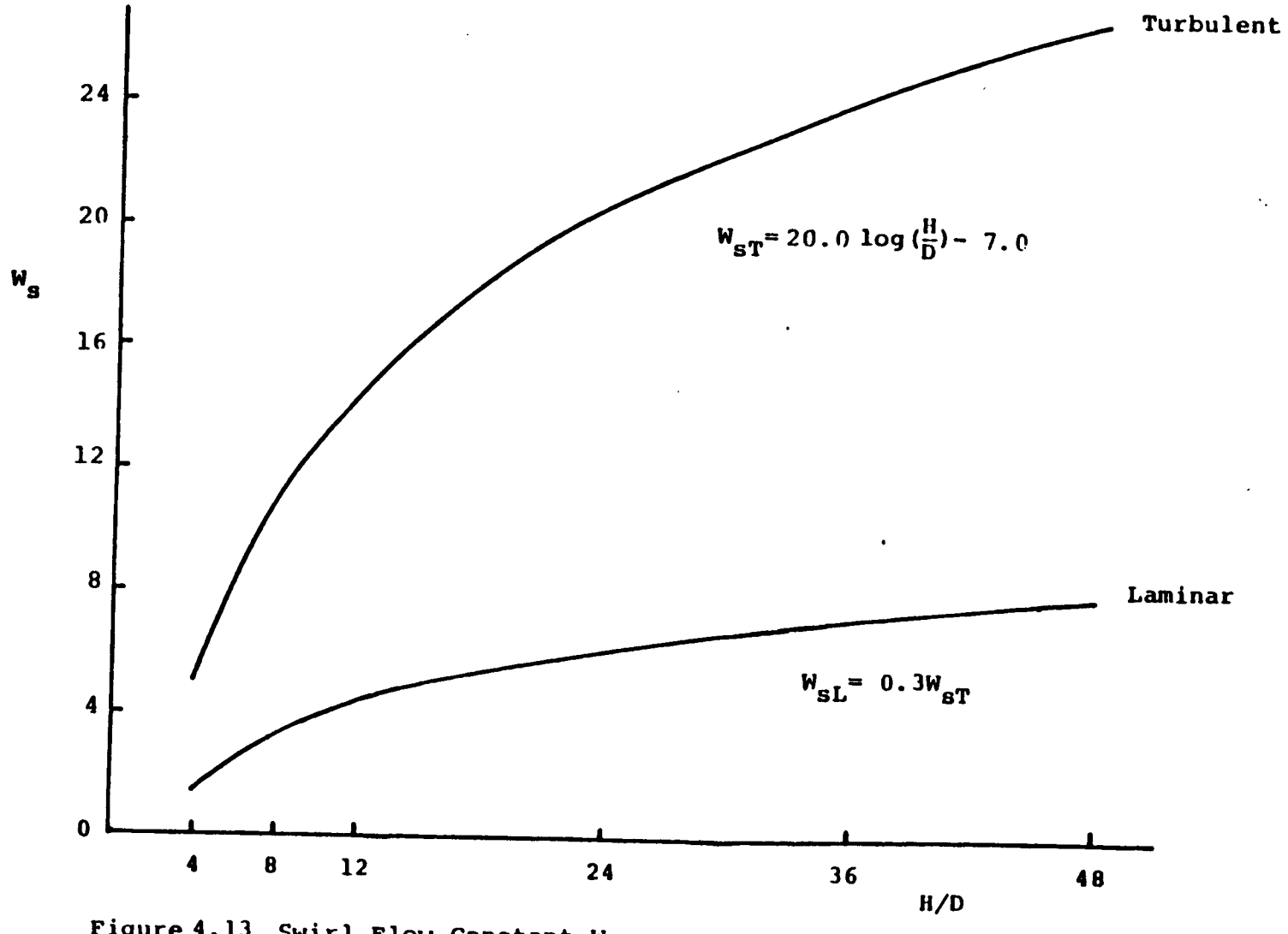

Figure 4.13 Swirl Flow Constant W_s

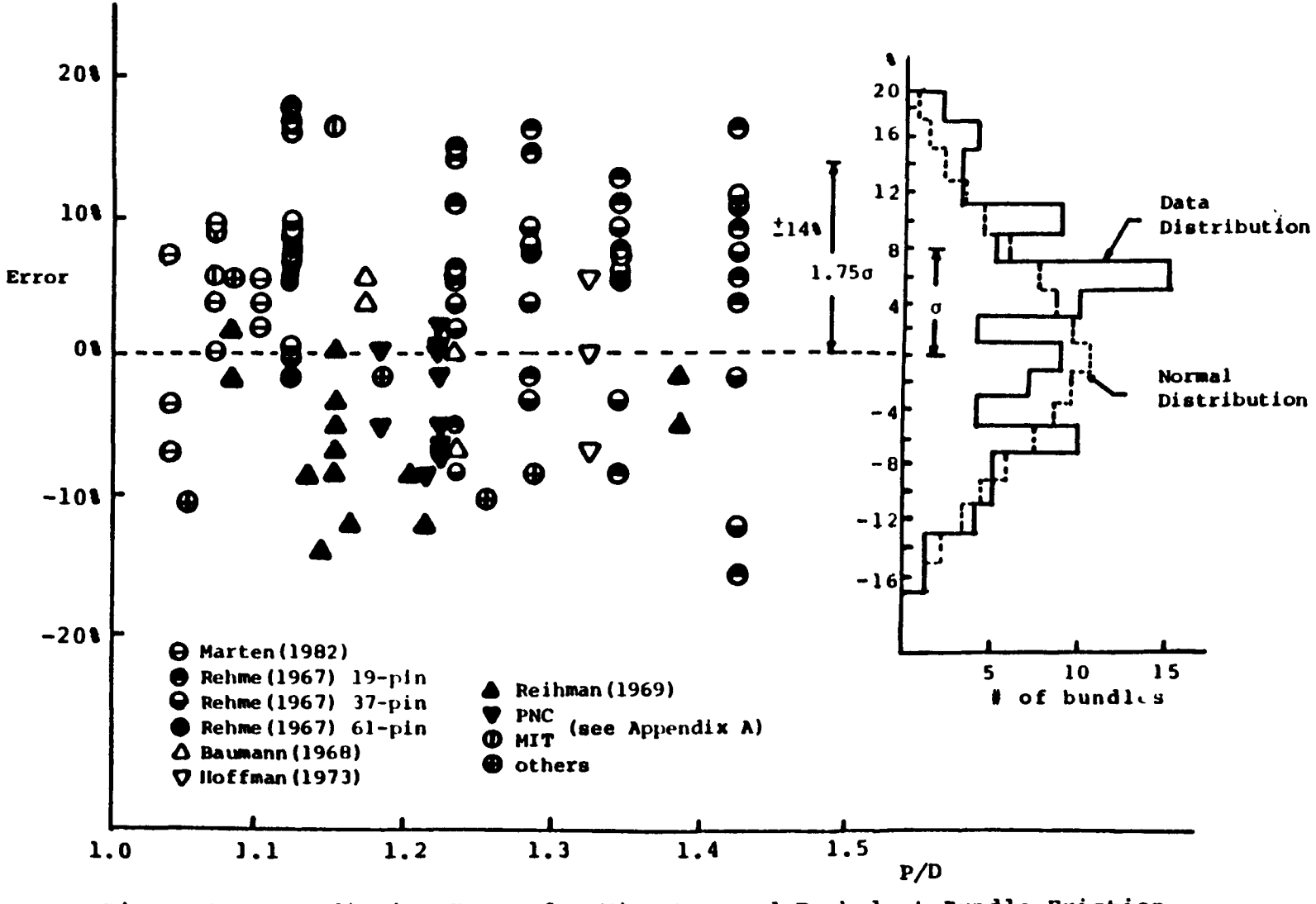

Figure 4.14 Prediction Error for Wire-Wrapped Turbulent Bundle Friction Factor Constant C_{fbT}

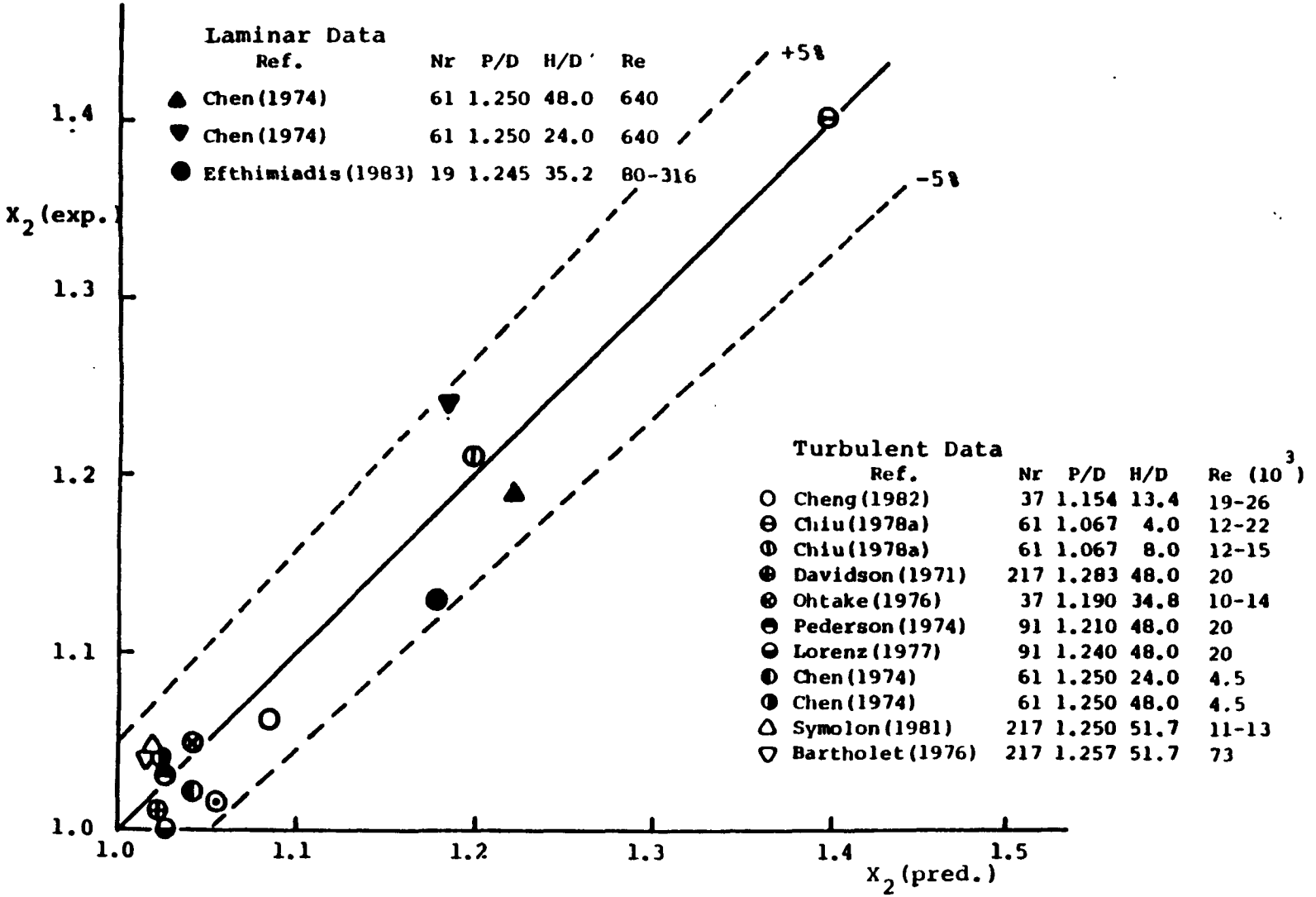

Figure 4.15 Comparison between Experimental Data and Predictions for Wire-Wrapped Edge Subchannel Flow Split Parameter

prediction values. All data are predicted within ±5% error. The accuracy of our correlations is within the experimental error of flow split experiments which are considered to be not less than 5%.

4.5.2 Empirical Constants for the Laminar Region: W_{dL}, W_{sL}

The data in the laminar region are very limited, especially for flow split data as discussed in Section 4.2. Only 19 bundles of our collected data have laminar friction factor data, 9 of which are Marten's low P/D bundles. Table 4.9 lists the investigators, geometries and laminar fRe data of these 19 bundles.

As Table 4.9 shows, there is a large inconsistency between the data for bundles with blanket assembly geometry (P/D ≈ 1.07, H/D ≈ 8.0); the fRe for Chiu's 61-pin is 90, Engel's 61-pin is 99, and Marten's 37-pin is 68. Because of this inconsistency and the lack of laminar flow split data, some assumptions have to be adopted to reduce the complexity in calibrating the laminar constants, W_{dL} and W_{sL}.

First, a similarity in geometrical dependence of W_d and W_s between the turbulent and laminar flow cases is assumed. Therefore, the variations of W_{dL} and W_{sL} as functions of geometrical parameters are the same as that of W_{dT} and W_{sT} respectively, and only two ratios, W_{dL}/W_{dT} and W_{sL}/W_{sT}, need to be determined.

Second, a similarity in Reynolds number dependence between the laminar to turbulent region regarding the relationship of the drag coefficient of a single circular cylinder to that of wires in the model is proposed, i.e.,

$$C_{dL}/C_{dT} \approx C_{DL}/C_{DT} \qquad (4.65)$$

Table 4.9

Comparison between Data, Predictions of the Proposed Correlation and Predictions of Westinghouse Correlation Eq.(4.7) for Laminar $f_b \cdot Re_b$

Investigators	N_r	P/D	H/D	H(cm)	$f_b \cdot Re_b$	This Model	W.H. Model
Marten(1982)	37	1.041	8.38	13.4	45.0	48.4	92.9
	37	1.041	12.60	20.1	45.0	47.2	75.8
	37	1.041	17.01	27.2	45.0	46.5	65.2
	37	1.072	8.34	12.9	68.0	64.0	98.9
	37	1.072	12.54	19.5	56.0	62.0	80.4
	37	1.072	16.68	25.9	56.0	61.0	69.8
	37	1.101	8.31	12.6	80.0	74.7	104.2
	37	1.101	12.31	18.6	74.0	72.1	85.7
	37	1.101	16.61	25.1	68.0	70.7	73.8
Efthimiadis(1983)	19	1.245	35.20	66.6	82.2	87.4	54.5
Cheng(1982)	37	1.154	13.40	20.2	94.2	81.1	88.4
Itoh(1981)	127	1.176	38.00	20.9	72.7	80.5	89.3
Itoh(1981)	169	1.214	47.40	30.8	77.1	83.3	77.1
Carelli(1981)	61	1.05	20.00	25.4	60.0	51.8	68.3
Burns(1980)	37	1.156	21.00	26.7	85.0	79.4	77.0
Spencer(1980)	217	1.252	51.70	30.0	84.0*	85.5	81.8
Engel(1979)	61	1.082	7.78	10.0	99.0**	68.3	113.9
Chiu(1978b)	61	1.067	4.00	5.1	160.0*	65.7	156.0
Chiu(1978b)	61	1.067	8.00	10.2	90.0	62.5	110.5

* Data used to calibrate W.H. correlation.

** Original published value is 110.0 whichwas revised later [Markley (1982)].

where C_{dL} = drag coefficient of wires at one laminar Re_L

C_{dT} = drag coefficient of wires at one turbulent Re_T

C_{DL} = drag coefficient of circular cylinder at Re_L

C_{DT} = drag coefficient of circular cylinder at Re_T

Re_L, Re_T are both based on D_w

An approximate value for W_{dL}/W_{dT} can then be derived from the drag coefficient of a circular cylinder, which is illustrated in Figure 4.16. For turbulent flow, $C_{DT} \approx 1.2$ and $C_{dT} = W_{dT}/Re_T^{0.18}$. For laminar flow, $C_{DL} = 10.0/Re_L$ and $C_{dL} = W_{dL}/Re_L$. Hence,

$$C_{dL}/C_{dT} = (W_{dL}/Re_L)/(W_{dT}/Re_T^{0.18})$$

and

$$C_{DL}/C_{DT} = (10.0/Re_L)/1.2$$

Substituting these results into equation (4.65) yields

$$W_{dL}/W_{dT} = 10.0/(1.2Re_T^{0.18}) \tag{4.66}$$

Typically, for $Re_T = 10^4$, $W_{dL}/W_{dT} = 1.6$; for $Re_T = 2\times10^4$, $W_{dL}/W_{dT} = 1.4$; and for $Re_T = 5\times10^4$, $W_{dL}/W_{dT} = 1.2$; therefore, for $10^4 \leq Re_{Dw} \leq 5\times10^4$, an average value for $W_{dL}/W_{dT} = 1.4$ is obtained. W_{dL} is then found to be

$$W_{dL} = 1.4W_{dT}$$

$$= [\ 41.3 - 196.0(\frac{D_w}{D}) + 561.0(\frac{D_w}{D})^2\ ](\frac{H}{D})^{-0.85} \tag{4.67}$$

Now the only constant left to be determined is W_{sL}/W_{sT}. This ratio is calibrated from the laminar bundle friction factor constant

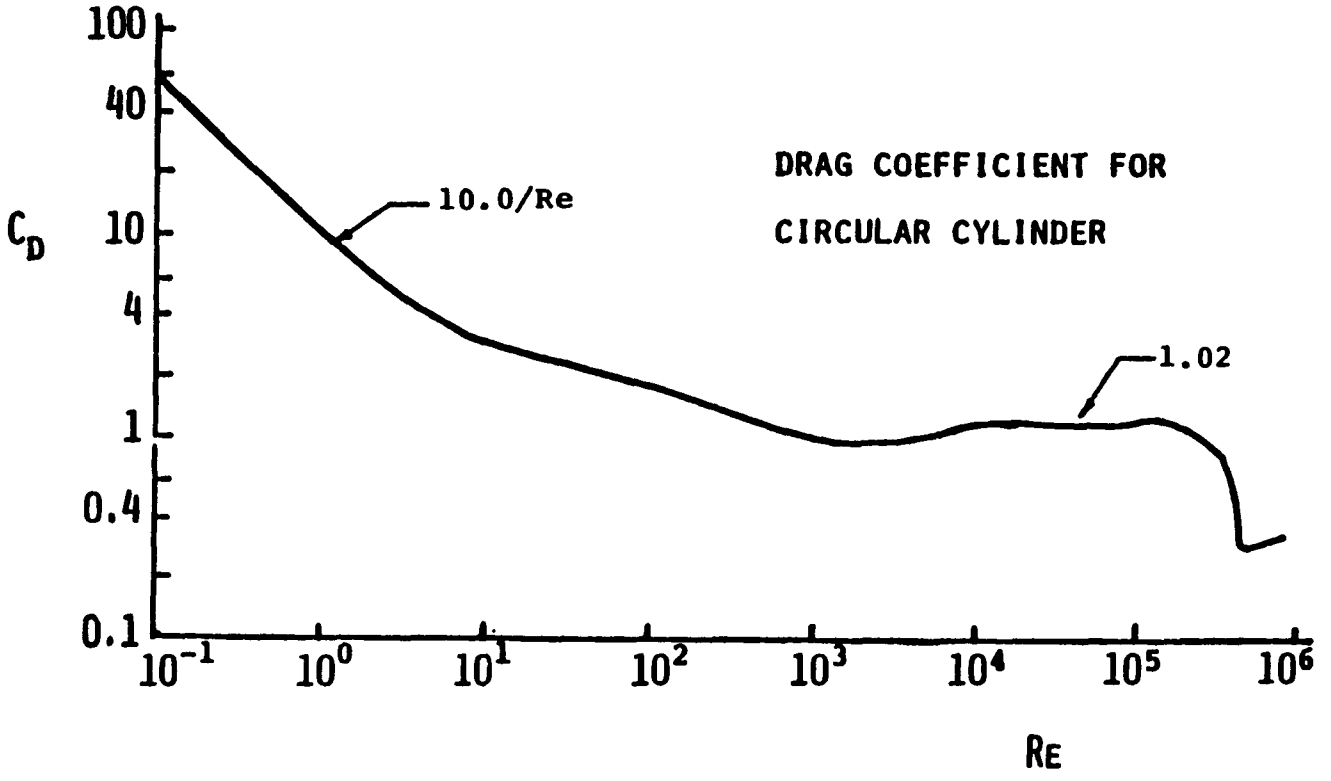

Figure 4.16 Drag Coefficient for Circular Cylinder

(f•Re) data listed in Table 4.9. The W_{sL}/W_{sT} ratio which makes the predictions for these bundles match the data is 0.3. Therefore,

$$W_{sL} = 0.3W_{sT}$$

$$= 6.0 \log(\frac{H}{D}) - 2.1 \qquad (4.68)$$

Figure 4.17 compares the predictions for laminar f•Re with the experimental values. Since only one constant, W_{sL}/W_{sT}, is calibrated by all the friction factor data and this correlation can well predict Marten's data, which are considered to be quite accurate, as well as the other high P/D (>1.1) data, the correlation for the laminar region is considerd optimum based on the existing data base.

This calibration result for W_{sL}/W_{sT}, 0.3, is very consistent with the data of local swirl flow ratio, C_{1L}, which is the ratio of the transverse velocity at the gap to average axial velocity in edge subchannels from mixing experiments i.e., $V_T|_{gap}/V_2$. The ratio of laminar to turbulent local swirl flow ratio, i.e.,

$$\frac{(C_{1L})_L}{(C_{1L})_T} = \frac{(V_T|_{gap}/V_2)_L}{(V_T|_{gap}/V_2)_T},$$

from these experiments varies from 0.3 to 0.6, whereas from the results just presented, the ratio of laminar (V_T/V_2) to turbulent (V_T/V_2) is $\sqrt{W_{sL}/W_{sT}}$, i.e., 0.55. Although the velocities V_T and $V_T|_{gap}$ are not defined identically, the ratio of their ratios with respect to V_2 in laminar and turbulent flow should be approximately the

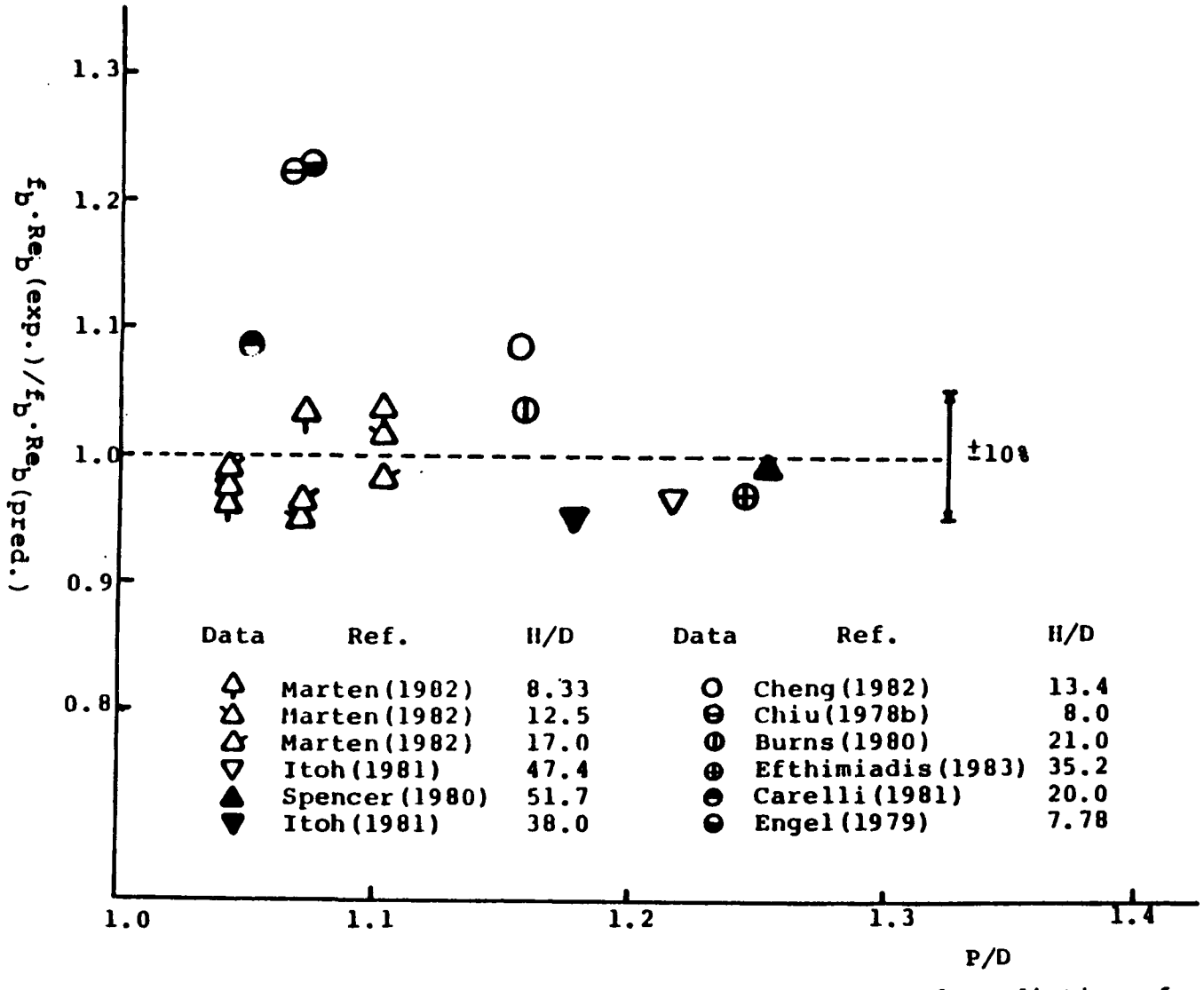

Figure 4.17 Comparison between Experimental Data and Predictions for Wire-Wrapped Laminar Bundle Average $f_b \cdot Re_b$

same, i.e.,

$$\frac{(V_T|_{gap}/V_2)_L}{(V_T|_{gap}/V_2)_T} \simeq \frac{(V_T/V_2)_L}{(V_T/V_2)_T}$$

Our values for these ratios of 0.3 to 0.6 ≃ 0.55 once again confirms the soundness of our model.

An indicator of the accuracy of these constants is the degree to which flow split predictions based on them agree with the available data existing of three bundles, i.e., Chen (11TR) two cases, Efthimiadis (1983). These comparisons are also shown in Figure 4.15, which indicates that these data are predicted within 5% error. Also, for those bundles which have transition flow split data but not laminar data, the predicted laminar flow split parameters for these bundles are around the right limit of these transition data for very low flow rate.

4.5.3 Empirical Constant for the Transition Region: γ, β

In the transition region, the empirical constants which need to be calibrated are the exponent γ for the intermittency factor ψ_i in equation (4.35) and β in equation (4.51). γ is calibrated from the bundle friction factor data in the transition region ($Re_{bL} < Re_b < Re_{bT}$) and is assumed to be the same for the three kinds of subchannels. Note that in this procedure, the transition flow split data are not used to calibrate any constants. After γ is found, the flow split parameters can be calculated from the pressure drop equation (4.36) and the mass balance equation (4.37) using subchannel friction factors calculated by equation (4.35). Since these are a set nonlinear equations, Newton's iteration method is used to solve for the flow

split parameters. Note that the flow split parameters calculated by this method satisfy the mass balance requirement.

The constant γ is adjusted to minimize the root mean square of the prediction error of all transition data points. By this method, γ is calibrated to be 1/3, which yields a root mean square of the prediction error of 9.3%. To illustrate the validity of this constant, Figures 4.18a and 4.18b show the comparison between the predictions and experimental data for bundle friction factor as function of Re for several new experiments which have produced data in all three flow regions. The trend in transition region is well simulated by this transition model.

The predictions for X_2 based on the assumption that γ is the same for all three kinds of subchannels always fall below the data as illustrated in Figure 4.19 for three bundles which have transition flow split data obtained by the isokinetic extraction method; i.e., IEM, [this work, Symolon(84TR), Chiu(41TR)]. Note that this means X_1 is overpredicted by this method because of the mass balance requirement. Many approaches have been investigated to eliminate this discrepancy, e.g., different γ's for different kinds of subchannels, different transition equation, e.g., the old model equation (1.4), or different γ's for laminar and turbulent components; however, no improvement could be obtained.

Since in IEM, there is a flow rate below which the flow can not be extracted from the interior subchannel, a systematic error is believed to exist in those data near that flow rate. The edge flow split

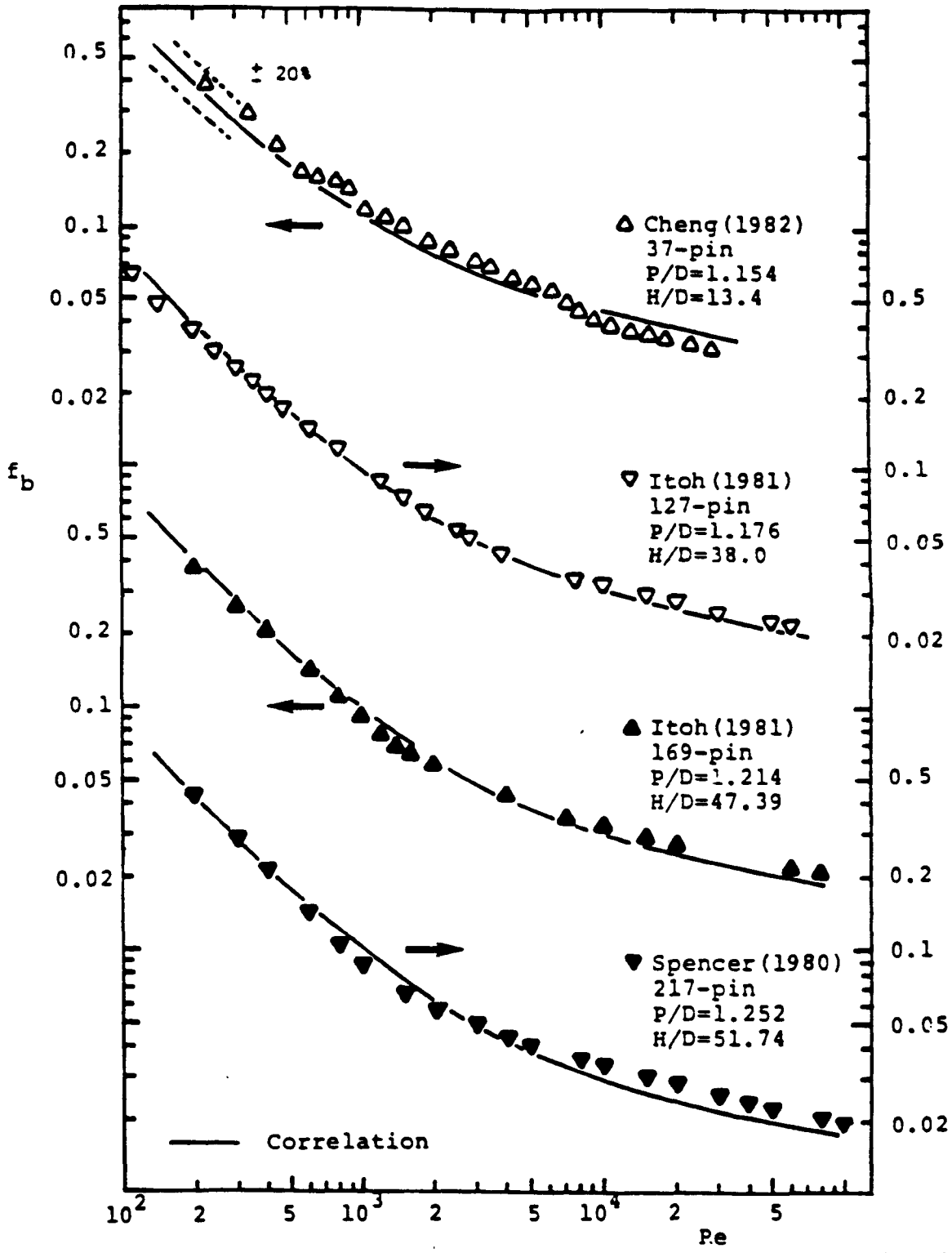

Figure 4.18a Comparison between Experimental Data and Predictions for Wire-Wrapped Bundle Friction Factor (P/D > 1.1)

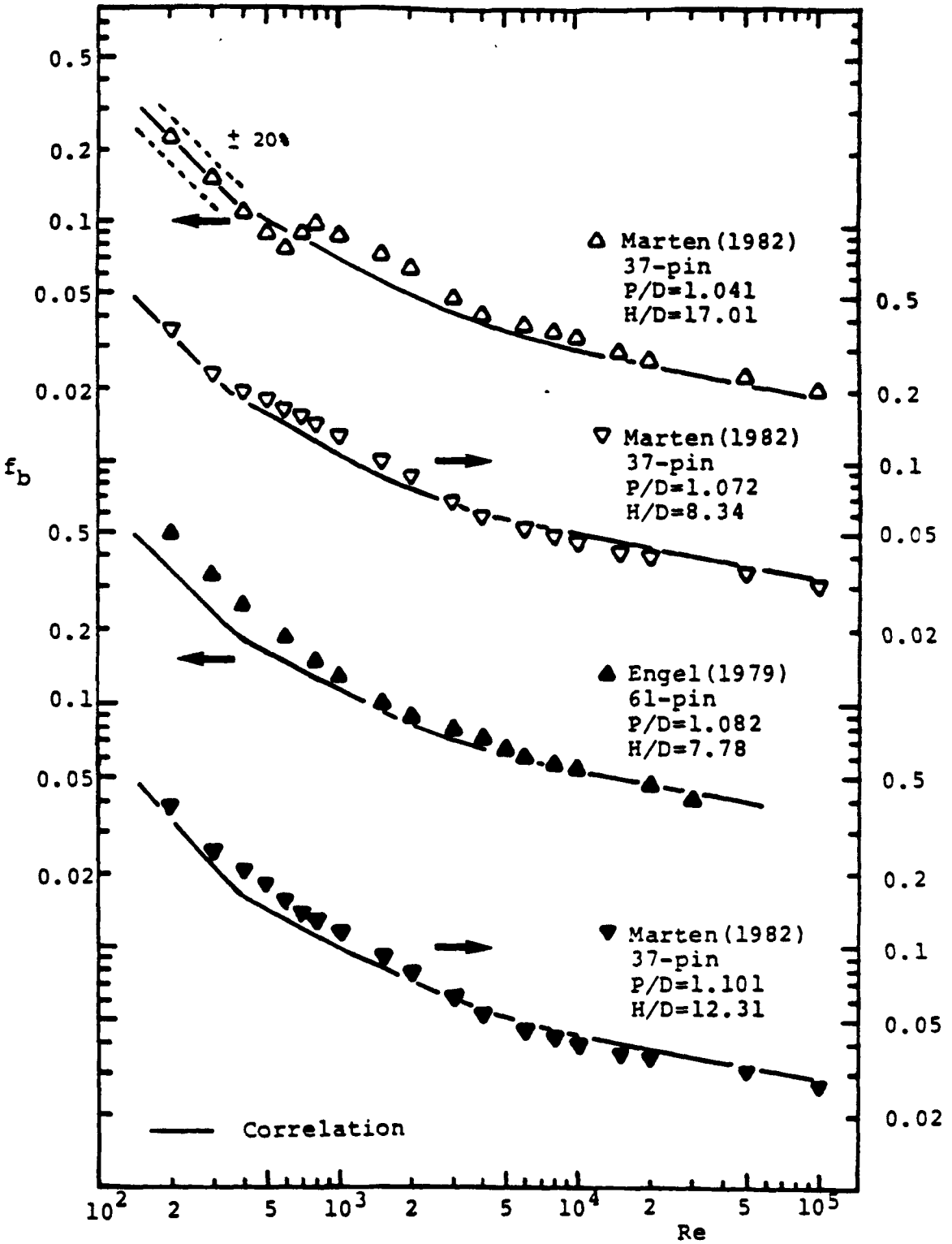

Figure 4.18b Comparison between Experimental Data and Predictions for Wire-Wrapped Bundle Friction Factor (P/D ≤ 1.1)

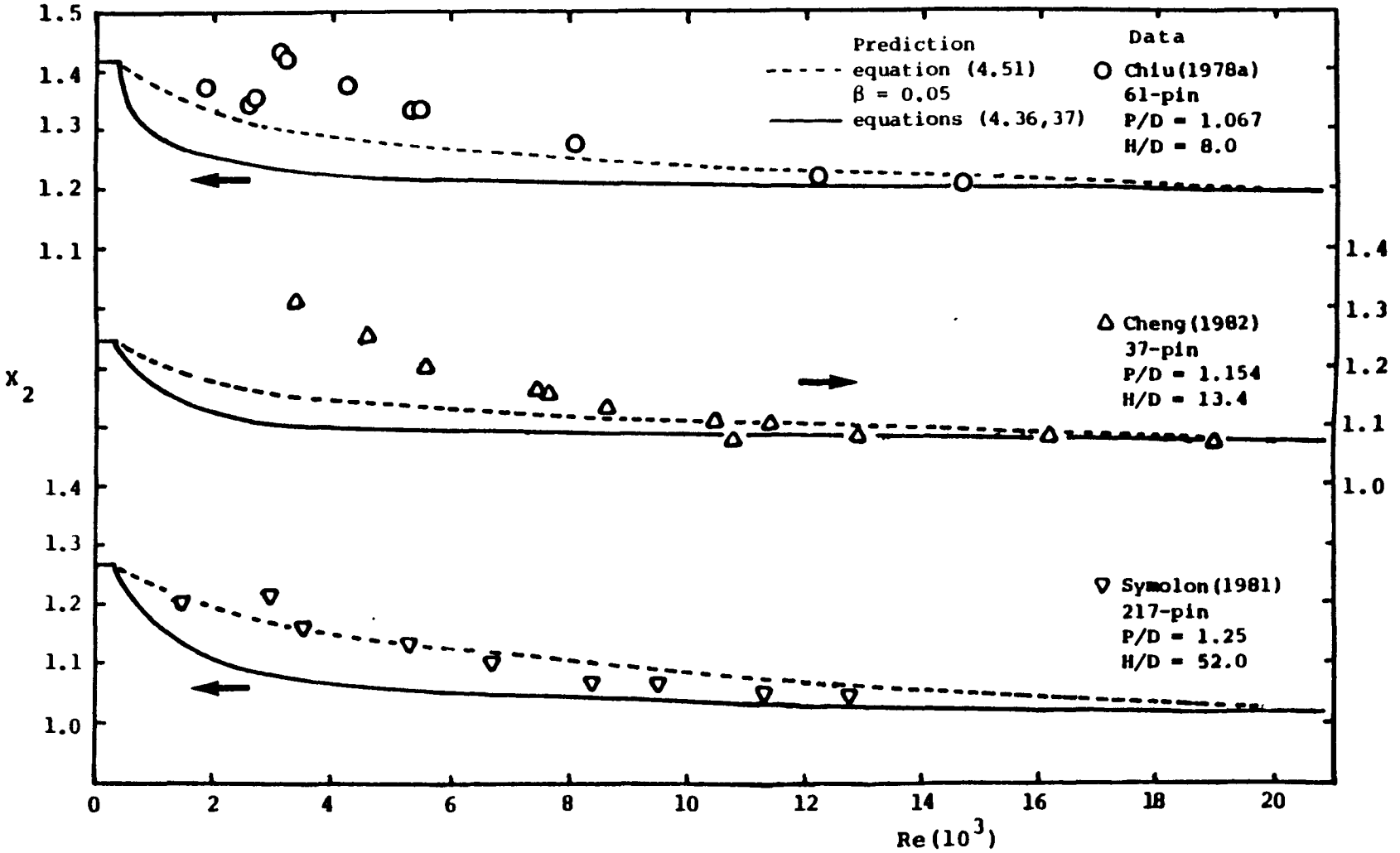

Figure 4.19 Comparison between Wire-Wrapped Edge Flow Split Data and Predictions in the Transition Region

parameter in these experiments is calculated by

$$X_2 = \frac{V_2}{V_b} = \frac{m_{2t}/A_{2t}}{m_t/A_t} \tag{4.69}$$

where m_{2t} = total flow rate extracted from edge subchannels

A_{2t} = total flow area for edge subchannels

m_t = total flow rate extracted from all subchannels

A_t = total bundle flow area

At this critical point $m_t = m_{2t}$ because no flow is extracted from interior subchannels. Hence

$$X_2 = \frac{A_t}{A_{2t}} \tag{4.70}$$

In the real situation, however, the flow in the interior subchannel should never be zero, and m_t is always higher than m_{2t}. Hence X_2 should be less than A_t/A_{2t}. Because of this breakdown of this technique, the flow split data obtained by IEM near this point are believed to be too high. This systematic error should gradually disappear as flow rate increases. From this point of view, the observation that the predictions fall below the edge flow split data is expected.

The approximate solution for transition flow split parameters, equation (4.51), with an empirical constant β, which adjusts the effect of the turbulent part, is one option to improve the predicitons. A β value of 0.05 gives the best match for transition flow split data. X_2 curves predicted by equation (4.51) with $\beta = 0.05$ are also shown as dash line in Figure 4.19 for comparison.

4.6 Summary of Correlations

4.6.1 Summary

The formulae for subchannel friction factors and flow split parameters have been derived in section 4.3 and summarized in section 4.3.5.

Calibration of the empirical constants, K_i, W_d, W_s, γ, and β of these correlations have been described in the last two sections. In summary,

K_{1L}, K_{2L}, K_{3L} from equation (4.54) and Table 4.1

K_{1T}, K_{2T}, K_{3T} from equation (4.54) and Table 4.6

W_{dL}, W_{dT} from equations (4.67) and (4.68), respectively

W_{sL}, W_{sT} from equations (4.68) and (4.64), respectively

$\gamma = 1/3$

$\beta = 0.05$

These correlations are valid over the following geometry and Re range for both Bare and Wire-wrapped bundles

$$19 \leq N_r \leq 217$$

$$1.0 \leq P/D \leq 1.42$$

$$4.0 \leq H/D \leq 52.0$$

$$50 \leq Re \leq 10^6$$

These correlations have been programed in a computer program WWCR which calculates the friction factors and flow split parameters for bare or wire-wrapped rod bundles. Appendix B2 of report 108TR presents

this program and its input and output formulations.

The parametric behavior of the bundle average friction factor and edge flow split parameter for the range of the P/D and H/D values calculated by WWCR for bare and wire-wrapped bundles in the laminar and turbulent regions will be presented in the following sections. The transition region will not be discussed since the values in this region are a combination of the laminar and turbulent values.

4.6.2 Parametric Behavior for Bare Rod Bundles

The bare rod bundle is a special case of these correlations in which the wire diameter is zero. Note that in the models, no restriction has been imposed on the wire diameter except that P should be greater than $(D+D_w)$. Hence the correlations are theoretically applicable to bundles with wire of one size whose diameter varies from zero to (P-D). However, they have only been verified at the two extreme conditions, i.e., bare rod bundles in which $D_w = 0$ and wire-wrapped rod bundles in which $D_w \simeq P-D$.

In contrast to the wire-wrapped empirical constants, which are calibrated from the data, the bare rod friction factor constants K_i's are obtained from theoretical results and then verified by comparison with subchannel and bundle friction factor data.

To illustrate the predictions for bare rod bundles, Figures 4.20 and 4.21 depict the bundle friction factor constants C_{fb} as function of P/D for a 37-pin bundle with W/D = P/D for turbulent and laminar cases,respectively. In both figures, the dependance of the constants as a function of P/D are quite similar to bare interior subchannels. According to the results of WWCR, these constants C_f's are a very

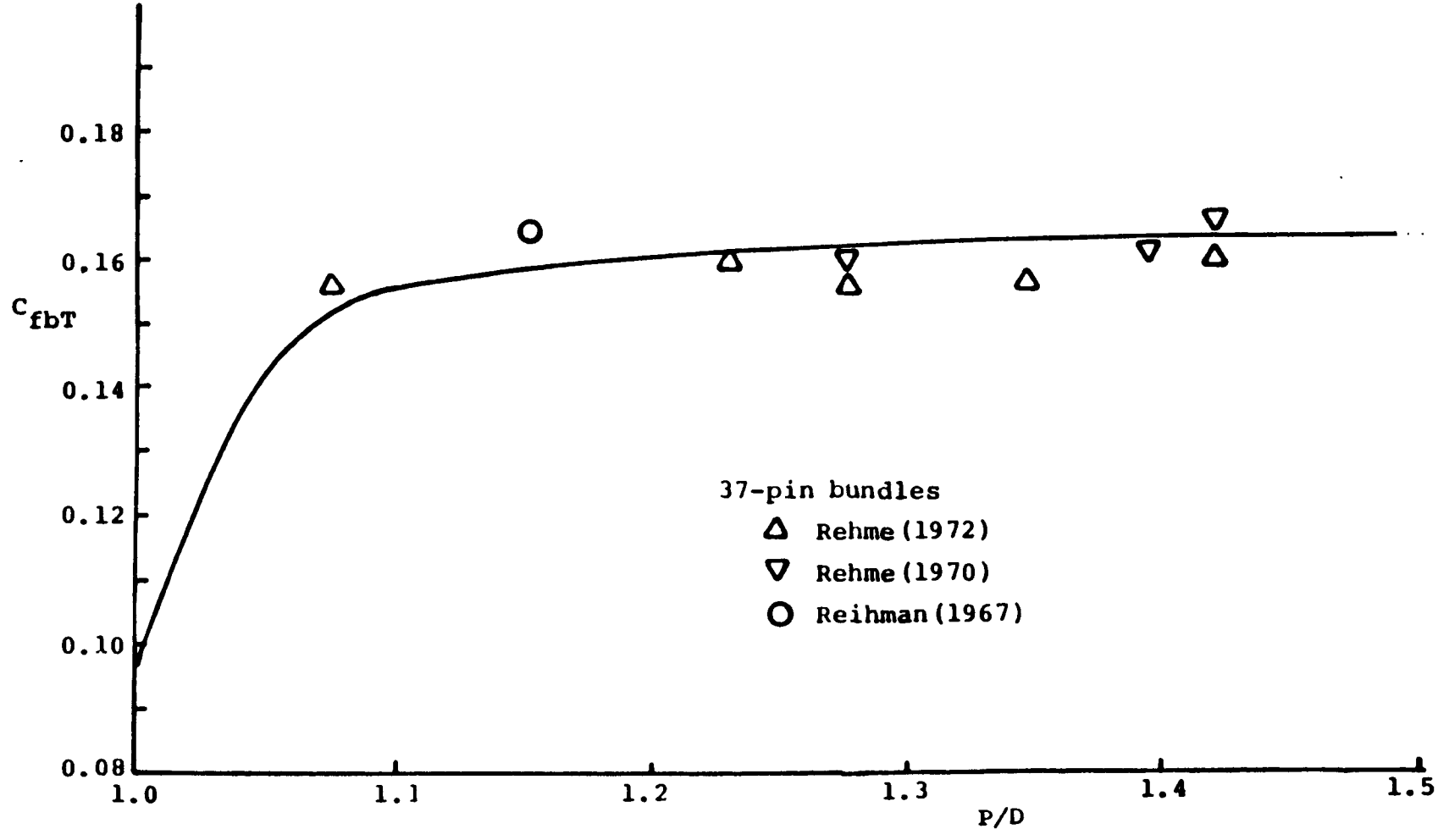

Figure 4.20 Comparison between Experimental Data and Predictions for Bare Rod 37-pin Turbulent Friction Factor Constant C_{fbT} (= $f_b \cdot Re_b^{0.18}$)

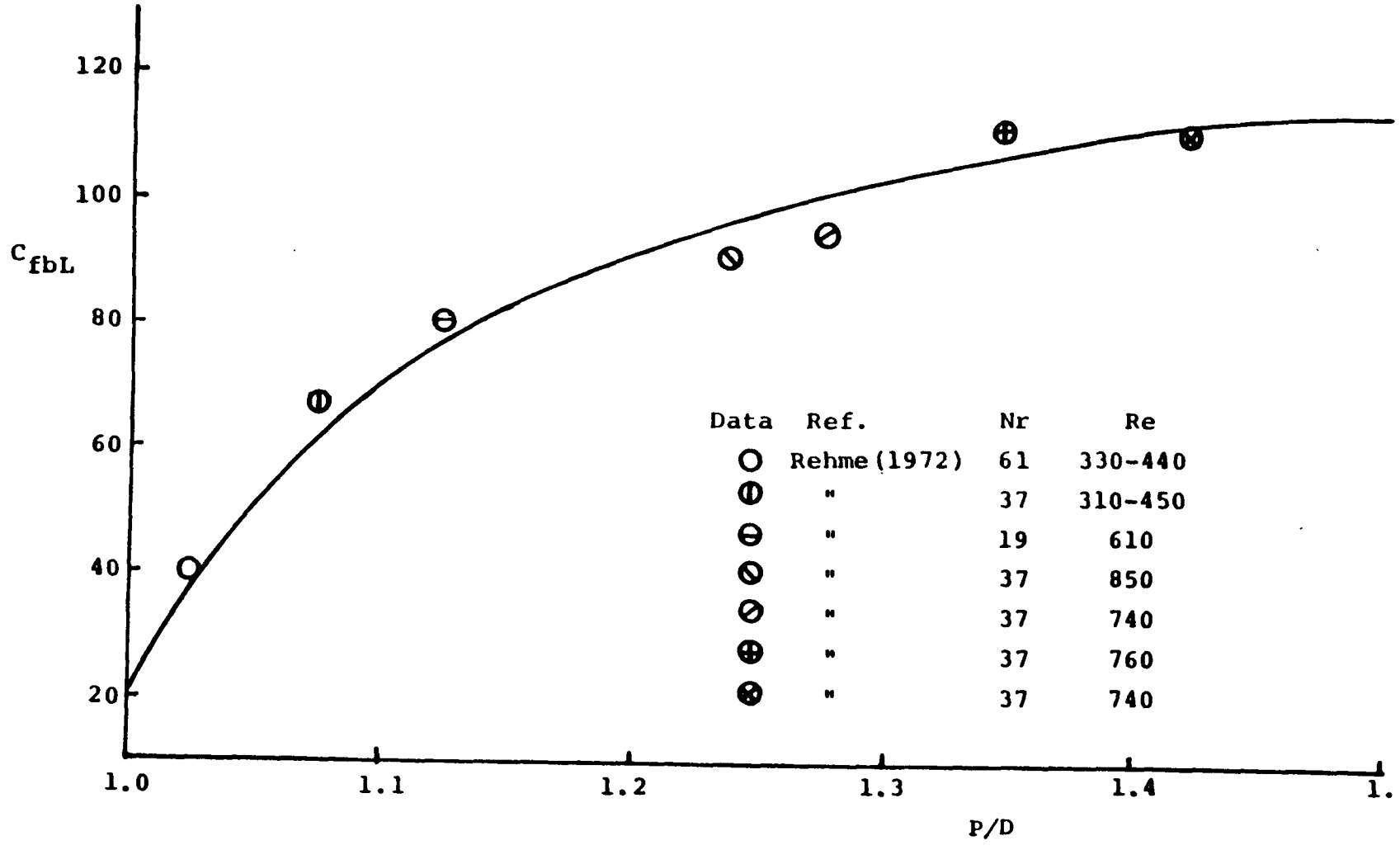

Figure 4.21 Predictions for Bare Rod 37-pin Laminar Friction Factor Constant C_{fbL} (= $f_b \cdot Re_b$)

slightly increasing function of bundle pin number, N_r.

Data for 37-pin turbulent friction factor constant are also shown in Figure 4.20 for comparison; however, no low P/D bundle fricition factor data are available and the predictions for low P/D cases can only be verified by subchannel data (c.f. Figure 4.8). The data for laminar friction factor constant in Figure 4.21 are from Rehme's results for bare rod bundles which have W/D = P/D. These data are well predicted by the model.

Figure 4.22 illustrates the edge flow split parameter as function of P/D for a 61-pin bare rod bundle with W/D = P/D. Because the equivalent diameter of an edge subchannel (with W/D = P/D) is always higher than that of interior subchannel, the edge flow split parameters are always higher than 1.0 as shown. The decreasing behavior of these curves is caused mainly by the difference in the change of equivalent diameter for different kinds of subchannels as P/D increases. The laminar value is consistently higher than turbulent value because of the difference in Reynolds number dependence (Re^{-1} vs. $Re^{-0.18}$) in friction factor equations.

4.6.3 Parametric behavior for Wire-Wrapped Bundles

4.6.3.1 Bundle Friction Factor Constants

Figures 4.23 and 4.24 depict the bundle friction factor constants, C_{fbT} and C_{fbL}, as functions of P/D and H/D for a 37-pin wire-wrapped bundle with W/D = P/D for the turbulent and laminar regions, respectively. The pin number effect is the same as bare rod case, i.e., these constants increases slightly as pin number

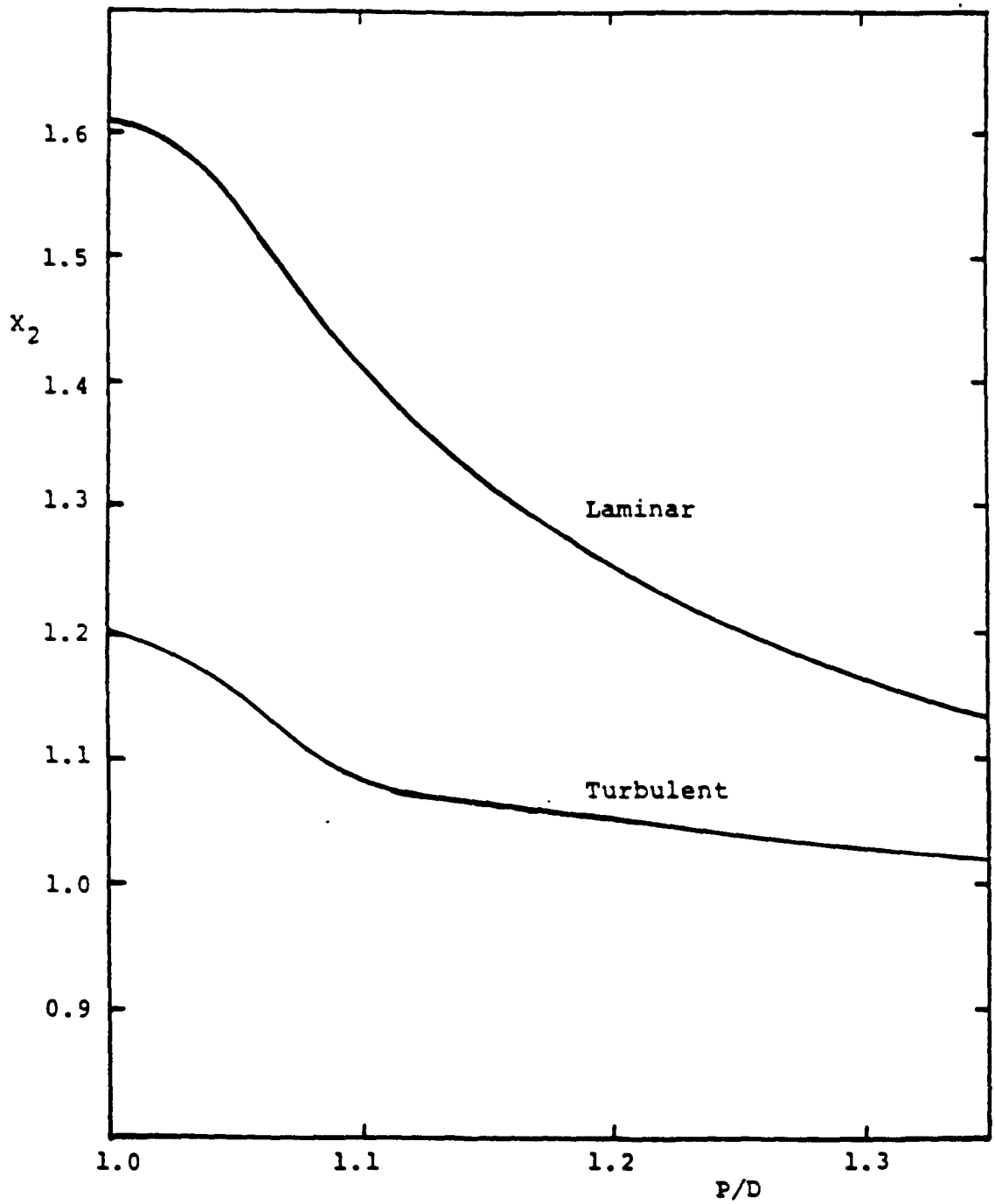

Figure 4.22 Predicted Edge Subchannel Flow Split Parameter for 61-pin Bare Rod Bundle

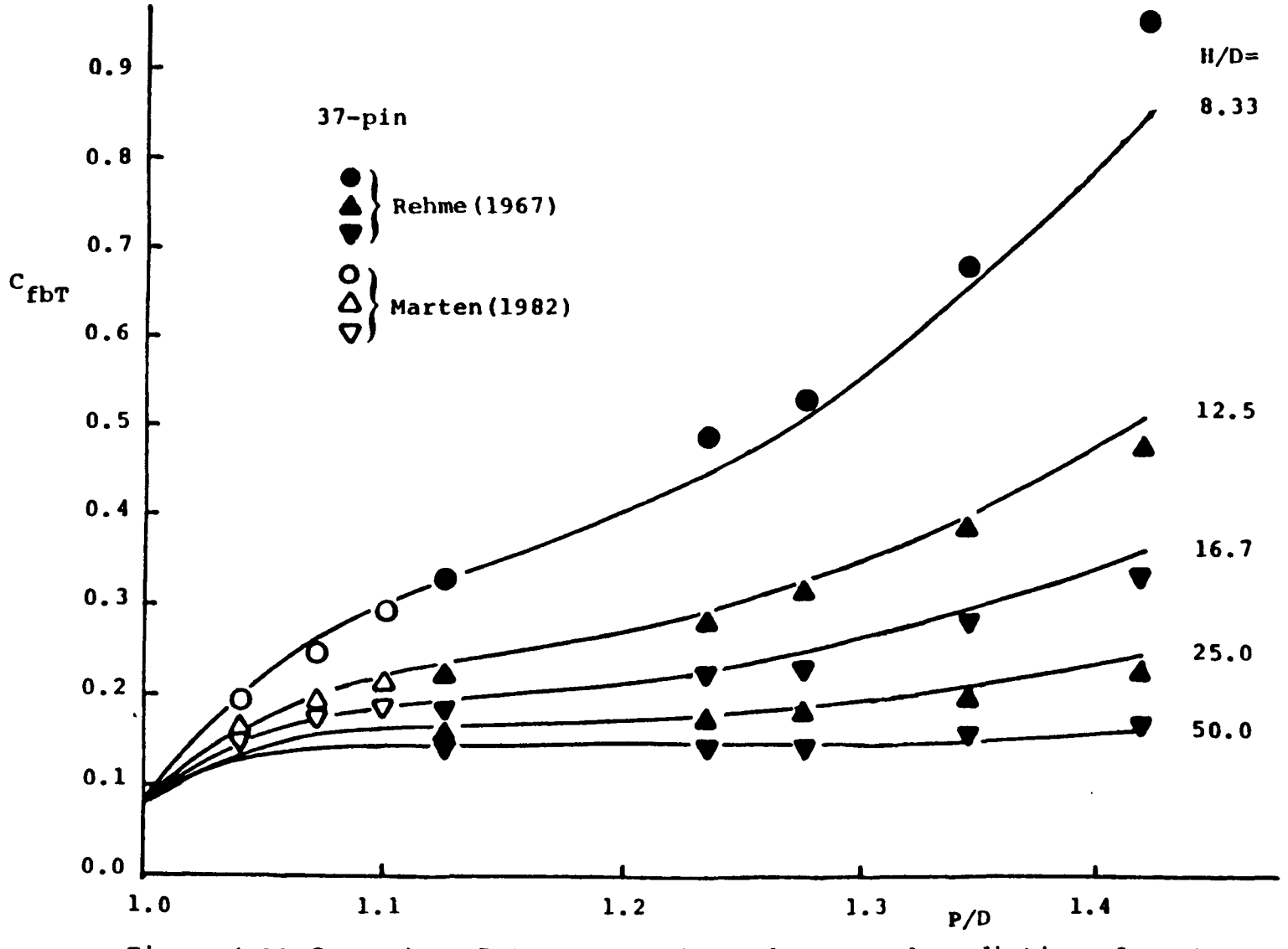

Figure 4.23 Comparison Between Experimental Data and predictions for Wire-Wrapped 37-pin Turbulent Friction Factor Constant C_{fbT} (= $f \cdot Re^{0.18}$)

increases. The P/D effect on these two constants is also similar to the bare rod case.

Although the H/D effect of these two constants is similar to each other, i.e., C_f increases as H/D decreases because of the wire drag effect, the change in absolute value is quite different from laminar to turbulent case. For the laminar case, C_f changes slightly from H/D = 50.0 to 8.0, while for turbulent case, C_f increases approximately five fold from H/D = 50.0 to 8.0. This indicates that the wire drag effect is much stronger in the turbulent region than that in the laminar region.

The turbulent data in Figure 4.23 are from Rehme's (1967) 37-pin bundles and Marten's (1982) 37-pin bundles. As shown in this figure, these correlations can predict not only Rehme's data (P/D > 1.1) but also Marten's data (P/D <1.1) which can not be well predicted by Rehme's correlation [Marten(1982)]. This confirms that the applicable range for P/D for these correlations is from 1.0 to 1.42.

The laminar data in Figure 4.24 are from Marten's (1982) 37-pin bundles together with Efthimiadis' (1983) 19-pin bundle and two high P/D, high H/D but higher N_r bundles. These data can be predicted by the correlations within 10% error, which is considered to be about the experimental error. Two other 61-pin bundle data of Chiu (42TR) and Engel (1979), are also shown for comparison. The inconsistence between data from blanket bundles is clear, and the correlations predict the value quite close to Marten's results rather than these other two data. This is because Marten's data were adopted as the basis upon which to base the correlation as discussed in Section 4.5.2.

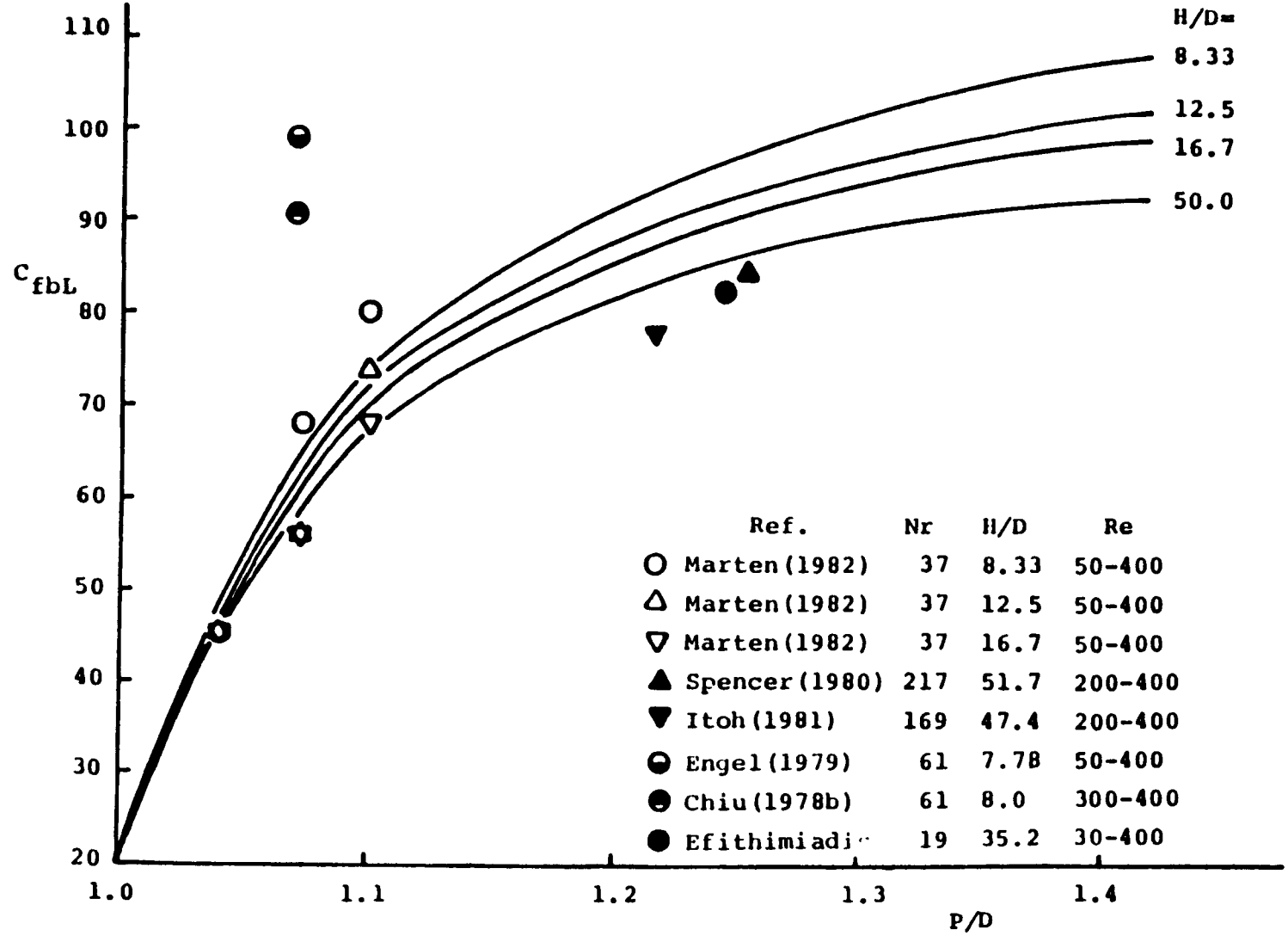

Figure 4.24 Comparison between Experimental Data and Predictions for Wire-Wrapped 37-pin Laminar Friction Factor Constant C_{fbL} (= f.Re)

The Westinghouse correlation, equation (4.7) can predict Chiu and Engel's data because it was calibrated by those data; however, it can not predict Marten's data and Efthimiadis data which has quite long H (66.6 cm). Table 4.9 compares the available laminar fRe data and the predictions from this correlation and Westinghouse correlation. Marten's data confirm the validity of this correlation and the lack of generality of Westinghouse correlation.

4.6.3.2 Flow Split Parameters

Figure 4.25 illustrates how the edge flow split parameter varies as a function of P/D and H/D in a 61-pin bundle with W/D = P/D for both laminar and turbulent flow conditions. Again, the P/D effect is similar to bare rod case because of the equivalent diameter effect. However, there is a minimum around P/D = 1.2 for H/D $\leq$ 24 in turbulent case. This is caused by the wire drag constant which increases as D_w/D becomes greater than 0.18. Hence the friction factor for interior subchannels increases relatively for D_w/D greater than 0.18 and this produces a higher velocity in edge subchannels.

The H/D effects for the laminar and turbulent cases are opposite to each other as shown in this figure. For the turbulent case, X_2 decreases as H/D increases, while for laminar case, X_2 increases as H/D increases. This may be explained from the effect of H/D on the interior subchannel friction factor, f_1, and the edge subchannel friction factor, f_2.

From equation (4.31), f_1 increases as wire drag effect increases, (i.e., H/D decreases). From equation (4.24), f_2 increases as swirl flow effect increases (i.e., H/D decreases). Note that although W_s

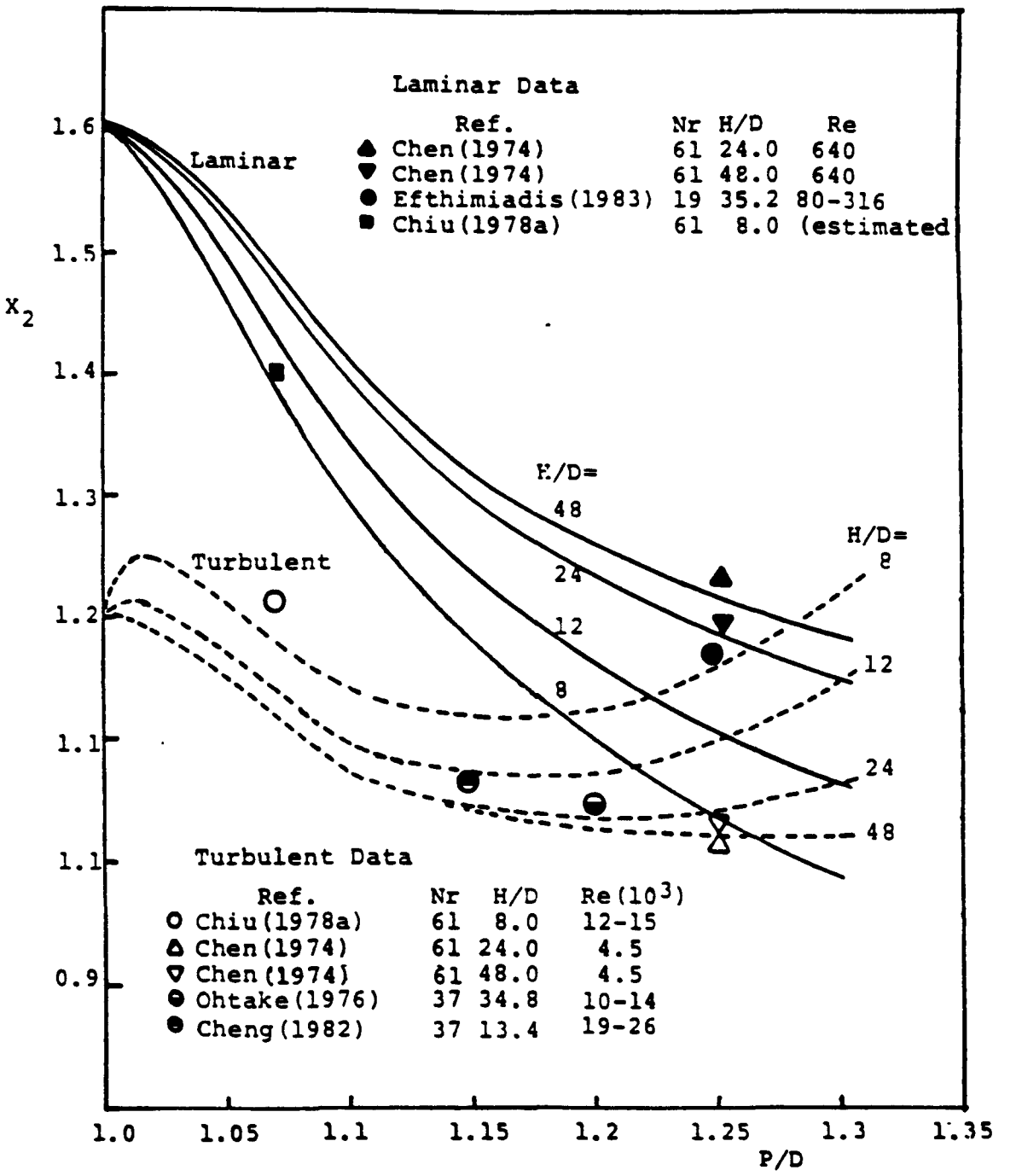

Figure 4.25 Predictions of Edge Flow Split Parameter for Wire-Wrapped 61-pin Rod Bundle

increases as H/D increases, the total swirl flow ratio, V_T/V_2 ($=\sqrt{W_s(A_T/A_l')\tan\theta}$), decreases from around 0.5 to around 0.05 as H/D increases from 8 to 48 for the turbulent case. Since in turbulent flow f_l is strongly affected by wire drag effect, this makes swirl flow effect relatively less important. Hence f_l increases more than f_2 does as H/D decreases; therefore, X_2 increases as H/D decreases. As for laminar flow, f_l is only slightly affected by wire drag effect, this makes swirl flow effect relatively more important. Hence f_l increases less than f_2 does as H/D decreases; therefore, X_2 decreases as H/D decreases.

To compare the predictions with data, some edge flow split data are also shown in Figure 4.25. The trend of these data is well predicted and all data can be predicted within 5% error.

4.6.4 Conclusion

A subchannel friction factor correlation applicable to both bare and wire-wrapped hexagonal rod bundles has been developed and calibrated. The validity of this correlation is confirmed by bare subchannel friction factor data, bare and wire-wrapped bundle average friction factor data, and wire-wrapped flow split data. The correlation can predict the bundle average friction factor data within ±14% with a 92% confidence interval and all the flow split data within ±5% except that in the transition region. This study concludes that the reported transition flow split data obtained by the isokinetic extraction method has a systematic error in this flow regime.

CHAPTER 5

MIXING PARAMETER CORRELATIONS

5.1 Physical Meaning of Mixing Parameters

The mixing parameters required for the ENERGY code as the input parameters discussed in Chapter 2 are, dimensionless effective eddy diffusivity (DEED), $\varepsilon^*_{1\eta}$; dimensionless eddy diffusivity for the edge region, $\varepsilon^*_{2\eta}$; edge transverse velocity ratio (ETVR), C_{1L}, and conduction shape factor, κ. Correlations for dimensionless effective eddy diffusivity and edge transverse velocity ratio have been developed by Chiu (56TR Rev1) and Burns (81TR); however, a different length scale, the interior subchannel equivalent hydraulic diameter, De_1, was used by these authors in defining DEED. Their parameter was denoted as ε^*_{1L} in all the paper or reports presented before this work, i.e.,

$$\varepsilon^*_{1L} \equiv \frac{\varepsilon}{V_1 De_i} \tag{5.1}$$

where ε is the effective eddy diffusivity between subchannels. The effective eddy diffusivity between edge subchannels was simply assumed to be the same value as that between interior subchannels in their approach.

In this study, $\varepsilon^*_{1\eta}$ is defined as

$$\varepsilon^*_{1\eta} \equiv \frac{\varepsilon}{V_1 \eta_{ij}}$$

The reasons for changing the definition for this parameter are as follows:

1) The characteristic length used to derive a dimensionless parameter for eddy diffusivity should be a distance related to two subchannels rather than an equivalent hydraulic diameter for one subchannel. The simplest length is the centroid to centroid distance η_{ij}. This has been pointed out by Nijsing and Eifler (1974) for bare rod cases; and

2) $\varepsilon^*_{l\eta}$ is a parameter reduced directly from the energy conservation equation, and has a physical meaning which is similar to the mixing Stanton number, M_{ij} = transverse mass flux/axial mass flux, in the literature. This has been discussed in chapter 2.

To further illustrate the physical meaning of $\varepsilon^*_{l\eta}$ and the assumption used for the ENERGY code to simulate the energy transfer by turbulent interchange and wire sweeping for the interior gap, Figure 5.1 shows the actual transverse velocity (averaged over the gap at one axial position) at one interior gap, $V_{T,ACT}$, along one axial lead length from WARD's air flow data measured by Roidt et al. (1980). The flow oscillates as the wire travels around the rod and is symmetric for each one-half lead length. This oscillating flow transports fluid from subchannel i to subchannel j over a portion of the axial length and from subchannel j to subchannel i over the remaining length. Figure 5.1 assigns the convention of positive $V_{T,ACT}$ to flow from subchannel i to j. Since the flow behavior from 0 to 180° and 180° to 360° are inversely symmetric, the following relation between flow velocities exists.

$$V_{T,ACT_{i-j}} = \left| V_{T,ACT_{j-i}} \right| \qquad (5.2)$$

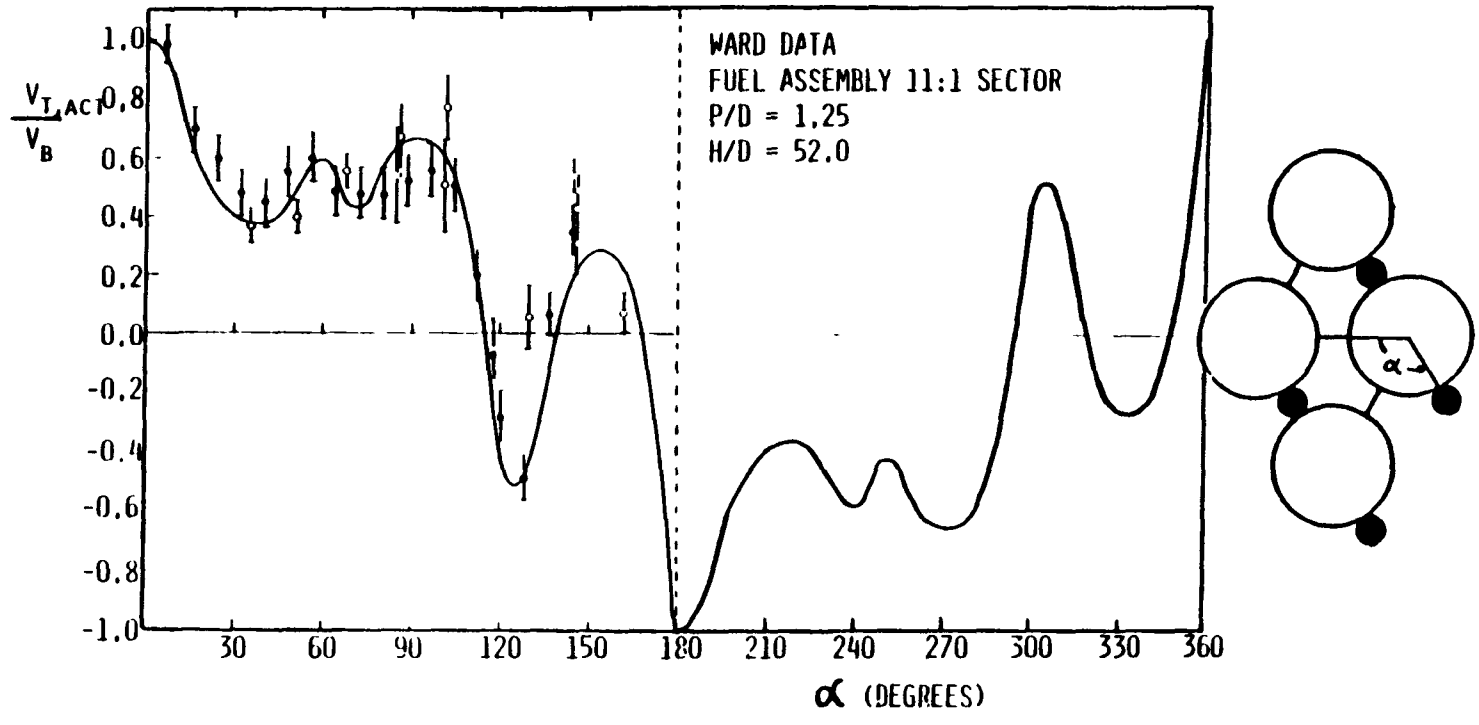

Figure 5.1 TYPICAL TRANSVERSE VELOCITY AT THE INTERIOR GAP AS A FUNCTION OF WIRE POSITION

Hence, one pseudo average transverse velocity $\tilde{V}_T$ can be considered which transports fluid both from subchannel i to j and from j to i as

$$\tilde{V}_T = \frac{1}{H} \int_0^H V_{T,ACT_{i-j}} dz = \frac{1}{H} \int_0^H V_{T,ACT_{j-i}} dz \tag{5.3a}$$

or since

$$\left|V_{T,ACT}\right| = V_{T,ACT_{i-j}} + \left|V_{T,ACT_{j-i}}\right|$$

$$\tilde{V}_T = \frac{1}{2H} \int_0^H \left| V_{T,ACT} \right| dz \tag{5.3b}$$

This velocity $\tilde{V}_T$ is constant over the lead length H and is related to the parameter W'^{W}_{ij}, the mass interchange rate per unit axial length, discussed in chapter 2, by

$$W'^{W}_{ij} = \rho \tilde{V}_T c \tag{5.4}$$

Superimposing the turbulent interchange mass rate per unit area, W'_{ij}/c, to $\rho\tilde{V}_T$ and dividing by the axial mass flux ρV_l, we obtain the parameter $\varepsilon^*_{l\eta}$. In addition to the approximation of using $\tilde{V}_T$ as the transport mechanism, we assume that the energy carried by $\tilde{V}_T$ is the average subchannel enthalpy. This energy transfer term is then shown in the energy equation (2.34) as the term associated with $\varepsilon^*_{l\eta}$.

The parameter $\varepsilon^*_{2\eta}$ is defined similarly to $\varepsilon^*_{l\eta}$ except that it only accounts for the turbulent interchange between the edge subchannels. $\varepsilon^*_{2\eta} = \varepsilon^*_{l\eta}$ is not assumed as in the old approach because the wire sweeps

the flow in one direction in the edge region and has no contribution to $\varepsilon^*_{2\eta}$; however, the wire might enhance the turbulence interchange because of the flow scattering by the wire.

The transverse velocity at the gap between edge subchannels along one axial lead length is shown in Figure 5.2 [Lafay and Benant(1975)]. The velocity has a maximum value as the wire approaches the gap at 120° clockwise from the gap and a minimum value as the wire leaves the gap at 30° counterclockwise from the gap. Other investigators [Chen et al.(11TR), Lorenz et al. (1977)] also have observed this phenomenon. To simulate this flow, the ENERGY code uses an axially uniform transverse velocity $\overline{V}_T$ along the assembly wall, which can be obtained from the continuity consideration.

$$\overline{V}_T = \frac{1}{H} \int_0^H V_{T,ACT}\Big|_{edge} \, dz \tag{5.5}$$

Note that only H appears in the denominator of the right hand side of equation (5.5) while, 2H appears in that of equation (5.4). The straight solid line in Figure 5.2 represents this $\overline{V}_T$. One can see that $\overline{V}_T$ is higher than the velocity following the wire direction, $V_A \tan\theta$, as shown in the dashed line. Detailed investigation of the available data for $\overline{V}_T$ shows that for H/D less than 15.0, $\overline{V}_T$ is less than $V_A \tan\theta$ while for H/D higher than 15.0, $\overline{V}_T$ is higher than $V_A \tan\theta$. Consistent with this, the ratio of $\overline{V}_T$ to $\overline{V}_A \tan\theta$ increases as H/D increases. The parameter C_{1L} is defined as the ratio of $\overline{V}_T$ and the average axial velocity in the edge subchannel, V_2.

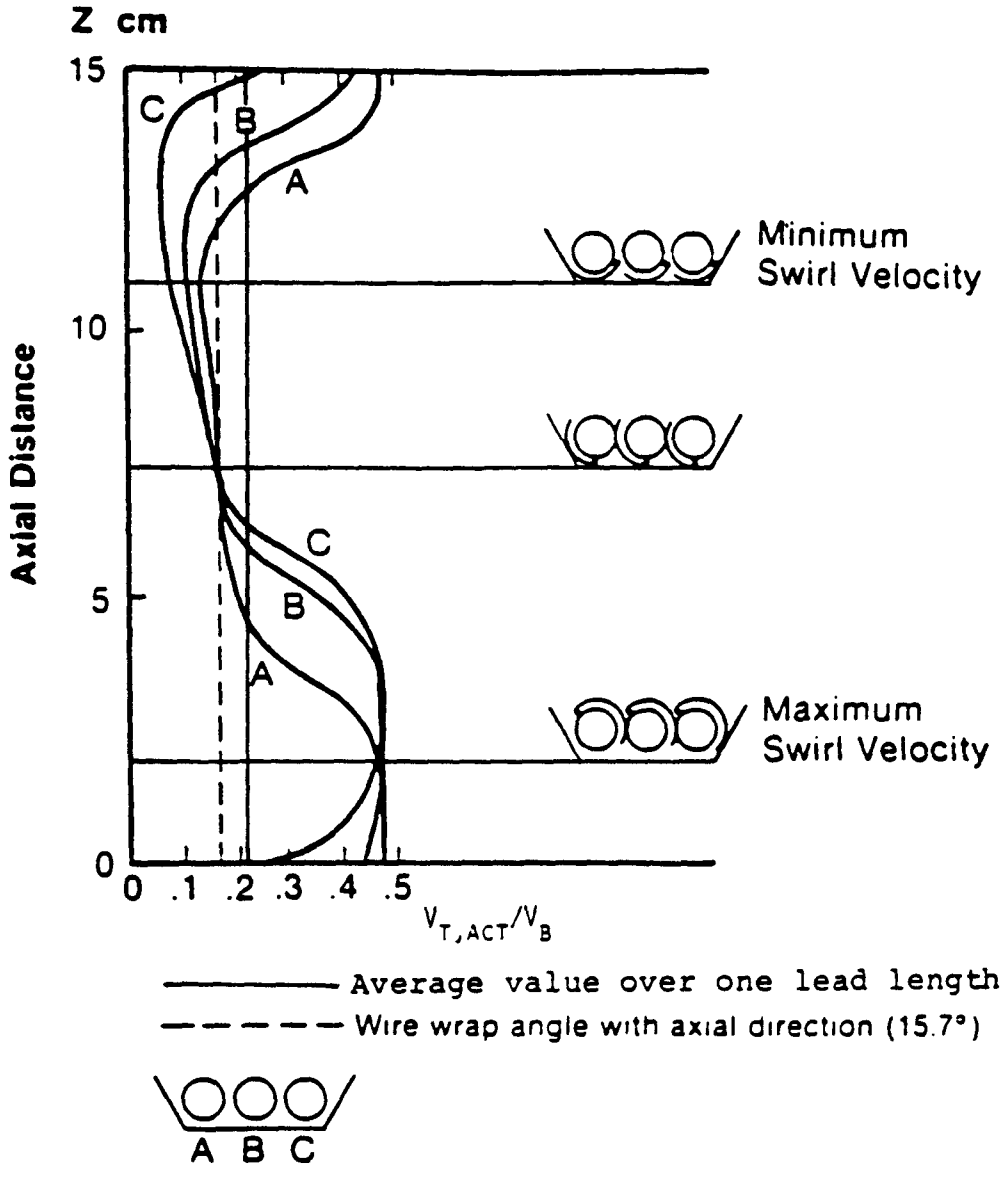

Figure 5.2 Typical Transverse Velocity at the Edge Gap (19-pin, P/D = 1.19, H/D = 18.75, H = 15 cm, from Lafay and Benant (1975))

The physical meaning of κ was discussed in chapter 2.(c.f. equation (2.11)).

In the following sections, the turbulent interchange mechanism is a bare rod bundle will be first discussed and a value for $\varepsilon^*_{2\eta}$ will be recommended. The models and correlations for $\varepsilon^*_{1\eta}$ and C_{1L} will then be developed. Finally, the correlation for κ will be suggested.

5.2 Recommended Value for $\varepsilon^*_{2\eta}$

The turbulent interchange between subchannels in a bare rod bundle has been studied by many investigators. The correlations for W'_{ij} between triangular and triangular (T-T) subchannels, triangular to square (T-S) subchannels, and square to square (S-S) subchannels have been developed by Rogers and Tahir (1975). They are

for T-T
$$\frac{W'_{ij}}{\mu} = 0.0018\ Re_i^{0.9}\ \left(\frac{c}{D}\right)^{-0.4} \tag{5.6}$$

for T-S
$$\frac{W'_{ij}}{\mu} = 0.0027\ Re_i^{0.9}\ \left(\frac{c}{D}\right)^{0.05}\left[1+\left\{\frac{1.101(1+c/D)^2-1}{1.273(1+c/D)^2-1}\right\}^{1.5}\right] \tag{5.7}$$

and

for S-S
$$\frac{W'_{ij}}{\mu} = 0.0050\ Re_i^{0.9}\ \left(\frac{c}{D}\right)^{0.106} \tag{5.8}$$

The relationship between (W'_{ij}/μ) and the dimensionless eddy diffusivity for turbulent interchange, $\varepsilon^*_{\eta T}$, can be easily obtained by the definition of $\varepsilon^*_{\eta T}$,

$$\varepsilon^*_{\eta T} \equiv \frac{W'_{ij}/c}{\rho V_i} = \frac{(W'_{ij}/c)De_i}{\frac{\mu\rho V_i De_i}{\mu}} = \left(\frac{W'_{ij}}{\mu}\right)\left[\frac{\frac{De_i}{c}}{Re_i}\right] \tag{5.9}$$

Using equations (5.6), (5.8), and (5.9) we can write $\varepsilon^*_{\eta T}$ as

$$\varepsilon^*_{\eta T} = a\left(\frac{De_i}{c}\right)\left(\frac{c}{D}\right)^b Re_i^{-0.1} \tag{5.10}$$

where for T-T $a = 0.0018$, $b = -0.4$

S-S $a = 0.0050$, $b = 0.106$

The definition of $\varepsilon^*_{\eta T}$ is the same as the mixing Station number M_{ij} for turbulent interchange. The mixing parameter β used in the COBRA series of codes is defined as

$$\beta = \frac{W'_{ij}}{\overline{G}} = M_{ij}\frac{G_i}{\overline{G}} = \varepsilon^*_{\eta}\frac{G_i}{\overline{G}} \tag{5.11}$$

where $\overline{G} = (G_i + G_j)/2$

If the velocities in two channels are not very different, β is the same as $\varepsilon^*_{\eta T}$. Considering the error associated with the data for these mixing parameters, which is around 20%, one can not distinguish between β and $\varepsilon^*_{\eta T}$ from the data. The parameter β has also been studied by some investigators, e.g., Rowe and Angle (1967) suggested

$$\beta = 0.0062\left(\frac{de_i}{c}\right)Re_i^{-0.1} \tag{5.12}$$

and Castellana et al. (1974) suggested that β for a square array with P/D = 1.334 should be

$$\beta = 0.0071\left(\frac{de_i}{c}\right)Re_i^{-0.1} \tag{5.13}$$

In the most recent version of the COBRA code, a constant value, 0.01 is used for β for all geometry and flow regions in LMFBR subchannel analysis [Khan(1982)].

The exponent for Reynolds number, -0.1, is from the theoretical derivation rather than fitting from the experimental data. The eddy diffusivity for the turbulent core in a tube can be derived as

$$\varepsilon_{H_{ij}} \propto \nu Re \sqrt{(f/2)} \tag{5.14}$$

Typically, if one uses $f = aRe^{-0.2}$ for turbulent flow, $\varepsilon_{H_{ij}} \propto Re^{0.9}$. Dividing $\varepsilon_{H_{ij}}$ by the mass flux, one obtains β or $\varepsilon^*_{\eta T} \propto Re^{-0.1}$. However, based on the scatter of the available data, one can not conclude the Reynolds number dependence of this parameter. Hence, we would assume that $\varepsilon^*_{\eta T}$ has no dependence on the Reynolds number, and developed a simpler correlation for $\varepsilon^*_{\eta T}$ (or β) which depends only on geometry. Figure 5.3 illustrates some available data as function of c/D. The Rogers and Tahir correlation for ε^*_{η}, equation (5.10), is also present for comparison. For the T-T array, the low c/D data of Petrunik (1968) and Walton (1969) do not appear consistent. Since Walton's result is consistent with other data at larger c/D, Petrunik's lowest c/D result is not used in the correlation proposed below.

For T-T $$\varepsilon^*_{\eta T} = 0.0016\left(\frac{c}{D}\right)^{-0.5} \tag{5.15}$$

S-S $$\varepsilon^*_{\eta T} = 0.0056\left(\frac{c}{D}\right)^{-0.3} \tag{5.16}$$

Figure 5.3 shows that for T-T, $\varepsilon^*_{\eta T}$ is about 0.008 - 0.02. The Typical results for $\varepsilon^*_{l\eta}$ are around 0.02 to 0.12 with P/D = 1.25, H/D = 48 to P/D = 1.067, H/D = 8. Hence for an interior subchannel, (T-T), the turbulent interchange part is around 10% of $\varepsilon^*_{l\eta}$.

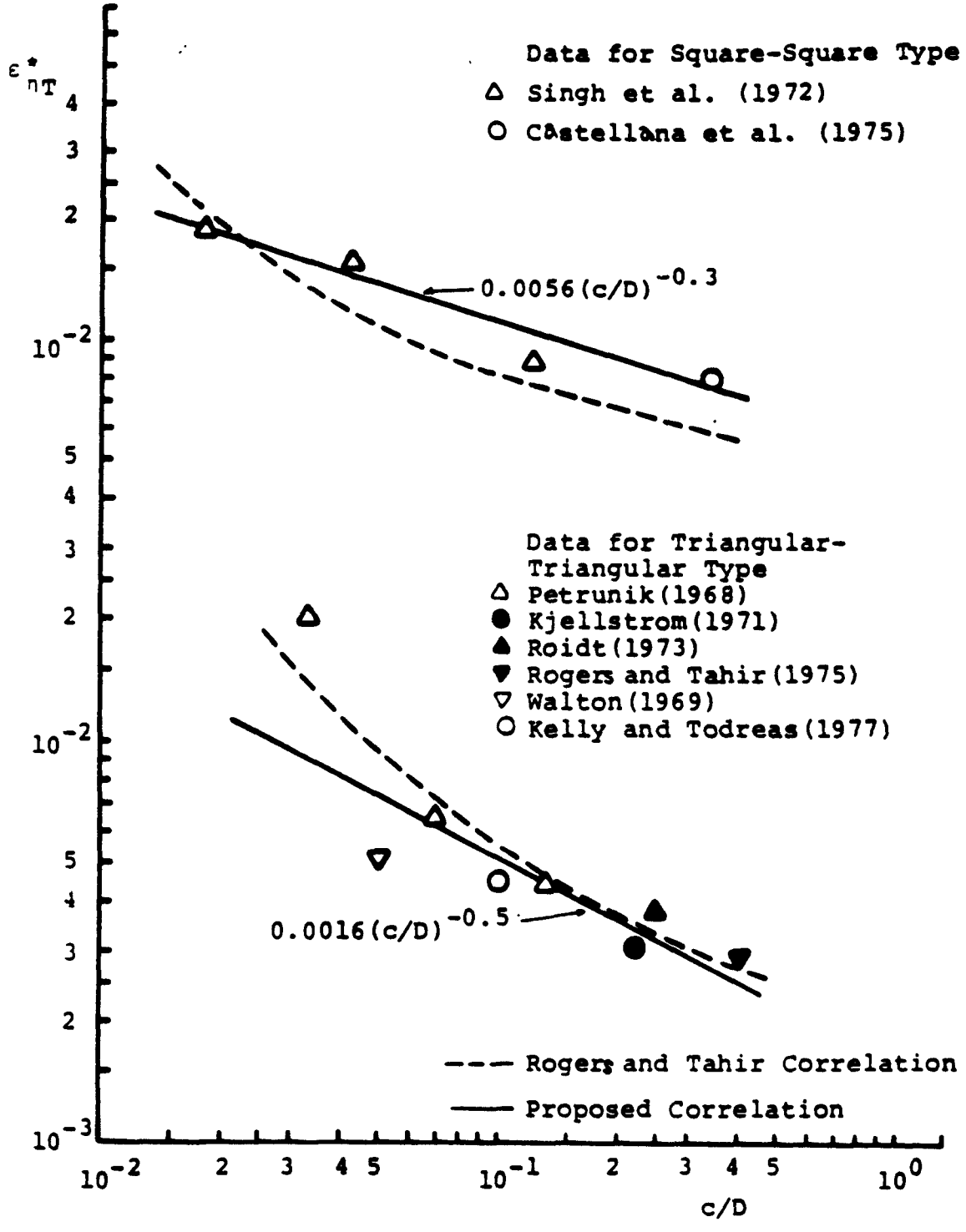

Figure 5.3 Turbulent Interchange Mixing Parameter for Bare Rod Bundle

The parameter $\varepsilon^*_{2\eta}$ is the turbulent interchange between edge subchannels. Rehme (1980a, 1982) has measured the detail turbulent structure in this kind of geometry. No global $\varepsilon^*_{2\eta}$ data, however, are available in the literature. From the data for T-T and S-S, we recommend that 0.01 can be used for $\varepsilon^*_{2\eta}$. This is consistent with what is used for β in the COBRA code.

5.3 Models for DEED and ETVR

5.3.1 Literature Review

The purpose of this section is to propose models for the transverse velocities $\tilde{V}_T$ and $\overline{V}_T$ and then formulate the correlations for DEED and ETRV from this model. The following is some previous work for modelling the wire sweeping flow.

Rogers and Todreas (1968) and Todreas and Turi (1972) performed detailed literature reviews on correlations for M_{ij} defined as V_T/V_A, where $V_T \equiv 2\tilde{V}_T$ for the interior gap and $V_T = \overline{V}_T$ for the edge gap for wire-wrapped rod bundles. The latter have showed that the most general form of the basic flow sweeping equation should be

$$M_{ij} = \alpha_f \frac{\pi(D + D_w)}{H} = \alpha_f \tan\theta \qquad (5.17)$$

where α_f is the fraction of the total subchannel free flow area swept out by wire wraps, i.e., Ar/A's; θ is the wire angle.

Rogers and Tarasuk (1968) assumed that the axial flow pressure drop over the axial distance traveled by mixing flow is approximately equal to the pressure drop experienced by the mixing flow as it passes from subchannel i to subchannel j. This leads to

$$M_{ij} = \left(\frac{2f_i}{K_m} \frac{(D + Dw)}{De_i} \theta_{ij}\right)^{1/3} \tag{5.18}$$

where f_i = subchannel friction factor

θ_{ij} = angular displacement between centroids of adjacent subchannels

K_m = transverse resistance coefficient to cross flow, function of (H/D) correlated differently for different kind of bundles.

Ginsberg (1972) recommended a forced-flow mixing model using the following expression for the forced-flow mixing rate

$$M_{ij} = F(P/D,\ H/D,\ Re)\ \frac{\pi(D+Dw)}{H}\ \delta_{ij} \tag{5.19}$$

where the correlation factor, function F, must be obtained experimentally. δ_{ij} = + 1, -1, and 0 when flow is transported from subchannel i to subchannel j, from subchannel j to i, and when no wire passes through i, j boundary, respectively. Thus, the model described above specifies a pulse type axial distribution of interchannel mixing rate. The model has been tested with only very limited experimental data.

The COBRA-WC wire-wrap model [Donovan et al. (1979)] is based on the assumption that the crossflow induced by the wire wrap passing through a gap is some fraction of the subchannel flow. The expression developed for the ratio of the transverse to axial flow rate was

$$\frac{W_{forced}/c}{G_i} = \left(\frac{\delta}{\Delta x}\right) \pi(D+D_w) \tag{5.20}$$

$$= DUR \tan\theta$$

where Δx = the axial node length

δ = the arbitrary parameter, usually set to $\Delta x/H$

DUR = $\delta(H/\Delta x)$

If one uses $\delta = \Delta x/H$, i.e., DUR = 1, then equation (5.20) becomes

$$\frac{W_{forced}/c}{G_i} = M_{ij} = \frac{\pi(D+D_w)}{H} = \tan\theta \qquad (5.21)$$

Equation (5.21) implies that the flow is exactly following the wire direction. In the COBRA code, the forced cross flow is held constant while solving the transversed momentum equations for the remaining cross flows.

Previous to this study, at MIT Chiu (55TR,Rev1) developed a model for the sweeping flow based on the assumption that the only driving force for this flow was the flow wake effect behind the wire. Chiu's result can be represented in the following form.

$$\frac{V_T}{V_A} = C\left(\frac{gap}{\eta}\right)^{n/2}\left(\frac{A_r}{A_s'}\right)^{1/2}\sin\theta \qquad (5.22)$$

where C = 0.235, n = -1 for the interior gap and C = 3.342, n = 0.7 for the edge gap. Note that V_T for the interior gap is $\tilde{V}_T$ while for the edge gap V_T is $\overline{V}_T$ as discussed before.

The above models are only valid in the turbulent region in which M_{ij} does not depend upon Reynolds number. As for the transition region Burns (81TR) suggested a model following Chiu's argument but with a Reynolds number dependence. The Reynolds number exponential dependence was taken from bare rod bundle friction factor data measured by Rehme (1973) and was evaluated after some manipulation to be 0.35, i.e,

$$\frac{V_T}{V_A} \propto Re_b^{0.35} \tag{5.23}$$

5.3.2 Models for the Transverse Velocity

Since the final correlations for the mixing parameters DEED and ETVR are empirically determined from the available data, we will not develop very complicated models for these parameters. Instead, only important geometrical parameters will be extracted and the constants of proportionality will be fitted from the data.

The general form for V_T/V_A, equation (5.17), is adopted for our purpose. Intuitively one recognizes that the flow more or less follows the wire direction. This gives equation (5.17) directly, i.e.,

$$\frac{V_T}{V_A} = \alpha_f \tan\theta \tag{5.24}$$

Here, we realize that α_f is a parameter related to A_r/A_s', which makes $V_T/V_A = 0$ as wire diameter goes to zero. Rather that using α_f directly proportional to A_r/A_s' , the relation

$$\alpha_f = C_m \left(\frac{A_r}{A_s'}\right)^{1/2} \tag{5.25}$$

where C_m could be function of D_w/D or H/D or both,
is proposed based on the following consideration.

Consider a wire-wrapped rod bundle and the pressure field associated with the wires shown in Figure 5.4. Because of the presence of wire, the flow is stagnant in front of the wire while a wake region

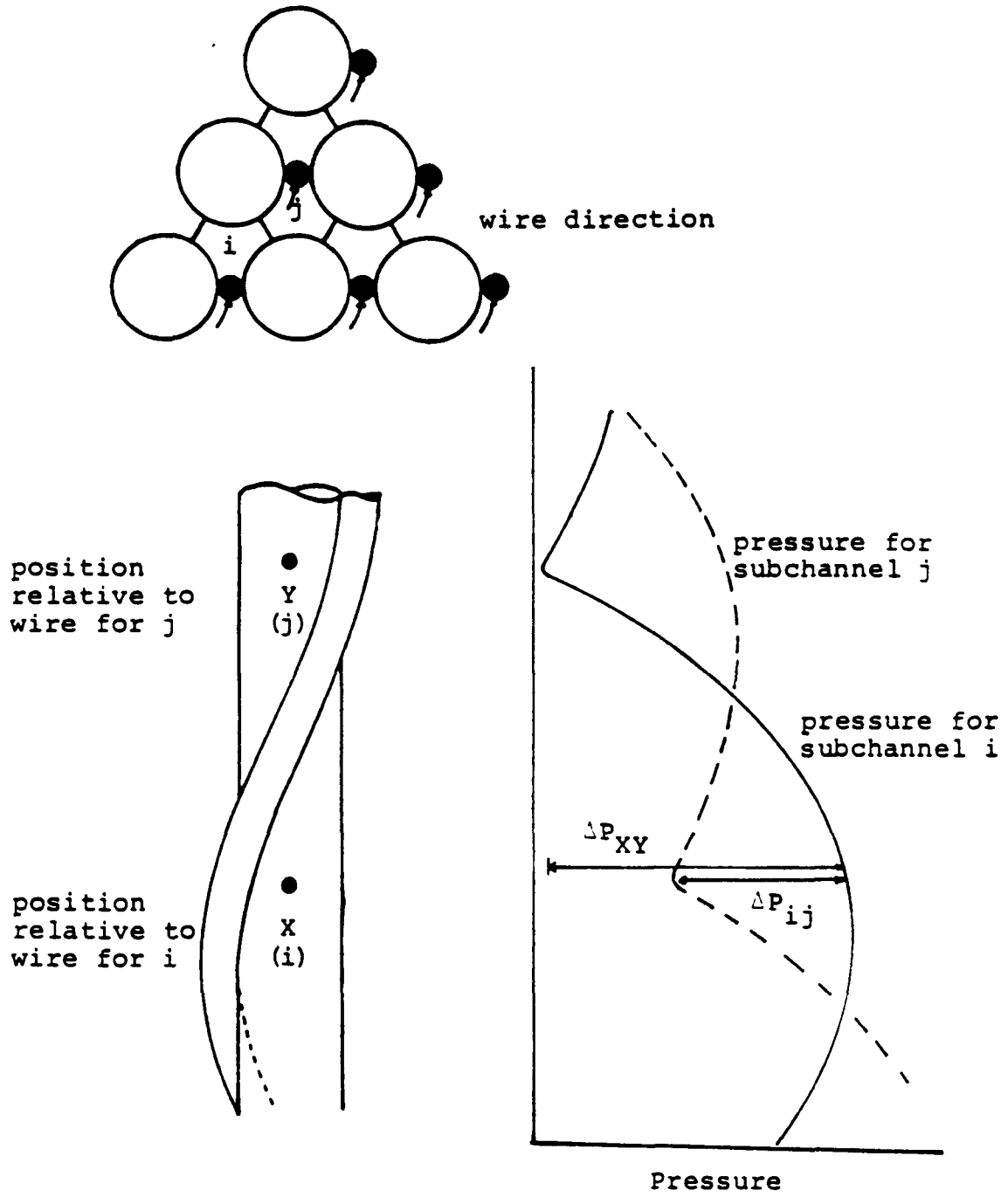

Figure 5.4 Pressure Distribution Relative to Wire Position

is produced downstream of the wire position. This produces the following static pressure distribution: a peak upstream of the wire (corresponding to X position) and a dip downstream of the wire (corresponding to Y position) shown in the right hand side of Figure 5.4. For the wire positions as located in the plan view at the top of Figure 5.4, subchannel i is in a position similar to position x while subchannel j is in a position similar to y. Pressure distribution curves A and B correspond to subchannel j and i, respectivley. The pressure drop from subchannel i to j is seen to not differ much from the pressure drop from X to Y.

The pressure drop ΔP_{XY} can be estimated from the typical wire drag force formulation as

$$\Delta P_{XY} = \frac{F_r}{A_s'} = C_d\left(\frac{\rho V_A^2}{2}\right)\frac{A_r}{A_s'} \tag{5.26}$$

where C_d = drag coefficient of wire

A_r = wire projected area

A_s' = bare subchannel flow area

If we assume that ΔP_{ij} can be related to V_T by the following form

$$\Delta P_{ij} = K_{ij}\left(\frac{\rho V_T^2}{2}\right) \tag{5.27}$$

where K_{ij} is the resistance coefficient for transverse flow, then from

$$\Delta P_{ij} \approx \Delta P_{XY} \tag{5.28}$$

we have

$$K_{ij}\left(\frac{\rho V_T}{2}\right) \approx C_d\left(\frac{\rho V_A^2}{2}\right)\frac{A_r}{A_s'} \tag{5.29}$$

i.e.,

$$\frac{V_T}{V_A} \propto \left(\frac{C_d}{K_{ij}}\right)^{1/2}\left(\frac{A_r}{A_s'}\right)^{1/2} \tag{5.30}$$

Therefore, we conclude that V_T/V_A is proportional to $(A_r/A_s')^{1/2}$. The The constant $(C_d/K_{ij})^{1/2}$ can be incorporated into the proportional constant and determined by the data.

The pressure distribution of Figure 5.4, however, does not exist between adjacent edge subchannels, because the wires are in phase in the edge region. Since a parameter related to A_r/A_s' is also required to make V_T/V_A go to zero as wire diameter goes to zero in the edge region, and since use of the parameter $(A_r/A_s')^{1/2}$ makes C_{1L} fit data well as will be shown in section 5.4, the parameter $(A_r/A_s)^{1/2}$ is also used to formulate (V_T/V_A) in the edge region.

Therefore, the final form for the the transverse velocity is then

$$\frac{V_T}{V_A} = C_m\left(\frac{A_r}{A_s'}\right)^{1/2}\tan\theta \tag{5.31}$$

5.3.3 Correlations for DEED and ETVR

The transverse velocity V_T in equation (5.31) represents either $\bar{V}_T$ for the interior gap or $\bar{\bar{V}}_T$ for the edge gap. The corresponding empirical constant C_m is determined from the data base of each geometrical region.

The DEED is comprised of both $\bar{\bar{V}}_T$ and a turbulent interchange part

W'_{ij}. However, since the turbulent interchange part of DEED contributes about 10% as discussed in Section 5.2, it can be assumed that

$$\varepsilon^*_{1\eta} \simeq \frac{\tilde{V}_T}{V_A} = C_{m1}\left(\frac{A_{r1}}{A'_1}\right)^{1/2} \tan\theta \tag{5.32}$$

Note that C_{m1} is determined from the data whih includes the turbulent interchange contribution.

On the other hand, ETVR is defined to encompass only the flow sweeping effect so that the parameter C_{1L} is directly expressed in terms of equation (5.31), i.e.,

$$C_{1L} = \frac{\bar{V}_T}{V_A} = C_{m2}\left(\frac{A_{r2}}{A'_2}\right)^{1/2} \tan\theta \tag{5.33}$$

Similar to the subchannel friction factor correlations, the correlations for DEED and ETRV are separated into three flow regions, i.e., turbulent ($Re_b \geq Re_{bT}$) transition ($Re_{bL} < Re_b < Re_{bT}$) and laminar ($Re_b \leq Re_{bL}$). Since the data indicate that both DEED and ETVR are independent of Reynolds number in the turbulent region, the empirical constants in this region denoted as C_{m1T} and C_{m2T}, would be formulated only as functions of geometry. For the laminar region, although the data are not sufficient to confirm that both DEED and EVTR are Reynolds number independent, we assume that they are independent for consistency with the flow split approach and easy formulation of the correlations. The empirical constants for the laminar flow region, denoted as C_{m1L} and C_{m2L}, would then be functions of geometry only.

In the transition region, both DEED and ETVR increase with Reynolds number. The empirical constants for the transition region, denoted as C_{mitr} and C_{m2tr} would be formulated as functions of both geometry and Reynolds number. A superposition method which combines the laminar and turbulent values would be developed for DEED and ETVR in the transition region in the next section.

5.4 Empirical Constants for DEED and ETVR

5.4.1 Empirical Constants for the Turbulent Region: C_{m1T} and C_{m2T}

In addition to the mixing experiments investigated in chapter 5, i.e., 37-pin data from this study and Chiu's two 61-pin data, the other mixing experiments for wire-wrapped rod bundles using different techniques have been discussed in detail by Khan et al. (12TR) and Khan (1980). The data from these experiments will be used to calibrate constants C_{m1} and C_{m2}.

DEED

Table 5.1 depicts the $\varepsilon^*_{1\eta}$ data available in the literature. The data of Okamoto (1970), Hines (1971), Collingham (1971), Skok (1973) were taken from Khan's (1974) reduction results for ε^*_1 by the old DRV code, which were transferred to $\varepsilon^*_{1\eta}$ by equation (5.17b) and the new flow split correlations. The Data from KfK [Baumann (1969), Hoffman (1973, 1975)] were reduced by their MISTRAL II code to get μ with units of % per cm, defined as the total mass interchange rate (% of axial flow) per unit length over all the gaps surrounding one subchannel. For an interior subchannel (3 gaps), μ can be related to $\varepsilon^*_{1\eta}$ by

Table 5.1 Available Data for $\varepsilon^*_{1\eta}$ in the Turbulent Region

Organization	Investigators	N_r	$D_{(cm)}$	$D_{w(cm)}$	P/D	H/D	Experiment Type	$\varepsilon_{1\eta}$	C_{mlT}
MIT	Cheng*	37	15.04	2.26	1.154	13.4	Salt tracer	0.065	0.343
	Chiu(1978c)**	61	12.73	0.80	1.067	4.0	"	0.294	0.60
	"	"	"	"	"	8.0	"	0.294	0.50
	Symolon(1981a)	61	6.35	1.59	1.250	24.0	"	0.047	0.38
	"	"	"	"	"	48.0	"	0.026	0.42
KfK	Baumann(1969)	61	6.00	1.00	1.167	16.67	Ht'd pin air	0.044	0.28
	Hoffman(1973)	61	6.00	1.90	1.317	16.67	Ht'd pin, Na	0.065	0.33
	"	"	"	"	"	33.33	"	0.033	0.33
	"	"	"	"	"	50.00	"	0.020	0.30
	Hoffman(1975)	61	6.0	1.20	1.200	16.67	"	0.054	0.32
	"	"	"	"	"	33.33	"	0.023	0.28
	"	"	"	"	"	50.00	"	0.013	0.24
WARD	Roldt(1980)**	217	63.5	15.9	1.250	52.0	Cobra probe+	0.017	0.30
	"	61	63.5	4.50	1.070	7.9	tracer, air	0.140	0.53
ORNL	Fontana(1974)	19	5.84	1.42	1.244	52.0	Ht'd pin, Na	0.020	0.35
HEDL	Collingham(1971)	217	5.84	1.40	1.240	52.0	Salt tracer	0.014	0.25
GE	Hines(1971)	127	6.35	1.78	1.280	24.0	Hot Water	0.043	0.33
Japan	Okamoto(1970)	91	6.30	1.39	1.221	40.48	Salt tracer	0.018	0.25
France	Skok(1973)	7	21.0	3.0	1.142	14.29	Hot Water	0.046	0.26
	"	"	"	"	"	21.43	"	0.030	0.26
	"	"	"	"	"	28.57	"	0.023	0.26
	"	"	16.9	6.0	1.355	26.63	"	0.023	0.18

* This work
** Data reduced by the Author

$$\mu(\%/cm) \equiv \frac{W'_{ij}}{\dot{m}_i} = \left(\frac{W'_{ij}/c}{\dot{m}_i/A_i}\right)\frac{c}{A_i} = 3\varepsilon^*_{l\eta}\left(\frac{c}{A_i}\right) \tag{5.34a}$$

i.e.,

$$\varepsilon^*_{l\eta} = \left(\frac{\mu}{3}\right)\left(\frac{A_i}{c}\right) \tag{5.34b}$$

where A_i and c are in cm^2 and cm, respectively.

The data of Roidt et al. (1980) are from the measured transverse velocity at an interior gap. Using their results presented as Figure 5.1, we can calculate $\bar{V}_T/V_A$ from equation (5.3). The $\varepsilon^*_{l\eta}$ for these bundles can be estimated to be approximately equal to $(\bar{V}_T/V_A)$. The parameter C_{mlT} for all these bundles calculated by equation (5.34) are also present in Table 5.1. The reported error associated with the $\varepsilon^*_{l\eta}$'s listed in Table 5.1 is 20 - 30%.

Figure 5.5 illustrates C_{mlT} as a function of c/D. Although the data scattering for high c/D, the trend suggests that C_{mlT} increases as c/D decreases. As for the H/D effects for C_{mlT}, the data of Chiu's two bundles (P/D = 1.067, H/D = 4.8), Symolon's two bundles (P/D = 1.25, H/D = 24, 48), Hoffman's three bundles (P/D = 1.317, H/D = 16.67, 33.33, 50.0) and Skok's three bundles (P/D = 1.142, H/D = 14.29, 21.43, 28.57) show that these effects are very weak. The reason for the strong dependence on (c/D) of $\varepsilon^*_{l\eta}$ might be that the transverse resistance plays an important role for $\varepsilon^*_{l\eta}$ as seen from equation (5.30). The transverse resistance is strongly affected by the gap to diameter ratio, c/D, hence so is $\varepsilon^*_{l\eta}$.

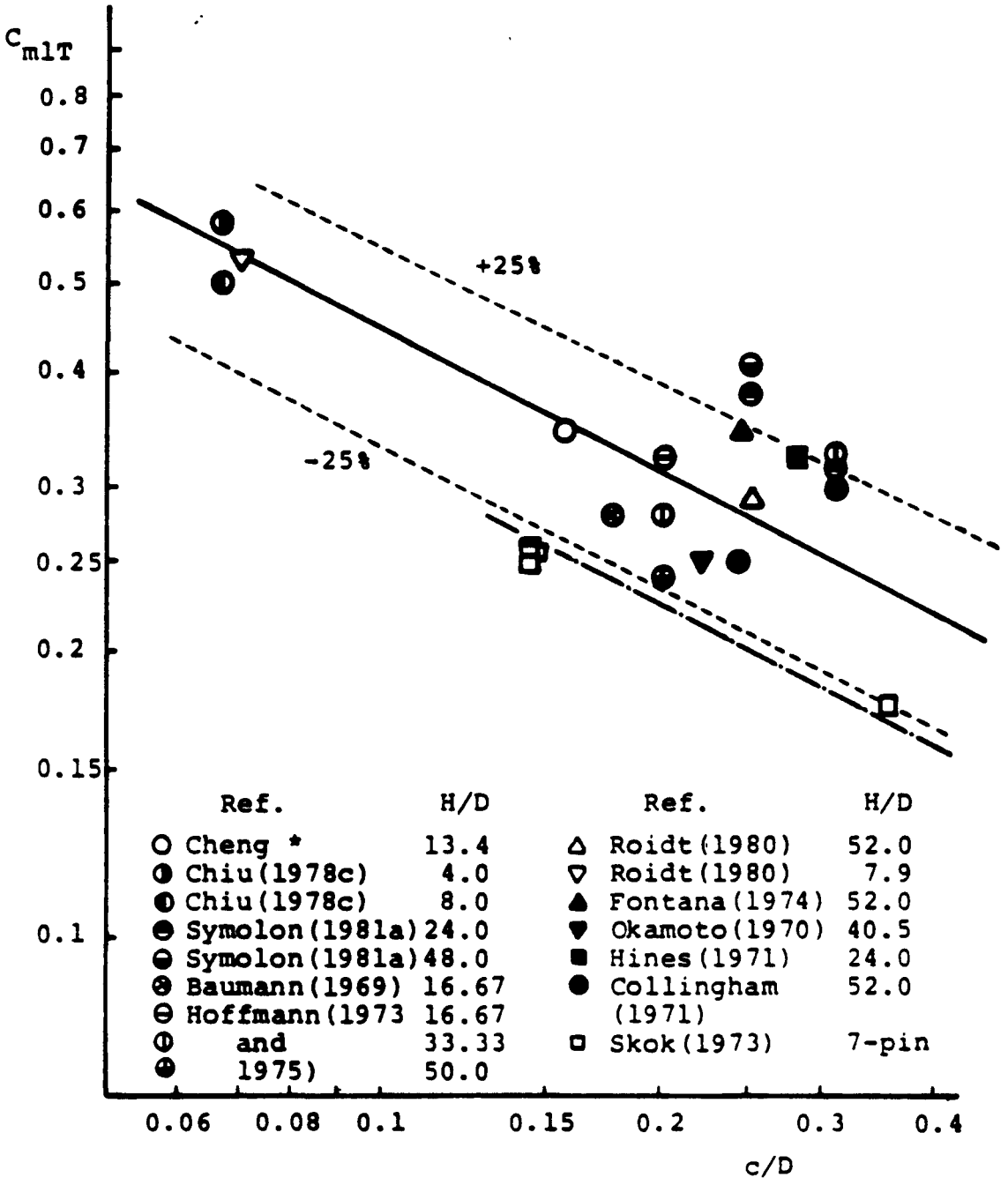

Figure 5.5 Data and Calibrating Results for C_{m1T} (i.e., ε^*_{in}) in the Turbulent Region

Therefore, C_{mlT} would be correlated as function of (c/D) only.

Since in a 7-pin bundle all the interior subchannels are adjacent to the edge subchannels, the $\varepsilon^*_{l\eta}$ reduced from these bundles does not fully represent the $\varepsilon^*_{l\eta}$ between interior and interior subchannels. As shown in Figure 5.5, the $\varepsilon^*_{l\eta}$ from Skok's 7-pin experiments are consistently lower than that from experiments with higher pin number ($\geq$19). Therefore, the results of Skok's experiments are seperated from the other results and correlated seperately for 7-pin bundle application.

The results for C_{mlT}, as illustrated in Figure 5.5 in correlation form are

$$\text{for } N_R \geq 19 \qquad C_{mlT} = 0.14\left(\frac{c}{D}\right)^{-0.5} \tag{3.35a}$$

$$\text{for } N_R = 7 \qquad C_{mlT} = 0.1\left(\frac{c}{D}\right)^{-0.5} \tag{3.35b}$$

These correlations can predict most of the data within ± 25% error except for Symolon's data, which are still within 35% of the prediction. Symolon recalibrated Hanson's salt injection experiment, which were the first experiments performed at MIT using this technique. Because of inexperience with this technique at that time, the larger error of the data might be expected.

ETVR

Table 5.2 depicts the C_{lL} data available in the literature. The data of Skok (1973), Fontana (1974), Pederson (1974) and Lorenz (1974) were also taken from Khan's (12TR) reduction results for C_l by the old DRV code, which were transfered to C_{lL} by the flow split correlation.

Table 5.2 Available Data for C_{1L} in the Turbulent Region

Organization	Investigators	N_r	D(cm)	D_w(cm)	P/D	H/D	Experiment Type	C_{1L}	C_{m2T}
MIT	Cheng*	37	15.04	2.26	1.154	13.4	Salt tracer	0.268	1.65
	Chiu(1978C)**	61	12.73	0.80	1.067	4.0	"	0.470	1.14
	"	"	"	"	"	8.0	"	0.284	1.38
	Symolon(1981A)	61	6.35	1.59	1.250	24.0	"	0.22	1.98
	"	"	"	"	"	48.0	"	0.18	3.33
	Symolon(1981)	217	5.89	1.47	1.250	51.72	"	0.11	2.22
	Chen(1974)	61	6.35	1.59	1.250	24.0	LDA	0.22	1.98
	"	"	"	"	"	48.0	"	0.13	2.42
ANL	Pederson(1974)	91	6.35	1.27	1.210	48.0	Hotwater	0.136	2.73
	Lorenz(1977)	91	12.7	3.05	1.240	48.0	Salt tracer	0.137	2.53
ORNL	Fontana(1974)	19	5.84	1.42	1.244	52.0	Ht'd pin, Na	0.115	2.28
France	Lafay(1975)	19	8.00	1.50	1.188	18.75	FV+	0.247	1.93
France	Skok(1973)	7	21.0	3.0	1.142	14.29	Hot Water	0.20	1.30
	"	"	"	"	"	21.43	"	0.15	1.46
	"	"	"	"	"	28.57	"	0.13	1.69

* This work

** Data Reduced by the Author

\+ Flow Visualization Technique

(c.f. equations (5.10),(5.12)) Chen's (11TR) data were measured by a laser doppler anemometer (LDA) at Re_b = 4500. Observing the data in the transition region from our study, we find that the value for C_{1L} at this Reynolds number is around 90% of its turbulent value. Hence, the reported value divided by 0.9 is estimated to be the turbulent value. Collingham's (1971) 217-pin edge injection data reduced by Khan (12TR) are not included in this table because they are apparently much lower than (40%) all the other data for bundle geometry resembling a fuel assembly. The bundle size effect could not be confirmed since the recent Symolon (84TR) 217 pin data showed consistent values with the data from the small size bundle with similar geometry. The parameter C_{m2T} for all these bundles calculated by equation (5.33) is also present in Table 5.2. The reported errors associated with C_{1L}'s listed in Table 5.2 are around 20%.

Figure 5.6 illustrates C_{m2T} as a function of H/D. The trend of C_{m2T} in this figure strongly suggests that it is a function of H/D only. As H/D increases, C_{m2T} increases. Only slight scatter of these values is indicated at the H/D ≈ 50 end, at which all the data are from a geometry similar to a fuel assembly.

The characteristic of the transverse velocity in the edge gap is not the same as that in the interior gap. The pressure driving source illustrated in Figure 5.3 does not exist in the edge gap since all the wires are in phase. Hence the transverse velocity in the edge gap is mainly created by the wire sweeping. As the data show, these wire-sweeping effects create flow with an average angle with respect to the rod axis less than the comparable wire angle for low H/D and

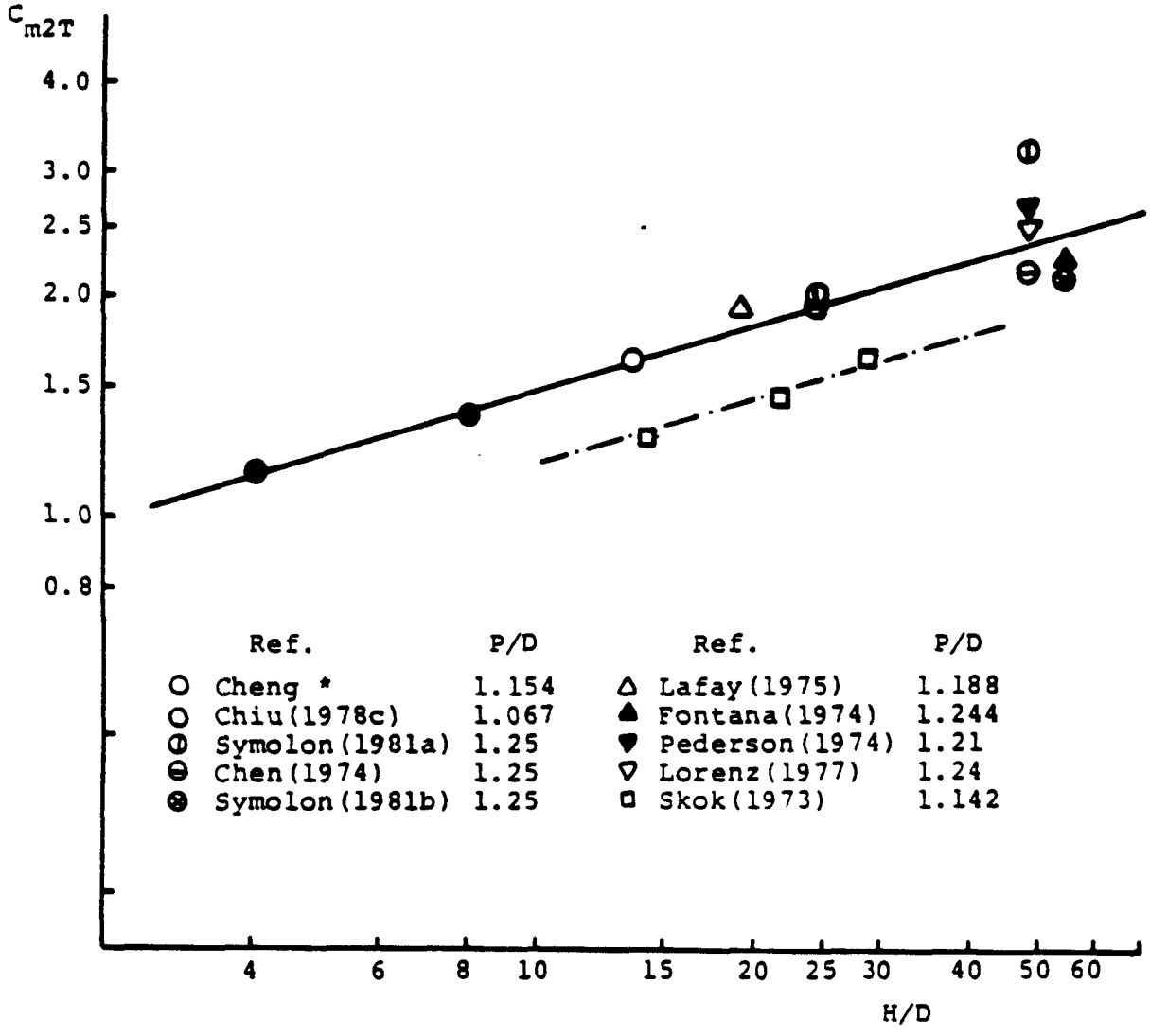

Figure 5.6 Data and Calibrating Results for C_{m2T} (i.e., C_{1L}) in the Turbulent Region

greater than the wire orientation for high H/D. The breaking point for this phenomenon is around H/D = 15.

Similar to the $\varepsilon^*_{1\eta}$ case, consistently lower values of C_{1L} for 7-pin bundles from Skok's data than that from other bundles' data are found. Since all the edge gaps in a 7-pin bundle connect an edge subchannel to a corner subchannel, the transverse velocity might be retarded by this character. Again, the results of Skok's experiments are correlated seperately for 7-pin bundle application.

The fitted results for C_{m2T} as illustrated in Figure 5.6 are

$$\text{for } N_R \geq 19 \quad C_{m2T} = 0.75(H/D)^{0.3} \tag{5.36a}$$

$$\text{for } N_R = 7 \quad C_{m2T} = 0.6(H/D)^{0.3} \tag{5.36b}$$

These correlations can predict all the data for C_{1L} within ± 15%.

The consistency between the H/D dependence of C_{m2T} and W_{sT}, the swirl flow constant in the subchannel friction factor models, (c.f. equations, (4.20), (4.64)) is worth pointing out. Comparing equation (4.20) to (6.33) one finds that $\sqrt{W_{sT}}$ corresponds to C_{m2T}. Although the absolute magnitude is quite different for these two parameters, the dependence of (H/D) for these parameters is almost the same, i.e., the parameter $\sqrt{W_{sT}}$ is almost proportional to $(H/D)^{0.3}$ from equation (4.64).

To illustrate the parameter behavior of $\varepsilon^*_{1\eta}$ and C_{1L}, Figures 5.7 and 5.8 illustrate the predicted $\varepsilon^*_{1\eta}$ and C_{1L} as functions of P/D and H/D, respectively. Some data from Tables 5.1 and 5.2 are also present in these figures for comparison.

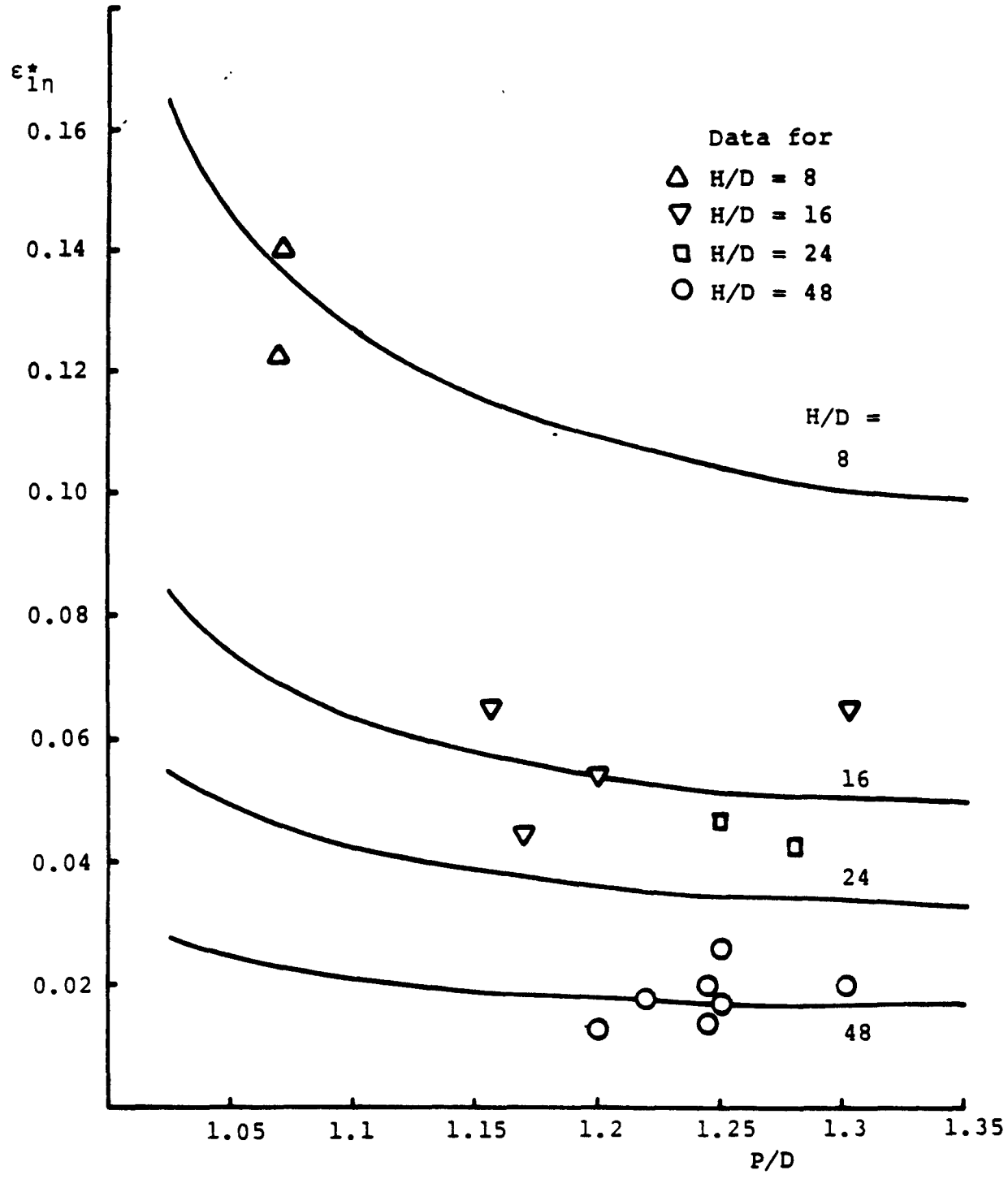

Figure 5.7 Parametric Behavior of ε^*_{ln} in the Turbulent Region

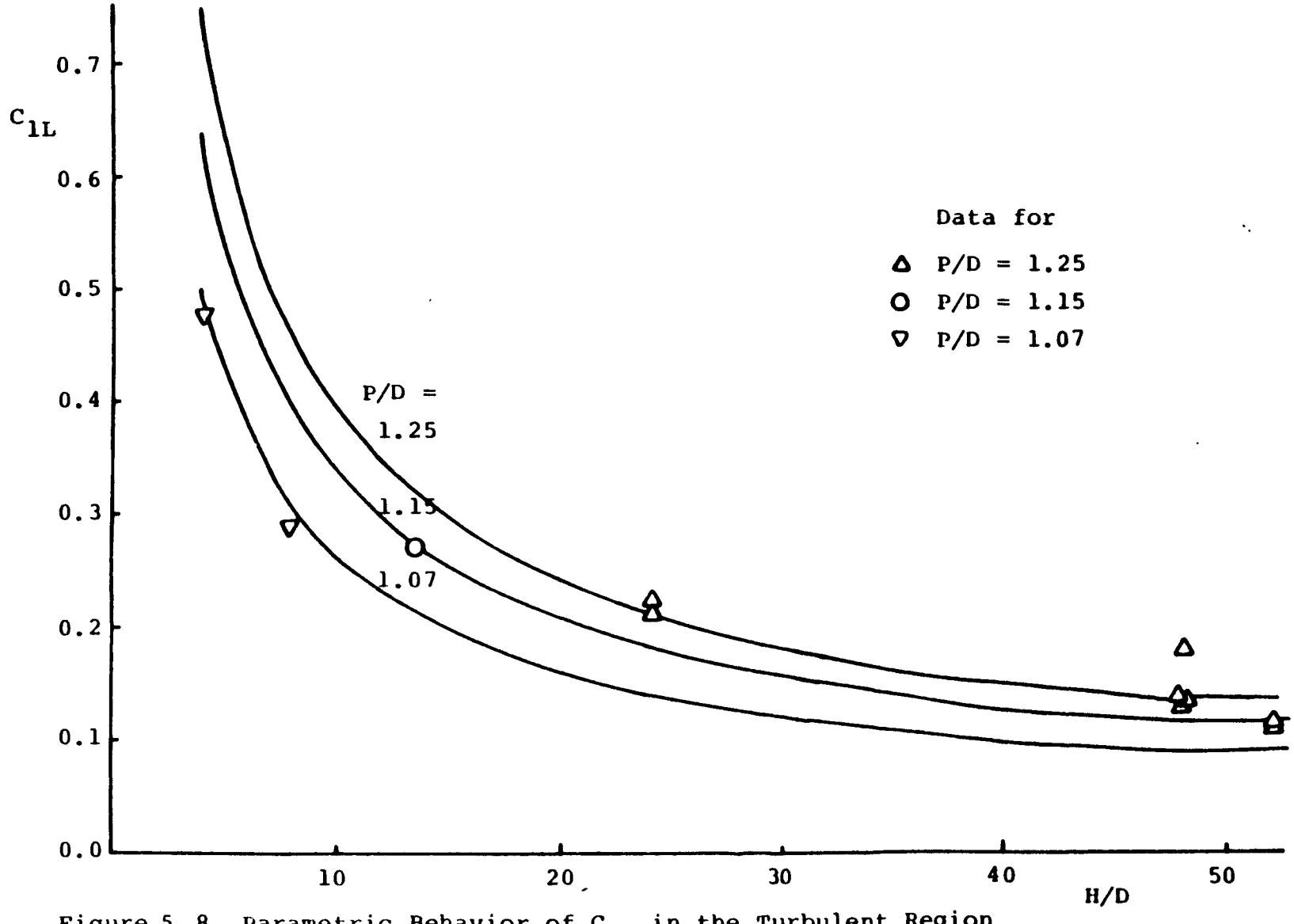

Figure 5.8 Parametric Behavior of C_{1L} in the Turbulent Region

5.4.2 Empirical Constants for the Laminar Region: C_{m1L} and C_{m2L}

Only Chiu (43TR) and Symolon (84TR) performed similar experiments to the mixing experiments, in this study at low flow rates. Using a laser doppler anemometer, Chen (11TR) measured transverse and axial velocities in the edge region at $Re_b = 430$ in two 61-pin bundles with P/D = 1.25 and H/D = 24 and 48. These are the only available data for the mixing parameters $\varepsilon^*_{1\eta}$ and C_{1L} in the laminar region.

Because of the insufficient data base in the laminar region, assumptions of the relation between laminar and turbulent values for these parameters have to be made. We assume that the ratios between laminar and turbulent values of $\varepsilon^*_{1\eta}$ and C_{1L} are the same for both parameters, i.e.,

$$\frac{\varepsilon^*_{1\eta}\Big|_{\text{laminar}}}{\varepsilon^*_{1\eta}\Big|_{\text{turbulent}}} = \frac{C_{1L}\Big|_{\text{laminar}}}{C_{1L}\Big|_{\text{turbulent}}} = C_{mLT} \tag{5.37}$$

The parameter C_{mLT} can be estimated from the data described above. However, since large scatter is found in Symolon's data for low flow rates, estimation of C_{mLT} from his data is not achievable. Further, the lowest flow rates in Chiu's experiments were beyond the laminar laminar region (i.e., $Re_b = 860$ vs 400). The laminar values of $\varepsilon^*_{1\eta}$ or C_{1L} of Chiu's bundle were estimated by extrapolating the data in the transition region to $Re_b \approx 400$. As for Chen's data, the corrected turbulent values for C_{1L} listed in Table 5.2 are used to calculate C_{mLT}. Table 5.3 lists the calculated results of C_{mLT} for these bundles.

Table 5.3 Available Data for C_{mLT}

Investigators	N_r	P/D	H/D	C_{mLT} for $\varepsilon^*_{1\eta}$	C_{mLT} for C_{1L}
Cheng*	37	1.154	13.4	~0.6	~0.6
Chiu(1978c)	61	1.067	4.0	~0.3	~0.3
	"	"	8.0	~0.3	~0.3
Chen(1974)	61	1.25	24.0	-	~0.68
	"	"	48.0	-	~0.63

* This work

Investigating C_{mLT} in Table 5.3, one finds that this parameter is an increasing function of P/D. The following correlation can satisfactorily fit these values as function of P/D.

$$C_{mLT} = 1.5(\frac{c}{D})^{0.6} \tag{5.38}$$

The laminar values of $\varepsilon^*_{1\eta}$ and C_{1L} can then be calculated from equation (5.38) and their corresponding turbulent values.

Equation (5.38) gives C_{mLT} a value from 0.3 to 0.7 as P/D varies from 1.067 to 1.25. The nominal value of C_{mLT} is around 0.5. This implies that the wire sweeping effect decreases as the flow changes from turbulent to laminar. Note that in the subchannel friction factor correlations, the parameter $\sqrt{W_{sL}/W_{sT}}$, which physically corresponds to C_{mLT}, was calibrated to be 0.55 by the friction factor data. Hence two sets of these correlations are consistent in modelling the hydraulic character for wire-wrapped rod bundles.

5.4.3 Empirical Constants in the Transition Regions: C_{m1tr} and C_{m2tr}.

In the transition region, the data show that the mixing parameters $\varepsilon^*_{1\eta}$ and C_{1L} increase as the Reynolds number increases. One can imagine that the wire sweeping effect gradually increases, starting from the value for laminar flow and ending at the value for turbulent flow. Therefore, the following form is formulated for these parameters in the transition region,

$$MP = MP_L + (MP_T - MP_L)\psi_i^{\lambda} \tag{5.39}$$

where MP = mixing parameter $\varepsilon^*_{1\eta}$ or C_{1L}

MP_L = MP in the laminar region

MP_T = MP in the turbulent region

ψ_i = intermittency factor defined in the subchannel friction factor models

$$\equiv \frac{\log (Re_i/Re_{iL})}{\log (Re_{iT}/Re_{iL})}$$

i = 1 for the interior region, i.e., for $\varepsilon^*_{1\eta}$

i = 2 for the edge region, i.e., for C_{1L}

λ = exponent fitted from the data

Note that the ψ_i^λ changes from 0 to 1 as Re_i changes from Re_{iL} to Re_{iT}. The subchannel Reynolds numbers, Re_i's are calculated from the flow split correlation developed in Chapter 4.

By matching the transition data of our 37-pin results and Chiu's two 61-pin results, a value of 2/3 for λ was found to be optimum. The empirical constants C_{m1tr} and C_{m2tr} are then

$$C_{mitr} = C_{miL} + (C_{miT} - C_{miL})\psi_i^{2/3} \qquad (5.40)$$

where i = 1 for $\varepsilon^*_{1\eta}$

= 2 for C_{1L}

Figures 5.9 and 5.10 compare the calculated $\varepsilon^*_{1\eta}$ and C_{1L} and the data for our 37-pin bundle, respectively. Similar comparisons are illustrated in Figures 5.11 and 5.12 for $\varepsilon^*_{1\eta}$ and C_{1L} for Chiu's

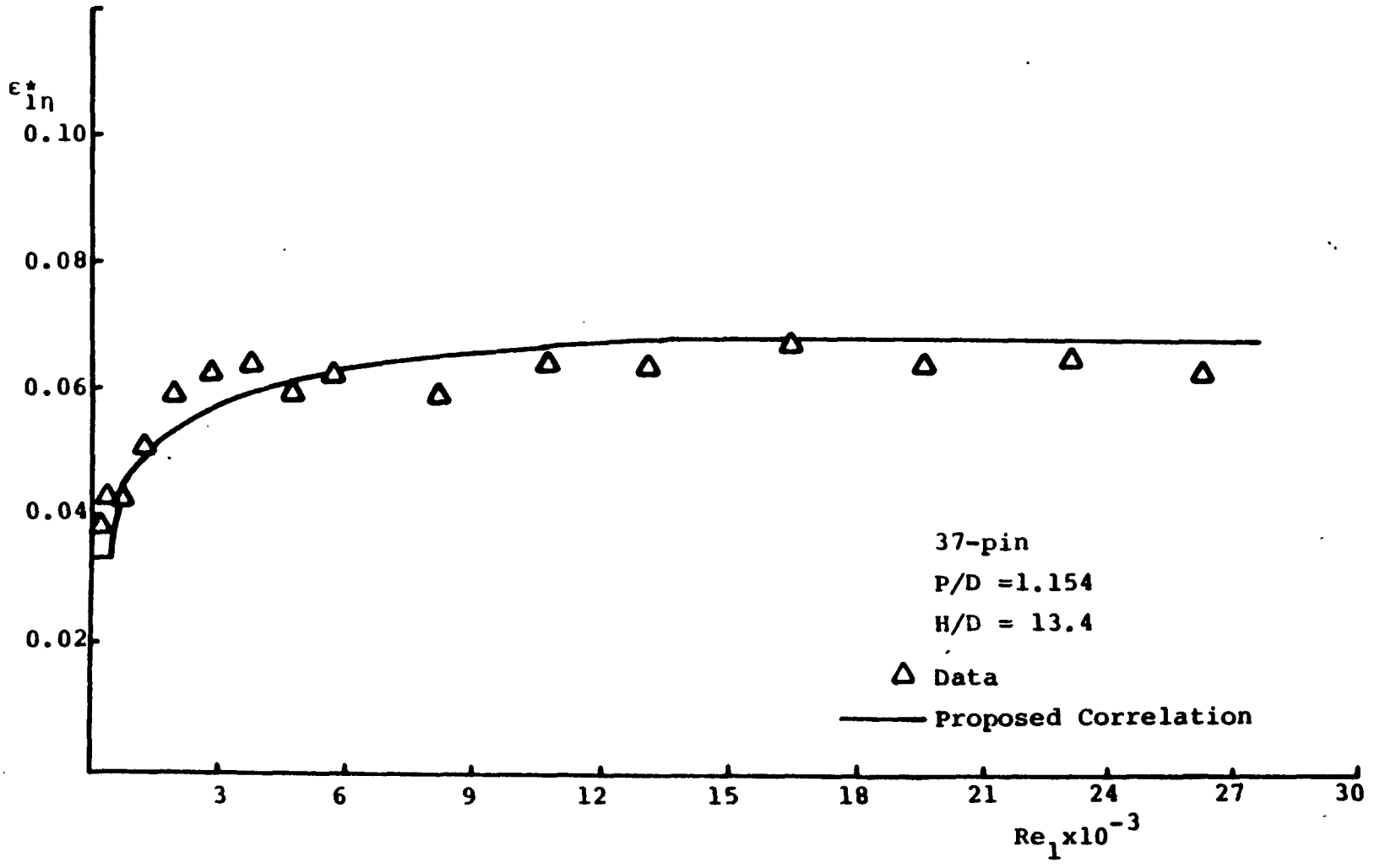

Figure 5.9 Comparison between Proposed Correlation and Data for $\varepsilon^*_{1\eta}$ of 37-pin Results

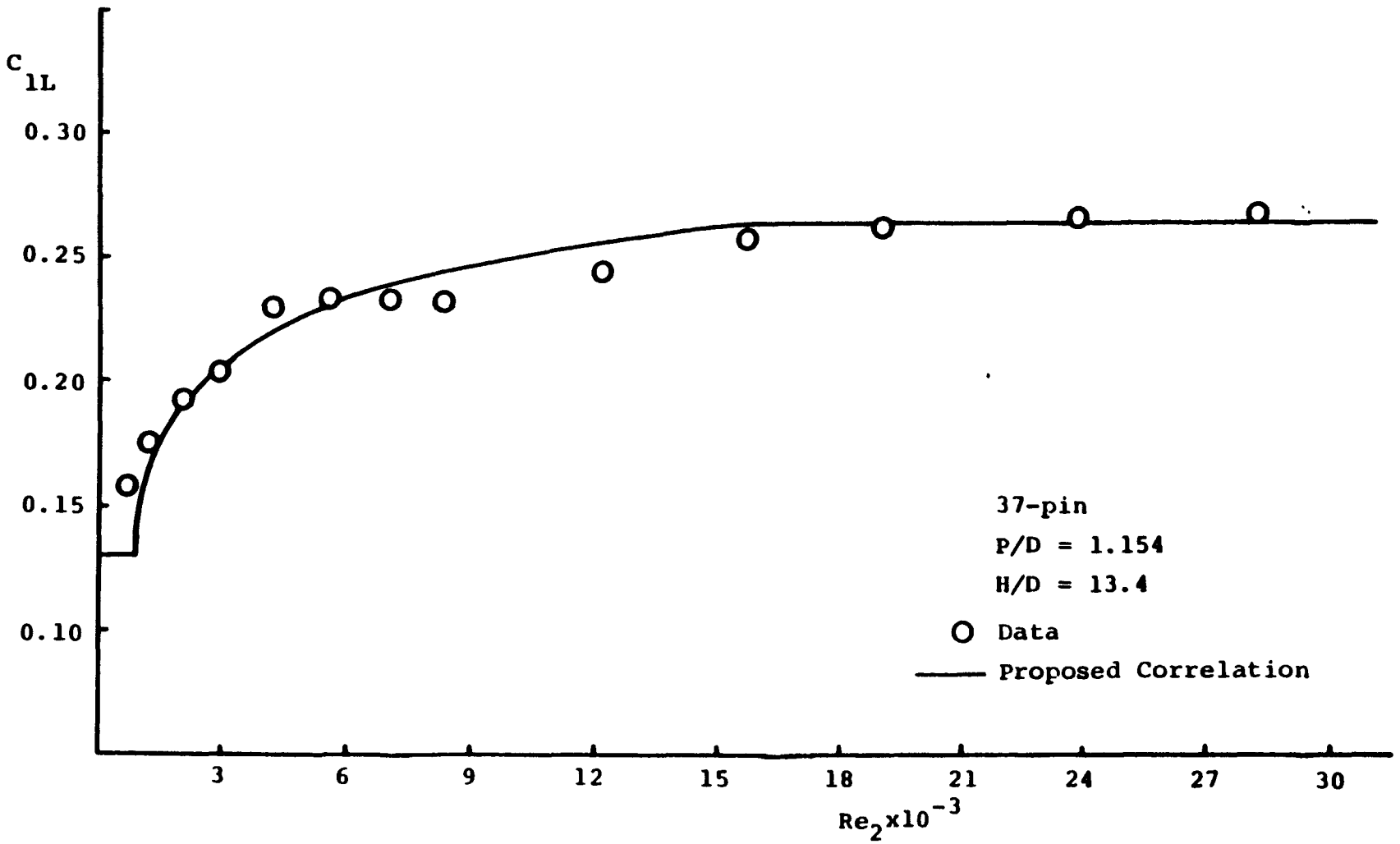

Figure 5.10 Comparison between Proposed Correlation and Data for C_{1L} of 37-pin Results

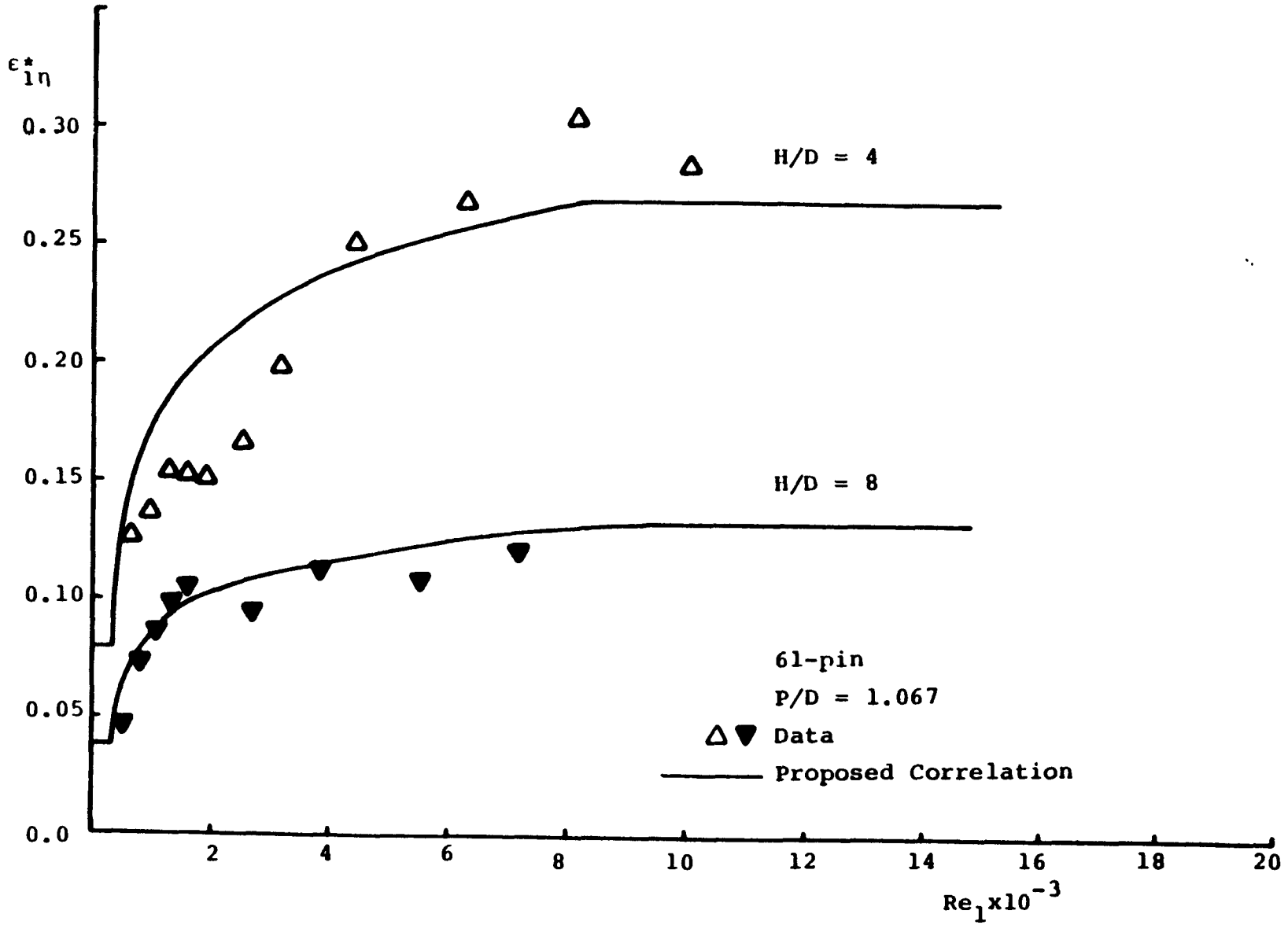

Figure 5.11 Comparison between Proposed Correlation and Data for $\varepsilon^*_{1\eta}$ of 61-pin Results

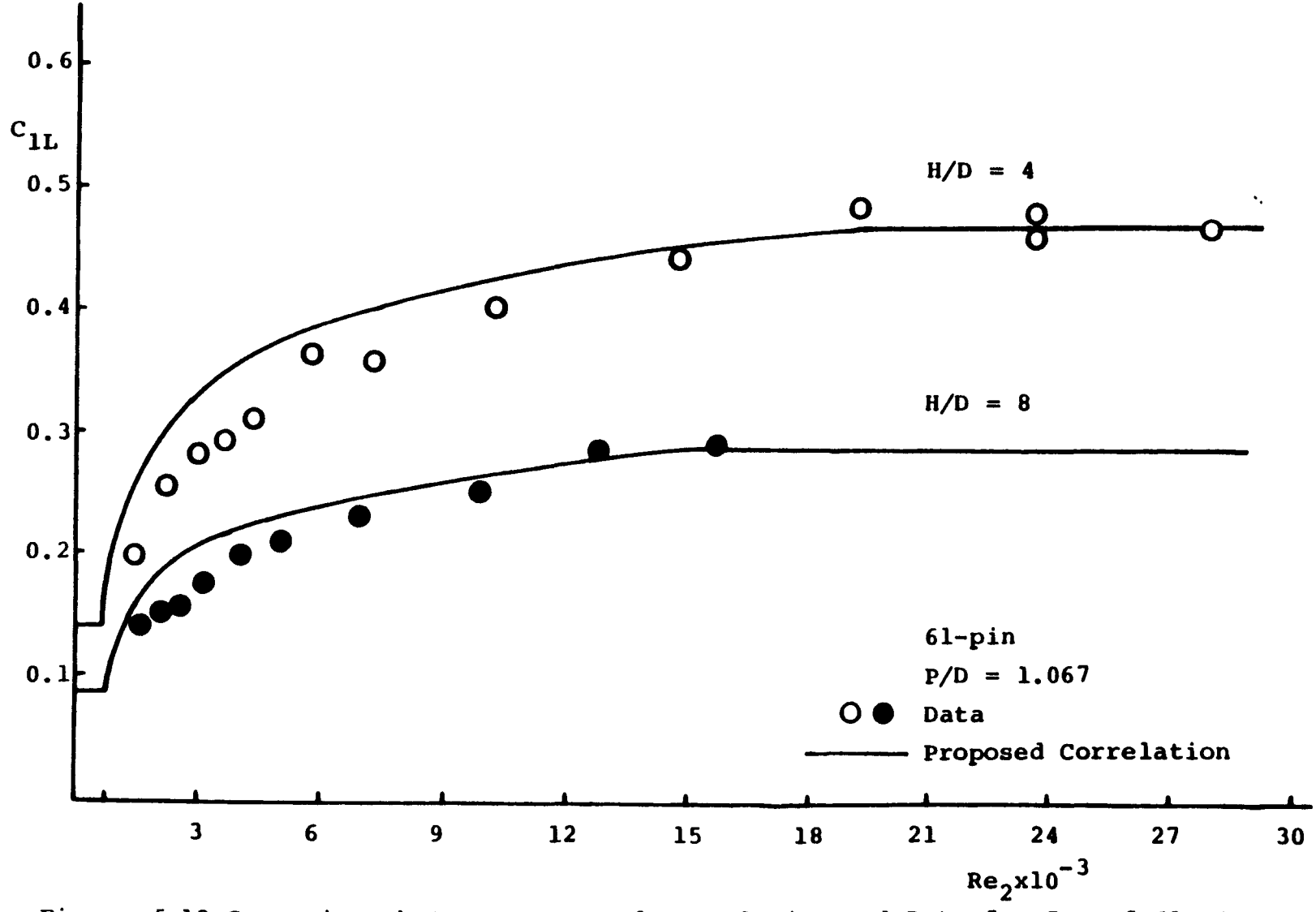

Figure 5.12 Comparison between Proposed Correlation and Data for C_{1L} of 61-pin Results

results, respectively. The trend of our 37-pin results is excellently predicted by this proposed correlation. For $\varepsilon^*_{l\eta}$, fairly good prediction is found for Chiu's H/D = 8 bundle, while overprediction is found for his H/D = 4 bundle. For C_{lL}, the correlation overpredicts all Chiu's data about 15%. Considering the error associated with these data (±20%), we conclude that this correlation can satisfactorily predict $\varepsilon^*_{l\eta}$ and C_{lL} in the transition region.

5.5 Correlation for Conduction Shape Factor, κ

5.5.1 Introduction

The conduction shape factor (SF) discussed in Chapter 2 is defined by equation (2.11),

$$\kappa_{ij} \equiv \frac{\eta_{ij}}{\ell_{ij}}$$

where ℓ_{ij} is the molecular mixing length defined in equation (2.10). In the literature, however, another parameter L_{ij} defined as

$$L_{ij} \equiv \frac{\ell_{ij}}{\eta_{ij}} = \frac{1}{\kappa_{ij}} \tag{5.41}$$

is often used. Since the investigation of SF by either theoretical or experimental study is in itself a large effort, we did not perform these studies in our work. Instead, the available results of SF from literature will be reviewed. By using these results, a correlation for conduction shape factor is recommended. Note that all investigations

described in the next section are for bare rod case only. In turbulent flows the shape factor effect is small compared to the wire driven effective eddy diffusivity. Since the wires will strongly influence the velocity and temperature fields, the importance of the bare rod shape factor results to the wire-wrapped rod bundle is probably limited to the transition or laminar region. However, under these low flow conditions at typical heat fluxes, thermal plume effects appear to induce significant mixing. Further, flow redistribution effects transport significant energy. Therefore, the importance of the shape factor is wire wraped bundles is probably restricted to $Gr_{\Delta T}/Re_b$ envelope. The correlation for shape factor is discussed in Chapter 8 of report 108TR in conjunction with a proposed correlation for the enhancement of the effective eddy diffusivity. Both correlations are tested in Chapter 8 and flow redistribution effects are also assessed against available sodium cooled bundle data.

5.5.2 Conduction Shape Factor in the Literature

France and Ginsberg (1973, 1974) performed an analytical study to investigate the utility and accuracy of the lumped parameter approach to heat transfer analysis in a nuclear reactor subassembly. They found that the molecular mixing lengths are geometry-dependent only. They are shown to be independent of radial power distribution across the subassembly, and asymptotic values which are equal to length scales corresponding to the thermally fully developed condition may be used in the thermally developing entry region which encompasses the entire

axial length of typical nuclear reactor assemblies. Both unheated and heated rod cases for triangular rod arrays were investigated.

Ramm et al. (1974, 1975) investigated thermal mixing flowrates and length scales for pure molecular conduction as well as simultaneous conductive and turbulent intersubchannel transport in triangular rod arrays for unheated and heat rods cases, respectively. They concluded that mixing parameters are only slightly affected by variations in initial and boundary conditions.

Yeung and Wolf (1980) developed an analytical method to determine the theoretical effective mixing length for subchannels in a hexagonal rod bundle. The results showed that the effective mixing length in a strong function of P/D. However, for one P/D, it appears that the asymptotic (fully developed) value of the effective mixing lengths of various subchannel pairs are so close that they can be approximated by a single characteristic value for most practical purposes. By this conclusion, we assume that for one P/D, $\kappa_{11} = \kappa_{12} = \kappa_{22} = \kappa_{23} = \kappa$, i.e., only one κ is used for all kinds of subchannel pairs.

In addition to those theoretical results, Fakuda (1979) performed an electrostatic analog simulation for a single region analysis. He proposed an empirical relation for the mixing length of conduction,

$$\frac{\ell_{ij}}{\eta_{ij}} = \frac{1}{\frac{1.38}{\sqrt{3}} \left(\frac{P-D}{D}\right)^{0.674} \left(\frac{P}{P-D}\right)} \qquad (5.42)$$

Table 5.4 lists the theoretical results of L_{ij} from above investigators for two boundary conditions: heated and unheated rod (plane source) cases as well as Fakuda's correlated value from equation (5.42).

Table 5.4 Theoretical Results for asymptotic

(fully developed)

$$L_{ij} \equiv \frac{\ell_{ij}}{\eta_{ij}}$$

P/D	France & Ginsberg(1973) unheated (plane source)	heated	Ramm et al. (1973) unheated (plane source)	Ramm et al. (1975) heated	Young & Wolf (1980) heated	Fukuda (1979)
1.05	-	-	0.508	0.56	-	0.45
1.08	-	-	-	-	0.69	0.51
1.10	0.628	-	0.590	0.66	-	0.54
1.20	0.697	0.783	0.652	-	-	0.62
1.24	-	-	-	-	0.80	0.636
1.30	0.717	0.817	0.676	0.79	-	0.652

5.5.3 Recommended Correlation for Conduction Shape Factor

Since the velocity and temperature solutions are dependent upon boundary conditions and initial conditions, it should be expected tht molecular mixing length similarly depend on these conditions. In our application for calculating temperature distribution for LMFBR subassembly, the value from heated rod case solution should be used.

Figure 5.13 illustrates L_{ij} listed in Table 5.4 as function of P/D. For the heated rod boundary condition cases, there L_{ij}'s can be fitted similar to equation (5.42) as

$$\frac{1}{L_{ij}} = \kappa = 0.66 \left(\frac{P}{D}\right)\left(\frac{c}{D}\right)^{-0.3} \tag{5.43}$$

Equation (5.43) gives a value of κ varying from 1.25 to 2.0 as P/D varies from 1.25 to 1.025.

5.6 Summary of the Mixing Parameter Correlations

The correlations for the mixing parameters in the forced convection condition, $\varepsilon^*_{1\eta}$, $\varepsilon^*_{2\eta}$, C_{1L}, and κ have been developed in this chapter. In summary,

$$\varepsilon^*_{2\eta} = 0.01$$

$$\varepsilon^*_{1\eta} = C_{m1} \left(\frac{A_{r1}}{A'_1}\right)^{1/2} \tan\theta \tag{5.32}$$

where C_{MIT} is given by equations 3.35a and b and $[\varepsilon^*_{1\eta}]_{laminar}$ is given in terms of $[\varepsilon^*_{1\eta}]_{turbulent}$ by equations 5.37 and 5.38.

$$C_{lL} = C_{m2} \left(\frac{A_{r2}}{A_2'}\right)^{1/2} \tan\theta \qquad (5.33)$$

where C_{M2T} is given by equations 5.36a and b and $[C_{lL}]_{laminar}$ is given in terms of $[C_{lL}]_{turbulent}$ by equations 5.37 and 5.38 and transition regime values for C_{mi} are given by equation 5.40. Finally K is given by equation 5.43.

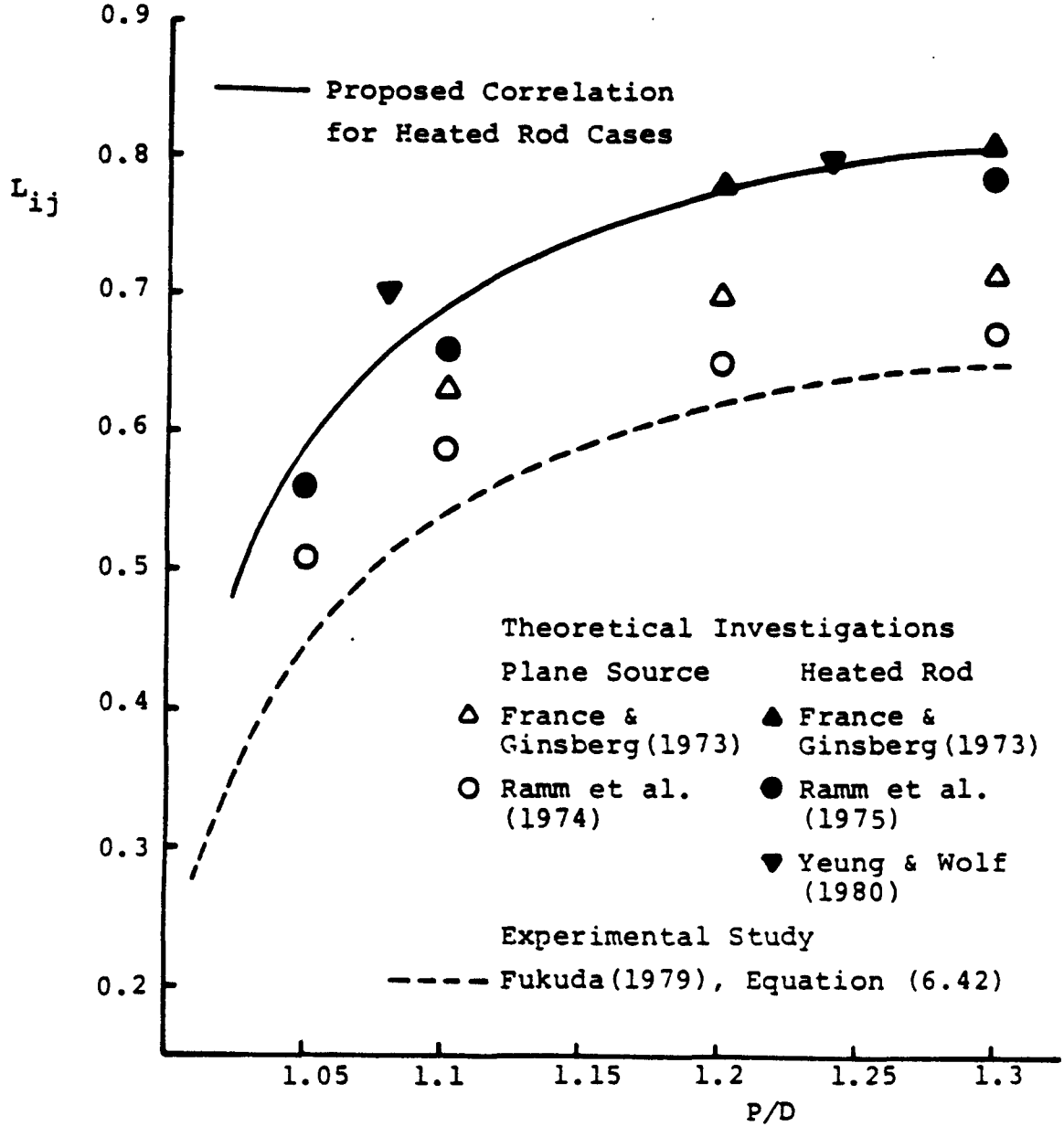

Figure 5.13 Available Investigations and Fitting Result for Conduction Shape Factor $\kappa \equiv L_{ij}$

where

for the turbulent region ($Re_b > Re_{bT}$)

$$N_r \geq 19$$

$$C_{m1T} = 0.14\left(\frac{c}{D}\right)^{-0.5}$$

$$C_{m2T} = 0.75\left(\frac{H}{D}\right)^{0.3}$$

$$N_r = 7$$

$$C_{m1T} = 0.1\left(\frac{c}{D}\right)^{-0.5}$$

$$C_{m2T} = 0.6\left(\frac{H}{D}\right)^{0.3}$$

for the laminar region ($Re_b \leq Re_{bL}$)

$$C_{miL} = 1.5\left(\frac{c}{D}\right)^{0.6} C_{miT}$$

for the transition region

$$C_{mitr} = C_{miL} + (C_{miT} - C_{miL})\psi_i^{2/3}$$

and

$$\kappa = 0.66\left(\frac{P}{D}\right)\left(\frac{c}{D}\right)^{-0.3}$$

The above correlations can predict the data within ±25% for $\epsilon^*_{1\eta}$ and ±15% for C_{1L} in the following geometrical ranges,

$$7 \leq N_r \leq 217$$

$$1.067 \leq P/D \leq 1.317$$

$$4 \leq H/D \leq 52$$

$$400 \leq Re_b \leq 10^6$$

Chapter 6

Experimental Technique Development

A large number of test bundles as listed in Table 6.1 were used in this project to develop the data needed to formulate the input parameter correlations. These data included pressure drop, flow split and outlet channel salt conductivity measurements. The techniques developed and refined for these measurements are discussed in reports 77TR, 80TR and 62TR respectively. All measurements were made in water and supplemented the large bank of sodium temperature measurements made in other facilities.

The pressure measurements were made in subchannels through fuel rod taps built primarily to inject salt solution. Duct static pressure measurements were also made. Flow split measurements were made by an isokinetic extraction procedure developed with considerable effort in a number of theses. This method becomes inapplicable as the channel flow velocity decreases so that errors involved in the laminar flow split data are large. In our later work under a followup contract, a hot wire anemometer has been used successfully in this low velocity, laminar flow region.

Salt injection techniques were developed for use in the turbulent regime as an analogy to heated pin experiments. Since the salt was injected as a point versus line source, this approach gives a sensitive indication of bundle hydrodynamic behavior. Significant care is necessary to select the optimum depth of injection as discussed in the

Table 6.1 Experiments Performed at MIT

Student	Report	Nr	P/D	H/D	Measurements	Comment
Chen and Ip	11 TR	61	1.25	24.48	Edge axial and Transverse Velocities	by Laser Dopler Anemometer
Hanson	51 TR	61	1.24	24.48	Pressure drop flow split and salt concentration	revised later by Symolon (51TR)
Chiu	41, 42, 43 TR	61	1.067	4.8	flow split, pressure drop and salt concentration	revised later by Cheng (108TR)
Chiu and Burn	SM Thesis	37	1.15	21.0	flow split, pressure drop and salt concentration	data flawed by bundle distortions
Wang	86 TR	61	1.067	8	flow split, pressure drop and salt concentration	Wire shaved to half diameter in the edge region
Symolon	84 TR	217	1.25	52.0	flow split, pressure drop and salt concentration	edge region only
Cheng	108 TR	37	1.154	13.4	flow split, pressure drop and salt concentration	

reports reporting bundle tests cited in Table 6.1.

The conditions under which salt conductivity testing is a valid analogy to heated pin testing is an important point, this question is discussed next.

The main purpose of the salt injection experiment is to simulate the coolant energy mixing process in an LMFBR bundle and to provide quantitative results for this process. The experiments employ water in place of sodium coolant. The geometrical characteristics of our bundle are similar to those of an LMFBR bundle. The question of the applicability of the mixing parameters based on salt injection into water experiments to the sodium energy mixing process has been investigated by Chiu (43TR). To investigate this question, we consider the two step process: salt mixing to heat mixing in water followed by heat mixing in water to heat mixing in sodium. Therefore, successful simulation primarily depends on the following conditions:

a) similarity between salt mixing and heat mixing due to eddy and wire sweeping effects only of a wire-wrapped subassembly in a water loop.

b) Similarity of heat mixing in water and in sodium for a given wire-wrapped bundle.

These two similarities will be investigated in this section.

From the definition of C_{1L} and $\varepsilon^*_{1\eta}$ in chapter 2, one realizes that C_{1L} represents the ratio of the actual average transverse flow rate to the average axial flow rate in the edge region while $\varepsilon^*_{1\eta}$

represents the combination of effects of turbulent interchange, W'_{ij}, which includes eddy effects only, and wire sweep flow, W'^{W}_{ij} on energy transfer between subchannels. This sweep flow is physically the lateral flow between subchannels. For a given bundle, working fluid (water) and flow condition, the edge transverse flow and the interior wire sweeping flow bear the same value for both salt mixing and heat mixing. Further, if one assumes that W'_{ij} for mass interchange equals that for heat interchange, similarity condition (a) above is easy to confirm since the salt diffusion is negligible in comparison with the total mixing (about 10^{-4} from [Chiu (43TR)]), i.e.,

$$\text{effects of diffusion} + W'_{ij} \text{ for mass} + W'^{W}_{ij} \text{ for mass}$$

$$= W'_{ij} \text{ for heat} + W'^{W}_{ij} \text{ for heat}$$

Similarity condition (b) will be investigated in detail here employing a revision of Chiu's argument. Since the velocity field in forced convection, is independent of the temperature field, it can be determined by solving the mass and momentum equations only. In nondimensional form, these equations are

$$\text{mass} \qquad \nabla^* v^* = 0 \tag{6.1}$$

$$\text{momentum} \qquad (v^* \cdot \nabla^*)v^* = -\nabla^* P^* + \frac{1}{Re} \nabla^{*2} v^* \tag{6.2}$$

where $v^* \equiv \frac{v}{U} = \frac{\rho v De}{Re \mu}$ for a given Reynolds number

where $U \equiv$ characteristic velocity and $Re \equiv \frac{\rho U De}{\mu}$

$v \equiv$ velocity vector

$$P^* \equiv \frac{P}{\rho u^2}$$

$$V^* \equiv DeV$$

De ≡ characteristic length, usually equivalent hydraulic diameter

The only dimensionless parameter which appears in these two equations is the Reynolds number. Consequently, if this parameter is the same for the water and the sodium flow, the solution of v^* in both cases is the same. Therefore at a given bundle and a given Re, the parameter $(\rho v/\mu)$, where v represents a velocity vector, has the same value for both cases. This leads to the conclusion that C_{1L} and (W'^{W}_{ij}/μ) are the same for both cases because C_{1L} equals to V_T/V_A and W'^{W}_{ij} can be written as

$$W'^{W}_{ij} = \rho s_{ij} \bar{V}_T \tag{6.3}$$

where s_{ij} = the gap between rods

V_T = transverse velocity at the gap

$$\bar{V}_T = \frac{1}{H}\int_0^{H/2} V_T dz,$$

The quantitative difference between $[\varepsilon^*_{1\eta}]_{Na}$ and $[\varepsilon^*_{1\eta}]_{H_2O}$ can be represented in terms of a simulation error (S.E.)

$$S.E. = \frac{[\varepsilon^*_{1\eta}]_{H_2O} - [\varepsilon^*_{1\eta}]_{Na}}{[\varepsilon^*_{1\eta}]_{Na}} \tag{6.4}$$

From its definition,

$$\epsilon^*_{ln} = \frac{(W'_{ij} + W'^{W}_{ij})/s_{ij}}{\rho V_A}$$

$$= \frac{1}{Re}\left(\frac{De}{s_{ij}}\right)\left(\frac{W'_{ij}}{\mu} + \frac{W'^{W}_{ij}}{\mu}\right) \qquad (6.5)$$

Substituting equation (6.5) into equation (6.4) and using the identity, $[W'^{W}_{ij}/\mu]_{H_2O} = [W'^{W}_{ij}/\mu]_{Na}$, we get:

$$S.E. = \frac{\left[\frac{W'_{ij}}{\mu}\right]_{H_2O} - \left[\frac{W'_{ij}}{\mu}\right]_{Na}}{\left[\frac{W'_{ij}}{\mu}\right]_{Na} + \left[\frac{W'^{W}_{ij}}{\mu}\right]_{H_2O}} \qquad (6.6)$$

Ramm and Johannsen (1975) proposed a theoretical correlation for (W'_{ij}/μ) as a function of geometry, Reynolds number and Prandtl number. Using this correlation Figure 6.1 was constructed to illustrate $(W'_{ij}/\mu)/(W'_{ij}/\mu)_{Pr=3}$ as a function of Pr for P/D = 1.15 bundle at $Re = 10^4$ and 10^5. The parameter (W_{ij}/μ) decreases as Pr decreases. For water, Pr≈3, while for sodium, Pr≈0.004, hence from this figure we have

$$\text{at } Re = 10^4 \qquad \left[\frac{W'_{ij}}{\mu}\right]_{Na} \approx 0.1\left[\frac{W'_{ij}}{\mu}\right]_{H_2O} \qquad (6.7a)$$

$$Re = 10^5 \qquad \left[\frac{W'_{ij}}{\mu}\right]_{Na} \approx 0.3\left[\frac{W'_{ij}}{\mu}\right]_{H_2O} \qquad (6.7b)$$

The simulation error of equation (6.6) can be bounded by utilizing equation (6.7a) and neglecting the quantity $\left[\frac{W'_{ij}}{\mu}\right]_{Na}$ in the denominator, i.e.,

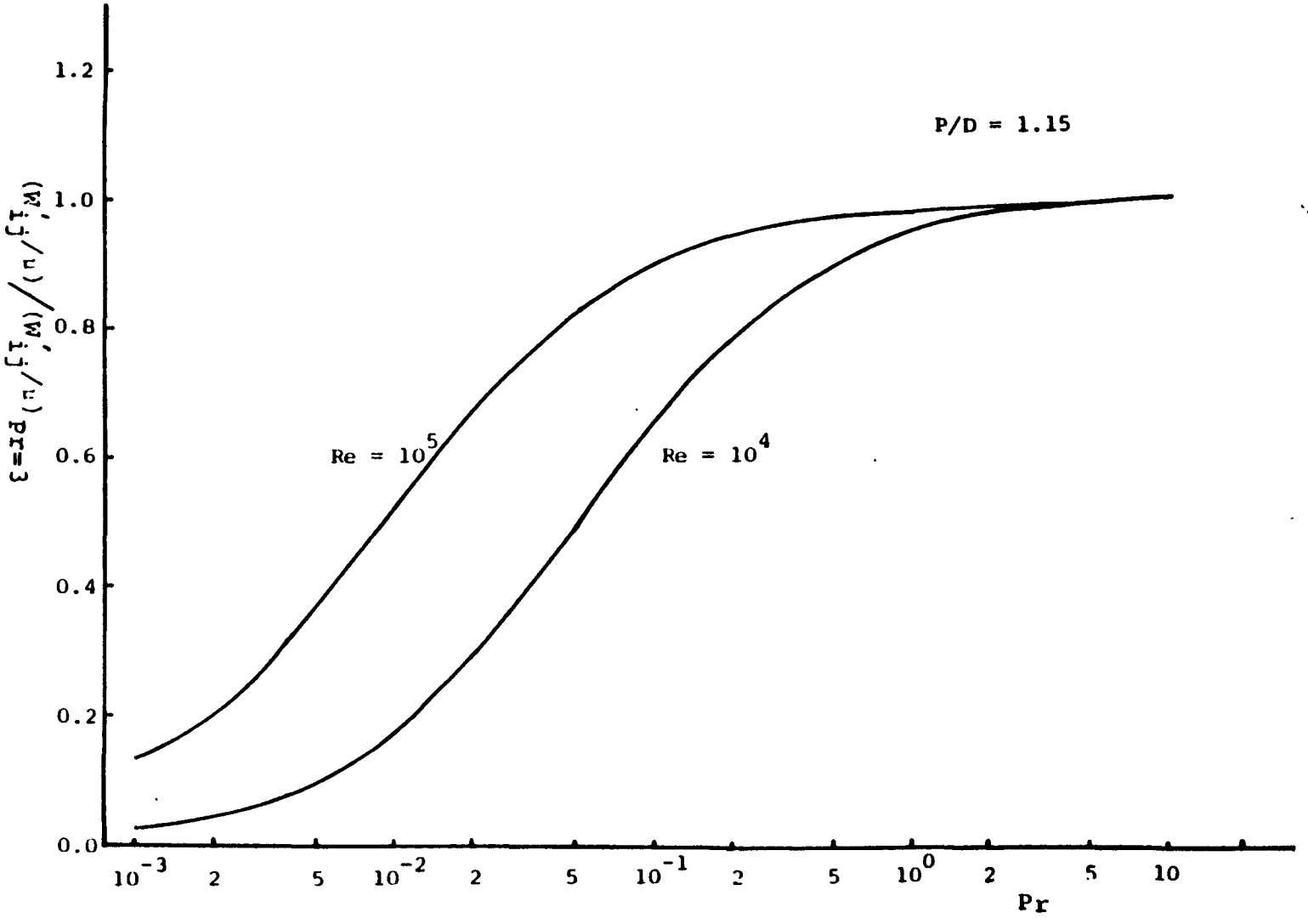

Figure 6.1 Turbulent Mixing Parameter (W'_{ij}/μ) from Ramm et al. Correlation

$$\text{S.E.} \leq \frac{0.9\left[\frac{W'_{ij}}{\mu}\right]_{H_2O}}{\left[\frac{W'^{W}_{ij}}{\mu}\right]_{H_2O}} = \frac{0.9\left[W'_{ij}\right]_{H_2O}}{\left[W'^{W}_{ij}\right]_{H_2O}} \tag{6.8}$$

Equation (6.8) shows that the similarity between $\left[\varepsilon_{l\eta}^{*}\right]_{H_2O}$ and $\left[\varepsilon_{l\eta}^{*}\right]_{Na}$ holds under the condition that $\left[W'^{W}_{ij}\right]_{H_2O}$ is much larger than $\left[W'_{ij}\right]_{H_2O}$ so that the mismatch between $\left[W'_{ij}/\mu\right]_{Na}$ and $\left[W'_{ij}/\mu\right]_{H_2O}$ can be neglected. As will be discussed in the next chapter $\left[W'_{ij}\right]_{H_2O}$ is around 10 % of $\left[W'^{W}_{ij}\right]_{H_2O}$, hence the S.E. of the mixing parameter $\varepsilon_{l\eta}^{*}$ reduced from salt injection experiment is about 9%.

CHAPTER 7

The ENERGY-IV CODE

7.1 Structure of the ENERGY-IV code

A new version of the ENERGY series code, ENERGY-IV, was written for predicting coolant temperature distributions in wire-wrapped rod assemblies used in the Liquid Metal Fast Breeder Reactor. The ENERGY-IV Code is applicable to both steady-state forced and mixed convection operation for a single isolated assembly. (The SUPERENERGY Code, [Basehore (57TR)] is applicable to core wide forced convection analysis.) ENERGY-IV is an empirical code designed to be fast running. Hence the core designer can use it as an inexpensive thermal hydraulic design or diagnosis tool.

The main structure of the ENERGY-IV is similar to the old versions, ENERGY-I, II, III; however, most of the statements have been revised. Figure 7.1 depicts the flow chart for ENERGY-IV, in which the names of the subroutines are identified. Figure 7.2 briefly describes the structure of the subroutines and their functions. Because of the implementation of the subroutine NUMB, (originally developed by Basehore (1980)), which assigns the subchannel and rod scheme in a hexagonal assembly, the code automatically generates the noding and connection logic. This dramatically simplifies the required input information. Figure 7.3 shows the rod identification number assigned by the subroutine NUMB for a 61-pin bundle. The subchannel identification number was shown in Figures 3.17 and 5.12 of Report 108TR for 37-pin and 61-pin bundles, respectively. The correlations for the required forced

Figure 7.1 Flow Chart for the ENERGY-IV

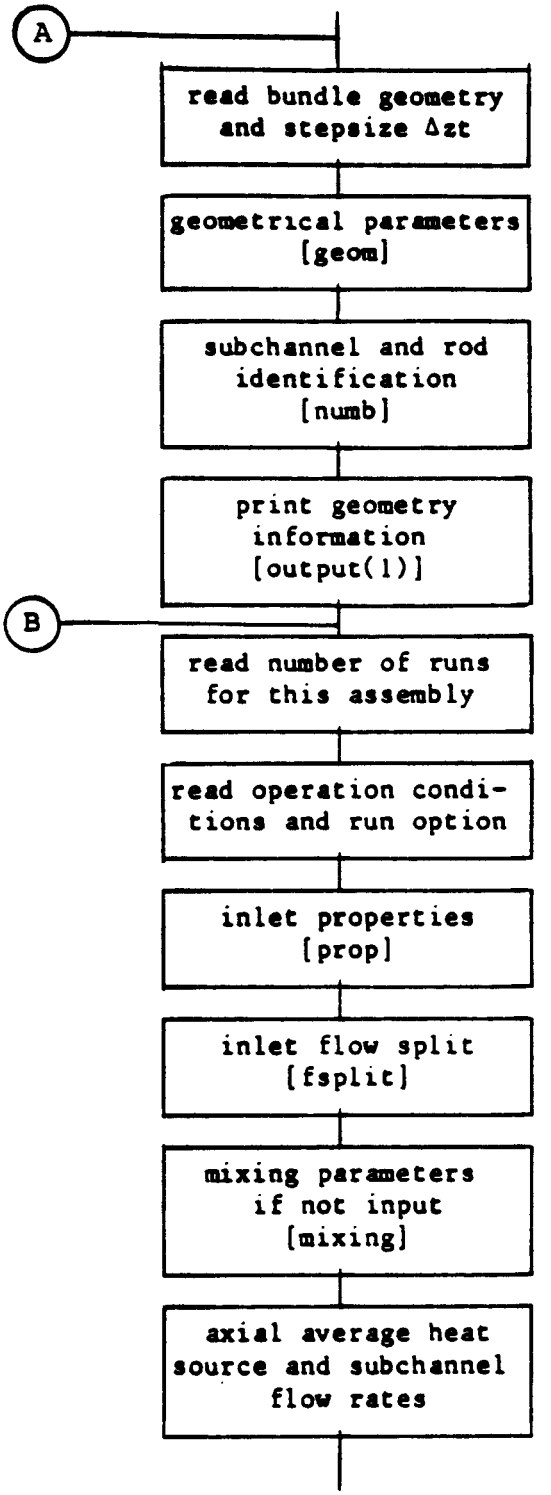

Figure 7.1 Continued

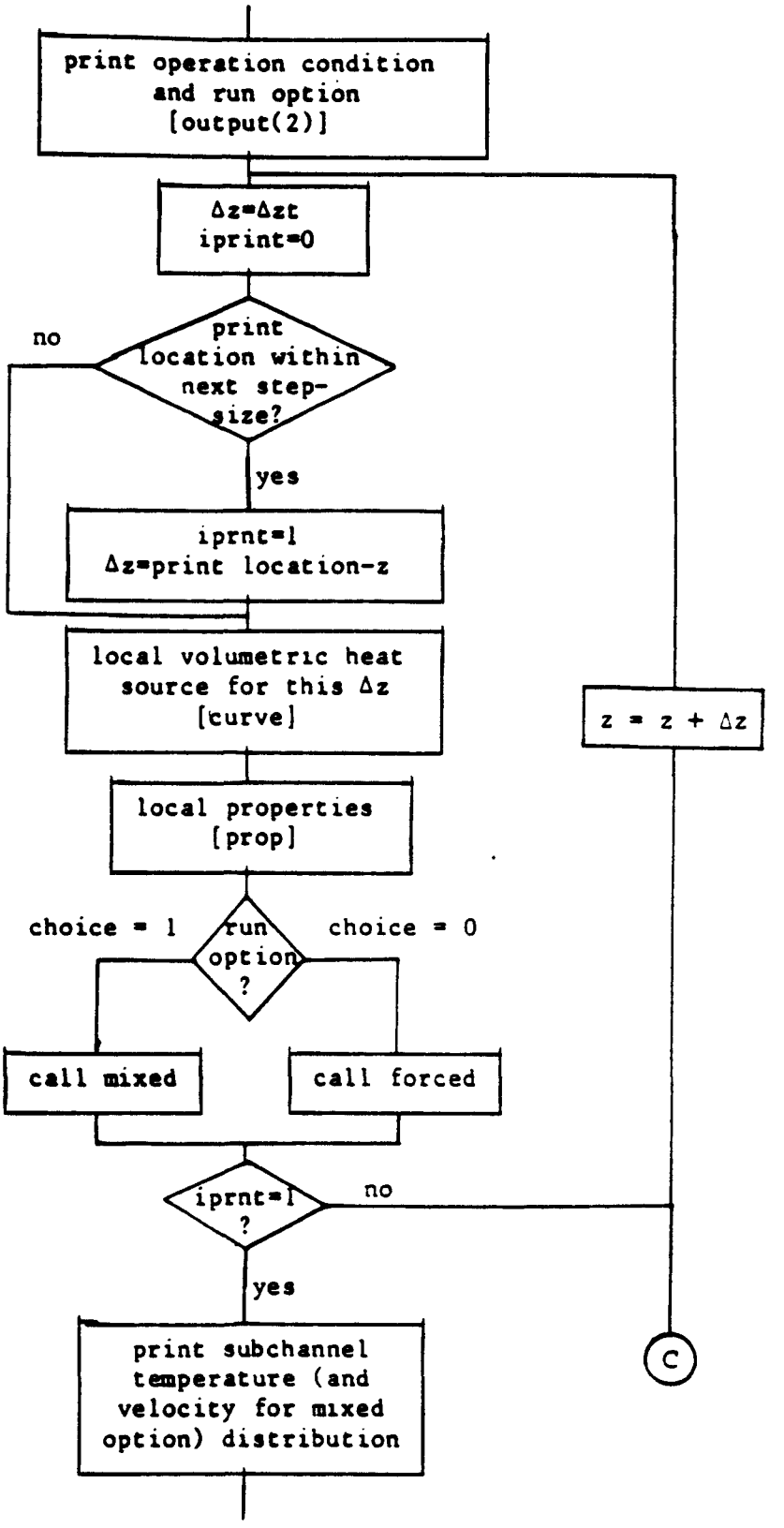

Figure 7.1 Continued

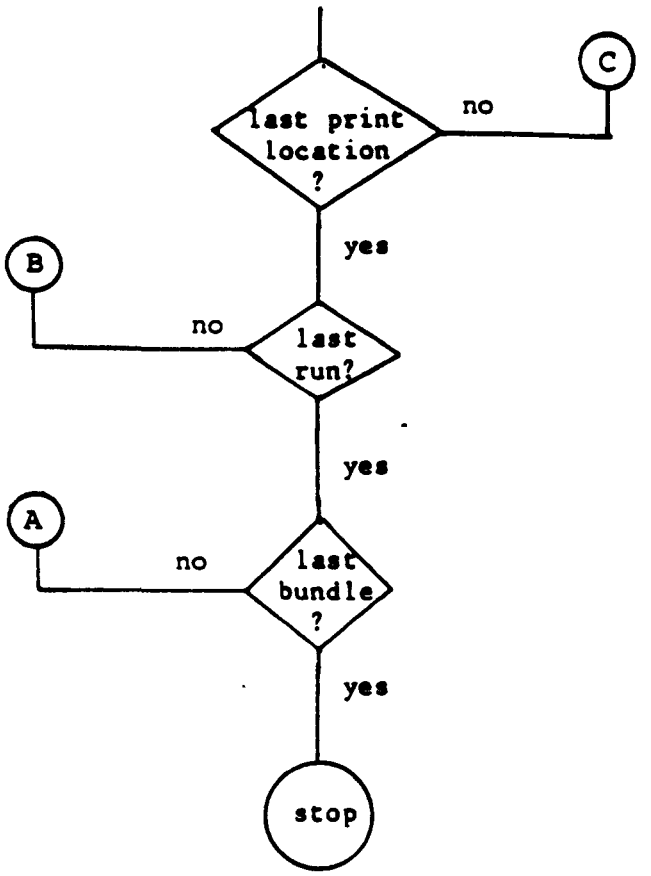

Figure 7.2 Functions of the Subroutines in ENERGY-IV

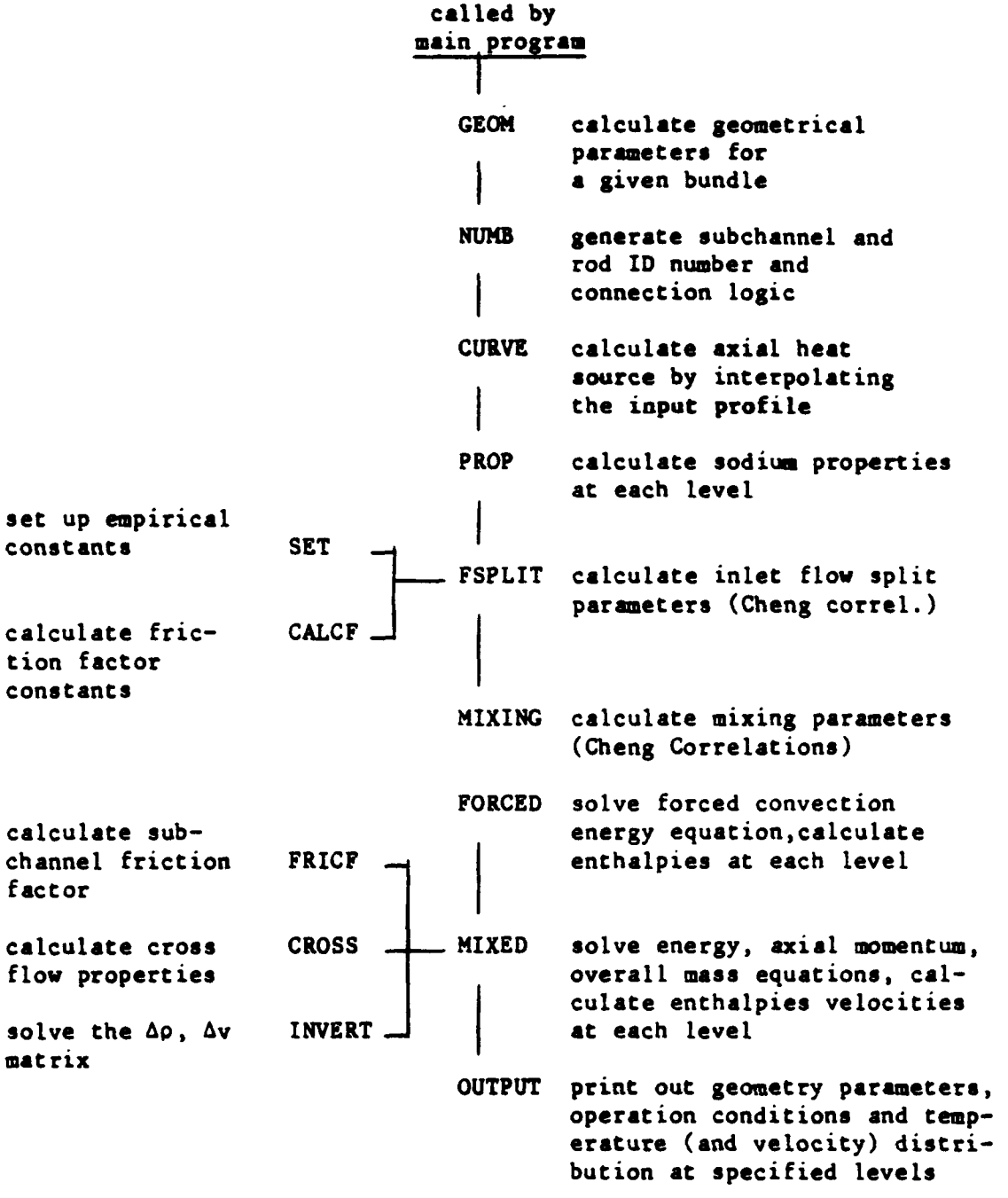

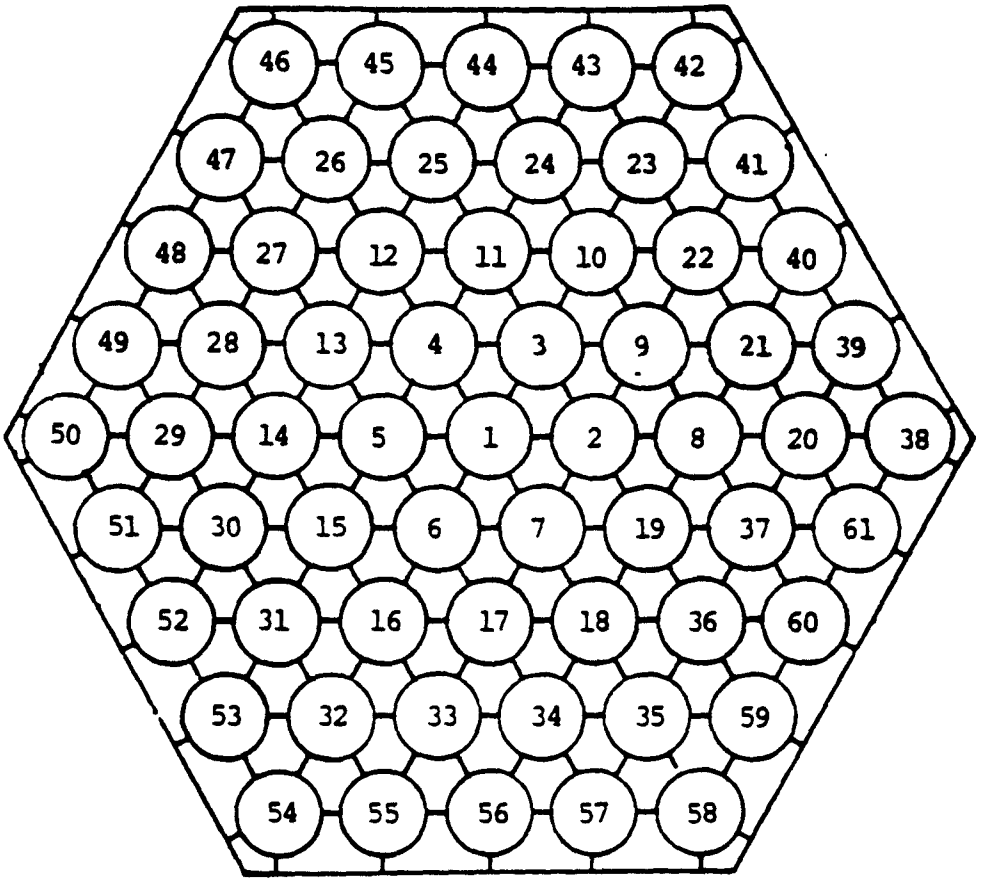

Figure 7.3 Rod Identification Number Assigned by Subroutine NUMB

convection input parameters: flow split parameters (X_i), subchannel friction factors (f_i), and mixing parameters ($\varepsilon^*_{1\eta}$, $\varepsilon^*_{2\eta}$, C_{1L} and κ) developed in Chapter 4 and Chapter 6 of report 108TR were implemented in the subroutines FSPLIT, FRICF and MIXING, respectively. Additionally, the correlation for the enhanced mixing due to thermal plumes (ε^*_η) developed in Chapter 8 of Report 108TR was implemented in the main program. The sodium properties at each level are calculated by the subroutine PROP.

The subroutines FORCED and MIXED are formulated according to the different equations derived in Chapter 2 for the forced convection condition and the mixed convection condition, respectively. They solve the subchannel enthalpies (and velocities for the mixed convection option) at each axial level. The calculation results are printed out at the user specified levels. Appendix D1 of Report 108TR describes the input format for ENERGY-IV and Appendix D2 of Report 108TR lists this code.

In the next two sections, the numerical methods used for the forced and mixed convection option will be discussed.

7.2 Numerical Method for the Forced Convection Option

A numerical marching scheme is used to solve the forced convection energy equations. For each axial step, the enthalpies on the right hand side of equations (2.34), (2.35), and (2.36) are evaluated at the node inlets. The enthalpy rise for each subchannel over the axial step may then be computed explicitly. This explicit method eliminates the need for a simultaneous solution. As a result, a substantial reduction in computational storage and running time is possible when compared to implicit formulations.

The disadvantage of this explicit method is that the axial node length size is stablity limited. The right hand side of equations (2.34), (2.35) and (2.36) must remain positive in the most limiting case, since the coolant enthalpy should never be negative. This limiting case occurs when the heat generation term is zero and when h_i, h_j and h_k are small compared to h_n ($n = 1, 2, 3$). For an interior subchannel, this criterion becomes

$$0 < h_1(z + \Delta z) = h_1 - \Delta z\left(\frac{C}{A_1}\right)\left[\frac{\kappa\alpha}{v_1 \eta_{11}} + \varepsilon^*_{1\eta}\right](-3h_1) \tag{7.1}$$

The conduction term in equation (7.1) can be further expressed as

$$\frac{\kappa\alpha}{v_1 \eta_{11}} = \frac{1}{Re_b}\left[\left(\frac{De_b}{\eta_{11}}\right)\left(\frac{\kappa}{X_1}\right)\frac{1}{P_r}\right] \equiv \frac{K^*_1}{Re_b} \tag{7.2}$$

therefore,

$$\Delta z < \frac{1}{3\left(\frac{c}{A_1}\right)\left[\frac{K^*_1}{Re_b} + \varepsilon^*_{1\eta}\right]} \tag{7.3}$$

Equation (7.3) shows that the limiting Δz is dependent upon Re_b: as Re_b decreases, the maximum allowable Δz decreases. Quantitatively, for $Re_b = 1000$, the limiting Δz is about 0.5 inch. Since the Re_b for most forced convection cases are higher than 1000, 0.5 inch is sufficient and recommended for the axial stepsize. For $1000 > Re_b > 500$, a stepsize of 0.25 inch is recommended.

The running time of the ENERGY-IV code for the forced convection option for a 61-pin bundle with around 100 axial nodes is less than 2 seconds in an IBM-370 computer.

7.3 Numerical Method for the Mixed Convection Option

The mixed convection option solves the energy, axial momentum and mass conservation equations simultaneously as discussed in chapter 2. A marching scheme is also employed in this option. The conservation equations for any subchannel contain three unknowns $\Delta\rho$, Δv, and ΔP. The pressure is assumed to be a constant in the transverse direction at any axial level. Thus for an N-channel problem, there exist 2N + 1 unknowns (N $\Delta\rho$'s, N Δv's, and one ΔP) with 2N + 1 equations. Figure 7.4 illustrates the equations and unknowns in matrix form for a 3-channel problem. (c.f. equations (2.47) and (2.48)). Note that the unknowns $\Delta\rho_i$ and Δv_i appear within the coefficient matrix. The quantities ρ_i, v_i, and h_i in the terms EEX_i and MEX_i are the average values within each node. They are approximated as

$$h_i = h_{iz} + \frac{1}{2} R_i \Delta\rho_i, \text{ where } R \equiv \left(\frac{\partial h}{\partial \rho}\right)_p \qquad (2.45d)$$

$$\rho_i = \rho_{iz} + \frac{1}{2} \Delta\rho_i \qquad (2.46a)$$

$$v_i = v_{iz} + \frac{1}{2} \Delta v_i \qquad (2.46b)$$

The quantities H_i^* and V_i^* are calculated by these average values. (c.f. equation (2.19)). These situations make the calculations of the $\Delta\rho$'s and Δv's an iterative procedure.

The technique used in the original version of ENERGY-III to solve the matrix equation was Gaussian Elimination. This method is very inefficient when dealing with a sparse matrix such as the one employed here. Greene (1980) suggested a simple technique applicable only to

the matrix form under consideration, for solving the matrix problem. Referring to the matrix of Figure 7.4, the technique is as follows:

1. Subtract row 1 from row 2 to eliminate E_1
2. Subtract row 1 from the last row to eliminate $C_{\rho 1}$
3. Subtract row 2 from row 1 to eliminate T_1
4. Subtract row 2 from the last row to eliminate C_{v1}

This procedure is repeated with rows 3 and 4 et cetera. At this point, the matrix has non zero terms on the diagonal and in the last column. All other entries are zero. After clearing the last column by repeated subtractions of the last row from the remaining rows, and normalizing the diagonal entries to 1, the right hand side vector will contain $\Delta\rho_i$, Δv_i, and ΔP.

The $\Delta\rho$'s and Δv's are set to zero for the first iteration. The newly calculated $\Delta\rho$'s and Δv's are used to calculate the coefficient in the matrix and update the quantities in the right hand side of the matrix equation in Figure 7.4. This procedure is continued until the deviation in the overall continuity equation is reduced to within a specified tolerance. The proposed convergence criterion is

$$\frac{\sum^{N} \Delta(\rho vA)}{\sum^{N} (\rho vA)} < 10^{-7} \qquad (7.4)$$

This method, however, was found to be unable to yield a solution satisfying equation (7.4) for low flow rate cases, say $Re_b < 1000$. The resultant $\sum^{N} \Delta(\rho vA) / \sum^{N} (\rho vA)$ oscillates around a value much higher than 10^{-7}.

Figure 7.4 Equation in Matrix Form for Mixed Convection Option

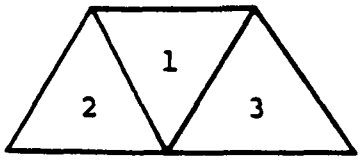

$$\begin{vmatrix} S_1 & T_1 & 0 & 0 & 0 & 0 & 0 \\ E_1 & F_1 & 0 & 0 & 0 & 0 & 1 \\ 0 & 0 & S_2 & T_2 & 0 & 0 & 0 \\ 0 & 0 & E_2 & F_2 & 0 & 0 & 1 \\ 0 & 0 & 0 & 0 & S_3 & T_3 & 0 \\ 0 & 0 & 0 & 0 & E_3 & F_3 & 1 \\ C_{\rho 1} & C_{v1} & C_{\rho 2} & C_{v2} & C_{\rho 3} & C_{v3} & 0 \end{vmatrix} \begin{vmatrix} \Delta\rho_1 \\ \Delta v_1 \\ \Delta\rho_2 \\ \Delta v_2 \\ \Delta\rho_3 \\ \Delta v_3 \\ 0 \end{vmatrix} = \begin{vmatrix} Q_1\Delta z + EEX_1 \\ G_1 + MEX_1 \\ Q_2\Delta z + EEX_2 \\ G_2 + MEX_2 \\ Q_3\Delta z + EEX_3 \\ G_3 + MEX_3 \\ 0 \end{vmatrix}$$

Energy equation: equation (2.47)

Momentum equation: equation (2.48)

Overall Continuity equation:

$$\sum_{}^{N} (C_{\rho i}\Delta\rho_i + C_{vi}\Delta v_i) = 0$$

where $C_{\rho i} = v_i + \Delta v_i$

$C_{vi} = \rho_i$

To improve the convergence of the solution, a relaxation factor (RLF) was introduced. Rather than directly insert the newly calculated $\Delta\rho$'s and Δv's into the matrix equation, the modified values,

$$\Delta\rho = RLF(\Delta\rho)_{new} + (1-RLF)(\Delta\rho)_{old} \tag{7.5a}$$

$$\Delta v = RLF(\Delta v)_{new} + (1-RLF)(\Delta v)_{old} \tag{7.5b}$$

were used. The RLF is initially set to be 1.0. If after 20 iterations (around 10 iterations should make the solution converge; otherwise, it starts oscillating) the solution is not converged, the code automatically subtracts 0.1 from RLF and restarts the iteration procedure from the intial guesses, i.e, $\Delta\rho$, $\Delta v = 0$. This procedure is continued until the solution converges. The resulting RLF value is stored and used as the initial value for the calculation at the next node. The minimum RLF is set to be 0.3. If a value of 0.3 for RLF can not make the solution converge, an error message will be printed out. The lowest value of RLF observed was 0.4, occuring at a Reynolds number of $Re_b \simeq 500$. This procedure is illustrated by the flow chart of the subroutine MIXED in Figure 7.5.

When the density and velocity increments have been calculated, the velocities and densities are calculated by incrementing the fields at the previous axial level, i.e.,

$$\rho_{z+\Delta z} = \rho_z + \Delta\rho$$

$$v_{z+\Delta z} = v_z + \Delta v$$

The enthalpy field is calculating using $\Delta\rho$ and the partial derivative $(\partial h/\partial\rho)p$,

Figure 7.5 Flow Chart of Subroutine MIXED

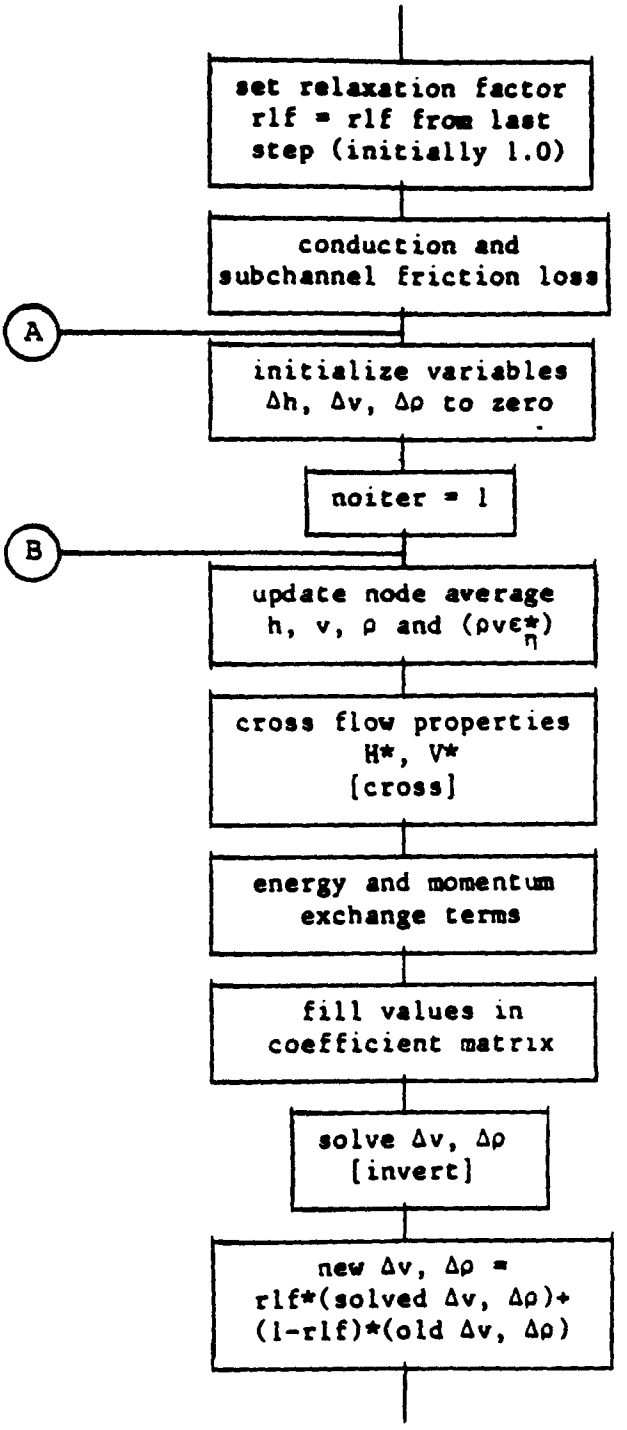

Figure 7.5 Continued

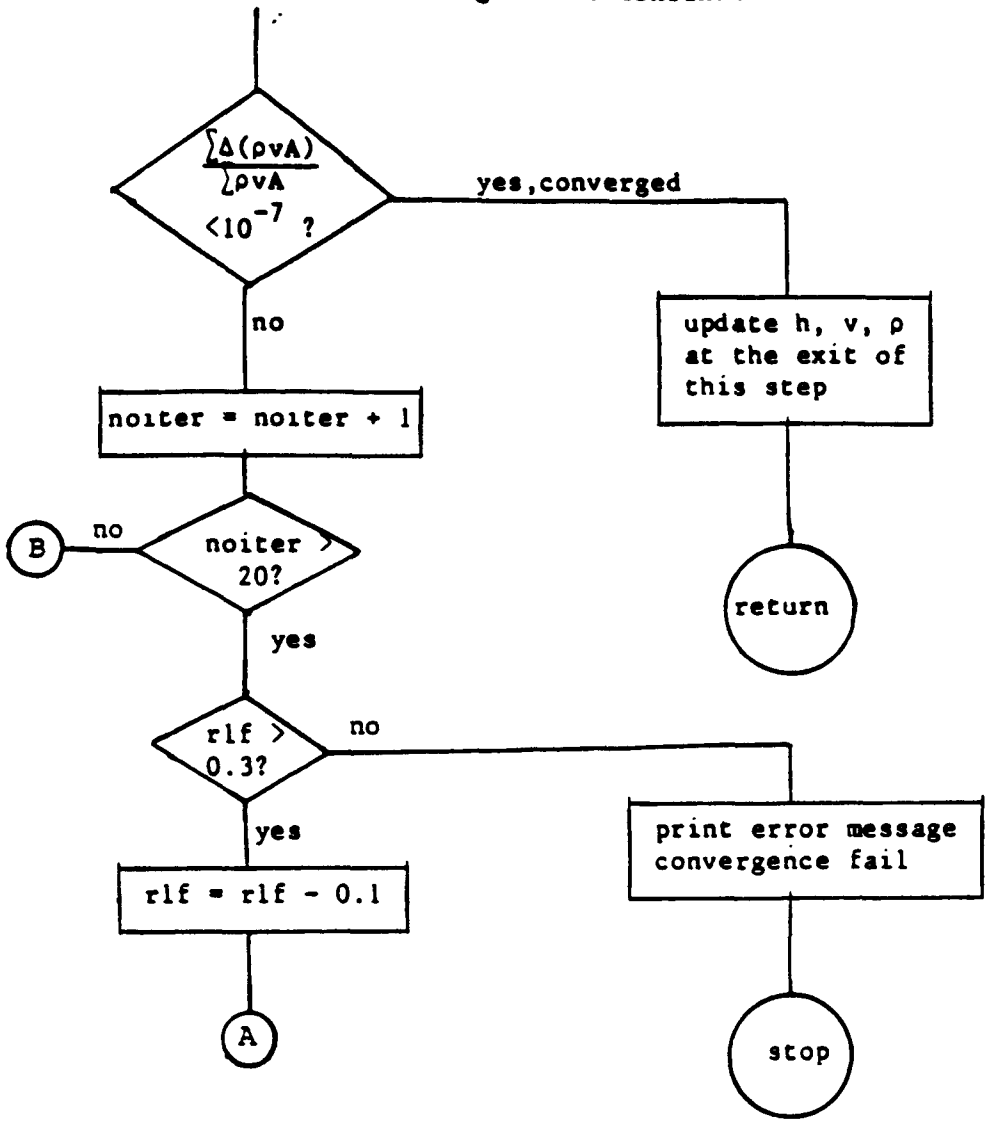

$$h_{z+\Delta z} = h_z + \left(\frac{\partial h}{\partial \rho}\right)_p \Delta\rho$$

The entire procedure is repeated at each axial level until the last printing location is reached.

The running time for the mixed convection option is proportional to the number of axial and radial nodes used. The stepsize was found to be not stability limited. Typically, 0.5 inch is recommended. For a 61-pin bundle with 126 nodes, the running time is about 0.5 second for each node. If the bundle length is 5 ft, i.e., 120 axial nodes, the running time is about 1 minute.

CHAPTER 8

VALIDATION OF THE ENERGY IV CODE

8.1 Introduction

The ENERGY-IV code is applicable to both forced and mixed convection conditions. In the forced convection condition, the buoyancy induced cross flow is negligible and a very simple method using only the energy equation and an explicit numerical scheme is employed. In the mixed convection condition, the buoyancy induced cross flow reduces the normalized peak temperature rise, defined as

$$\Delta T^* = \frac{T_i - T_{in}}{T_{out} - T_{in}}, \tag{8.1}$$

where T_i = subchannel temperature rise

T_{in} = bundle inlet temperature

T_{out} = bundle outlet temperature

and a more complicated method solving the overall mass, axial momentum, and energy conservation equations simultaneously in an implicit way is employed.

The operation condition at which the normalized peak temperature rise reduces from the forced convection value was investigated by Engel et al. (1982) in their blanket bundle. They developed a simple correlation to specify the transition between the forced convection and mixed convection regimes, i.e.,

$$\frac{Gr_{\Delta T}}{Re_b} = 0.04 \tag{8.2}$$

where $Gr_{\Delta T}$ = Grashof number based on temperature rise $\equiv \dfrac{g\beta(\frac{\Delta T_b}{L})\ De_b^4}{\nu^2}$

$\Delta T_b = T_{out} - T_{in}$

L = heated length

For a blanket assembly, the typical $Gr_{\Delta T}$ is around 400. Hence the mixed convection region is reached when the Re_b is less than 10000. For a fuel assembly, the typical $Gr_{\Delta T}$ is around 600. Assuming equation (8.2) is applicable, the mixed convection region is reached when the Re_b is less than 15000. Based on the flow regimes defined in chapter 4, one might roughly conclude that typically the turbulent flow regime corresponds to the forced convection condition while the transition and laminar flow regimes corresponds to the mixed convection condition. Note that if $Gr_{\Delta T}$ decreases to a lower value, the Re_b will proportionally decrease to make the flow condition mixed.

The correlations for the required input parameter for the ENERGY IV have been developed in Chapters 4 and 6 of report 108TR. The data used to calibrate these correlations were obtained in the forced covection condition. Although the individual models of the ENERGY-IV, such as, flow split, interchannel mixing and conduction shape factor, have been established this way, the combined thermal-hydraulic models in the ENERGY-IV are required to be validated by the temperature data of sodium cooled heated pin tests.

For the forced convection condition, these correlations are used without any modification. However, for the mixed convection condition, some modifications are required for these (forced convection) input parameters because of the existence of different thermal-hydraulic characteristics. First, since the friction factor increases as the buoyancy effect becomes important [Symolon (1982)], the subchannel friction factor used in the mixed convection regime should take into

account this buoyancy effect. Second, thermal plumes which surround the rods and interact with each other promoting turbulent mixing between channels have been visually observed by Bates and Khan (1980) and Symolon (1982) in their low flow rate tests. These thermal plumes are zones of locally heated fluid which rise more rapidly than the bulk fluid in the subchannel due to their lower density [Bates and Khan (1980)]. Thus an additional mixing parameter, $\varepsilon^*_{\eta M}$, defined similar to $\varepsilon^*_{2\eta}$ is required to represent the enhanced mixing between subchannels due to this thermal plume effect.

As discussed near the end of Chapter 6 of report 108TR the validity of using the bare rod conduction shape factor in the wire wrapped rod bundle needs to be evaluated. Typically, the conduction effect is not important in the forced convection regime; however, it contributes a large amount of energy transfer in some region of the mixed convection regime as we should discuss later in section 8.5.

In this chapter, the recent published out of pile temperature data from four different organizations: Westinghouse Advance Reactor Division (WARD), Oak Ridge National Laboratory (ORNL), Toshiba Corporation (Japan), and Grenoble (France), are used for testing the combined thermal-hydraulic models in ENERGY-IV. The thermal plume effect in the mixed convection regime will be modelled by adding a thermal plume mixing parameter (TPMP), $\varepsilon^*_{\eta M}$, to the interchannel mixing $\varepsilon^*_{1\eta}$ and $\varepsilon^*_{2\eta}$. This TPMP is estimated by matching the ENERGY-IV predictions to the mixed conveciton temperature data. A correlation is then proposed for $\varepsilon^*_{\eta M}$ as a function of geometry, $Gr_{\Delta T}$ and Re_b.

Finally, the relative importance of wire sweeping mixing, molecular conduction, thermal plume mixing and flow redistribution due to buoyancy, in the energy transfer between subchannels will be compared.

8.2 Description of the Tests Used for Validation

Table 8.1 depicts the characteristics of the test bundles for those four organizations. The WARD and Grenoble (FETUNA) bundles are similar to the blanket assembly while the ORNL and Toshiba bundles are similar to the fuel assembly. All tests used heated pins and were cooled by sodium. All bundles except the Toshiba bundle operated with a radial power skew in a row by row sense, i.e., each row of pins can operate at an independent power level. Figure 8.1 shows 9 rows for a 61-pin bundle. Table 8.2 describes the normalized power factor of each row for different power skew used in the WARD and ORNL 61-pin and 19 pin bundles. The radial power factor used in the Toshiba bundle will be described later. The corresponding subchannel identification number used in the ENERGY-IV (calculated by subroutine NUMB) for a 61-pin bundle is shown in Figure 8.2.

The test sections and thermocouple locations where the measured temperature data were obtained which will be used for ENERGY-IV validation purpose are briefly described as follows.

WARD 61-pin

Figure 8.3 shows the test section and axial loation of the thermocouples for the WARD 61-pin simulated blanket assembly tests.

Table 8.1 Characteristics of Test Bundles

Bundle	Nr	D (in)	Dw (in)	P/D	W/D	H/D	Heated length (in)	Axial power profile	Radial power skew	Flow regime
WARD 61-pin [Engel(1980)]	61	0.519	0.037	1.082	1.078	7.7	45.0	cosine 1.4/1*	1/1,2/1, 2.8/1**	Forced Mixed
ORNL 19-pin [Fontana(1974)]	19	0.230	0.056	1.244	1.244	52.2	21.0	uniform	1/1,3/1	Forced
ORNL 61-pin [Morris(1980)]	61	0.230	0.056	1.244	1.244	52.2	36.0	cosine 1.38/1	1/1,1.5/1 2/1,3/1	Forced Mixed
Toshiba 37-pin [Namekawa(1984)]	37	0.256	0.052	1.210	1.210	47.2	36.6	cosine 1.21/1	1/1,1.4/1 2/1	Forced Mixed
Grenoble 91-pin [Rameau(1980)]	91	0.622	0.042	1.067	1.067	11.4	59.0	cosine	1/1,2.5/1	Mixed

* maximum to average
** maximum to minimum

Table 8.2 Normalized Power Factor for Different Power Skew in WARD and ORNL Tests

Bundle	Radial Power Skew	Row 1	2	3	4	5	6	7	8	9
WARD 61-pin	2/1	0.710	0.745	0.800	0.870	0.960	1.060	1.180	1.300	1.450
	2.8/1	0.635	0.678	0.713	0.796	0.882	1.026	1.220	1.473	1.776
ORNL 61-pin	1.5/1	0.83	0.83	0.95	0.95	0.95	0.95	1.07	1.19	1.19
	2/1	0.72	0.72	0.84	0.96	0.96	1.08	1.20	1.20	1.32
	3/1	0.49	0.62	0.74	0.86	0.99	1.11	1.24	1.48	1.48
ORNL 19-pin	3/1	0.50	0.75	1.00	1.25	1.75				

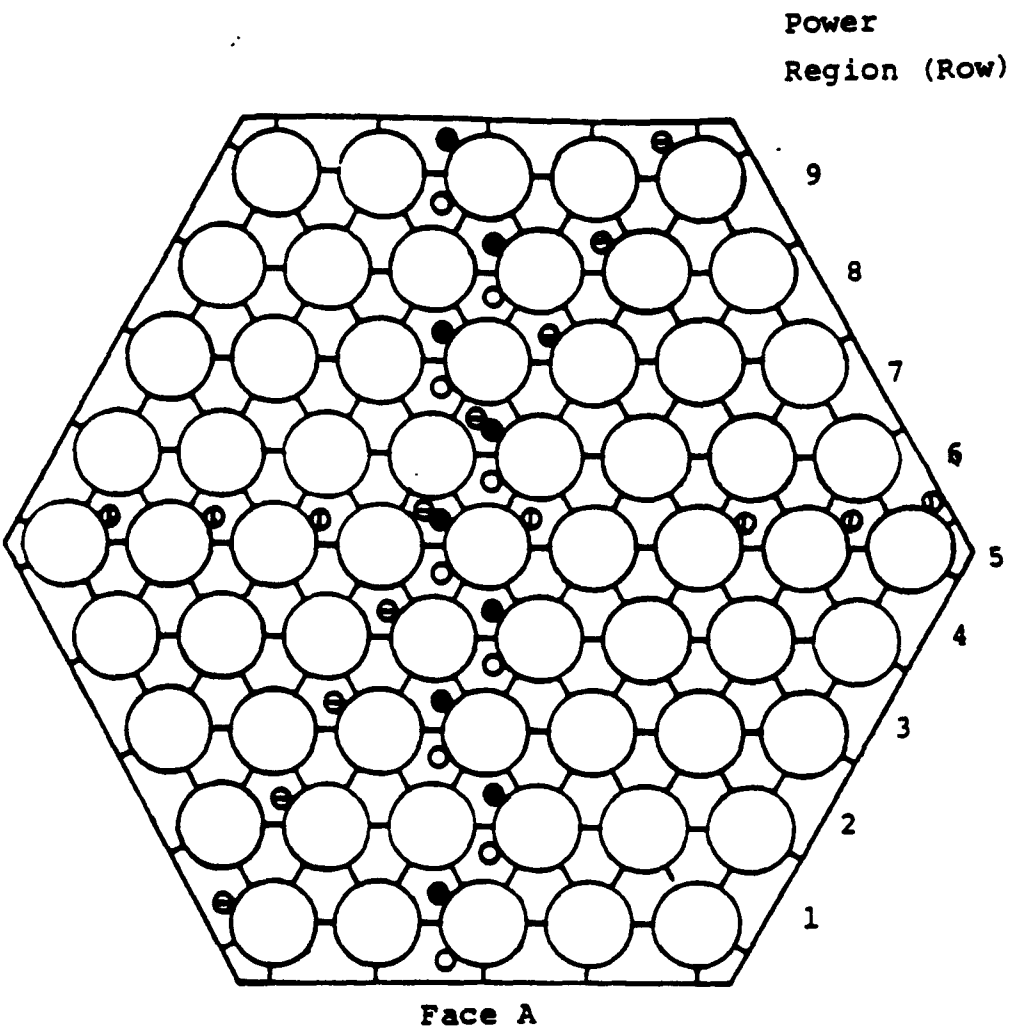

Figure 8.1 Power Regions and Thermocouple Locations for WARD and ORNL 61-pin Bundles

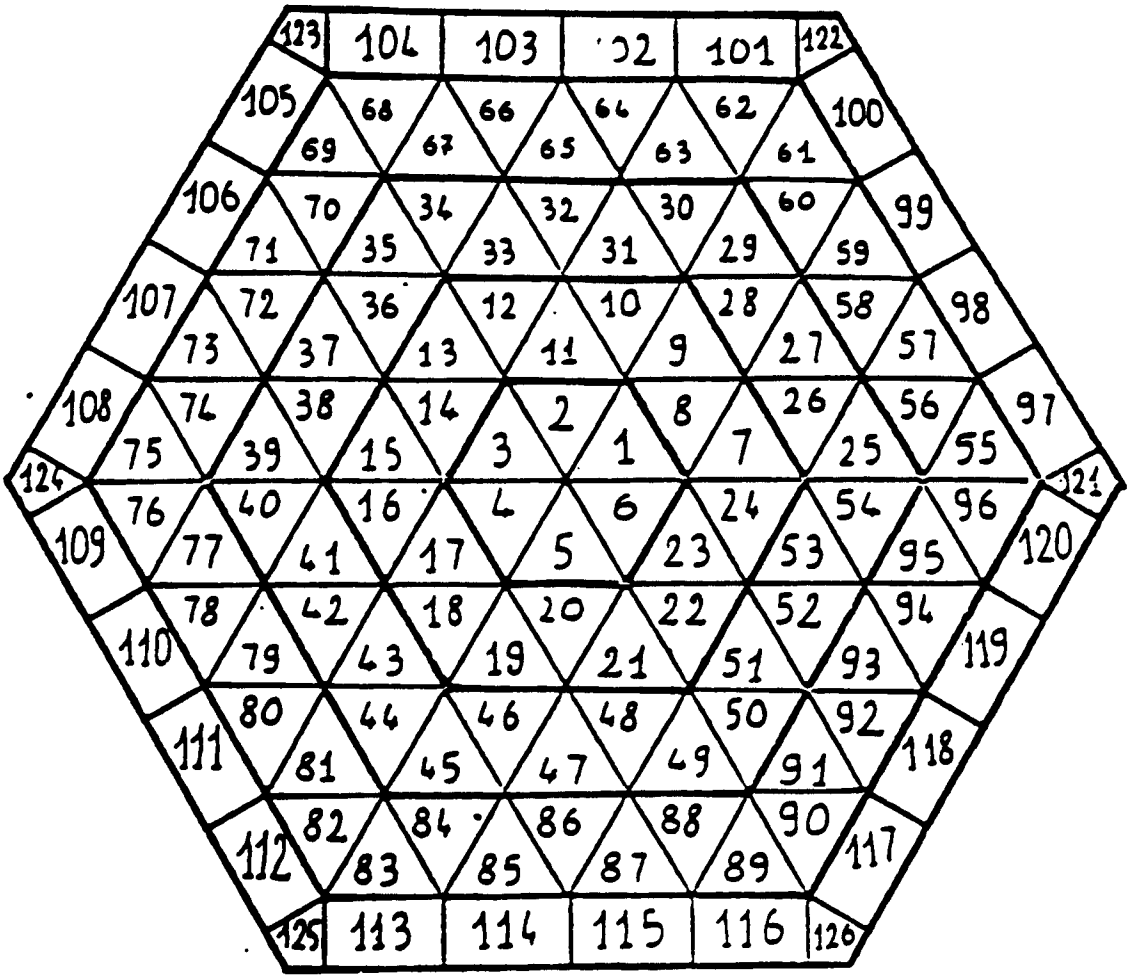

Face A

Figure 8.2 Subchannel Identification Number for a 61-pin Bundle by Subroutine NUMB

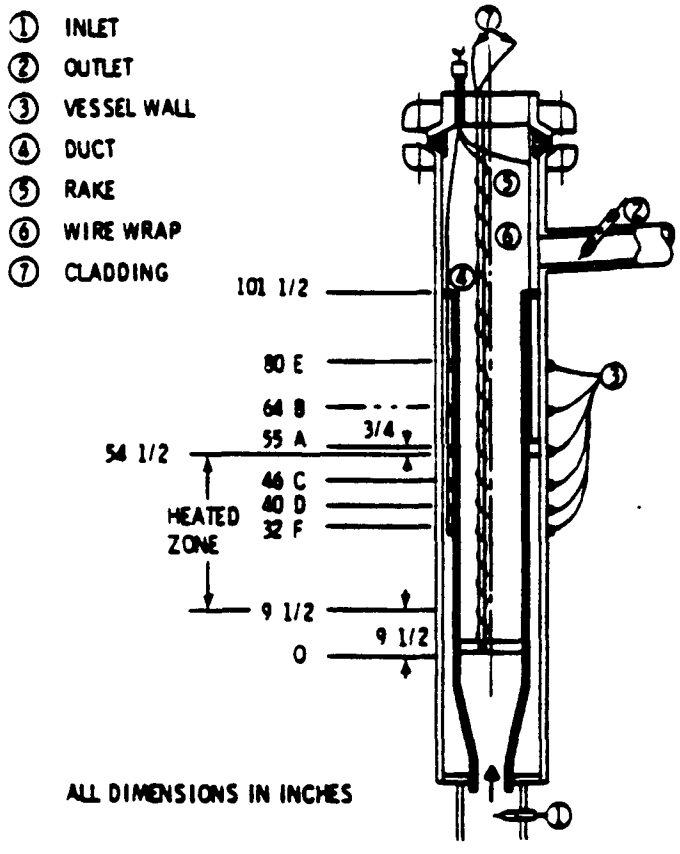

Figure 8.3 Test Section and Thermocouple Positions for WARD 61-pin Bundle Tests

[Engel et al. (1978, 1980, 1981), Markley and Engel (1981)]. The coolant enters the bundle 9.5 inches below the plane where the rods are heated so as to provide a fully developed flow field at the entrance to the heated section. Within each pin there is a resistance coil of nichrome wire wound so as to provide a chopped cosine axial heat flux profile over a 45-inch length. Thermocouples are located at three axial elevations in the heated zone and at three axial elevations above the heated zone. Only the data measured at levels E (25 inches downstream of the end of the heated zone), A (outlet of heated zone), and F (heated zone midplane) will be used for the validation. The thermocouples are implemented in the wire wraps. The position of these wire wrap thermocouples at levels E, A, F, are shown in Figure 8.1. They are distributed flat to flat across the bundle. Also there are thermocouples for most of the edge pins to measure the temperature in the edge subchannels.

ORNL 19 pin

The ORNL THORS-2A data [Fontana et al (1973, 1974)] was taken in the 19-pin bundle shown in Figure 8.4. The heated length of the rods is 21 inches. The cold entrance length is approximately 6 inches. Thermocouples are located in the rod walls and also in the wire wraps. An exit rake is located 3 inches above the exit of the heated bundle and is instrumented with thermocouples which directly measure coolant temperatures at the center of various subchannels (c.f. Figure 8.4). The axial power profile is uniform. The hexaganol duct is surrounded by guard heaters to minimize heat losses.

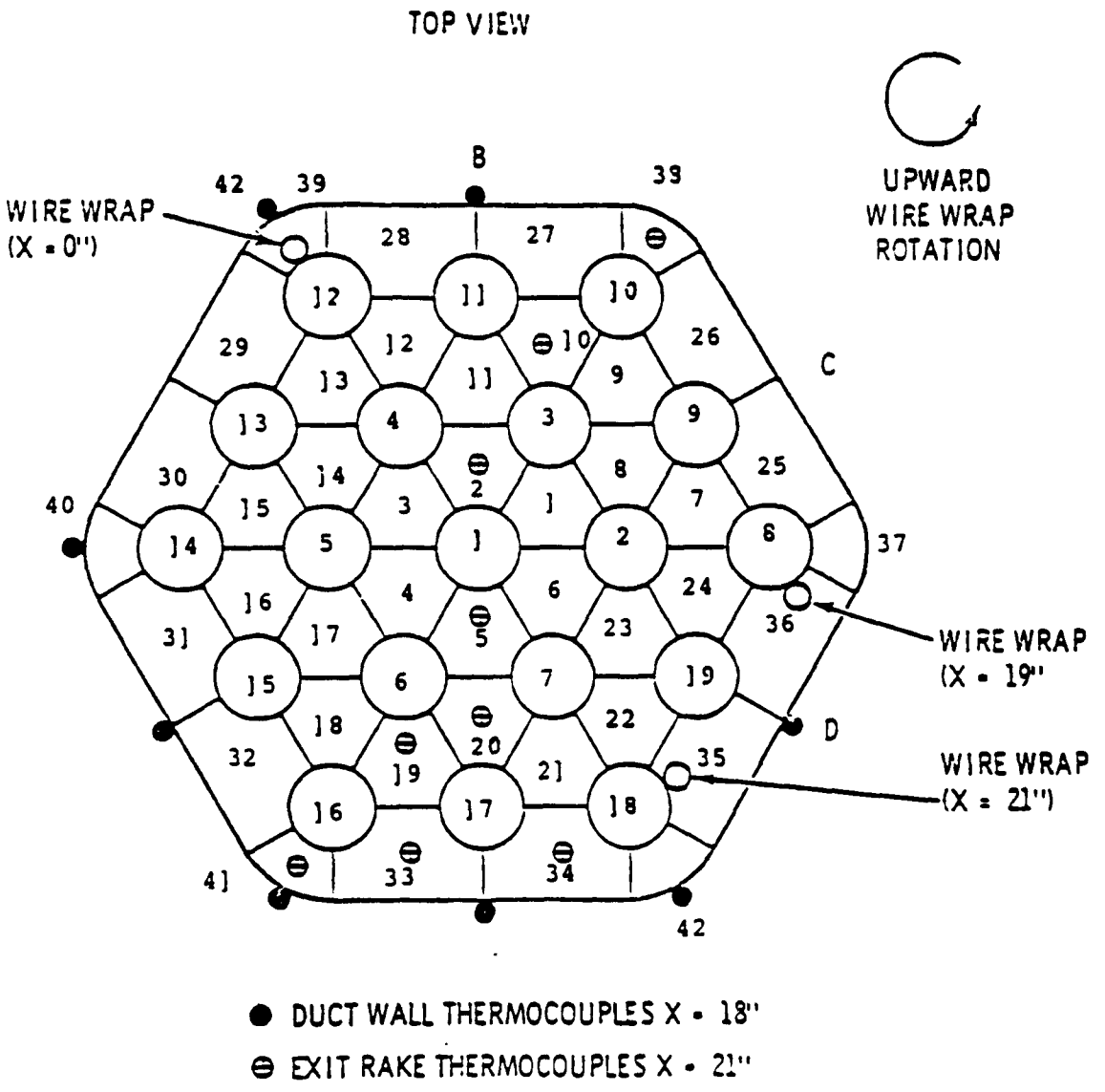

Figure 8.4 Rod and Subchannel Identification Number and Thermocouple Locations for ORNL 19-pin THORS 2A Bundle

ORNL 61-pin

The geometry of the THORS-9A 61-pin test bundle [Morris et al. (1980)] is similar to the THORS 2A test bundle except for the total number of pins and an axial varying power profile. The bundle was fabricated axially with a 9 inches cold entrance length and a 36 inches heated length that was followed by a 1 inch unheated length. Thermocouples were implemented in wire wraps and the assembly wall. The data at the 21-inch, 25-inch and 37-inch levels will be used for comparison. Note that the start of the heated length is defined to be the zero inch level. The thermocouple locations at these levels are also shown in Figure 8.1. They are distributed corner to corner across the bundle.

Toshiba 37-pin

The Toshiba test assembly [Namekawa et al. (1984)] contains 37 simulator rods within a hexaganol can, which is installed in a containment tube. There are many horizontal plates in the containment tube to prevent heat loss, since sodium is filled between the hexagonal can and containment tube. The cold entrance length is 15.7 inches following by a 36.6 inch heated length. Electrical power is supplied to the heated rods by three power control units. The axial power profile is a chopped consine shape with a 1.21 maximum to average ratio. The rod bundle is grouped into three divided regions, which correspond to three power control units. Radial power skew within the bundle is produced by the three divided regions as shown in Figure 8.5 The power factors for Region I, II, III are: 1.18, 1.0, 0.84, and

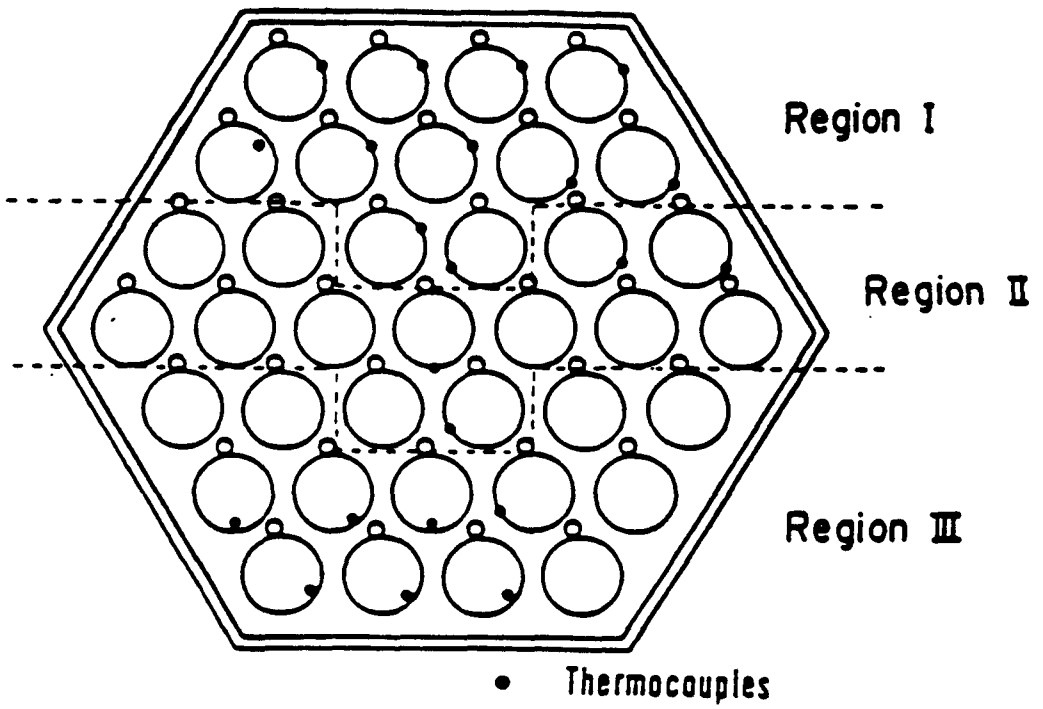

Figure 8.5 Thermocouple Locations and Power Regions for Toshiba 37-pin Bundle

1.36, 1.0, 0.694 for 1.4/1 and 2/1 power skew, respectively. The corresponding subchannel numbering scheme used in the ENERGY-IV is the same as that in Figure 3.17. Numerous thermocouples were embedded in the simulator rods to measure heat transfer characteristics within the rod bundle. The thermocouples were grouped into distinct horizontal planes at position L_1 (24.0 inches downstream of the inlet of heated zone) and L_2 (36.0 inches downstream of the inlet of heated zone.) The thermocouple locations are also shown in Figure 8.5.

Grenoble 91-pin

The Grenoble (FETUNA) GR.91 mock-up [Rameau (1984)] consists of an electricity heated 91-pin bundle within a hexagonal wrapper, which is surrounded by a jacket. The heated length is 53.15 inches. About 150 thermocouples were used to measure the temperature field in the bundle and wrapper tube. Only the mixed convection condition temperature data measured at the end of heated length were reported.

8.3 Validation of the ENERGY-IV in the Forced Convection Condition

Table 8.3 describes the operation conditions for the cases used to validate the ENERGY-IV in the forced convection condition. Two cases with "Edge" under column run are for the temperature distribution in the edge subchannels, while all the other ten cases are for the temperature distribution across the bundle: flat to flat for WARD and Toshiba bundles and corner to corner for the ORNL bundles. The temperature data and calculation results are represented by a

Table 8.3 Cases Used for Forced Convection Validation

Bundle	Run	Bundle Flow Rate (GPM)	Average Rod Power(kW/ft)	Power Skew	Re_b	T_{in} (F)	$\Delta T_b^{\dagger}$ (F)
WARD	223	36.8	1.143	2.8/1	8900	600	178
61-pin	415	36.8	1.143	2/1	8900	600	178
	226	36.8	1.143	1/1	8900	600	178
	Edge	36.8	1.143	2.8/1	8900	600	178
ORNL	14-101	54.0	5.0	3/1	67000	600	75
19-pin	Test 2	53.0	5.0	1/1	66000	600	77
	Edge	54.0	10.0	3-pin	67000	600	24
ORNL	19-101	104.0	4.44	3/1	49000	700	203
61-pin	1-4	156.0	6.67	1/1	73000	700	203
Toshiba	G37P22	15.72	0.484	2/1	8000	402	83
37-pin	E37P17	16.02	0.474	1.4/1	8300	409	80
	B37P02	23.57	0.475	1/1	12000	412	54

† Energy balance value

normalized temperature rise, ΔT^*, defined by equation (8.1). The temperature can be calculated from this ΔT^* utilizing the values of $\Delta T_b (\equiv T_{out} - T_{in})$ and T_{in} in Table 8.3.

8.3.1 Comparisons between Data and Predictions for WARD Bundle

Figures 8.6, 8.7, 8.8 compare the ENERGY-IV predictions with the temperature data for Runs 223, 403, and 226, respectively. For all three power skews, the ENERGY-IV results are observed to excellently predict the data. The maximum difference between the ENERGY-IV predictions and data occurs in the outlet of heated zone data (level "A") of Run 223 which has 2.8/1 power skew. A 0.07 overprediction for ΔT_b^* was found for this maximum difference (1.48 versus 1.41). Since ΔT_b = 178°F for this case, this gives a 12.5°F temperature difference.

The predictions of the COTEC code for Run 223 are also present in Figure 8.6 for comparison. The COTEC results have same degree of accuracy as that of the ENERGY-IV results in predicting levels "A" and "F" data. However, the level E data are not as well predicted by the COTEC as the ENERGY-IV does. The COTEC model might use a lower value for the interchannel mixing, which makes the gradient across the bundle of its predictions higher than that of the data.

To investigate the sensitivity of the ENERGY-IV prediction to ε_{1n}^* Figures 8.9, 8.10, and 8.11 illustrate the ENERGY-IV results with ε_{1n}^* values at +25% and -25% of the correlation value (0.122). Note that the accuracy of the correlation for ε_{1n}^* is ±25% as discussed in chapter 6. At outlet of the heated zone (level "A"), this ±25% change in ε_{1n}^*

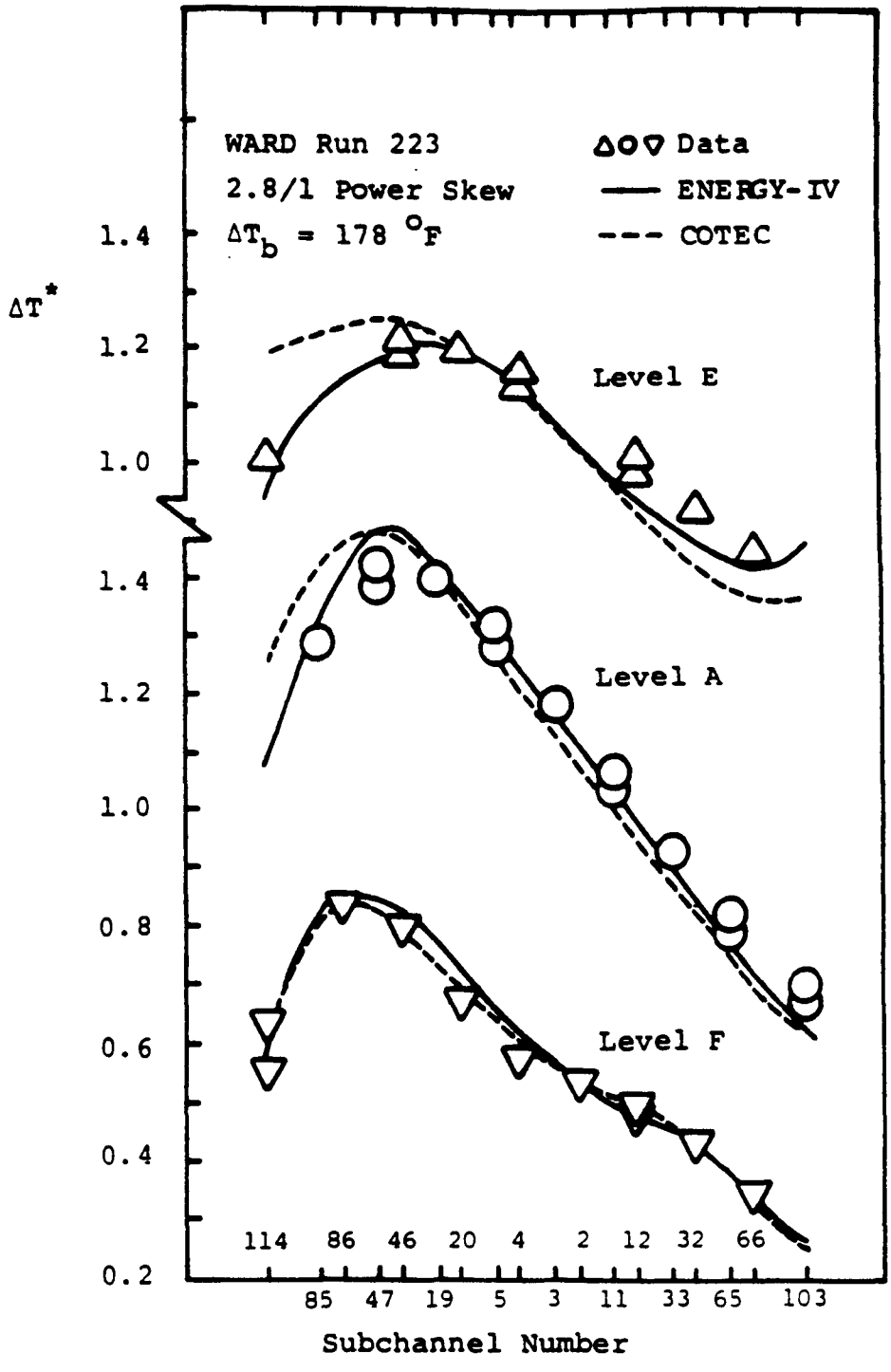

Figure 8.6 Measured and predicted Temperature Rise for WARD Run 223

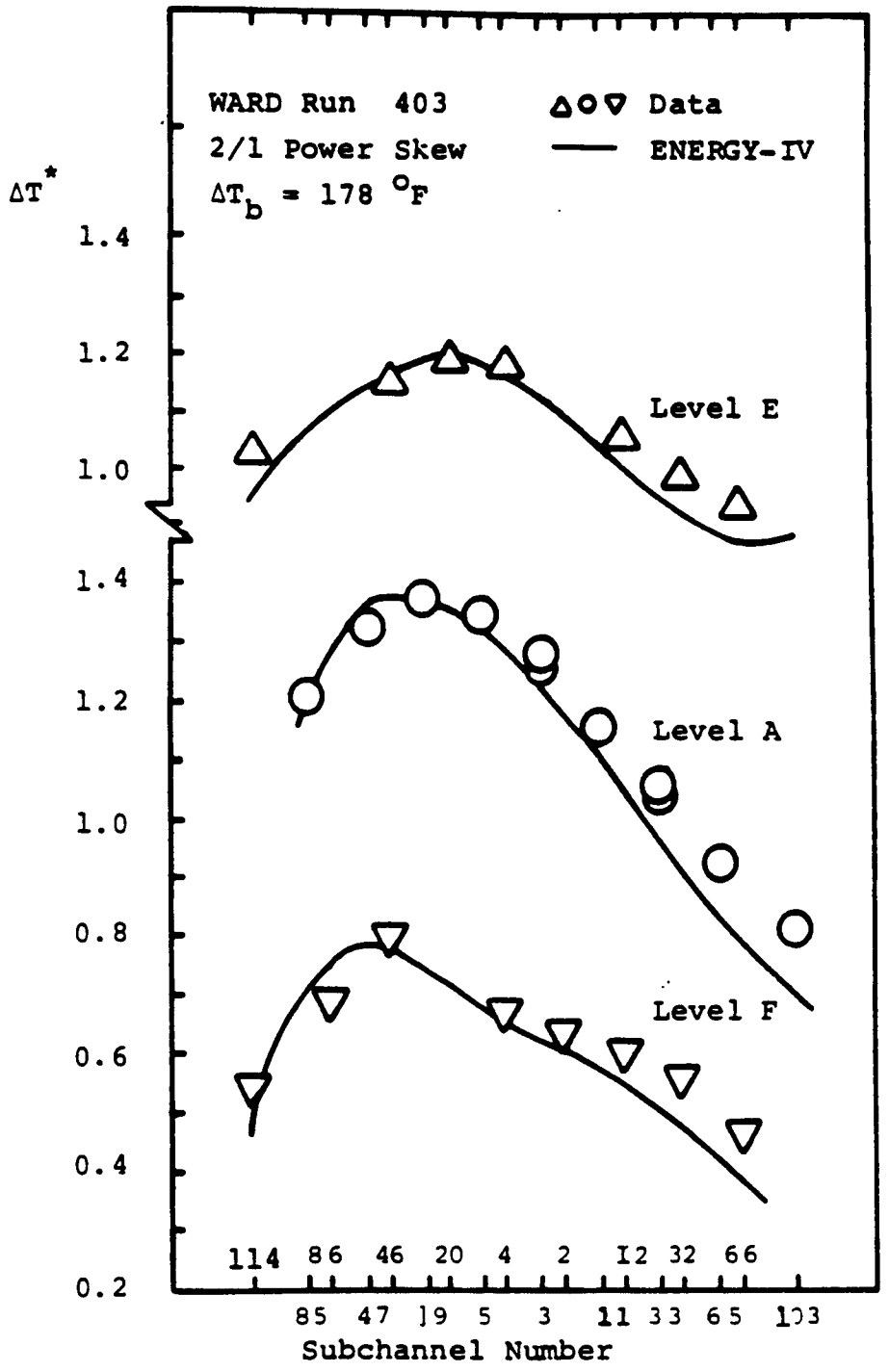

Figure 8.7 Measured and Predicted Temperature Rise for WARD Run 403

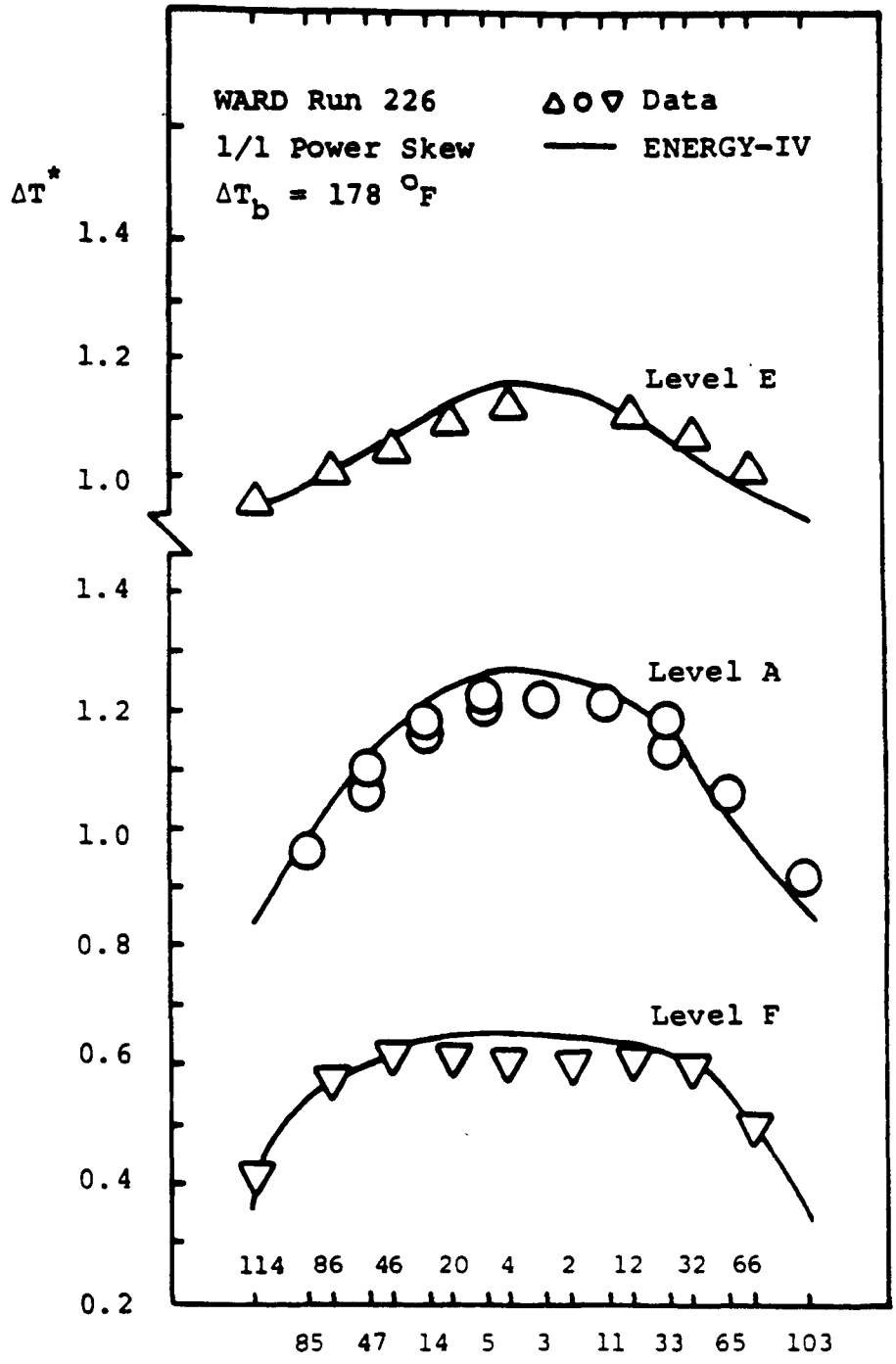

Figure 8.8 Measured and predicted Temperature Rise for WARD Run 226

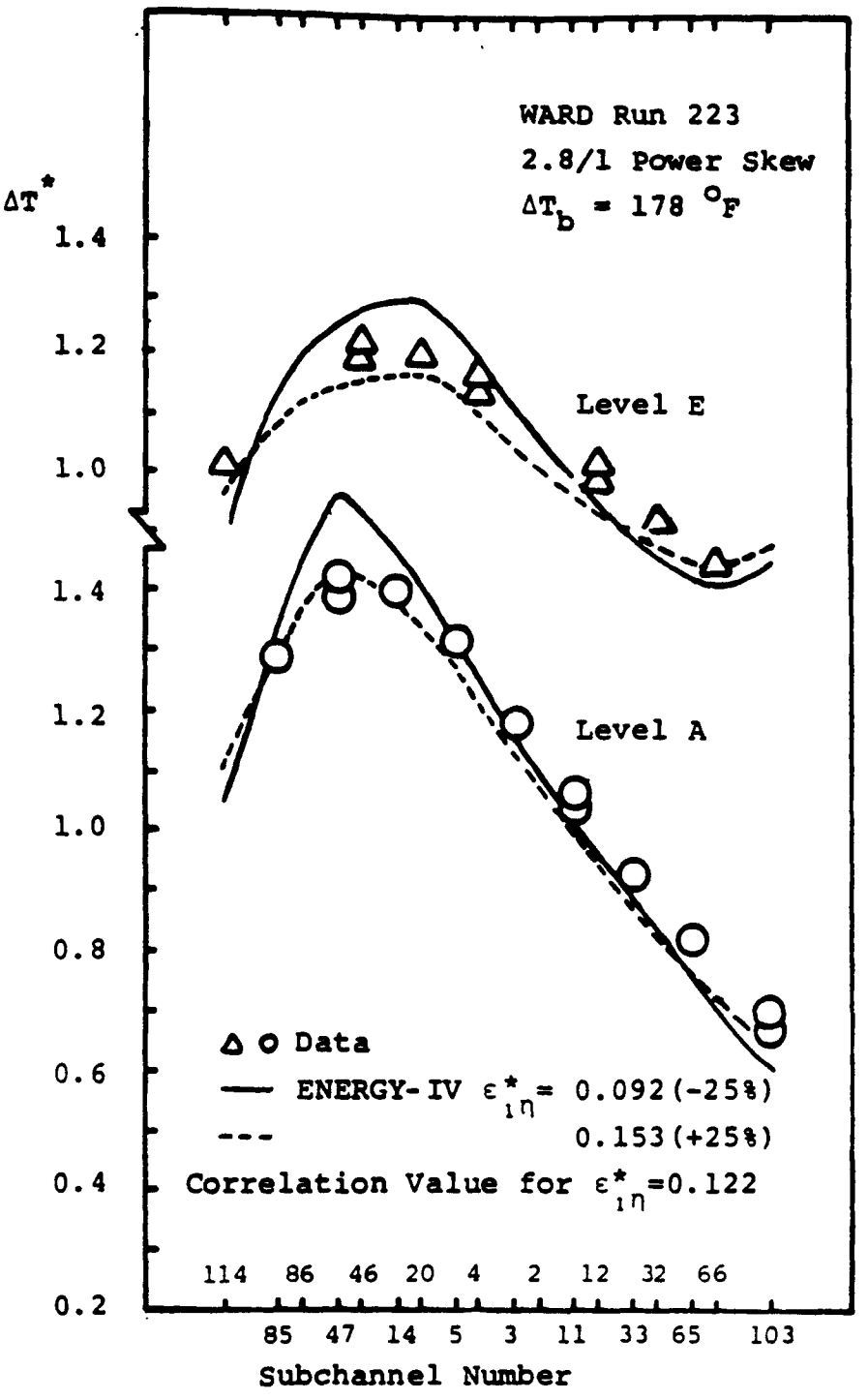

Figure 8.9 Sensitivity of the ENERGY-IV Results to $\epsilon^*_{1\eta}$ for WARD Run 223

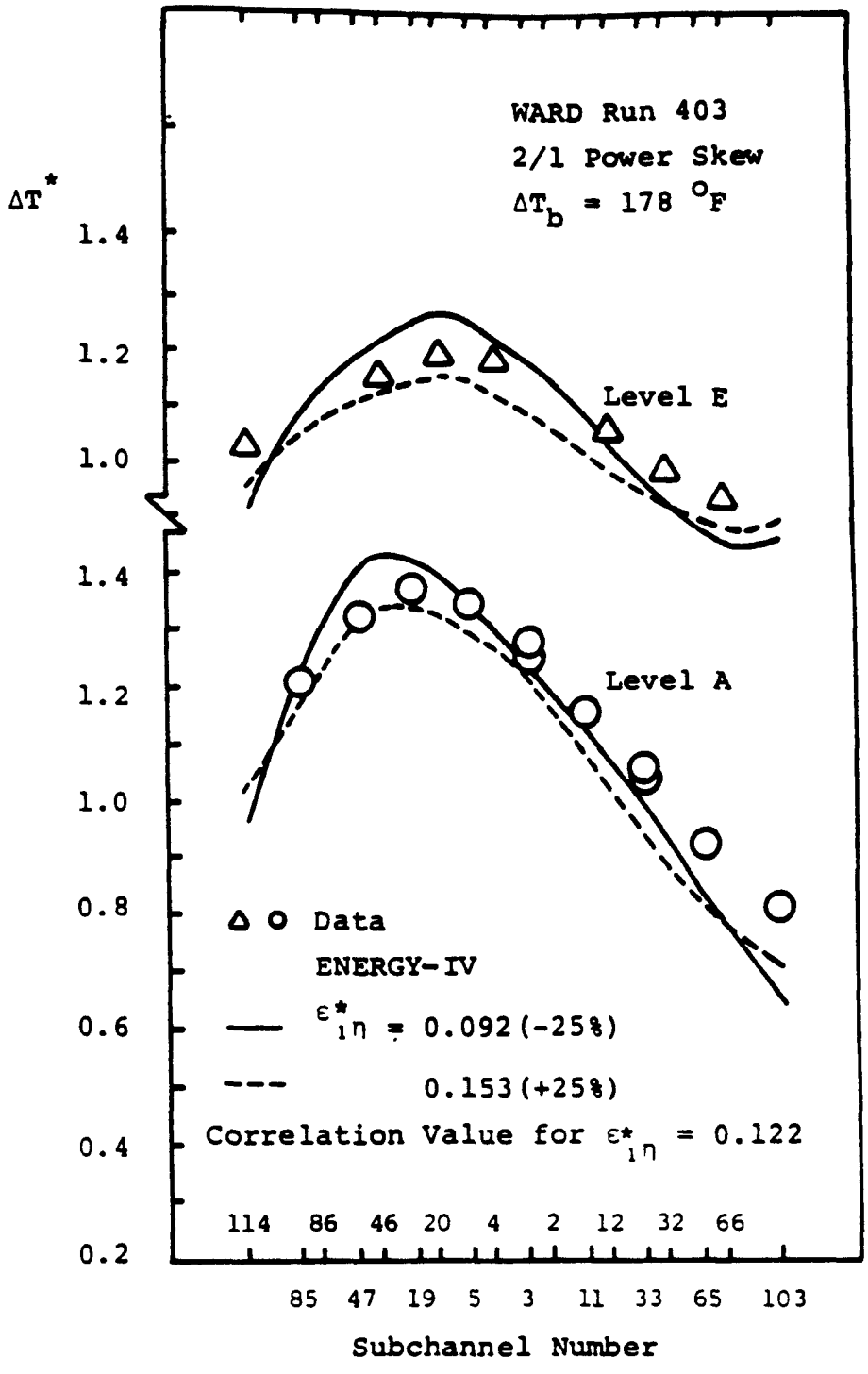

Figure 8.10 Sensitivity of the ENERGY-IV Results to $\varepsilon^*_{1\eta}$ for WARD Run 403

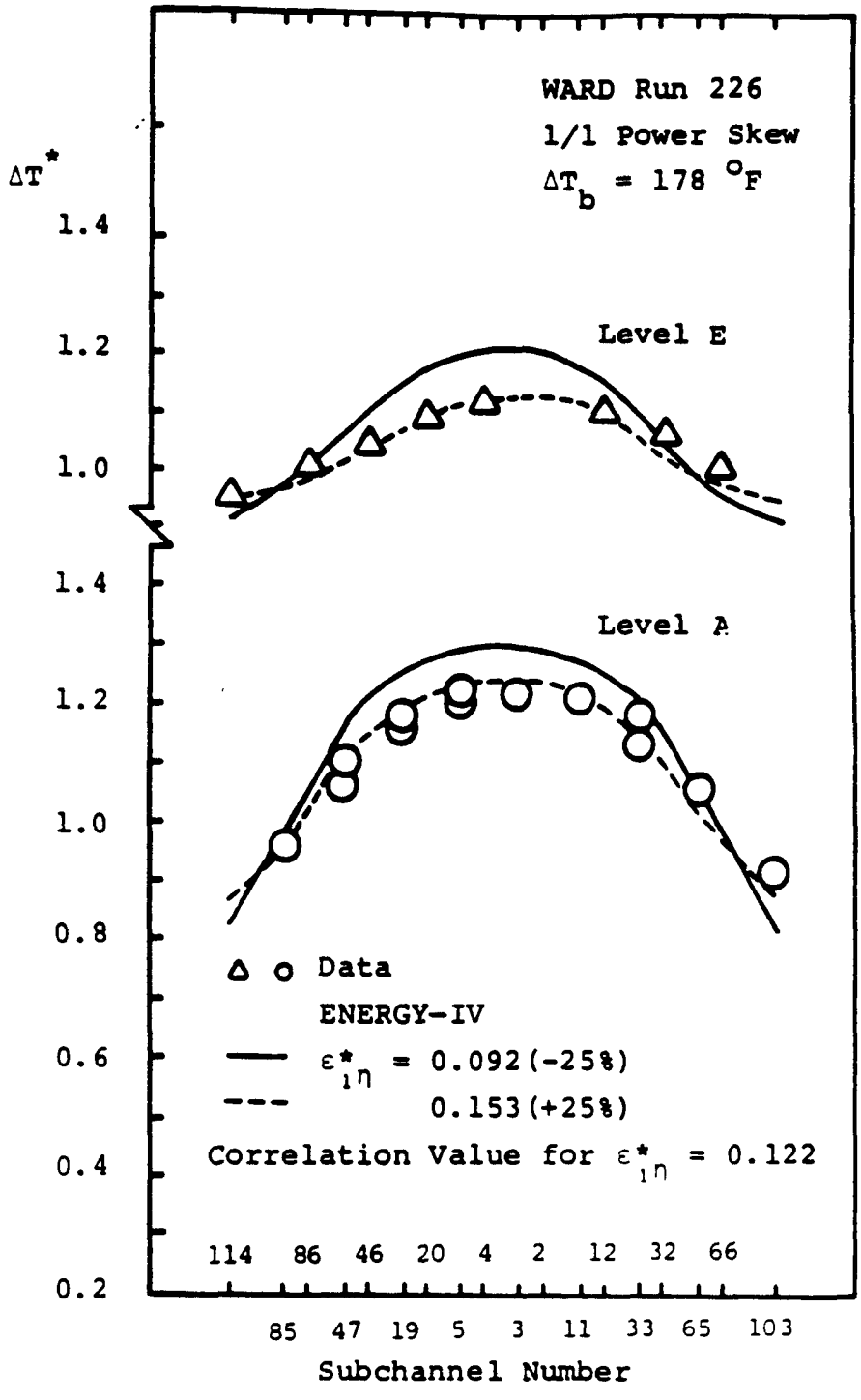

Figure 8.11 Sensitivity of the ENERGY-IV Results to $\varepsilon^*_{1\eta}$ for WARD Run 226

changes the calculated maximum ΔT^* $\mp$0.065 (44%), 0.045 (3.5%), and 0.03 (2.4%) corresponding to temperature differences $\mp$12°F, 8°F, and 5°F, for 2.8/1, 2/1, and 1/1 power skew, respectively.

Apparently, this temperature sensitivity to $\varepsilon^*_{1\eta}$ is much less than that for the salt concentration calculation in Chapter 5, which gave -20% of dimensionless salt concentration for +25% of $\varepsilon^*_{1\eta}$ and +34% of dimensionless salt concentration for -25% of $\varepsilon^*_{1\eta}$. The reason for this drastic difference is that the salt injection case is basically a local point source, while the heated pin case is a global (axially and radially) heat source. This global heat source diminishes the influence of $\varepsilon^*_{1\eta}$ to the calculated temperature distribution. Hence the $\varepsilon^*_{1\eta}$ reduced from the point source experiments will be much more accurate than that reduced from the heated pin experiment. Note that most of the reduced $\varepsilon^*_{1\eta}$ values used for calibrating our proposed correlation were from the point source experiments.

Despite the fact that the calculation results for the heated pin bundle are not as sensitive to $\varepsilon^*_{1\eta}$ as that for the point source case, $\varepsilon^*_{1\eta}$ is still the most important input parameter to accomplish good predictions. As seen from Figures 8.9, 8.10 and 8.11, most of the data, especially in the high temperature region, fall inside the calculation results using ±25% and -25% of the correlation value of $\varepsilon^*_{1\eta}$.

As for the temperature distribution along the edge subchannels, Figure 8.12 compares the data, the ENERGY-IV predictions, and the COTEC

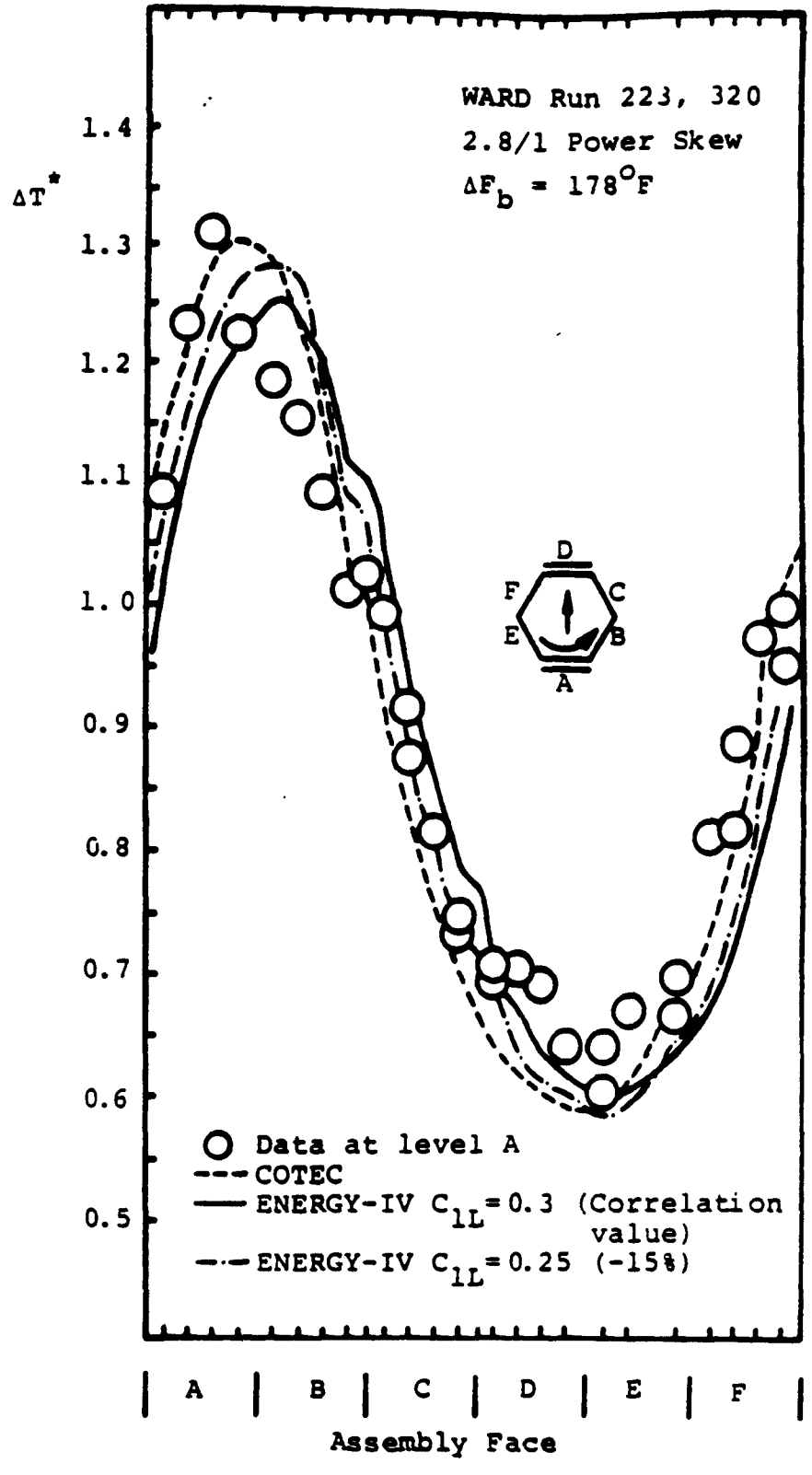

Figure 8.12 Measured and Predicted Temperature Rise in Edge Subchannels for WARD Bundle

predictions. Two ENERGY-IV results are shown in this figure, one with C_{1L} = 0.3 (correlation value), the other one with C_{1L} = 0.25 (-15% of the correlation value). Note that the accuracy of the correlation for C_{1L} is ±15%. The results with C_{1L} = 0.25 predicts the data better, although the maximum ΔT^* only increases 2% and its location moves backward one subchannel comparing the results with C_{1L} = 0.3. Similar to the $\varepsilon^*_{1\eta}$, this sensitivity is much less than that for salt injection calculation. The difference between the maximum ΔT^* for the data and for the calculation results with the correlation value of C_{1L} (0.30) is about 0.06, which gives 11°F temperature difference since ΔT_b = 178°F. The COTEC results match the data quite well. Incidentally, the COTEC calculation looks like a ENERGY-IV calculation with C_{1L} = 0.20 (-30% of correlation value).

8.3.2 Comparison between Data and Predictions for the ORNL Bundles

ORNL 19-pin

Figures 8.13 and 8.14 compare the ENERGY-IV prediction to the data for a 3/1 and 1/1 power skew, in the 19 pin THORS-2A bundle. The ENERGY-IV calculation predicts the 3/1 power skew data well, but it slightly overpredicts the peak temperature of the 1/1 power skew data by a value of 3°F (0.004 of ΔT^*).

The COBRA calculations [Khan et al. (1982), Donovan et al. (1979)] are also present in these figures for comparison. The input parameters used in the COBRA (-WC or -IV) are listed in Table 8.4. This set of input parameters have been validated by Khan et al. (1982) to be

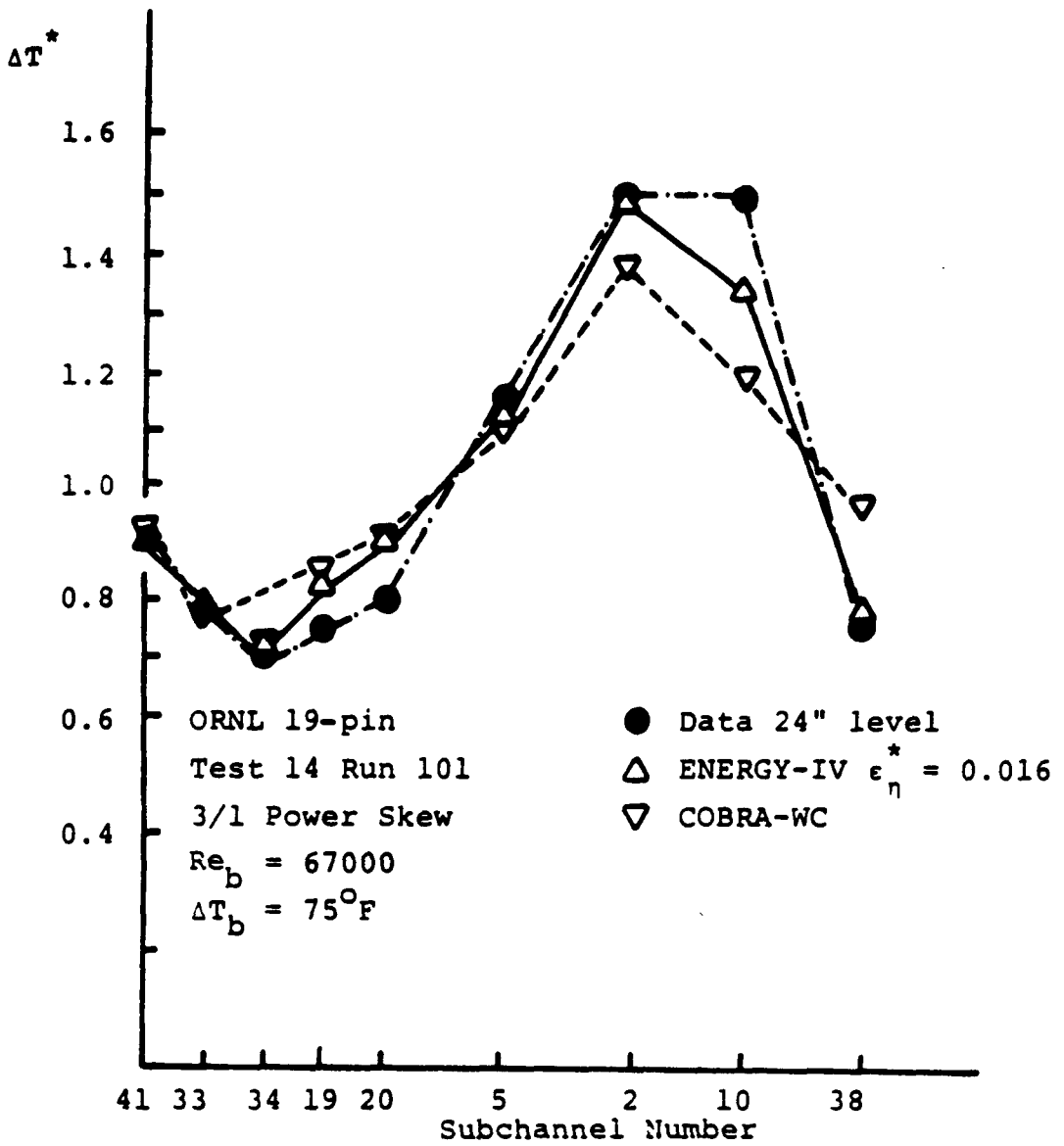

Figure 8.13 Measured and Predicted Temperature Rise for ORNL 19-pin 3/1 Power Skew

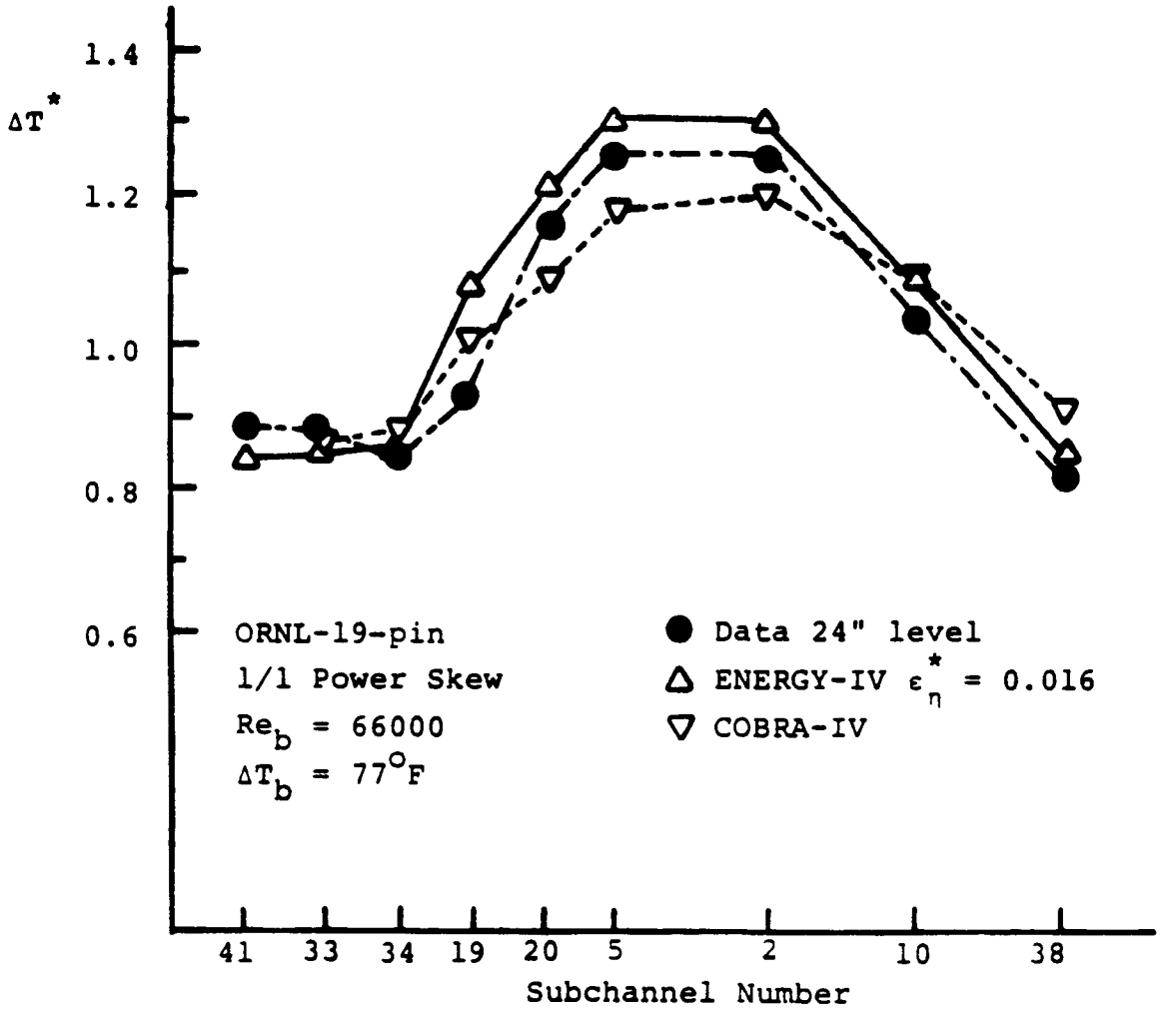

Figure 8.14 Measured and Predicted Temperature Rise for ORNL 19-pin Uniform Power Distribution

Table 8.4 Input Parameters for COBRA-WC (or -IV)

Parameter	Blanket	Fuel
wire-wrap sweep flow coefficient, DUR	1.0	1.0
crossflow resistance, K_{IJ}	0.5	0.5
momentum length, S/ℓ	0.5	0.5
conduction shape factor, G	0.5	0.5
fraction of bundle flat-to-flat tolerance accommodated at the wall	0.0	0.0
turbulent mixing parameter, ß	0.01	0.01[a] 0.00[b]
subchannel friction factors, f	$f = \frac{M f_{smooth}}{X_i^2} \frac{d_i}{d_{bundle}}$	

where

i = 1 for interior channels

i = 2 for wall channels

M = Novendstern's friction factor multiplier for wire wrapped rod bundles

f_{smooth} = smooth tube friction factor

X_i = flow split from (Khan 1980; Chiu 1978; Wang and Todreas 1981)

(a) For prediction of coolant temperature distribution across the assembly.

(b) For prediction of peak coolant temperature within the assembly.

applicable to wire-wrapped rod bundle in both forced an mixed flow required. Unless otherwise specified, all the COBRA predictions presented in this chapter use these input parameters. As shown in these two Figures, the COBRA results underpredict the data.

The sensitivity of the ENERGY calculations to $\varepsilon^*_{1\eta}$ can be estimated by the following discussion. As $\varepsilon^*_{1\eta}$ changes from the correlation value, 0.016, to the +50% value, 0.024, the peak temperatures predicted by the ENERGY-IV coincide with the data for the uniform power skew case, i.e., the maximum ΔT^* decreases a value of 0.04 or 3°F, For the 3/1 power skew case, the maximum ΔT^* decreases 0.06 or 4.5°F as $\varepsilon^*_{1\eta}$ increases 50%.

Figure 8.15 shows the comparison between the ENERGY-IV calculation and the temperature data in the edge subchannels for three edge pins heated. The trend of the data and the peak temperature location are well predicted by the ENERGY-IV. The maximum temperature difference is about 14°F in the peak temperature subchannel.

ORNL-61 pin

Figures 8.16 and 8.17 compare the data, the ENERGY-IV results and the COBRA-WC results for the ORNL-61 pin bundle with 3/1 power skew and uniform power skew, respectively. Excellent predictions by the ENERGY-IV are observed. The maximum difference between the data and ENERGY-IV results is about ΔT^* equal to 0.06, which gives a temperature difference of 12°F with ΔT_b = 203°F. As seen from these figures, the ENERGY-IV has a better capability in predicting the data than that of the COBRA-WC.

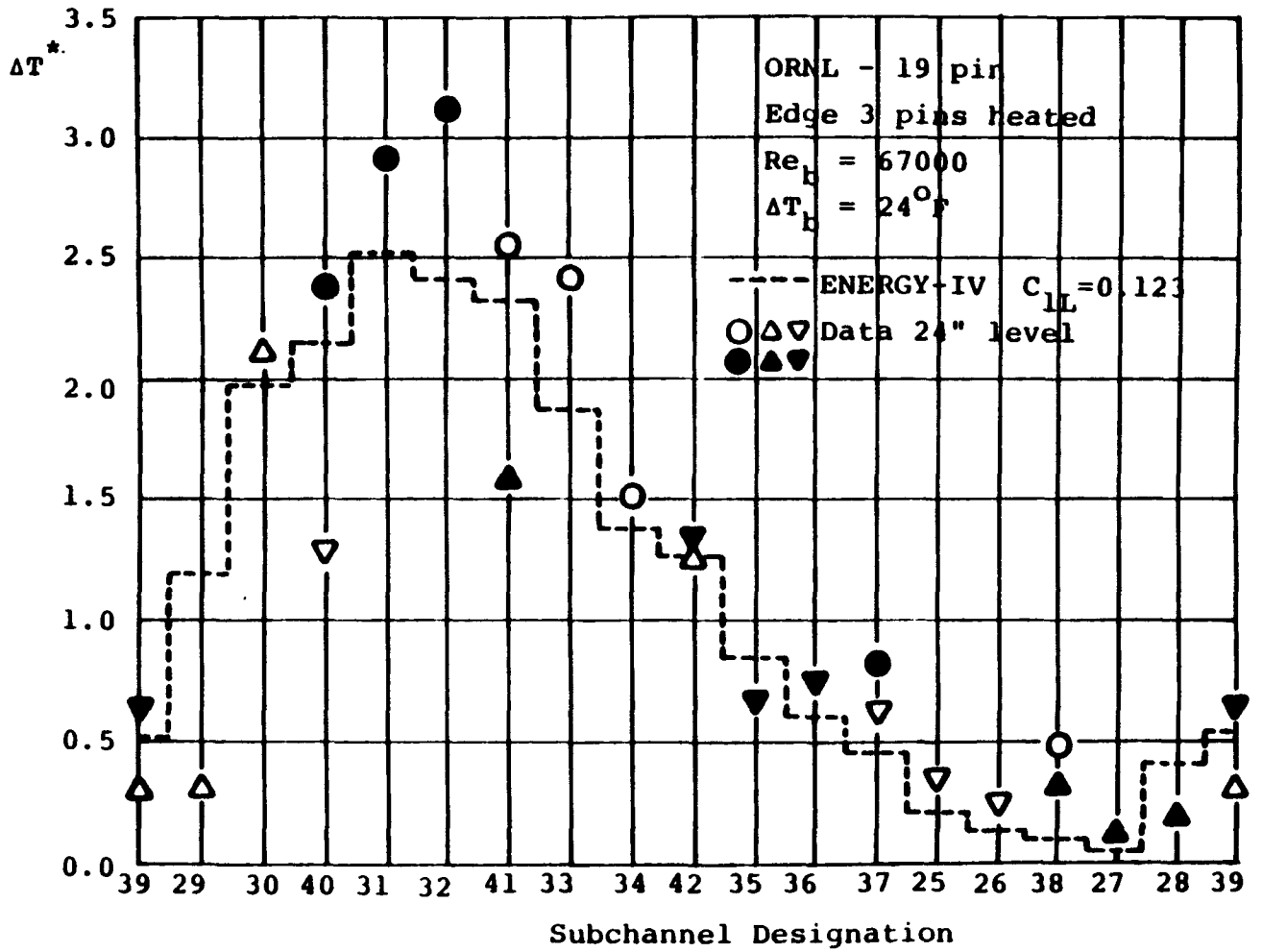

Figure 8.15 Measured and Predicted Temperature Rise in the Edge Subchannel for ORNL 19-pin Bundle

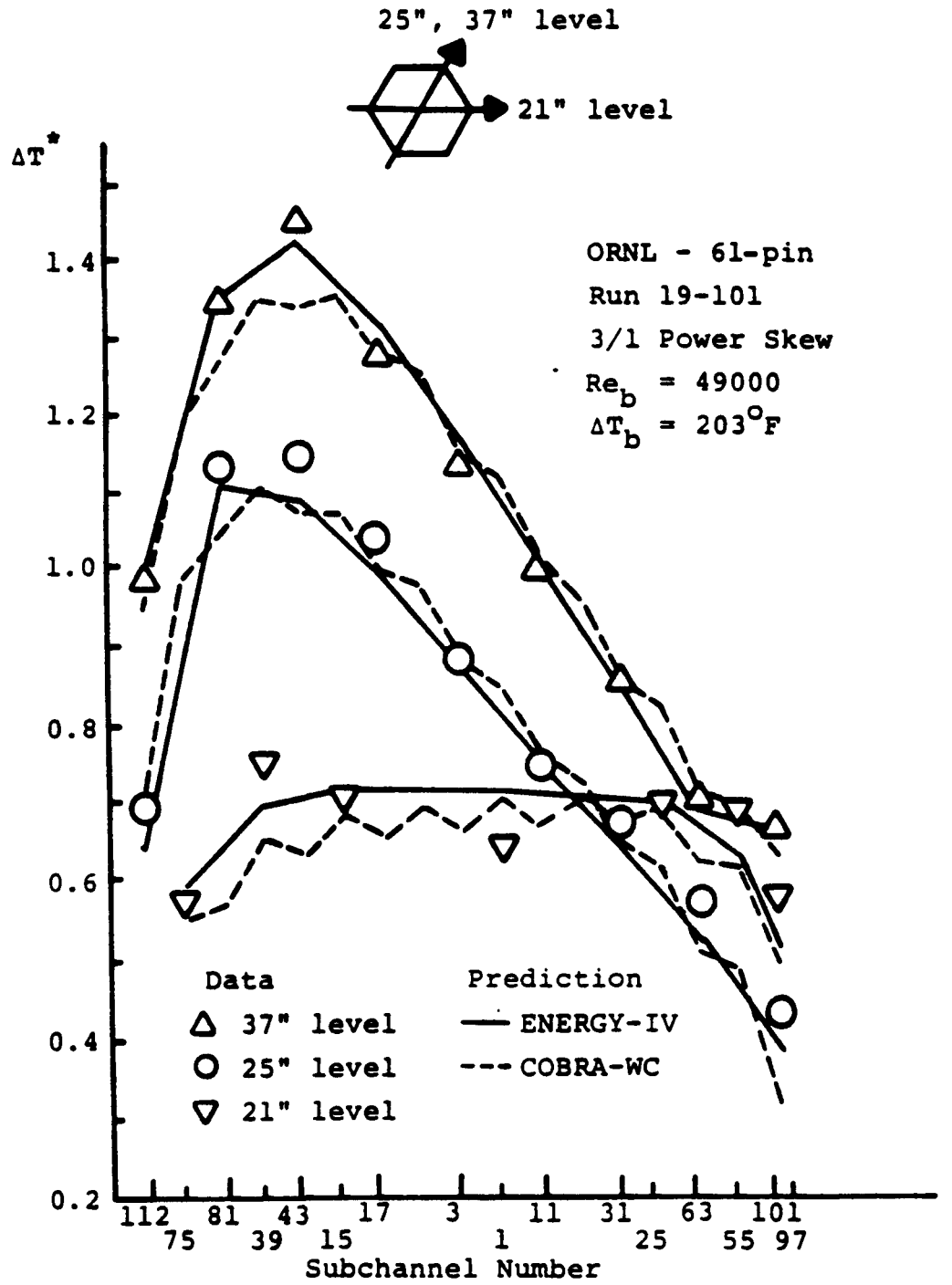

Figure 8.16 Measured and Predicted Temperature Rise for ORNL - 61-pin Run 19-101

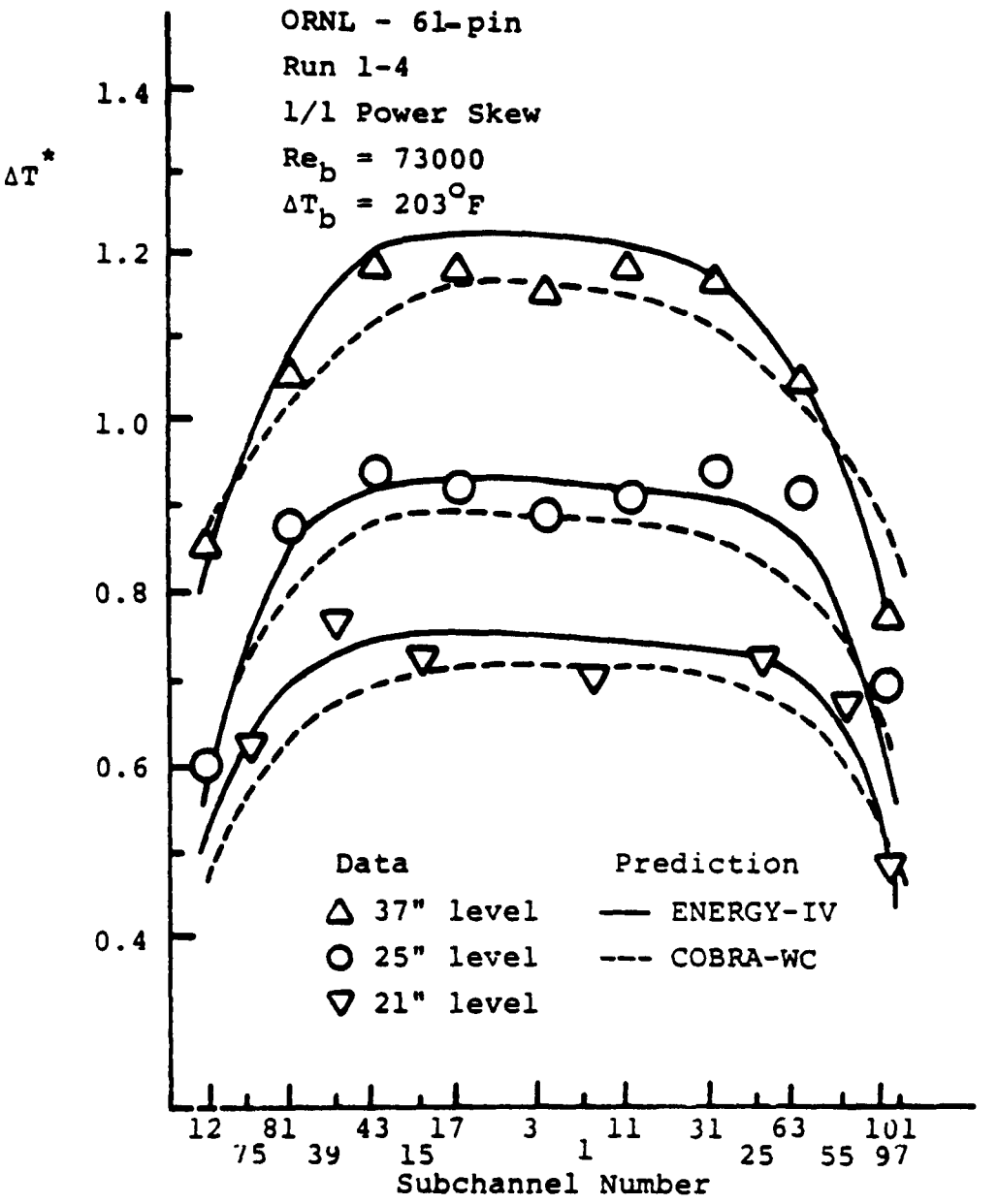

Figure 8.17 Measured and Predicted Temperature Rise for ORNL - 61-pin Run 1-4

Figure 8.19 shows the sensitivity of the calculation results of ENERGY-IV to $\varepsilon^*_{l\eta}$. With a ±35% (±0.05) change of $\varepsilon^*_{l\eta}$, the average change in ΔT in the high temperature region is about ± 0.04 or ±8°F.

8.3.3 Comparison between Data and Predictions for Toshiba Bundle

Figure 8.19 illustrates the comparison among the data at high flow rates of Toshiba bundle with different power skews, the ENERGY-IV predictions and the COBRA predictions. The COBRA input parameters for calculating Toshiba cases are depicted in Table 8.5. The maximum temperatures in different power skews are accurately predicted by both the ENERGY-IV and the COBRA codes. ENERGY-IV predicts well the temperatures in the high power region, while it overpredicts the temperatures in the lower power region, especially for the 2/1 power skew case. The COBRA predictions have just the opposite trends. The overall behavior of these data, however are satisfied by the predictions.

8.3.4 Conclusions

The validation of the ENERGY-IV for the forced convection condition has been illustrated in the previous sections with geometries ranging from typical fuel assembly geometries to blanket assembly geometries and power skew across the assemblies ranging from uniform to 3/1. The predictions of the ENERGY-IV are found to be more accurate than, or at least similar to that of the COBRA. The maximum temperature difference between the ENERGY predictions and the data are less than 7% of the bulk temperature rise (ΔT_b),i.e., 12.5°F for the most severe case.

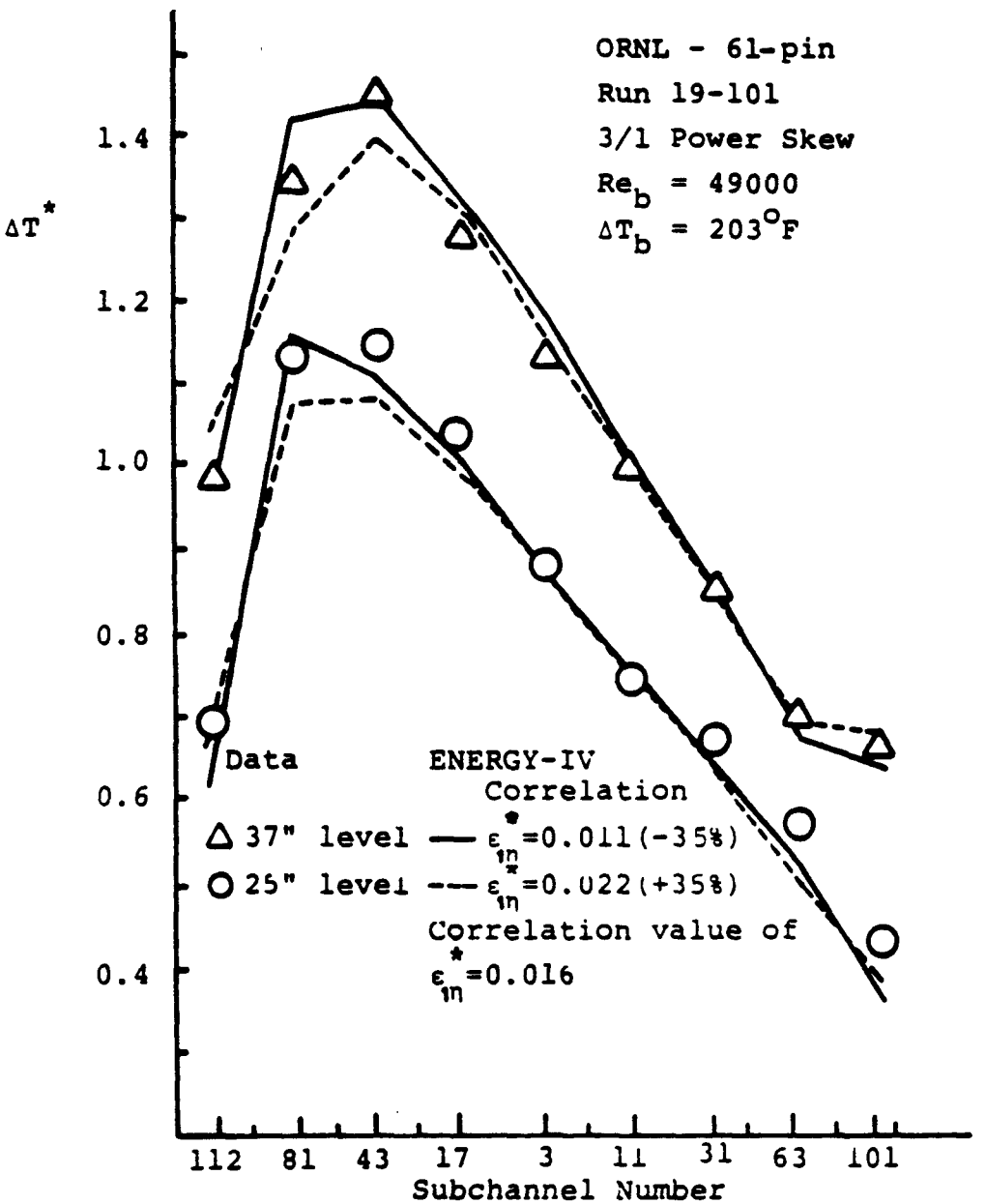

Figure 8.18 Sensitivity of $\varepsilon^*_{\eta\eta}$ to the ENERGY-IV Results for ORNL - 61-pin Run 19-101

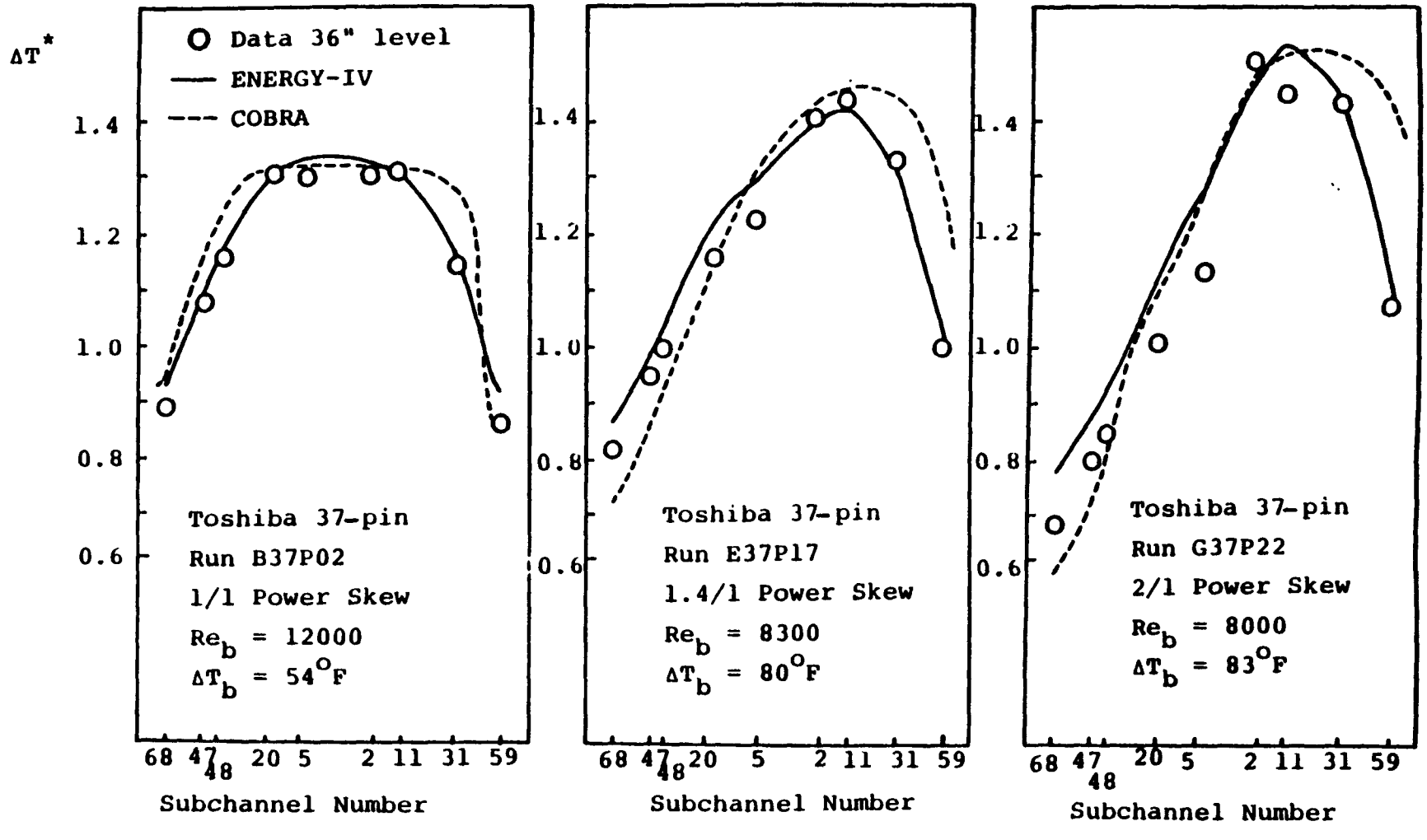

Figure 8.19 Measured and Predicted Temperature Rise for Toshiba 37-pin Bundle

Table 8.5 Input Parameters Used in COBRA-IV for Toshiba Tests

Summary of COBRA-IV input parameters

Parameter	
Turbulent mixing parameter	0.02 (Re ≥ 1200) 0.00 (Re < 1200)
Transverse momentum parameter	0.5
Wire wrap sweeping parameter	0.03
Conduction factor	0.5
Friction factor	$f = 41.7/Re + 0.12/Re^{0.159}$ (Re≥1200) $f = 37.3/Re^{0.872}$ (Re<1200)

The favorable comparison of ENERGY-IV to COBRA is not suprising when one realized that the empirical input parameters for the ENERGY-IV are much better calibrated than those for the COBRA-WC code. Although a much more complicated method is used in the COBRA-WC, a simplified method as employed in ENERGY-IV with fine calibrated input parameters can do a better job in the forced convection region. However, the COBRA-WC code is intended to be a bench-mark code which is assumed to be applicable outside its validation range, while the ENERGY-IV is a totally empirical code which can only be used inside the validation range as a fast running design tool.

As for the sensitivity of the calculation results of the ENERGY-IV to $\varepsilon^*_{1\eta}$. Table 8.6 shows the changes of maximum ΔT^* calculated by the ENERGY-IV for different power skews for both blanket and Fuel bundles. The temperature difference caused by 25% change of $\varepsilon^*_{1\eta}$ is about 6 - 12°F for typical fuel and blanket operation conditions, respectively.

8.4 Validation of the ENERGY-IV in the Mixed Convection Condition

The major difference between the forced convection option and the mixed convection option of the ENERGY-IV code is that flow redistribution due to the buoyancy force is modelled in the mixed convection option. This is accomplished by solving the overall mass, energy, and axial momentum conservation equations with the assumption of a uniform pressure across the bundle. Since the momentum equation is used, the subchannel friction factors are required as input parameters in addition to the input parameters required for the energy

Table 8.6 Sensitivity of the ENERGY-IV Calculation to ε^*_{ln}

Bundle	ε^*_{ln}	Change of ε^*_{ln}	Change of the Maximum ΔT^* Power Skew 3/1	2/1	1/1
WARD (Blanket)	0.122	per 25%	0.065	0.045	0.030
		per 0.01	0.021	0.015	0.010
ORNL (Fuel)	0.016	per 25%	0.030	-	0.020
		per 0.01	0.075	-	0.050

equation in the forced convection condition, i.e., the inlet flow split parameter, X_i, the dimensionless effective eddy diffusivity, $\varepsilon^*_{1\eta}$, $\varepsilon^*_{2\eta}$, the edge transverse velocity ratio, C_{1L}, and the conduction shape factor, κ. Use of these parameters in the equations for the mixed convection option was discussed in chapter 2.

As mentioned before, the conduction shape factor for wire-wrapped rod bundle is still an open quesion. In the following ENERGY-IV calculations, the bare rod values for κ developed in chapter 6 will be assumed to be applicable in wire-wrapped rod bundle. In section 8.5, it will be shown that this assumption is satisfactory.

In addition to these features, thermal plume effects, which enhance the mixing between subchannels, contribute a significant amount of energy transfer in the mixed convection regime. An estimation of this thermal plume mixing expressed as the parameter $\varepsilon^*_{\eta M}$ is required for the ENERGY-IV calculation.

In this section, the phenomena generated by the buoyancy effects, i.e., subchannel friction factor in the mixed convection condition, flow redistribution and thermal plume mixing will be discussed first. After a correlation for $\varepsilon^*_{\eta M}$ is proposed, the predictions of the ENERGY-IV code are compared to the data. Meanwhile the sensitivity of the ENERGY-IV predictions to the $\varepsilon^*_{\eta M}$ parameter will also be investigated. The data base selected for the validation of the ENERGY-IV in the mixed convection condition are depicted in Table 8.7.

Table 8.7 Cases Used for Mixed Convection Validation

Bundle	Run	Flow (GPM)	Rod (kW/ft)	Power Skew	Re_b	$Gr_{\Delta T}$	$\frac{Gr_{\Delta T}}{Re_b}$	T_{in} (F)	$\Delta T_b^{\dagger}$ (F)
WARD	221	18.1	0.571	2.8/1	4390	400	0.091	600	181
61-pin	229	4.8	0.150	2.8/1	1160	390	0.336	600	178
	231	2.3	0.075	2.8/1	560	410	0.732	600	186
	401	4.89	0.146	2/1	1180	375	0.318	605	171
	731	3.34	0.094	2/1	800	350	0.438	602	162
	720	2.29	0.062	2/1	520	360	0.692	600	165
	227	4.90	0.147	1/1	1180	370	0.314	602	171
	732	3.44	0.096	1/1	820	340	0.415	602	159
ORNL	19-105	4.2	0.270	3/1	2250	620	0.276	729	308
61-pin	18-105	4.2	0.278	2/1	2270	650	0.286	736	318
	17-105	4.3	0.281	1.5/1	2320	640	0.276	739	314
	12-114	2.2	0.067	1/1	1110	260	0.234	722	144
Toshiba	G37P25	5.24	0.484	2/1	3070	280	0.091	399	250
37-pin	L37P43	2.39	0.302	2/1	1500	450	0.300	401	345
	F37P20	5.24	0.477	1.4/1	3060	280	0.092	400	246
	F37P27	2.85	0.289	1.4/1	1700	320	0.188	400	274
	C37P06	5.47	0.364	1/1	2920	170	0.058	378	178
	E37P13	1.54	0.119	1/1	880	230	0.261	404	208
Grenoble	1a	24.11	0.352	1/1	3420	404	0.118	600	148
91-pin	1b	12.24	0.177	1/1	1740	400	0.230	600	146
	1c	4.45	0.062	1/1	630	380	0.603	600	140
	2	12.61	0.186	2.5/1	1790	410	0.230	600	150

† Energy balance value

8.4.1 Phenomena Caused by Buoyancy Effects in the Mixed Convection Condition

8.4.1.1 Subchannel Friction Factors

The subchannel friction factor correlations developed in chapter 4 are for the forced convection condition only. In the mixed convection condition, buoyancy increases the velocity gradient near the wall, thus increasing the friction factor. Hence the forced convection subchannel friction factor needs to be modified to take into account these buoyancy effects.

The effects of buoyancy on the friction factor in a circular tube was studied by Bishop et al. (1980). An analytical solution of the conservation equations was found for fully developed flow. From the solution for the velocity field, the friction factor was obtained. An algebraic fit to the analytical results was found to be:

$$\frac{f}{f_o} \equiv \left[1 + 2.97 \times 10^{-3} \frac{Gr_q}{Re}\right]^{0.655} \equiv F \qquad (8.3)$$

where f = friction factor taking into account buoyancy effects

f_o = forced convection friction factor

Gr_q = Grashof Number based on heat flux

$\equiv \beta g D_e^4 q''/k\nu^2$

Equation (8.3) will be assumed to be also applicable to the subchannel friction factor. The subchannel mixed convection friction factors are taken equal to the forced convection correlations multiplied by the factor F. The local (subchannel) value of the

Grashof number based on subchannel heat flux is used for calculating F. The parameter generally used in this chapter is a global Grashof number based on bundle axial averaged temperature gradient, $(\Delta T_b/L)$. The bundle average Gr_q can be related to $Gr_{\Delta T}$ as

$$Gr_q = \frac{Re\ Pr}{4\left(\frac{De_b}{D_H}\right)} Gr_{\Delta T} \tag{8.4}$$

where $D_H \equiv \frac{4A_b}{P_H}$

A_b = Bundle flow area

P_H = Bundle heated perimeter

An estimate of the value of F for typical sodium mixed convection conditions is

$\frac{De_b}{D_H} \approx 1.0$

$Pr \simeq 0.004$

$Gr_{\Delta T} \simeq 500$ for typical operation,

hence $(Gr_q/Re) \approx 0.5$. Substituting this value of (Gr_q/Re) into equation (8.3), yields $F \approx 1.001$. Thus only about a 0.1% increase in friction factor due to buoyancy effects is anticipated. We therefore conclude that for typical mixed convection operation, the increase in subchannel friction factors due to buoyancy effects is negligible. However, this correction factor was implemented in the ENERGY-IV for completeness of the correlation.

8.4.1.2 Flow Redistribution

The flow redistribution due to buoyancy effects is modelled by the ENERGY-IV in a much simpler way than that in the COBRA code as discussed in chapter 2. The COBRA code calculates the diversion cross flow utilizing the transverse momentum equation. This equation is not used in the ENERGY-IV code.

The validity of the simple model for calculating flow redistribution in ENERGY-IV can be checked by comparing the axial velocity fields at different axial levels calculated by ENERGY-IV to those calculated by COBRA-WC. Figure 8.20 compares the axial velocity distribution across the bundle from high power region to low power region at different axial levels for the WARD Run 229 with Re_b = 1160 and $Gr_{\Delta T}$ = 390. Two ENERGY-IV calculation results, one for $\varepsilon^*_{1\eta}$ = 0.082 (forced convection correlation values) and the other one for $\varepsilon^*_{1\eta}$ = 0.20 (including a 0.118 increment to the correlation value), are presented. As we should see later, the 0.118 increment is the enhancement due to the thermal plume effects. This figure shows that the velocity distributions calculated by ENERGY-IV are very close to those calculated by COBRA, especially for the $\varepsilon^*_{1\eta}$=0.20 case in which the values are almost the same for the central region. Discrepancies between the COBRA and ENERGY-IV ($\varepsilon^*_{1\eta}$ = 0.20) predictions, however, are found in the edge subchannels and the interior subchannels adjacent to the edge subchannels. Dips in the interior subchannels next to the edge region are always exhibited in the COBTA results. This might be the reason that the velocities in the edge subchannels for the COBRA

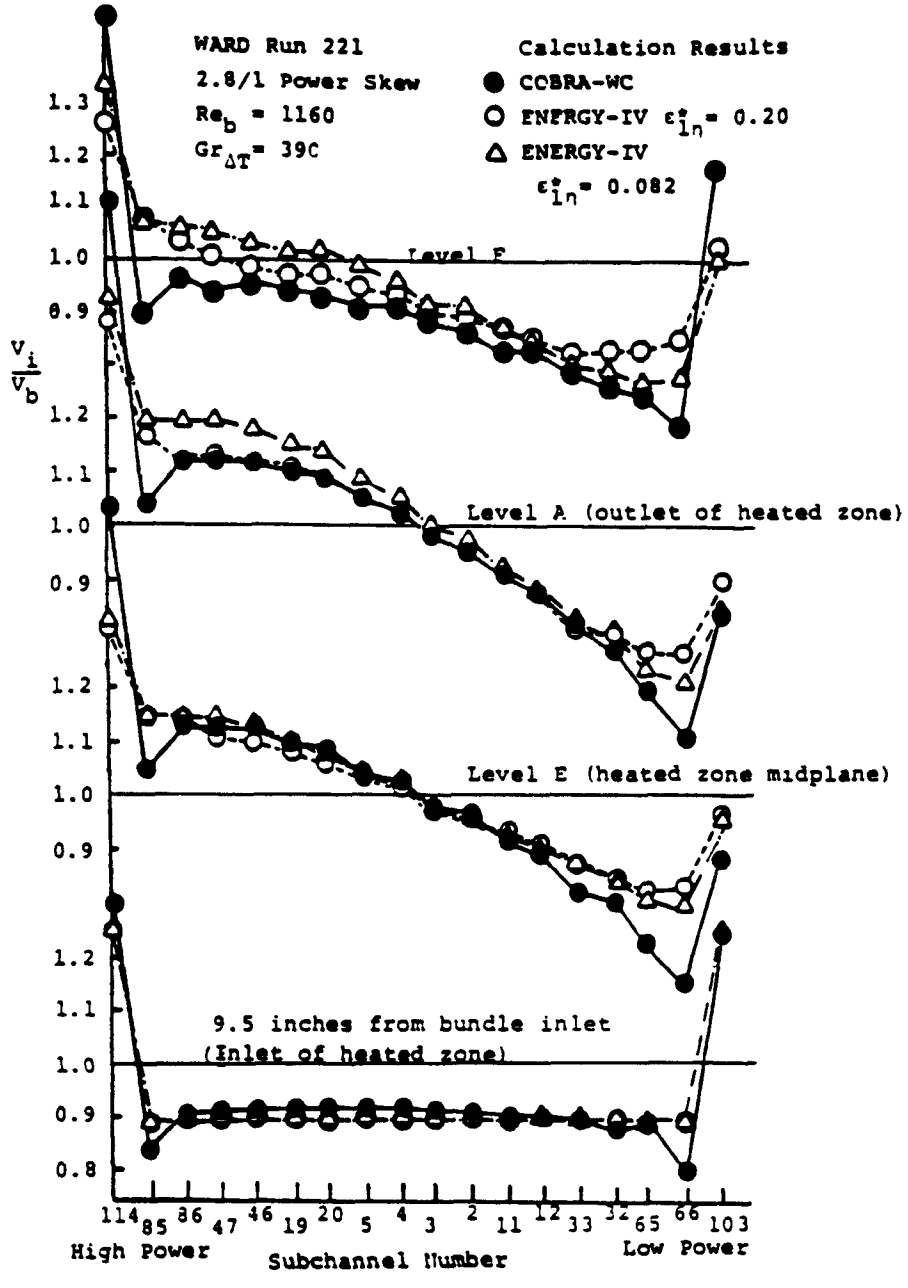

Figure 8.20 Velocity Distributions Calculated by COBRA-WC and ENERGY-IV in the Mixed Convection Condition

results are higher than those for the ENERGY-IV results. This situation must be caused by the pressure distribution calculated by COBRA, which generates this solution through the transverse momentum equation. The physical reason for this phenomenon, however, is not clear to us.

8.4.1.3. Mixing Enhanced by Thermal Plume Effects

Thermal plumes have been visually observed by Bates and Khan(1980) and Symolon (1982) for heated bundles in low flow rate operations. In this study, use of only the forced convection value of $\varepsilon^*_{l\eta}$ in the ENERGY-IV code were always found to overpredict the maximum ΔT^* of the mixed convection data. Since ENERGY-IV predicts the forced convection temperature data very well, and the flow redistribution seems to be correct as discussed in the last subsection, we conclude that an additional mixing mechanism exists in the mixed convection regime. The thermal plume phenomenon is probably the origin for this mixing mechanism.

A Thermal Plume Mixing Parameter (TPMP), $\varepsilon^*_{\eta M}$, was defined similar to $\varepsilon^*_{l\eta}$, i.e.,

$$\varepsilon^*_{\eta M} = \frac{\text{transverse mass flux due to thermal plume effects}}{\text{axial mass flux}}$$

to quantitatively represent the enhanced mixing caused by thermal plumes. Symolon (1982) investigated a simple model for this mixing mechanism. According to similar fundamental consideration, Appendix E1 presents a model for $\varepsilon^*_{\eta M}$ which indicates that $\varepsilon^*_{\eta M}$ should be a

function of bundle geometry, $Gr_{\Delta T}/Re$, and local relative power density. Although $\varepsilon^*_{\eta M}$ should be a local phenomenon which depends on local power to flow ratio, we recommend use of a bundle global value for simplicity. Use of a local value of $\varepsilon^*_{\eta M}$ as a function of relative power density was investigated but found not to improve the predictions significantly.

Cases listed in Table 8.7 were used to estimate the thermal plume enhanced mixing parameter $\varepsilon^*_{\eta M}$ as a function of geometry, $Gr_{\Delta T}/Re$, and power skew by matching the ENERGY-IV calculating to the data. The power skew influence on this global $\varepsilon^*_{\eta M}$ was found to be insignificant. The correlation constructed for $\varepsilon^*_{\eta M}$ according to this procedure was,

$$\varepsilon^*_{\eta M} = 0.1\left(\frac{c}{D}\right)^{-0.5}\left(\frac{Gr_{\Delta T}}{Re_b}\right) \qquad (8.5)$$

For ENERGY-IV calculations in the mixed convection condition, the appropriate total interchannel mixing parameter is the sum of this enhanced parameter, $\varepsilon^*_{\eta M}$, and the forced convection dimensionless eddy diffusivity, $\varepsilon^*_{\eta F}$, ($\varepsilon^*_{1\eta}$ for the interior subchannel and $\varepsilon^*_{2\eta}$ for the edge subchannel)

8.4.2 Comparisons between Data and Predictions in the Mixed Convection Condition

8.4.2.1 WARD Bundle

Figure 8.21 illustrates the comparison among the data, the ENERGY-IV predictions and the COBRA predictions for WARD Run 221. Figure 8.22 compares the calculation results of ENERGY-IV with four

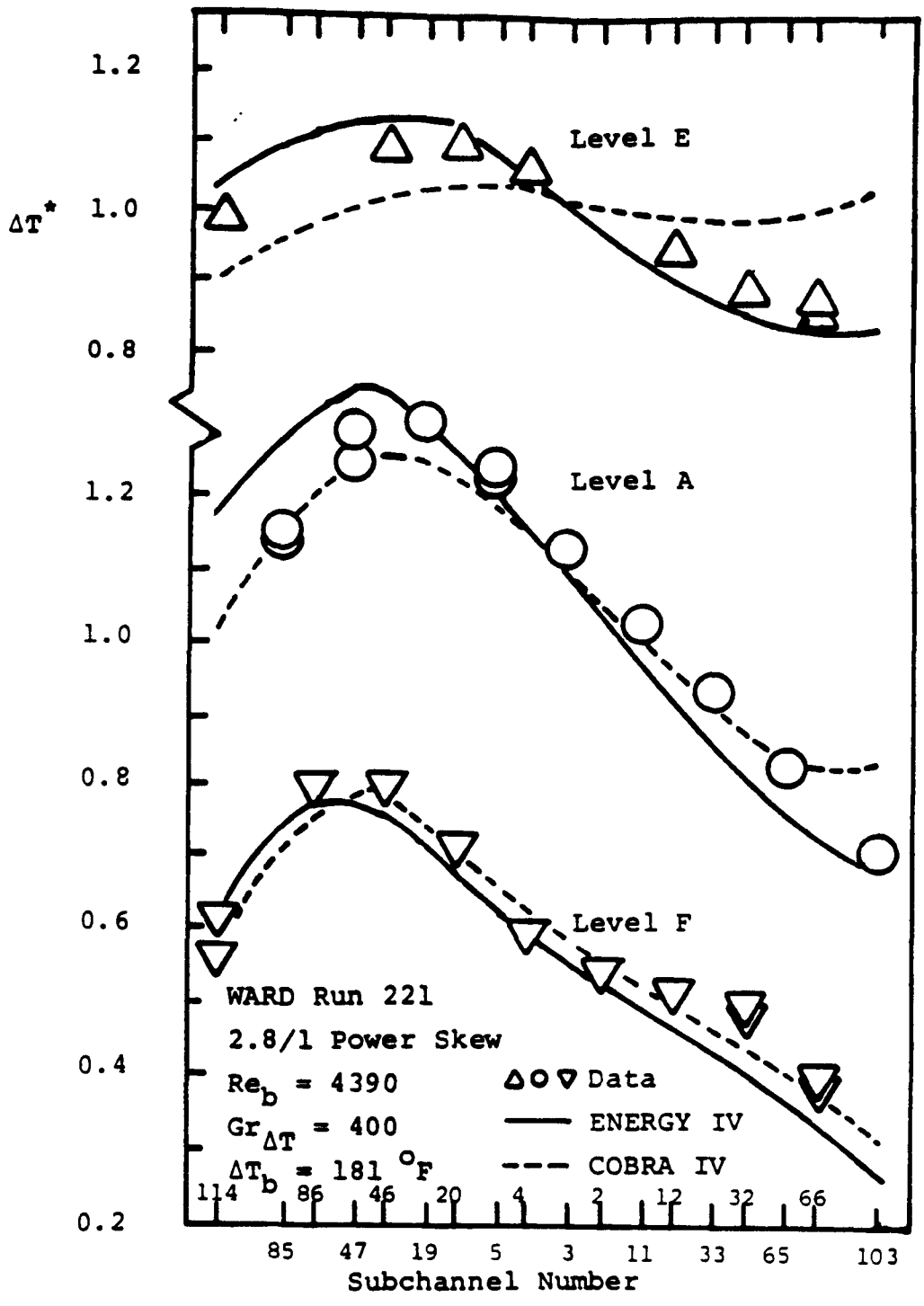

Figure 8.21 Measured and Predicted Temperature Rise for Ward Run 221

different options: recommended ε^*_η (i.e., $\varepsilon^*_{\eta F} + \varepsilon^*_{\eta M}$), $\varepsilon^*_{\eta F}$ only, recommended ε^*_η plus one additional $\varepsilon^*_{\eta M}$ increment (i.e., $\varepsilon^*_{\eta F} + 2\varepsilon^*_{\eta M}$) and the forced convection method with $\varepsilon^*_{\eta F}$ (i.e., no flow redistribution). Similarly, Figures 8.23 and 8.24, and Figures 8.25 and 8.26 illustrate the comparisons and sensitivity of the computed ΔT^* to $\varepsilon^*_{\eta M}$ for WARD Run 229 and Run 231, respectively. The COBRA-IV predictions for Run 231 were not available in the literature.

Figures 8.22, 8.24, and 8.25 not only show the sensitivity of the calculation results to $\varepsilon^*_{\eta M}$ but also compare the effects of flow redistribution to the temperature distribution. The flow redistribution reduces the maximum ΔT^* by values of 0.05, 0.17, and 0.22 for Runs 221, 229, and 231, corresponding to $Gr_{\Delta T}/Re_b$ = 0.091, 0.336, and 0.732, respectively. As the $Gr_{\Delta T}/Re_b$ increases, the flow redistribution effect becomes more and more dominant in establishing the temperature distribution. The maximum ΔT^* decreases by 0.04, 0.035, and 0.025 for each $\varepsilon^*_{\eta M}$ increment, (0.032, 0.117, and 0.256) for Run 221, 229, and and 231, respectively.

The sensitivity study of $\varepsilon^*_{l\eta}$ illustrates the way we estimated $\varepsilon^*_{\eta M}$ for each case. For these three cases, the temperature data in the low power region were always higher than the predictions even when high $\varepsilon^*_{\eta M}$ were used. Use of a mean square indicator method such as that in chapter 5 might not be adequate since a very high $\varepsilon^*_{\eta m}$ would be required to match the temperature data in low power region to give a minimum mean square indicator. Instead, we estimate $\varepsilon^*_{\eta M}$ by engineering judgements based on two considerations: the maximum temperature rise

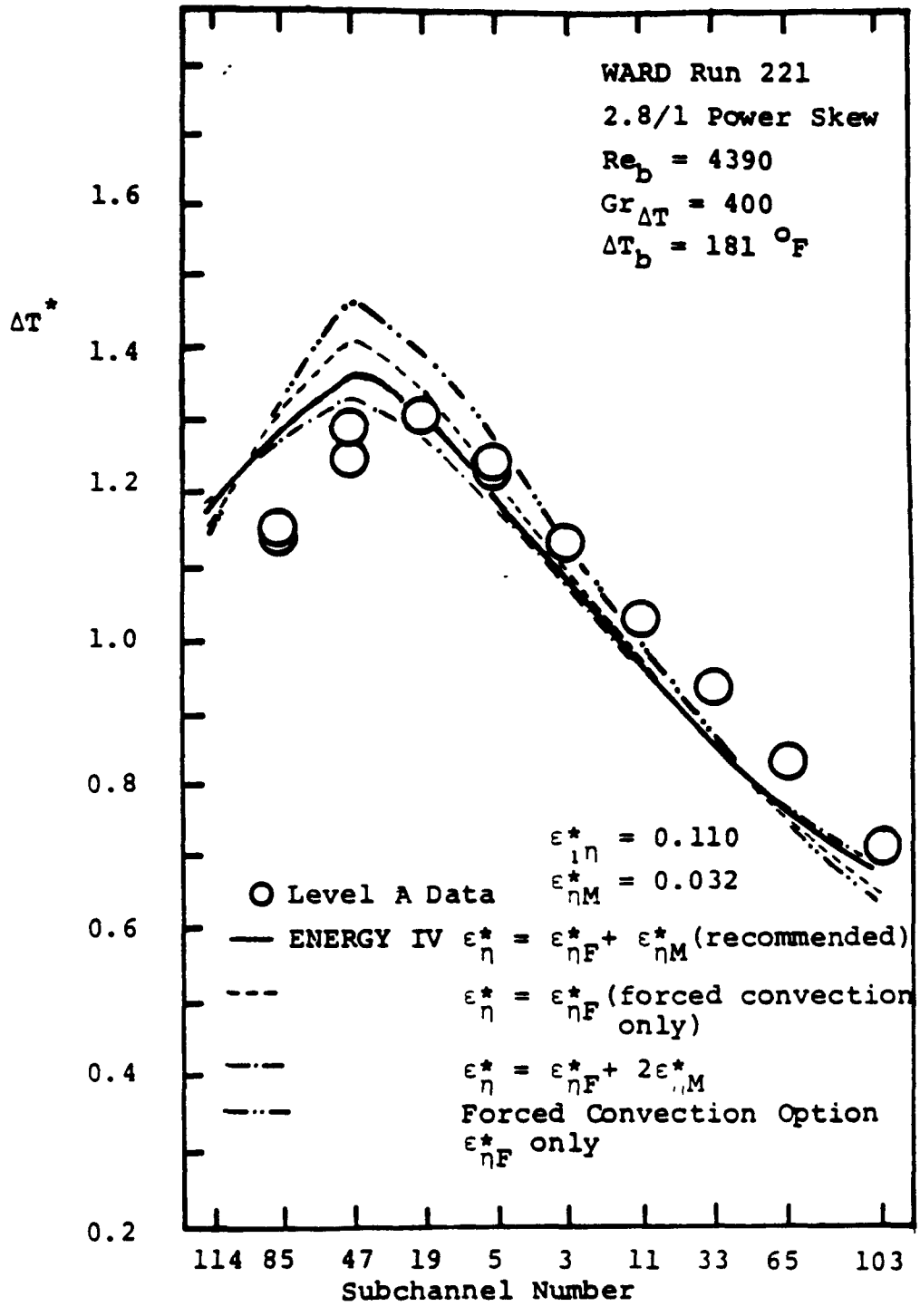

Figure 8.22 Sensitivity of $\varepsilon^*_{\eta M}$ to ENERGY-IV Results for WARD Run 221

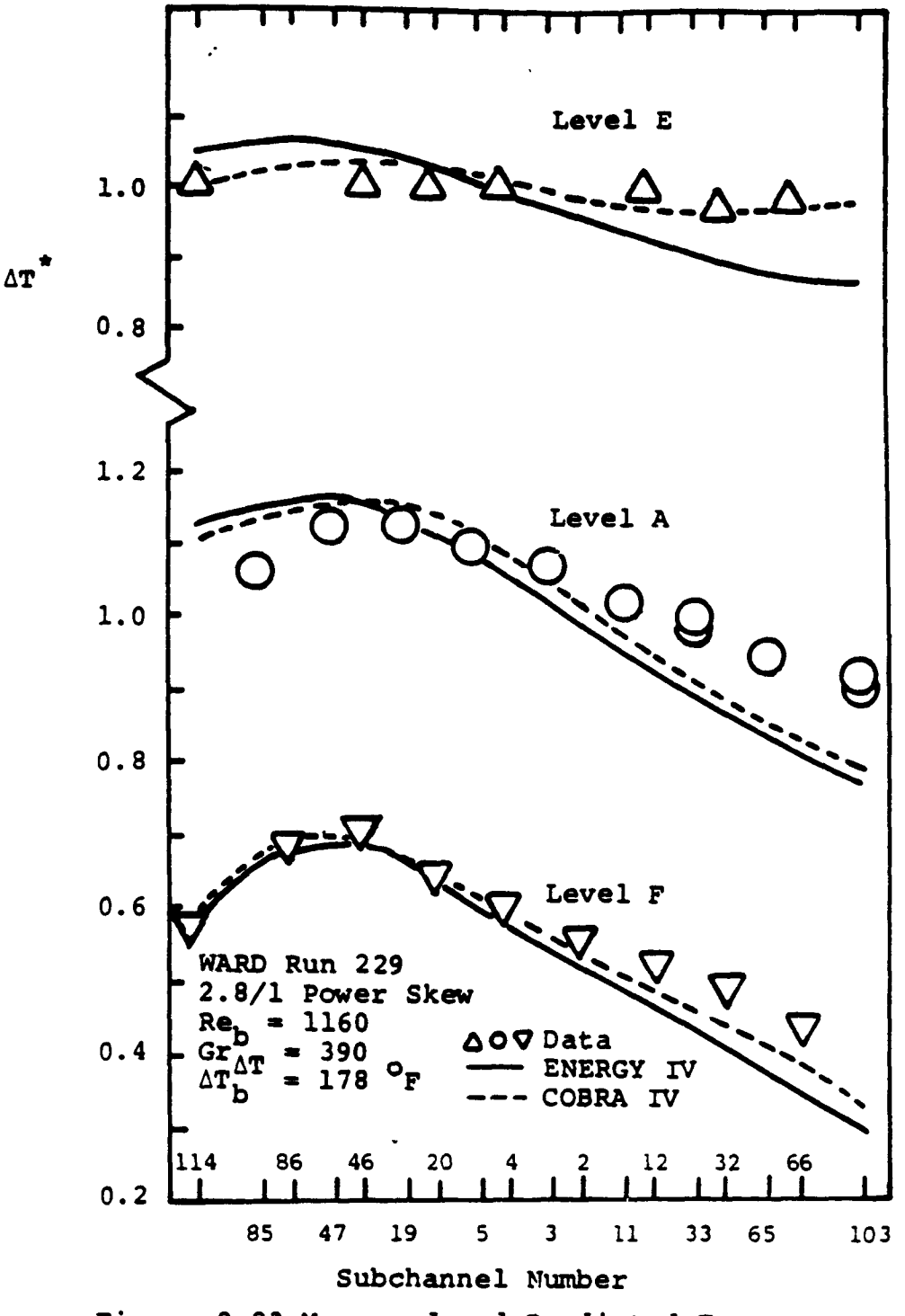

Figure 8.23 Measured and Predicted Temperature Rise for WARD Run 229

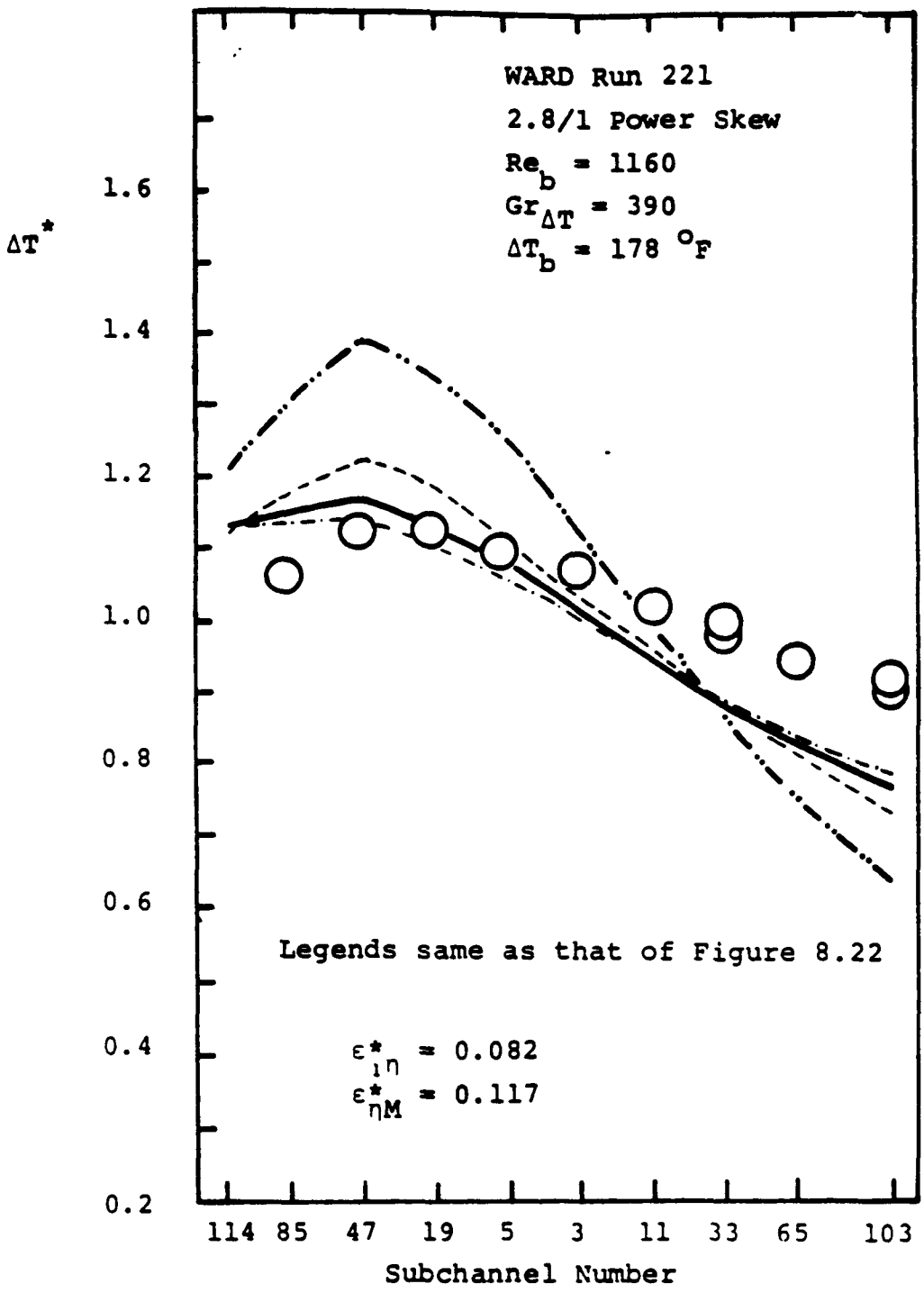

Figure 8.24 Sensitivity of the ENERGY IV Results to $\varepsilon^*_{\eta M}$ for WARD Run 229

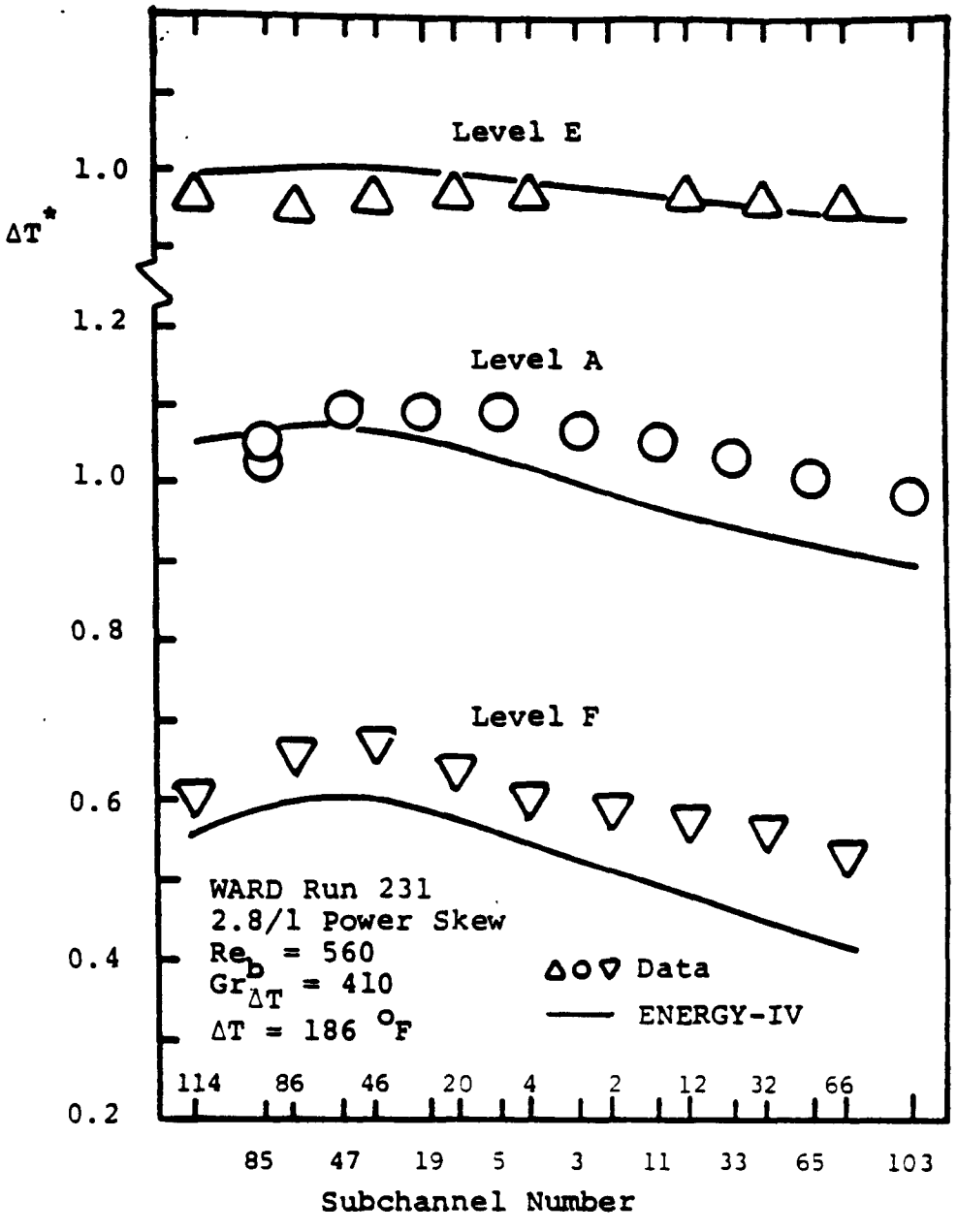

Figure 8.25 Measured and Predicted Temperature Rise for Ward Run 231

should be reasonably predicted, and the shape of temperature profiles should be comparable. This method was found to allow securing consistent $\epsilon^*_{\eta M}$ values for all the other cases and lead to the proposed correlation, equation (8.5).

As shown in Figures 8.21 and 8.23, Th predictions of ENERGY-IV have the same degree of accuracy as that of COBRA-IV. For the high $Gr_{\Delta T}/Re_b$ case in Figure 8.25 (Run 231, $Gr_{\Delta T}/Re_b = 0.732$), the shape of the data is predicted by the ENERGY-IV; however, all the ΔT^* data at level A are higher than 1.0 indicating that an energy balance error might exist in the measured data.

For 2/1 power skew cases, Figures 8.27, 8.28, 8.29 compare the data and ENERGY-IV predictions for Runs 401, 731, and 720 respectively. The mixed convection calculations by ENERGY-IV using $\epsilon^*_{\eta F}$ only are also presented in these figures. Similar comparisons for uniform power skew cases, Run 227 and Run 732, are illustrated in Figures 8.30 and 8.31, respectively. As observed from these figures, the sensitivity of $\epsilon^*_{\eta M}$ is almost the same as for different power skews.

The ENERGY-IV code predicts all these WARD cases very well except for the level A data of 2/1 power skew cases and Run 229 (2.8 power skew). Although the maximum ΔT^*'s for these cases are well predicted, the prediction of the subchannel location of maximum temperature are shifted to the high power side, and underpredictions are found in the lower power region. This situation, however, is not observed in the prediction for other bundles with similar power skews as we will see

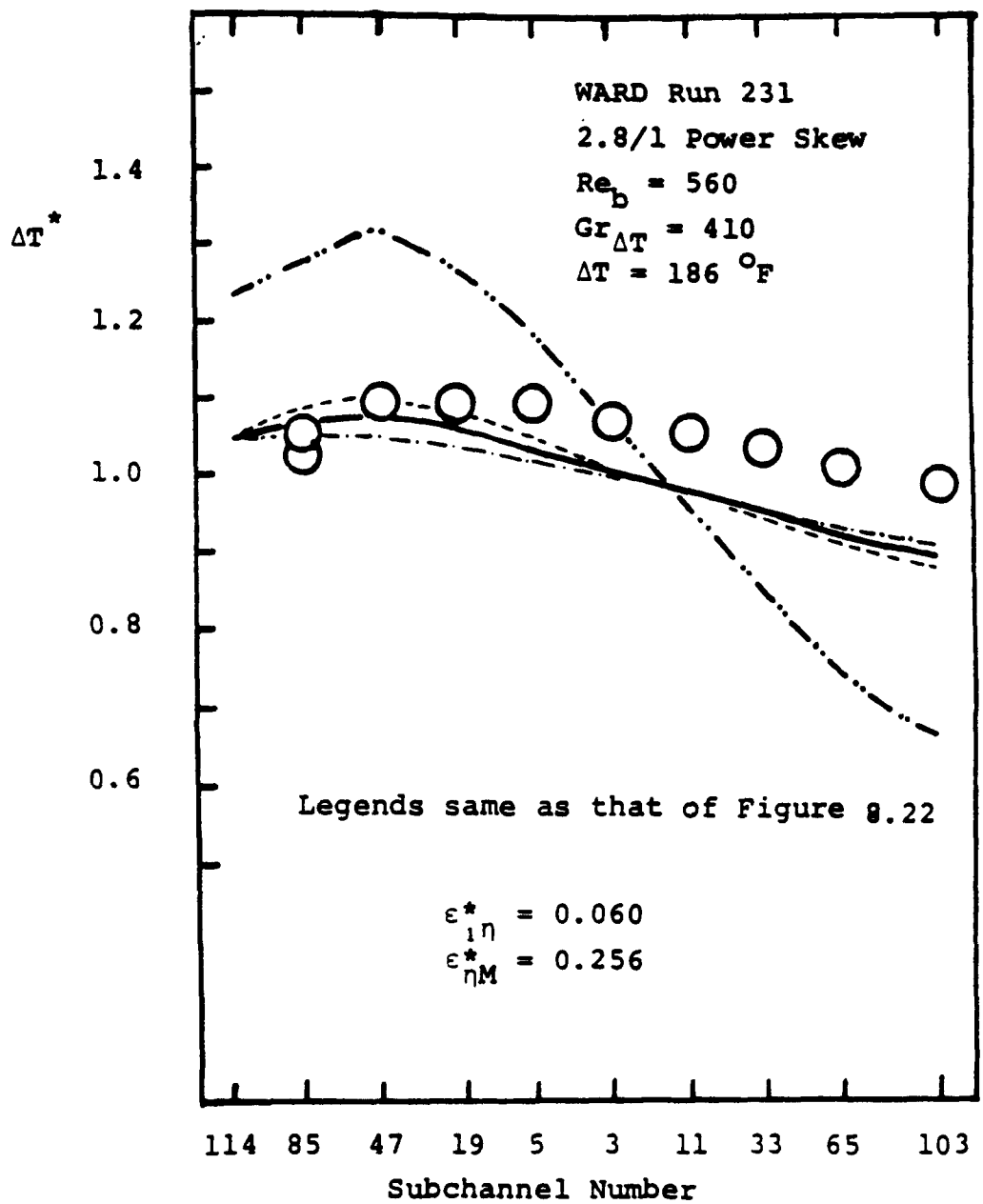

Figure 8.26 Sensitivity of ENERGY-IV Results to $\varepsilon^*_{\eta M}$ for WARD Run 231

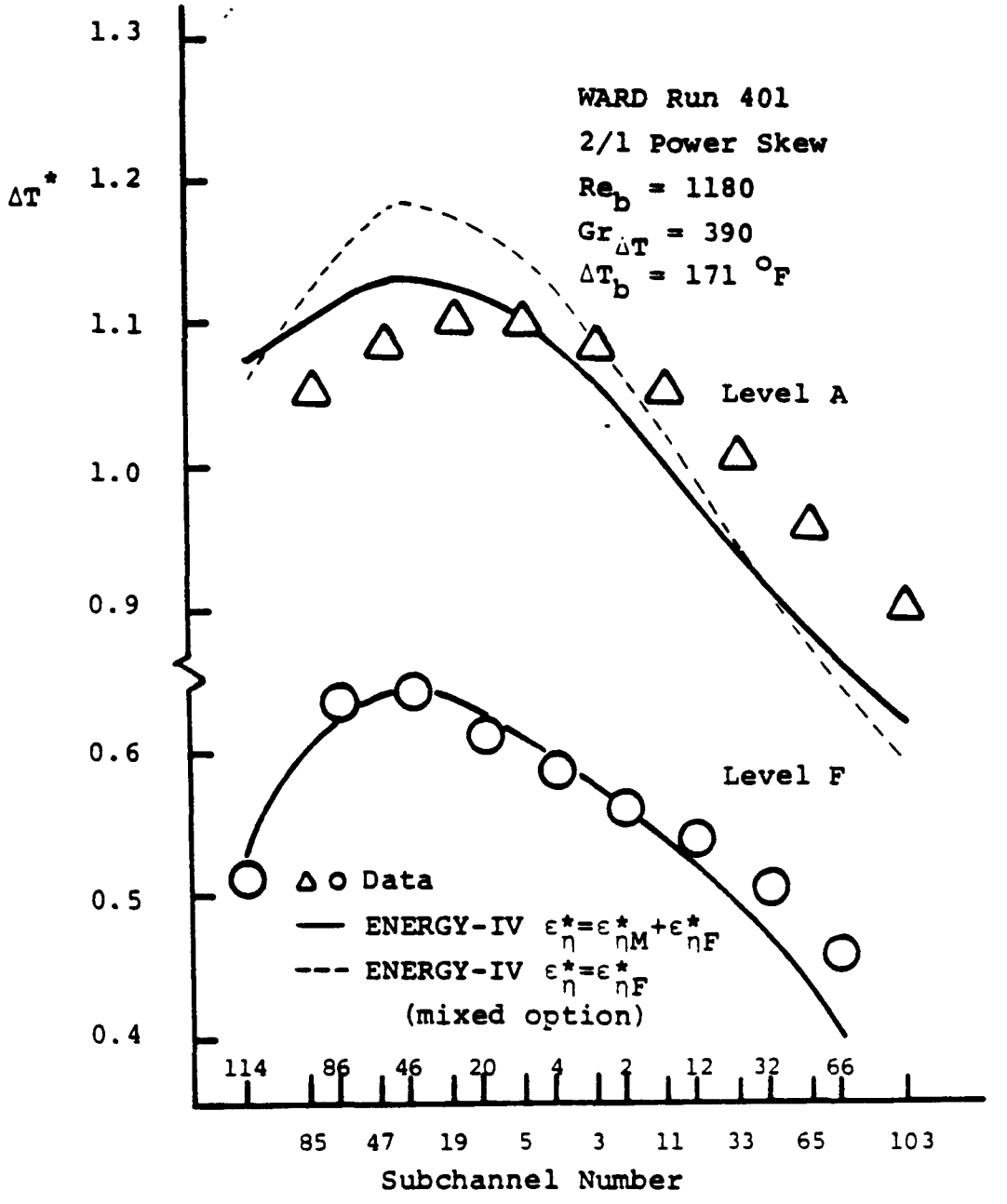

Figure 8.27 Measured and predicted Temperature for WARD Run 401

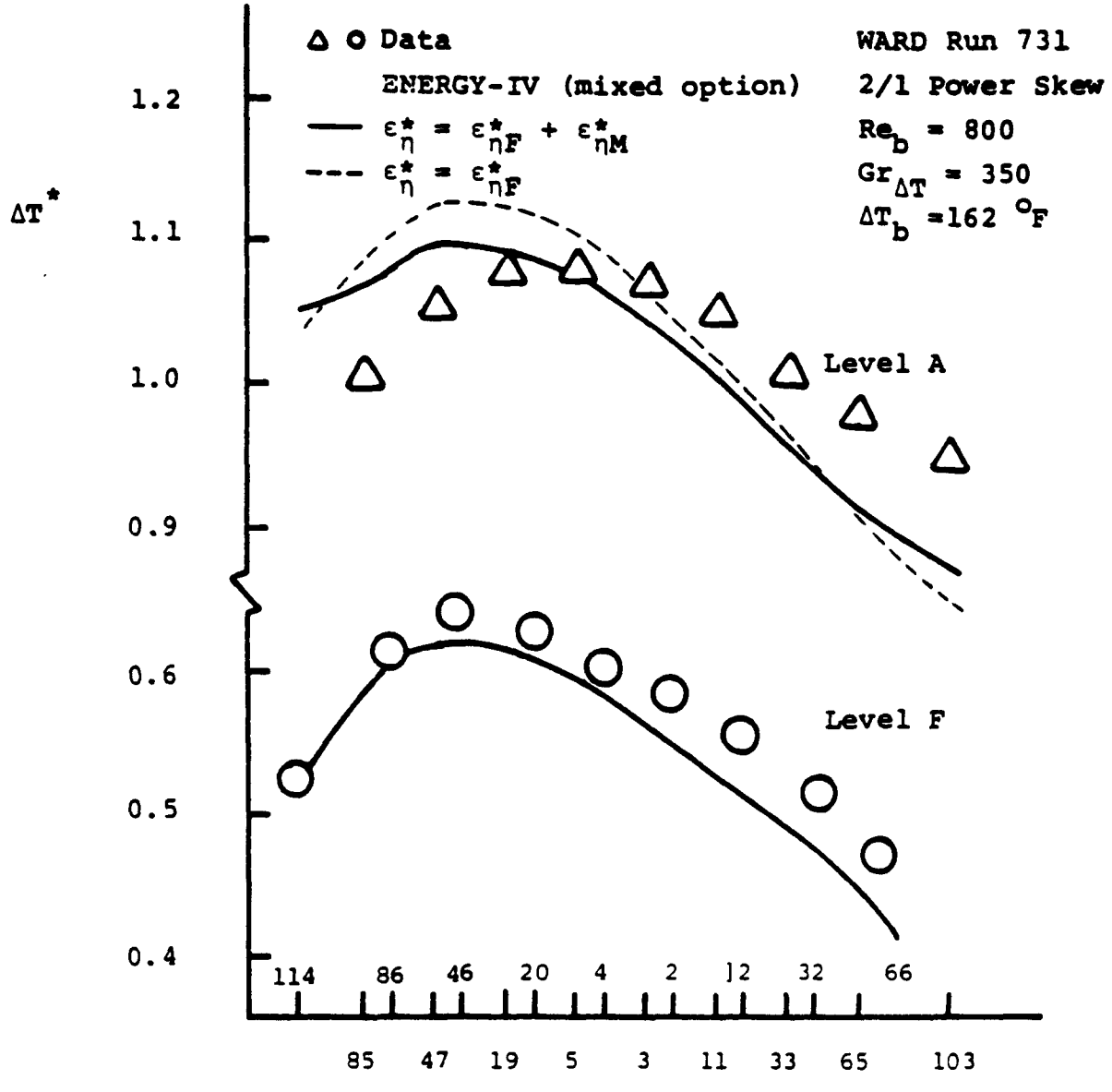

Figure 8.28 Measured and Predicted Temperature Rise for WARD Run 731

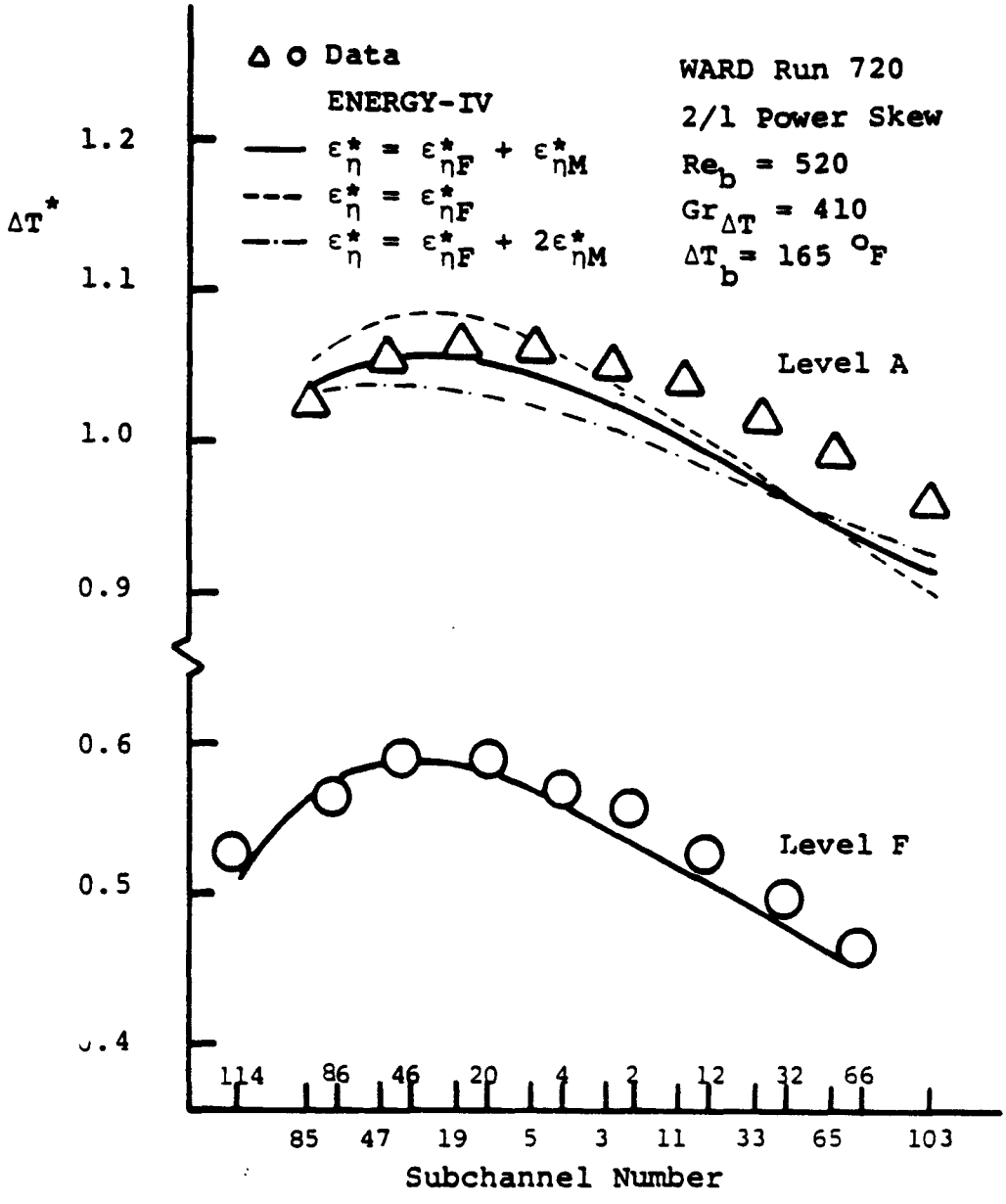

Figure 8.29 Measured and Predicted Temperature Rise for WARD Run 720

later. The maximum temperature difference between the predictions and data occurs in Run 229 with about 11% underprediction of ΔT_b in the farest subchannel of low power side. This gives about a 20°F difference. As for the peak temperature rise, the ENERGY-IV can predict within 7% of ΔT_b for all cases.

8.4.2.2 ORNL-61 pin Bundle

Figures 8.32, 8.33, 8.34 illustrate the comparisons among the data and the ENERGY-IV calculations with $\varepsilon_\eta^* = \varepsilon_{\eta F}^* + \varepsilon_{\eta M}^*$, $\varepsilon_\eta^* = \varepsilon_{\eta F}^*$, and $\varepsilon_\eta^* = \varepsilon_{\eta F}^* + 2\varepsilon_{\eta M}^*$ for ORNL 61-pin bundle Test 19 Run 105 (3/1 power skew), Test 18 Run 105 (2/1 power skew), and Test 17 Run 105 (1.5/1 power skew), respectively. The data of ΔT^* in these Figures were calculated from the temperature data corrected by energy balance considerations and the energy balance ΔT_b. The measured $(T_{out} - T_{in})$ were 290°F, 290°F, and 291°F, while the same ΔT_b from the energy balance were 308°F, 318°F, and 314°F, for these three cases, respectively. Hence energy lossed of about 6% - 9% appear to exist for the tests. The outlet temperature was measured at a distance of 61 inches from the start of the heated section of the bundle. Hence if heat loss was proportional to the averge temperature along the bundle length, the data at the 37" level could be corrected to account this loss by multiplying them by a factor of {1+[(37 x average temperature over heated length)/(37 x average temperature over heated length + (61-37) x outlet temperature)] x percentage of total energy loss}.

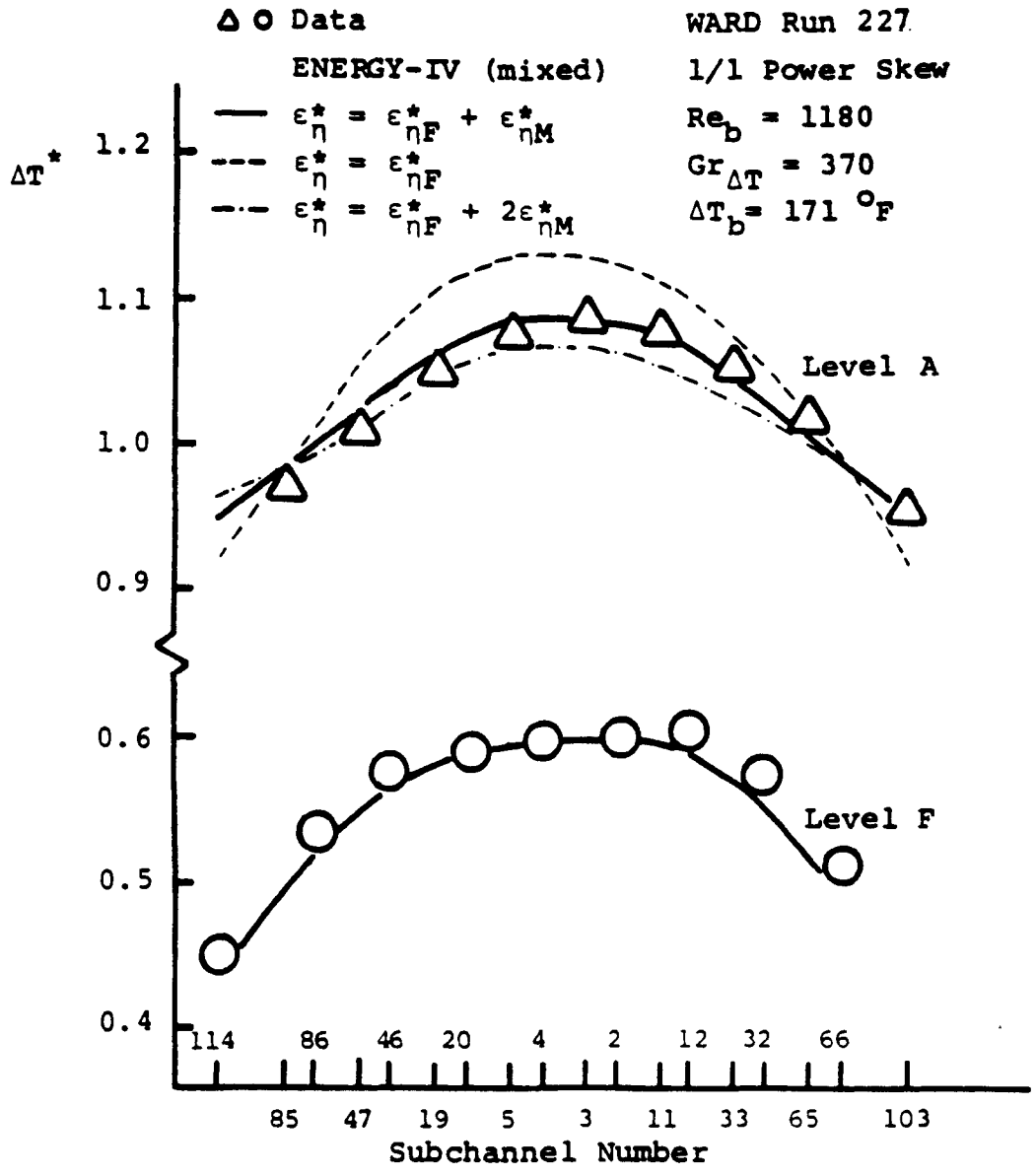

Figure 8.30 Measured and Predicted Temperature Rise for WARD Run 227

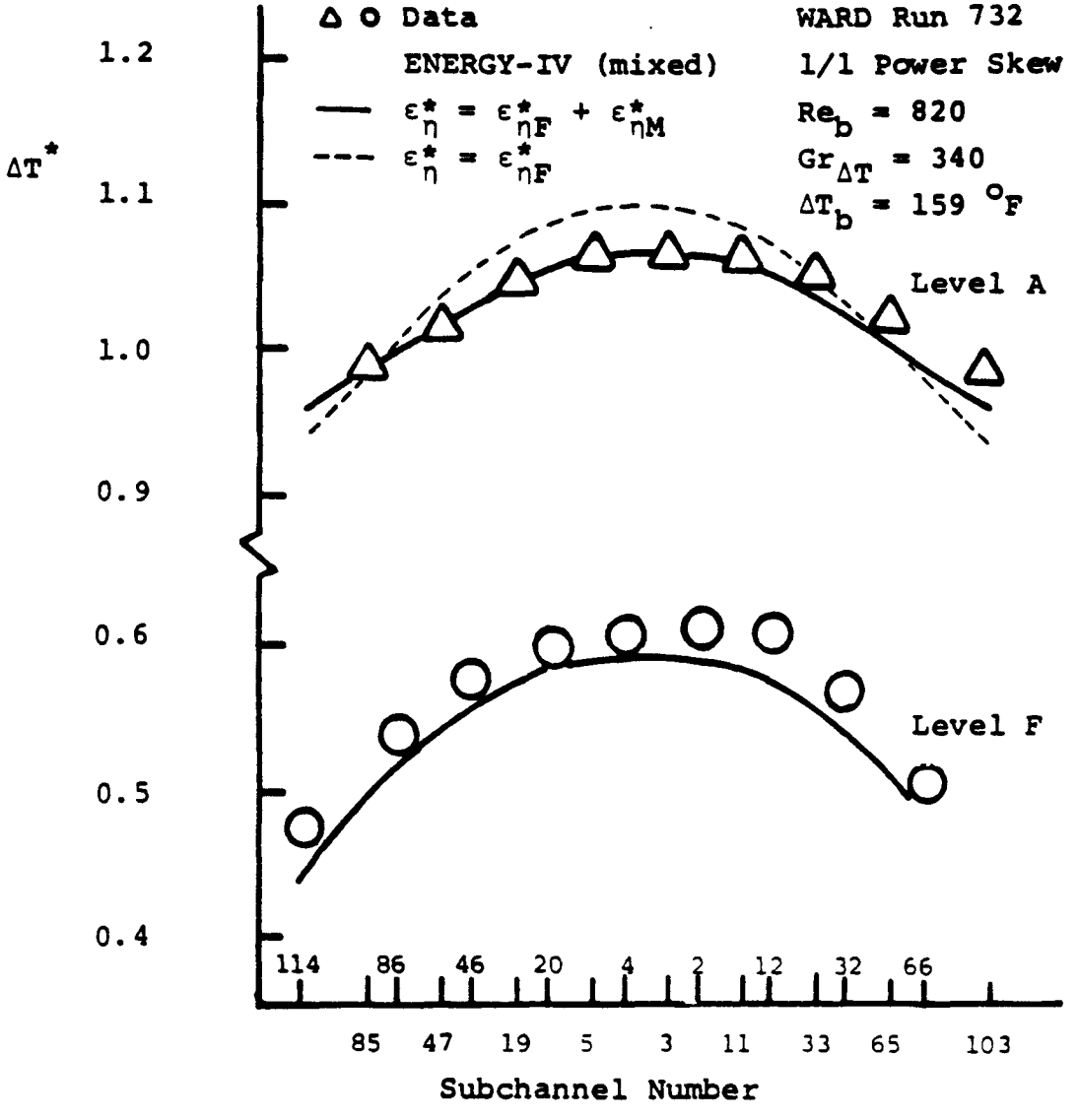

Figure 8.31 Measured and Predicted Temperature Rise for WARD Run 732

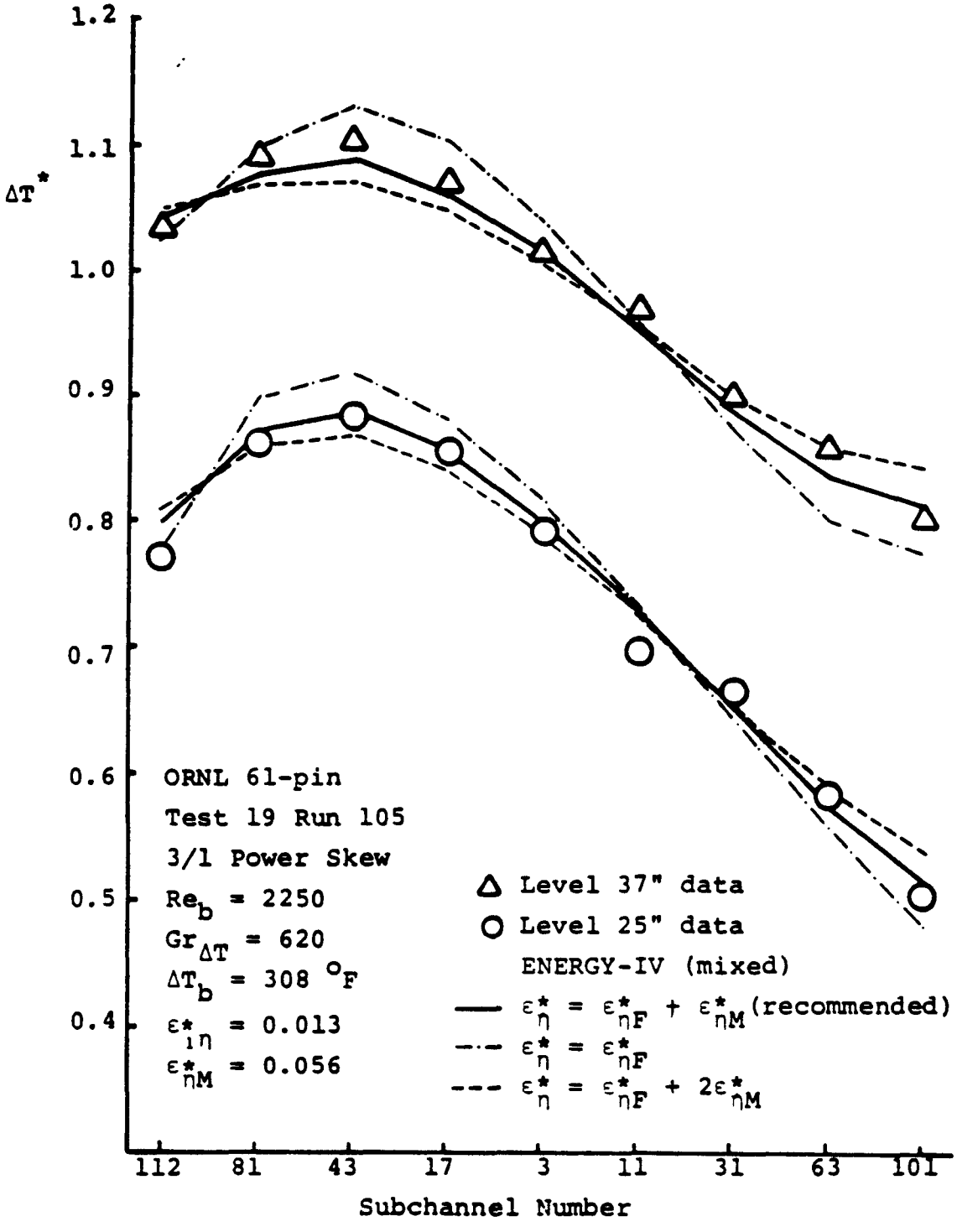

Figure 8.32 Measured and Predicted Temperature Rise for ORNL 61-pin Bundle Test 19 Run 105

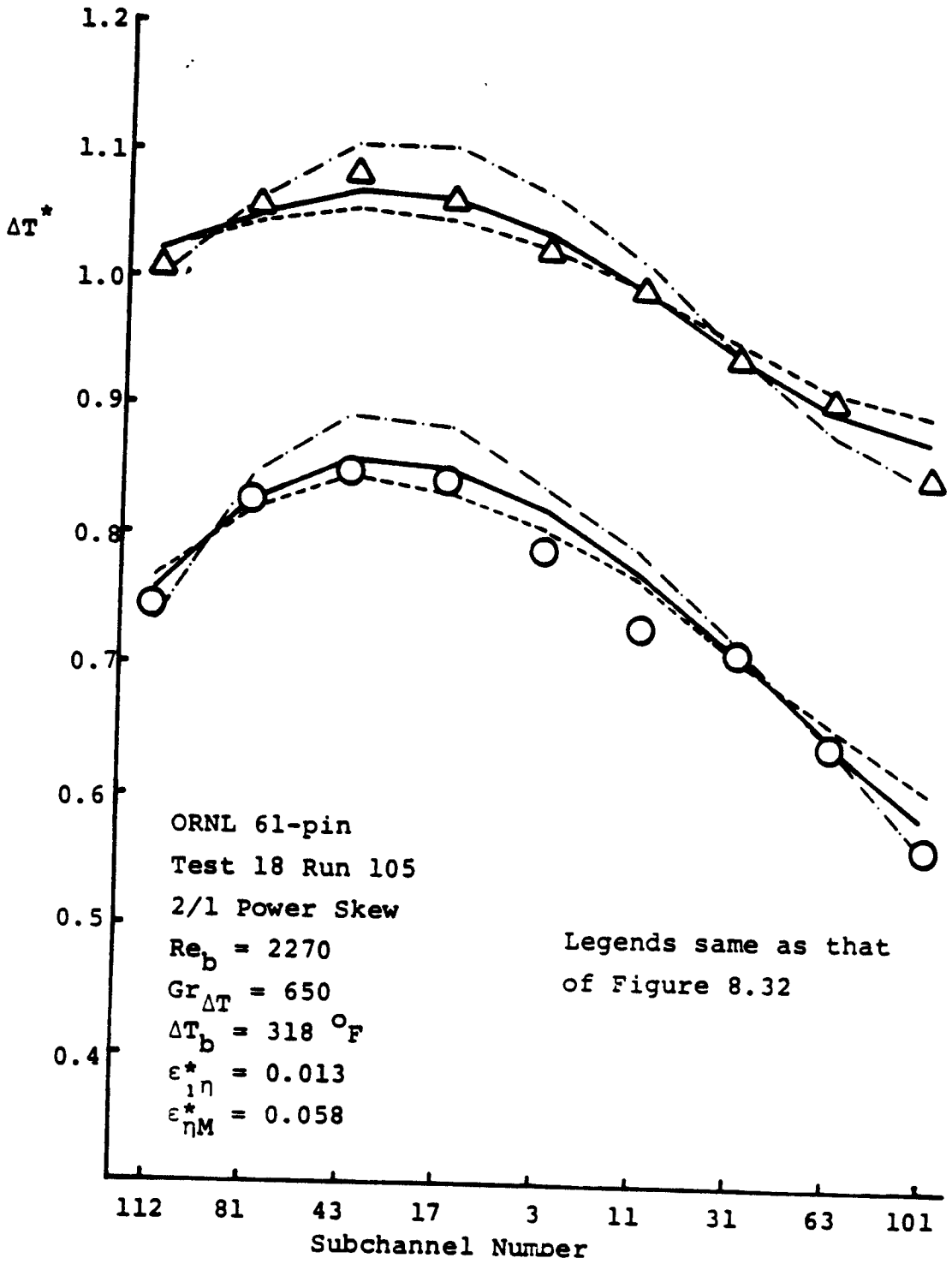

Figure 8.33 Measured and Predicted Temperature Rise for ORNL 61-pin Bundle Test 18 Run 105

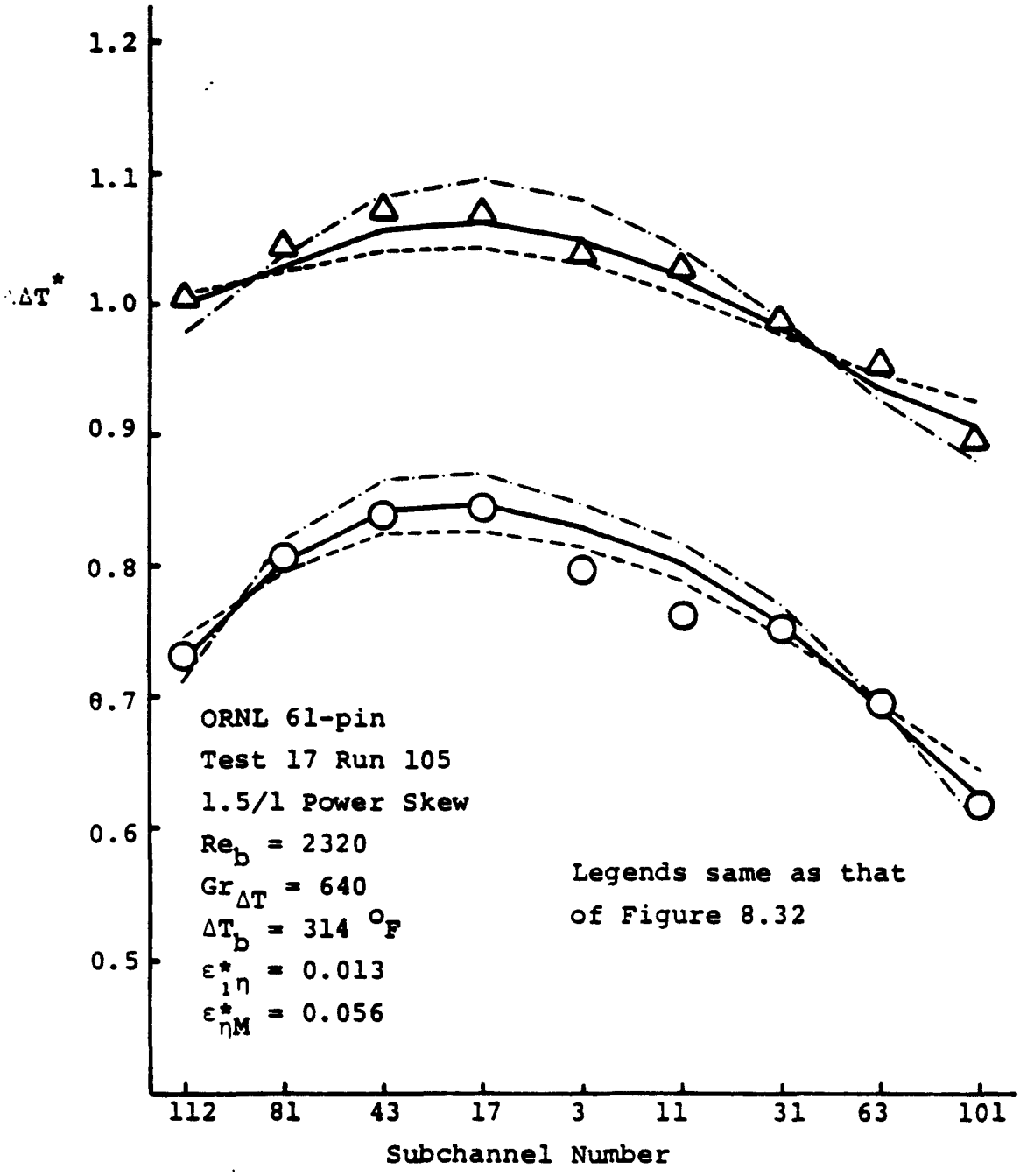

Figure 8.34 Measured and Predicted Temperature Rise for ORNL 61-pin Bundle Test 17 Run 105

A similar correction factor could be developed for data at the 25" level. Note that the profiles of the temperture distribution would not be changed by these corrections. The correction values for temperatures were about 5% of ΔT_b, i.e., about 15°F. As seen from these Figures, ENERGY-IV excellently predicts these corrected data. The maximum difference between the data and predictions is about 2% of ΔT_b, i.e., 6°F. The COBRA-WC predictions performed by Khan et al. (1981) for Test 19 Run 105 were almost exactly the same as the ENERGY-IV calculations with $\varepsilon_\eta^* = \varepsilon_{\eta F}^*$ only. Figure 8.35 illustrates the COBRA-WC results, the ENERGY-IV with $\varepsilon_\eta^* = \varepsilon_{\eta F}^*$ only, and the ΔT^* calculated from the reportedtemperature data (not corrected by above heat balance method). Figure 8.36 illustrates similar comparisons for uniform power skew case, Test 12 Run 114.

8.4.2.3 Toshiba Bundle

Figure 8.37 illustrates the comparisons among the data, the ENERGY-IV calculations and the COBRA calculations for Toshiba 37-pin tests with different power skews at Re_b near 3000. The sensitivity of predicted ΔT^* to variations of $\varepsilon_{\eta M}^*$ for these tests are illustrated in Figure 8.38. Figure 8.39 illustrate comparisons similar to Figure 8.36 for the low flow rate tests, Re_b = 900 to 1500. The ENERGY-IV predicts all these data as well as COBRA does as observed from these comparisons. The maximum temperature rises are well predicted by the ENERGY-IV, except that an underprediction of 4% ΔT_b was observed in Run F37P20. The maximum ΔT^* difference between predictions and data

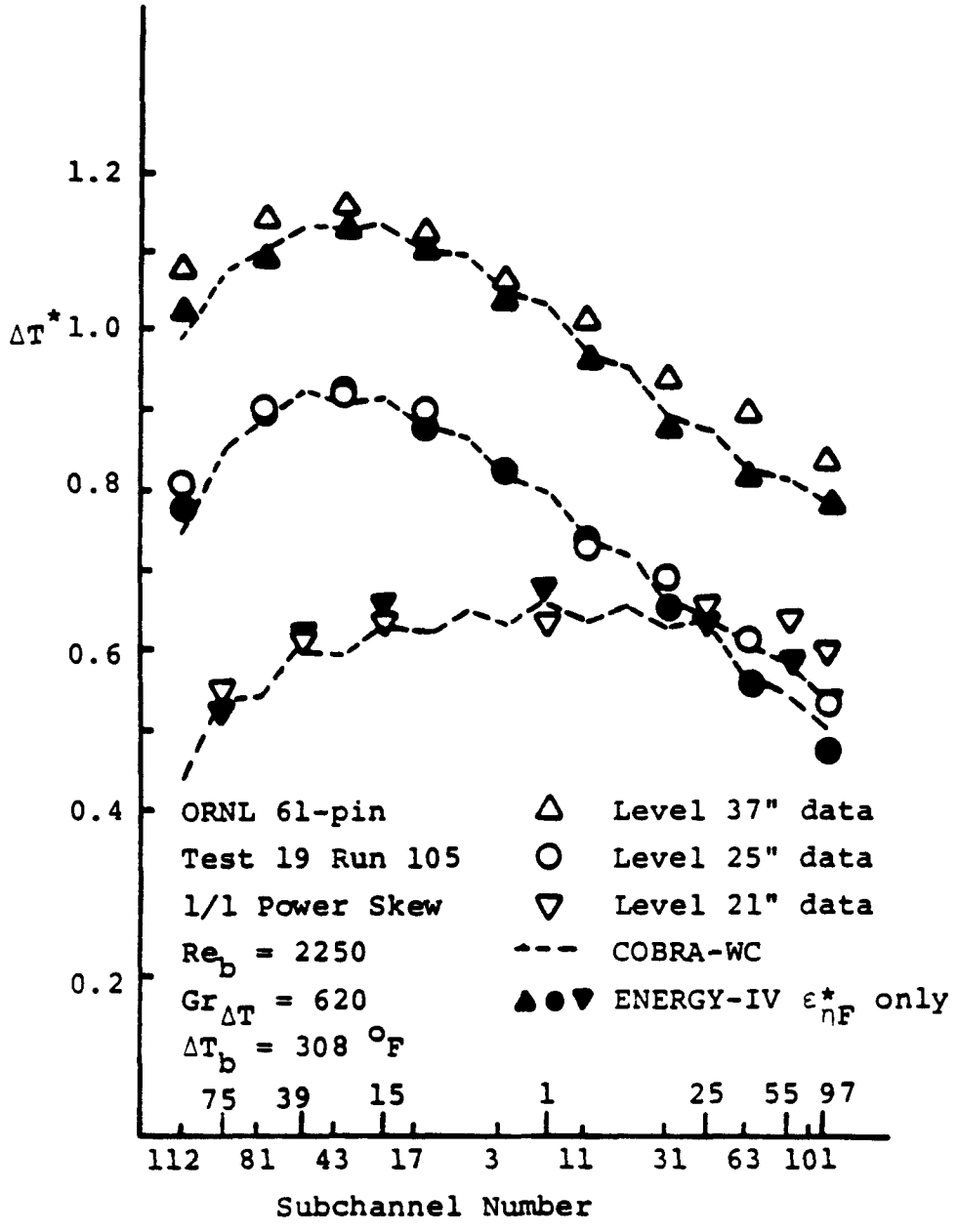

Figure 8.35 Comparsion among Data, ENERGY-IV Results ($\varepsilon^*_{\eta F}$ only) and COBRA-WC Results for Test 19 Run 105

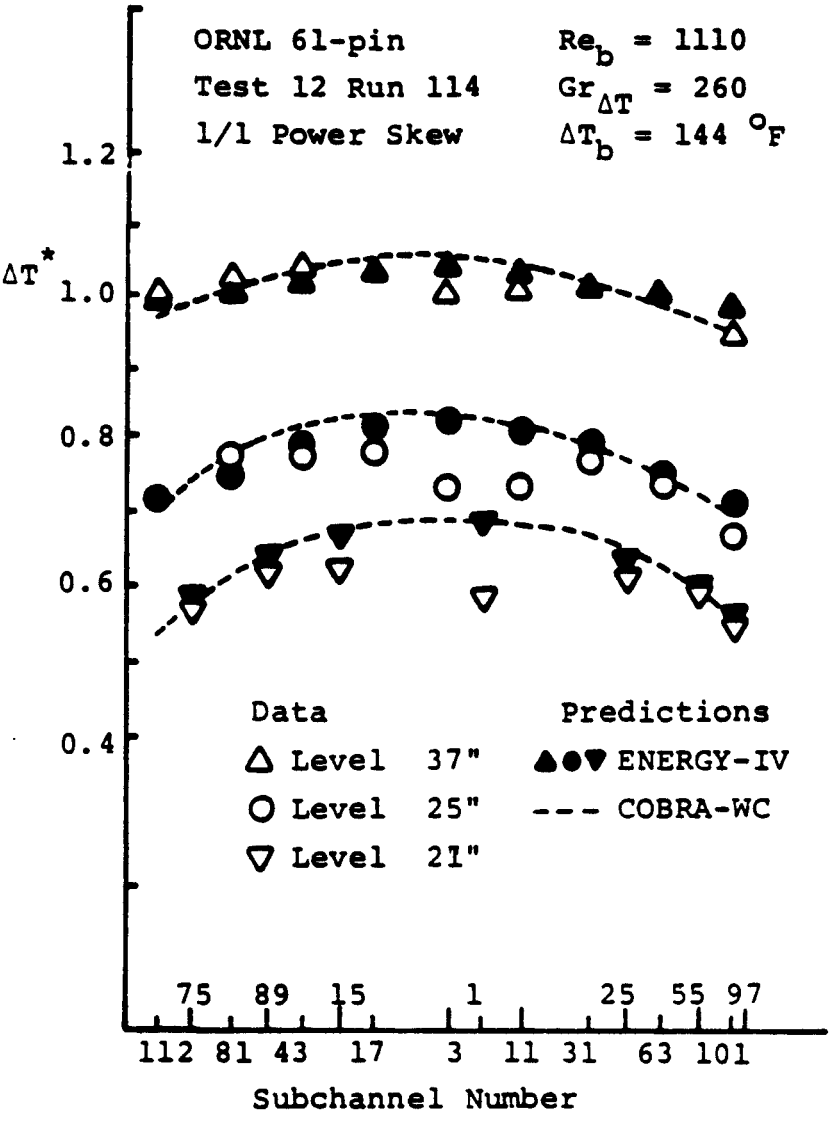

Figure 8.36 Measured and Predicted Temperature Rise for ORNL 61-pin undle Test 12 Run 114

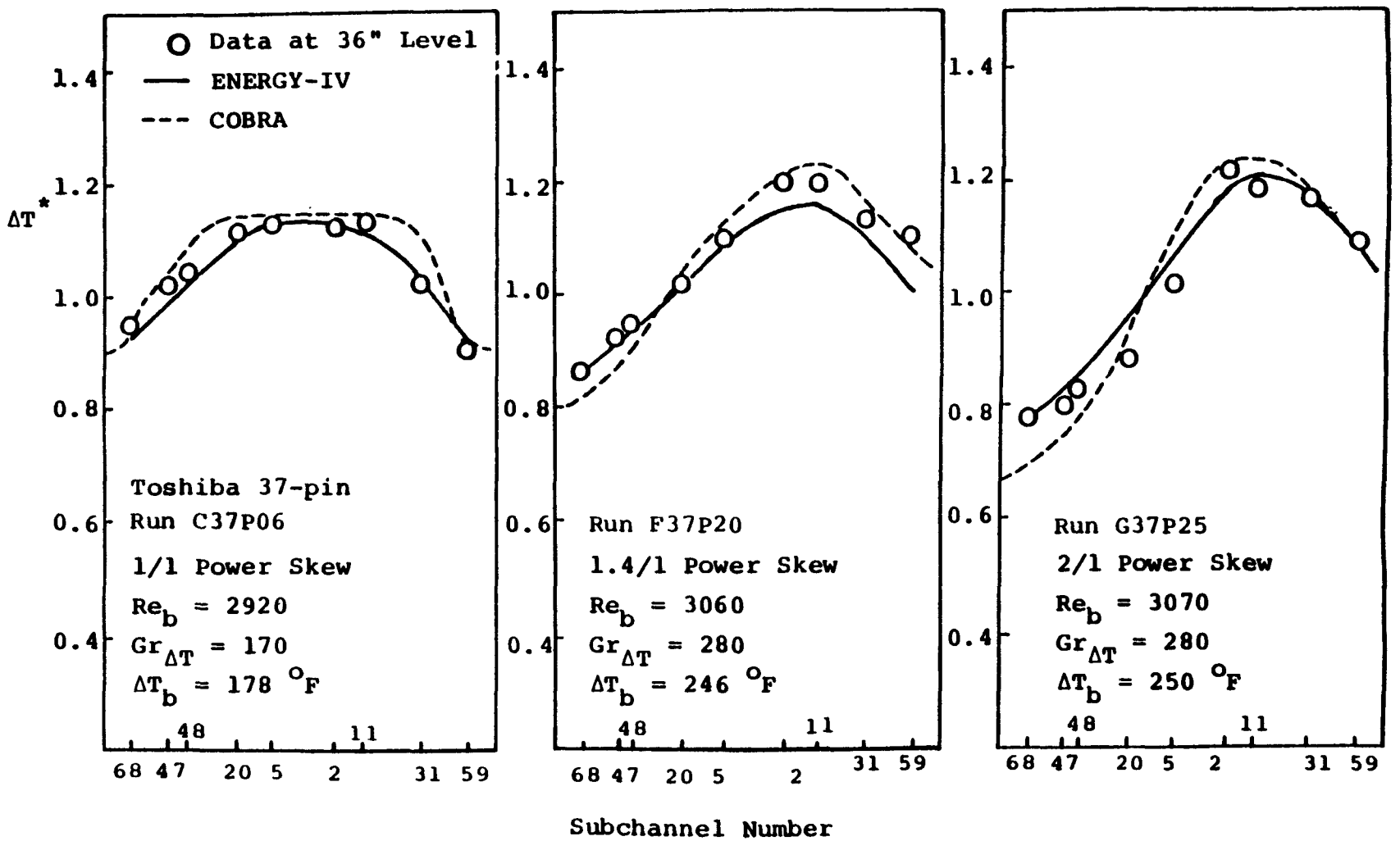

Figure 8.37 Measured and Predicted Temperature Rise for Toshiba 37-pin Test at Re_b=3000

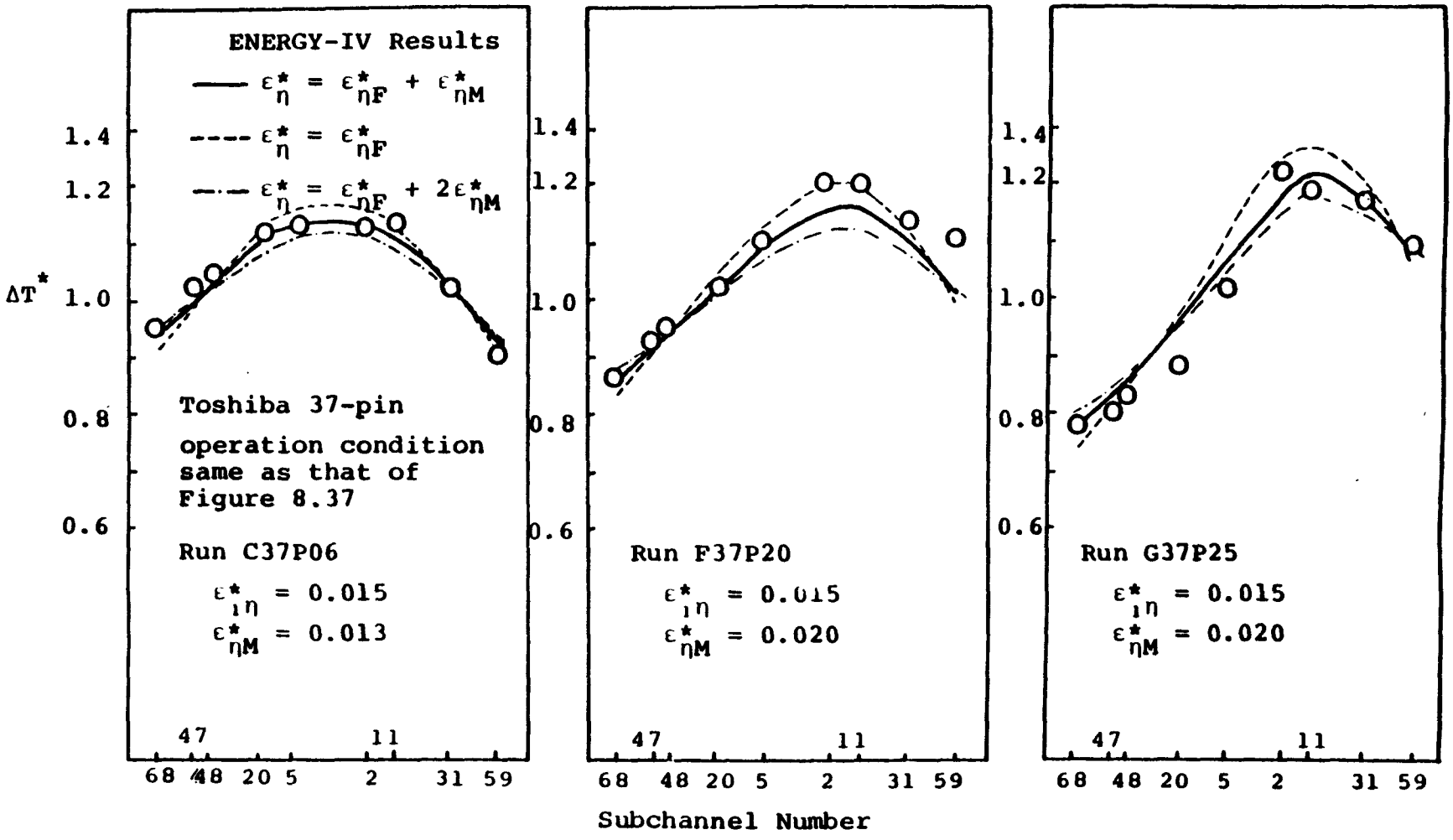

Figure 8.38 Sensitivity of the ENERGY-IV Results to $\varepsilon^*_{\eta M}$ for Toshiba Tests

occured in the low power region of Run G37P25. A 9% difference of ΔT^* was found in subchannel 20 in this case. This gives a temperature difference of 22.5°F.

8.4.2.4 Grenoble (FETUNA) Bundle

Figure 8.40 illustrates the comparisons among the data, the ENERGY-IV predictions and the predictions of the investigators' computer code, BACCHUS [(Rameau (1984)], for the uniform power skew of FETUNA tests with different Re_b. The data were better predicted by ENERGY-IV than by BACCHUS. Figure 8.41 compares the ENERGY-IV predictions to the data for two power skews, 2.5/1 and 1/1 at Re_b = 1790. BACCHUS results are not available for the 2.5/1 power skew case since it is only a 2D code. About a 10% ΔT_b difference between ENERGY-IV predictions and data were found in the 2.5/1 power skew case.

8.4.3 Conclusions

The validation for the ENERGY-III code for the mixed convection condition has been illustrated in the previous subsections. The ranges of geometries and power skews are the same as that considered for the forced convection condition. The mixed convection operation conditions examined range from Re_b = 4400 to Re_b 520 and $Gr_{\Delta T}$ = 650 to $Gr_{\Delta T}$ = 170. The ranges of the parameter $(Gr_{\Delta T}/Re_b)$ is 0.058 to 0.732.

An additional mixing mechanism due to thermal plume effects was considered in the mixed convection flow regime. These thermal plumes

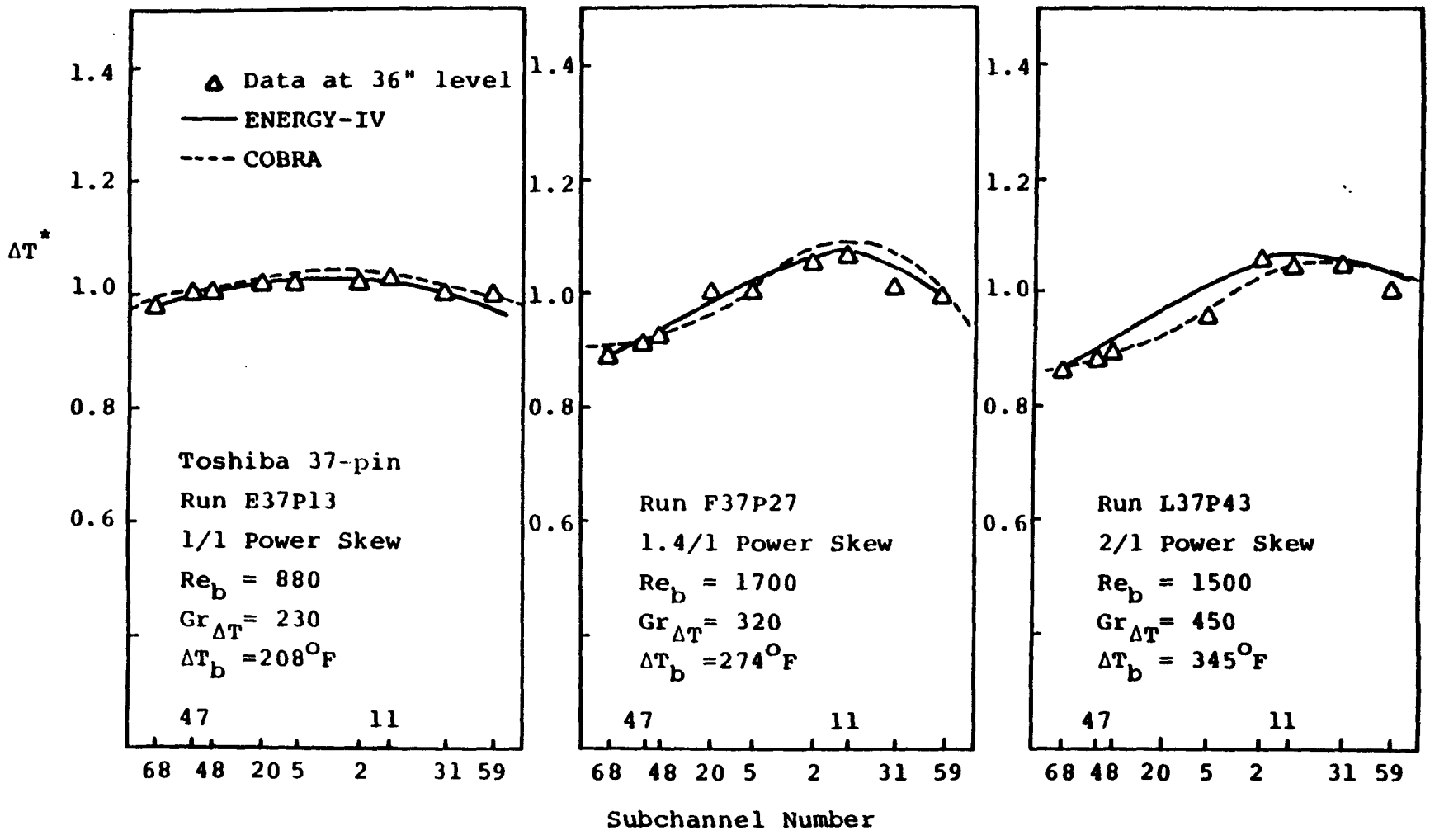

Figure 8.39 Measured and Predicted Temperature Rise for Toshiba 37-pin Low Flow Tests

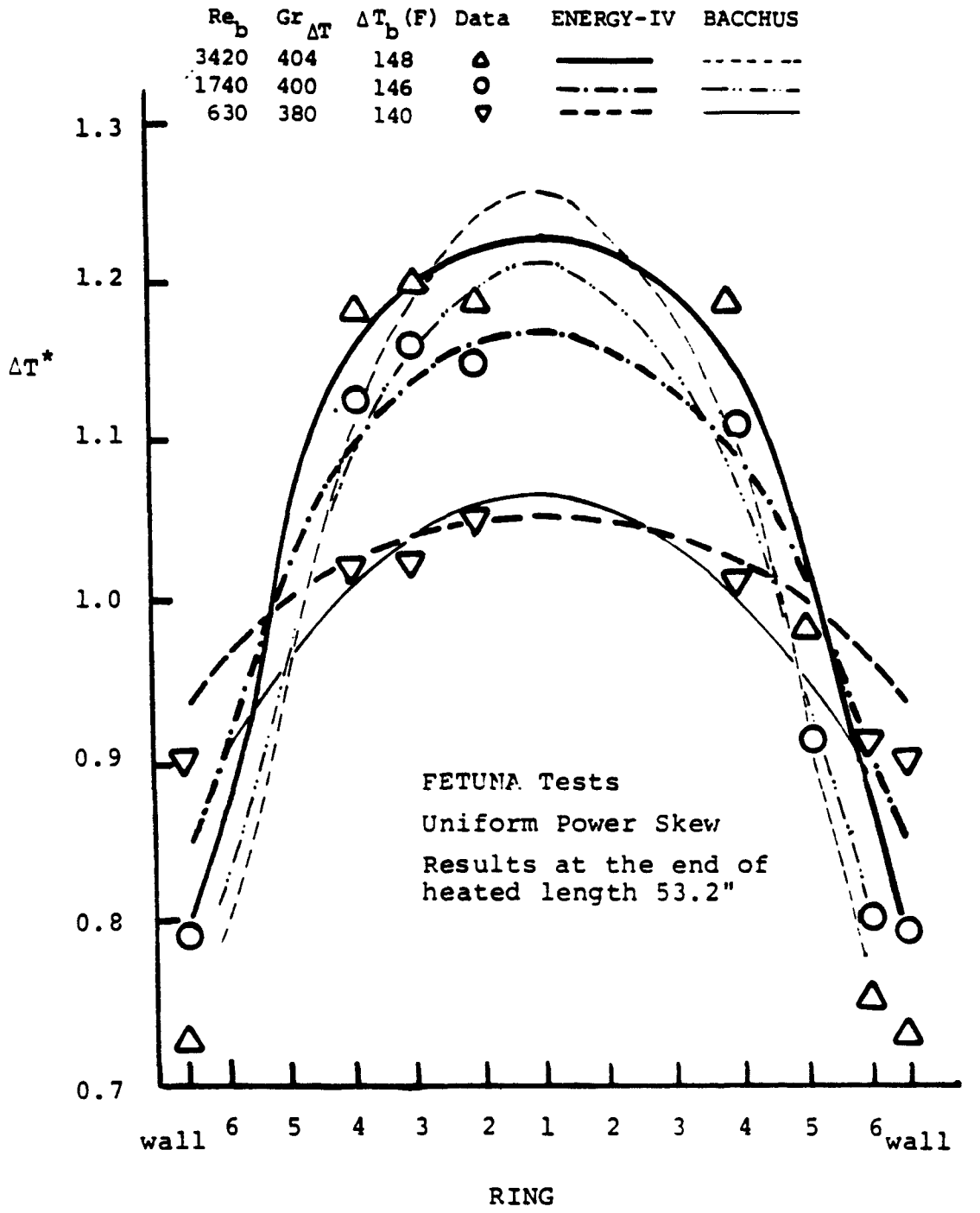

Figure 8.40 Measured and Predicted Temperature Rise for FETUNA Tests with Uniform Power Skew

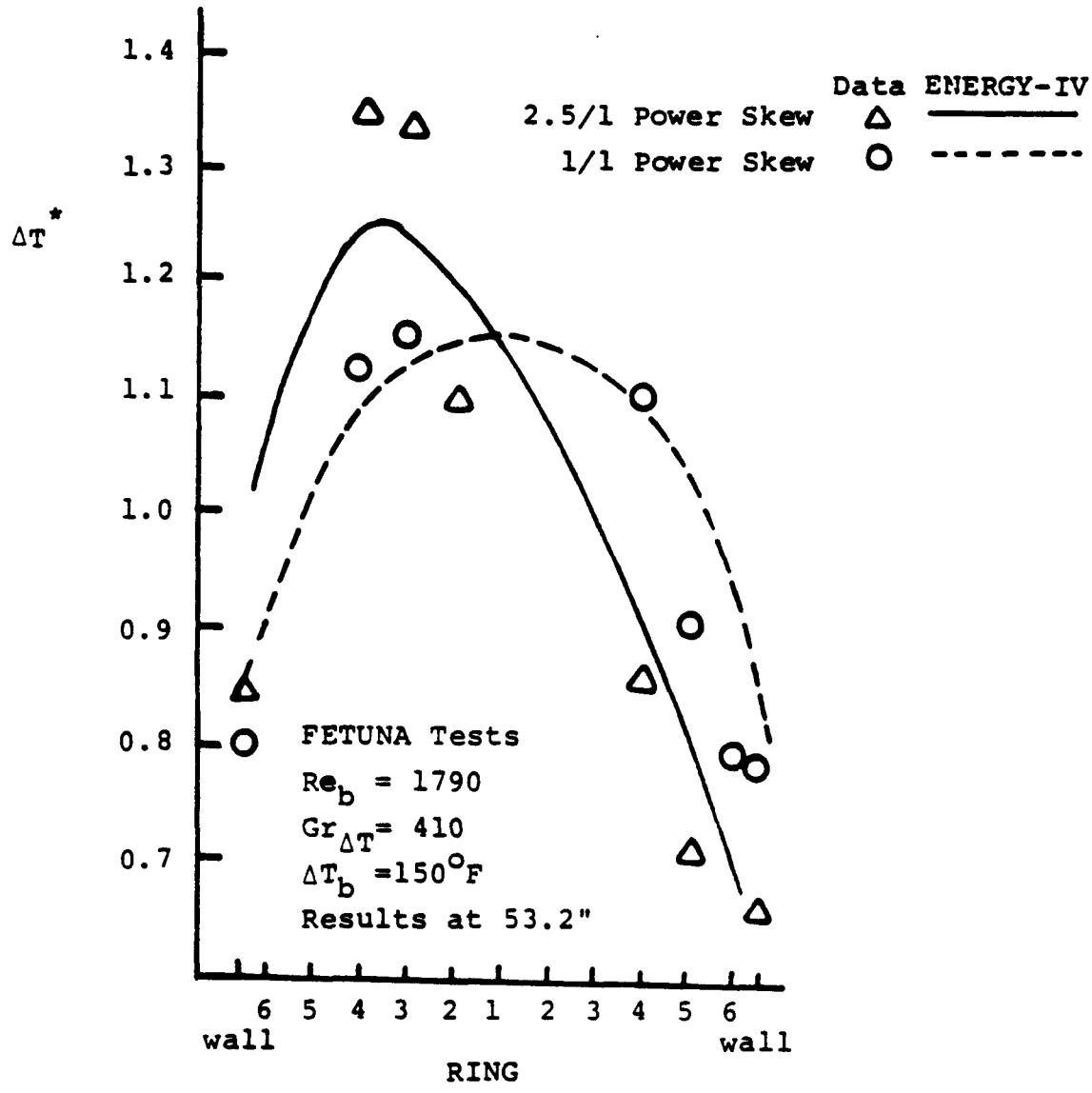

Figure 8.41 Measured and Predicted Temperature Rise for FETUNA Tests at Re_b = 1740

are caused by buoyancy effects when $Gr_{\Delta T}/Re_b$ becomes significant, say ≥ 0.04. To match the ENERGY-IV calculations to the data base in Table 8.7, the following correlation was found to be satisfactory,

$$\varepsilon^*_{\eta M} = 0.1 \left(\frac{c}{D}\right)^{-0.5} \left(\frac{Gr_{\Delta T}}{Re_b}\right) \tag{8.5}$$

The forced convection mixing parameter $\varepsilon^*_{1\eta}$ and $\varepsilon^*_{2\eta}$ are enhanced by $\varepsilon^*_{\eta M}$ when the mixed convection option of the ENERGY-IV code is used.

With these mixing parameters and the conduction shape factor suggested from base rod results, the predictions of ENERGY-IV in the mixed convection condition were confirmed to have the same degree of accuracy as that of COBRA. The peak temperature rises were predicted within 7% of the bundle average temperature rise. The maximum difference between predictions and data occured in the lower power region of the power skew cases. About 10% differences between measured and predicted ΔT^* were observed for the most severe cases. This gave the maximum difference between predicted temperture and data a value of 23°F.

8.5 Relative Importance of Energy Transfer Mechanisms in the Mixed Convection Condition

As discussed in the last section, four energy transfer mechanisms exist in the mixed convection flow regime, i.e., wire sweeping and turbulent mixing, molecular conduction, thermal plume mixing, and convective energy transfer due to flow redistribution. In this

section, the relative importance of the mechanisms will be investigated, and the regimes in which these parameters dominate will be identified.

For the molecular conduction, a parameter called the interior dimensionless thermal diffusivity, α_l^*, comparable to $\varepsilon_{l\eta}^*$, can be established from the energy equation for interior subchannels,(c.f. equation (2.27))

$$\Delta h_l = \frac{Q_l \Delta z}{\rho v_l} + \frac{c\Delta z}{A_l}\left[\left(\frac{\kappa\alpha}{v_l \eta}\right) + \varepsilon_{l\eta}^*\right](h_i + h_j + h_k - 3h_l) \qquad (2.27)$$

and

$$\alpha_l^* \equiv \frac{\kappa\alpha}{v_l \eta} \qquad (8.6)$$

Expressing α_l^* in dimensionless parameters, we get

$$\alpha_l^* = \frac{\frac{\kappa\alpha}{\eta}}{\left(\frac{v_b De_b}{\nu}\right)\left(\frac{v_l}{v_b}\right)\left(\frac{\nu}{De_b}\right)} = \frac{1}{Re_b}\frac{1}{P_r}\left(\frac{\kappa}{X_l}\right)\left(\frac{De_b}{\eta}\right) \qquad (8.7)$$

For the thermal plume mixing, a correlation equation (8.5) has been developed to evaluate $\varepsilon_{\eta M}^*$. Note that $\varepsilon_{\eta M}^*$ is dependent upon both $Gr_{\Delta T}$ and Re_b, while $\varepsilon_{l\eta}^*$ and α_l^* are only dependent upon Re_b. These parameters have similar meaning relative to energy transfer and can be directly compared to each other. Table 8.8 describes these parameters as functions of Re_b for the blanket assembly with a typical $Gr_{\Delta T}$ of 400 and fuel assembly with a typcial $Gr_{\Delta T} \doteq 600$.

Regarding convective transfer by flow redistributive (FRD), no obvious parameter is available. The energy transfer by the flow

Table 8.8 Comparisons among $\varepsilon^*_{l\eta}$, α^*_l and $\varepsilon^*_{\eta M}$ for Balnket and Fuel Assemblies

	$\left(\frac{De_b}{\eta}\frac{\kappa}{\overline{X}_l}\frac{1}{P_r}\right)$	$Gr_{\Delta T}$		Re_b					
				2×10^4	10^4	5×10^3	2×10^3	10^3	5×10^2
Blanket (WARD)	185.6	400	$\varepsilon^*_{l\eta}$	0.122	0.122	0.120	0.100	0.075	0.055
			α^*_l	0.009	0.019	0.037	0.093	0.186	0.371
			$\varepsilon^*_{\eta M}$	0.007	0.014	0.028	0.070	0.140	0.280
Fuel (ORNL)	80.5	600	$\varepsilon^*_{l\eta}$	0.016	0.016	0.016	0.013	0.012	0.011
			α^*_l	0.004	0.008	0.016	0.040	0.080	0.161
			$\varepsilon^*_{\eta M}$	0.006	0.012	0.024	0.060	0.120	0.240

redistribution is a global phenomenon characterized by the cross flow enthalpy, H^*, and cross flow velocity, V^*, in equations (2.47) and (2.48), respectively. Here, a simple method is suggested to estimate the relative importance of energy transfer by flow distribution, FRD, to ε_η^* by examining the changes in maximum ΔT^* due to these two mechanisms. From the sensitivity study of $\varepsilon_{\eta M}^*$ in the mixed convection option, the changes of maximum ΔT^* due to the changes of ε_η^* can be estimated. For each of the cases, the changes of the maximum ΔT^* at the end of heated length due to flow redistribution effects can be estimated by running ENERGY-IV with both the forced convection option (no flow distribution) and with mixed convection option (with flow redistribution) using same values of ε_η^*, e.g., $\varepsilon_{1\eta}^*$ and $\varepsilon_{2\eta}^*$ were used for both runs. The relative importance in energy transfer of FRD to $\varepsilon_{1\eta}^*$ could then be estimated by dividing the change of maximum ΔT^* due to FRD effects to the change of maximum ΔT^* due to one increment of $\varepsilon_{1\eta}^*$ in ε_η^*, which is estimated by (change of maximum ΔT^* due one increment of $\varepsilon_{\eta M}^*$)$\times(\varepsilon_{1\eta}^* / \varepsilon_{\eta M}^*)$.

This relative importance of FRD to $\varepsilon_{1\eta}^*$ was found to be quite insensitive to both bundle geometries and power skew. On the other hand, it is a strong function of $Gr_{\Delta T}/Re_b$. Table 8.9 illustrates the changes of maximum ΔT^* due to FRD and one $\varepsilon_{1\eta}^*$ increment effects and the relative importance of FRD compared to $\varepsilon_{1\eta}^*$ as a function of $Gr_{\Delta T}/Re_b$.

Based on the relative importance of FRD compared to $\varepsilon_{1\eta}^*$ determined in the previous paragraph and the expressions for α_1^* and $\varepsilon_{\eta M}^*$ (c.f. Table 8.8), the relative importance of each of these four energy

Table 8.9 Relative Importance on Energy Transfer of Flow Redistribution to $\varepsilon^*_{1\eta}$

$\frac{Gr_{\Delta T}}{Re_b}$	Change of maximum ΔT^* per $\varepsilon^*_{1\eta}$	Change of maximum ΔT^* due to FRD†	Relative Importance of FRD to $\varepsilon^*_{1\eta}$
0.09	0.15	0.05	0.33
0.34	0.03	0.18	6.0
0.73	0.01	0.21	21.0

† Difference between ENERGY-IV result with forced convection option and that with mixed convection option using same $\varepsilon^*_\eta = \varepsilon^*_{\eta F}$

transfer mechanisms compared to $\varepsilon^*_{1\eta}$ as the base are illustrated in Figures 8.42 and 8.44 for blanket assembly and fuel assembly, respectively. At very high Re_b operation, only $\varepsilon^*_{1\eta}$ is important for energy transfer. As Re_b decreases, conduction, thermal plume and FRD become important. At very low Re_b operation, FRD becomes so important that all the other mechanisms are relatively insignificant. Note that the FRD and $\varepsilon^*_{\eta M}$ curves will shift to higher Re_b as $Gr_{\Delta T}$ increases as shown in Figure 8.43 for a blanket assembly.

Using Figures 8.42 and 8.43, the relative effect on energy transfer for each mechanism with respect to the total effect of all four energy transfer mechanisms as function of Re_b and $Gr_{\Delta T}$ can be estimated for blanket assembly. For example, Figure 8.45 illustrates the conduction effect relative to the total effect as a function of Re_b for blanket assembly at $Gr_{\Delta T} = 400$. The way to calculate (effect of α^*_1/total effect) is simply to divide the value of $(\alpha^*_1/\varepsilon^*_{1\eta})$ by the sum of the values of all four affects, e.g., at $Re_b = 1000$, $\alpha^*_1/\varepsilon^*_{1\eta} = 2.5$, $\varepsilon^*_{\eta M}/\varepsilon^*_{1\eta} = 1.9$, $FRD/\varepsilon^*_{1\eta} = 7.5$, hence $2.5/(2.5+1.9+7.5+1) = 19.4\%$. Similar curves can be constructed with different values of $Gr_{\Delta T}$ from Figure 8.43. By this method the two regions where α^*_1 and $\varepsilon^*_{\eta M}$ are significant were identified in Figures 8.46 and 47 for blanket and fuel assemblies, respectively. A 15% or greater effect with respect to the total effect of energy transfer was uses as the criterion of significance.

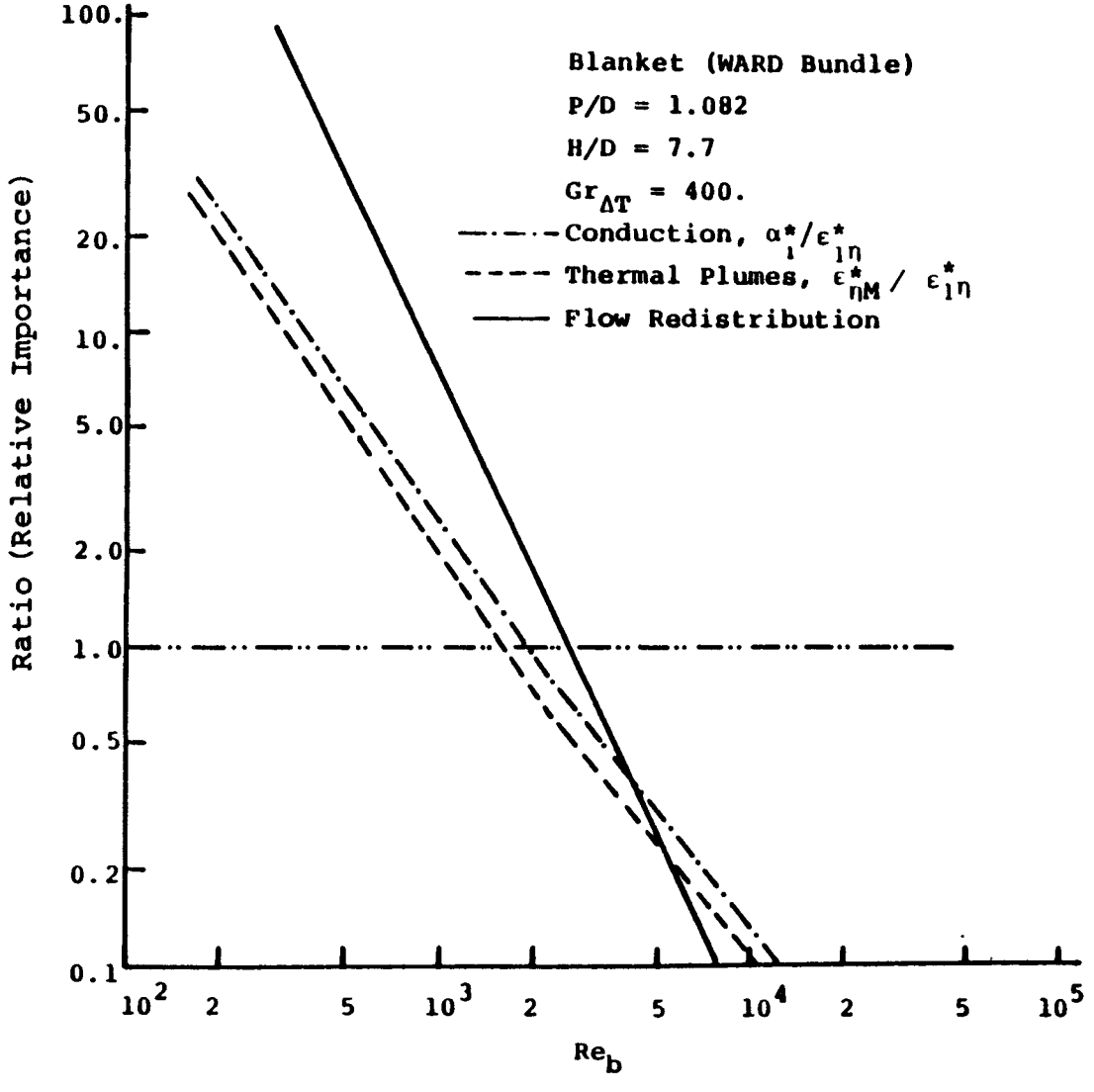

Figure 8.42 Relative Importance of Energy Transfer Mechanisms for Blanket Assembly

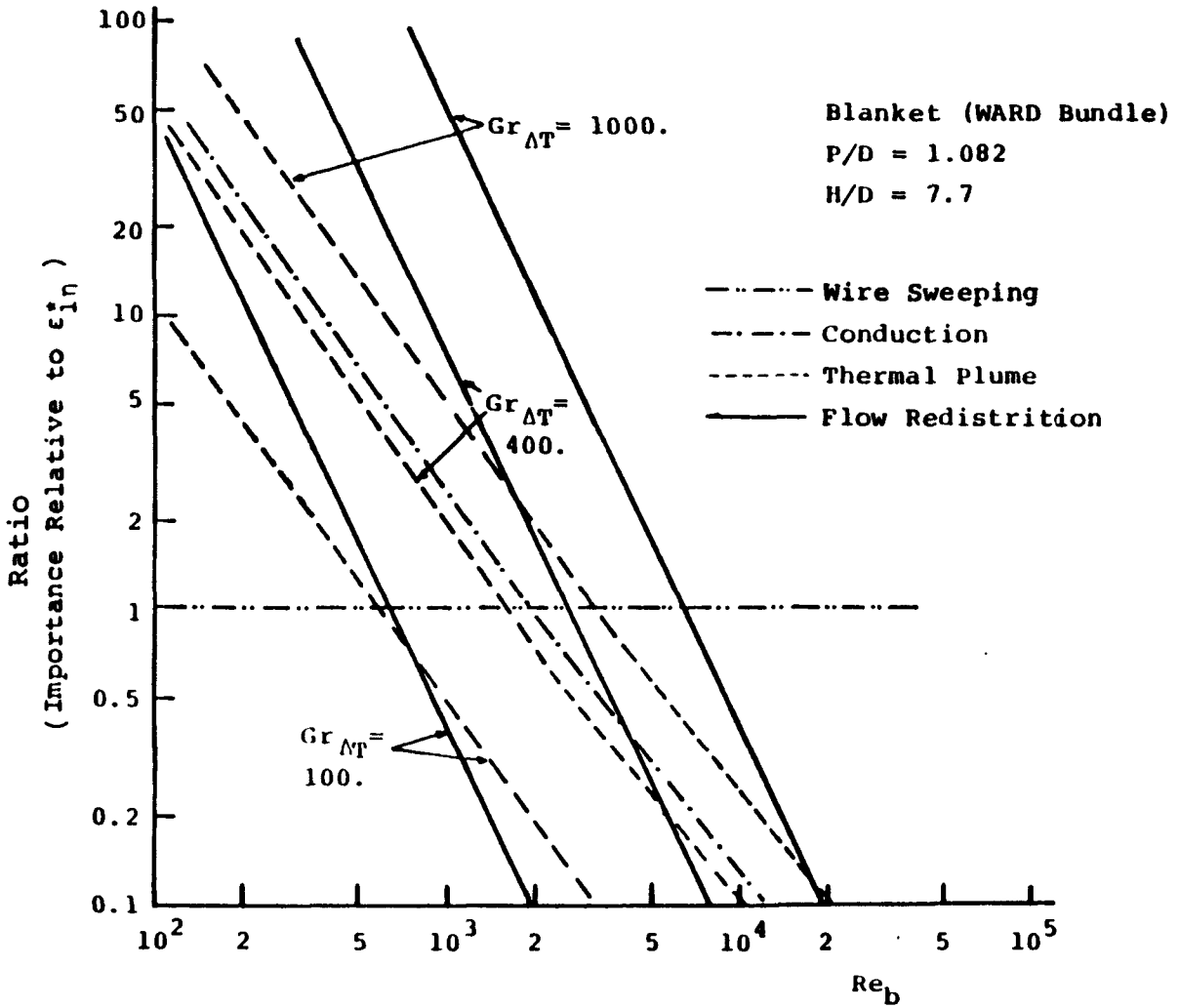

Figure 8.43 Relative Important of Energy Transfer Mechanisms for Blanket Bundle with Different $Gr_{\Delta T}$

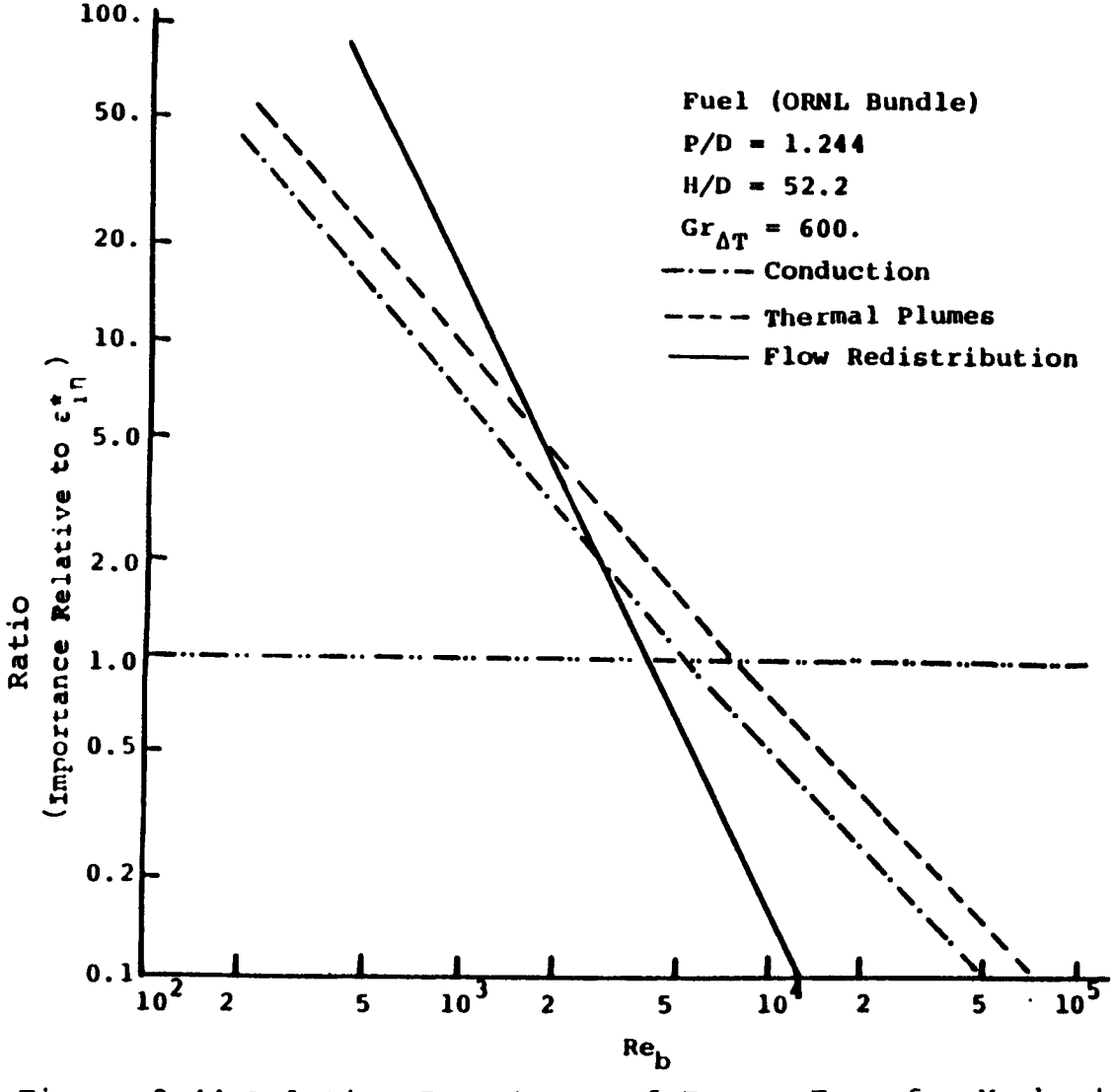

Figure 8.44 Relative Importance of Energy Transfer Mechanisms for Fuel Assembly

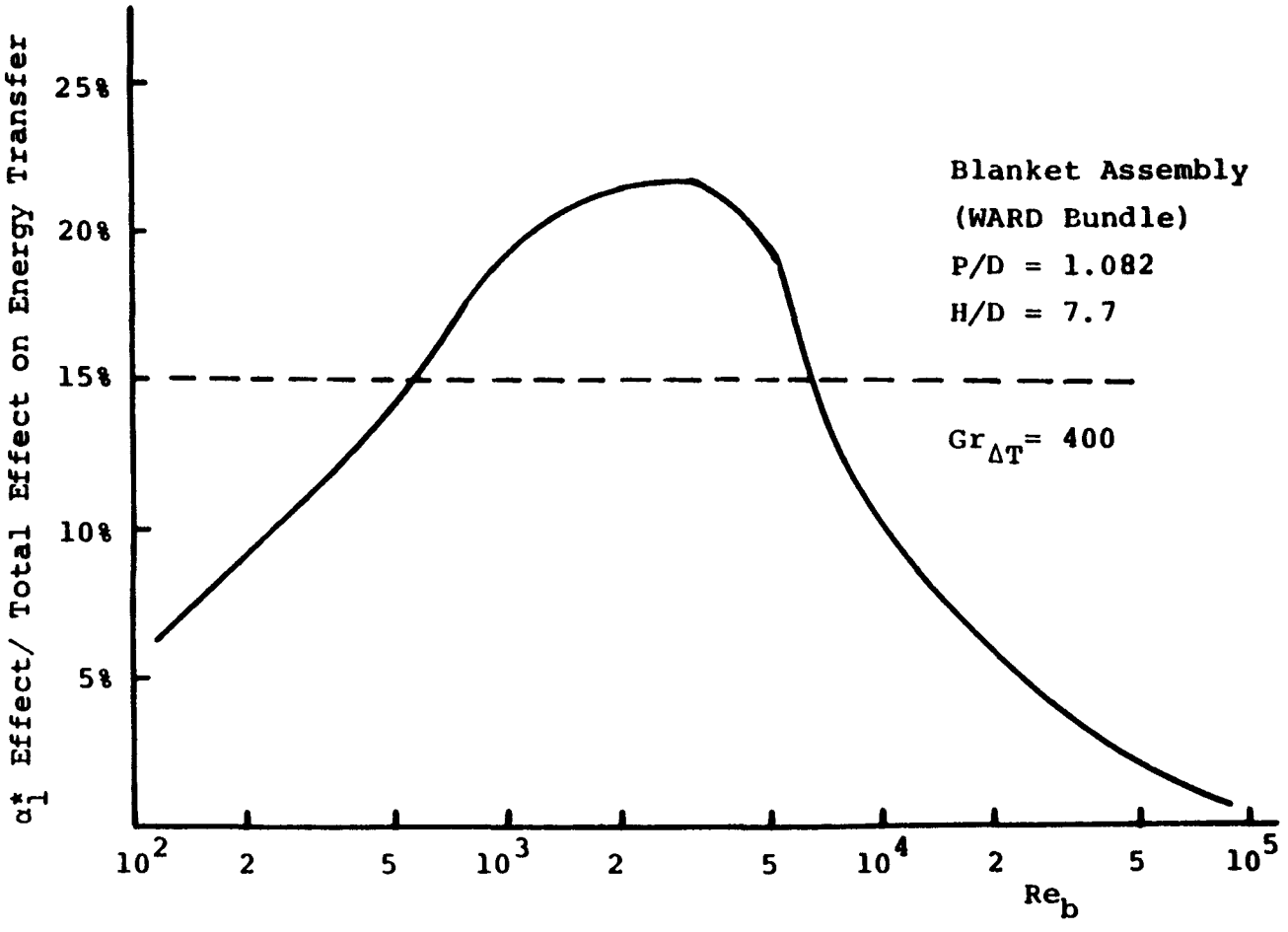

Figure 8.45 α_1^* Effect on the Total Energy Transfer

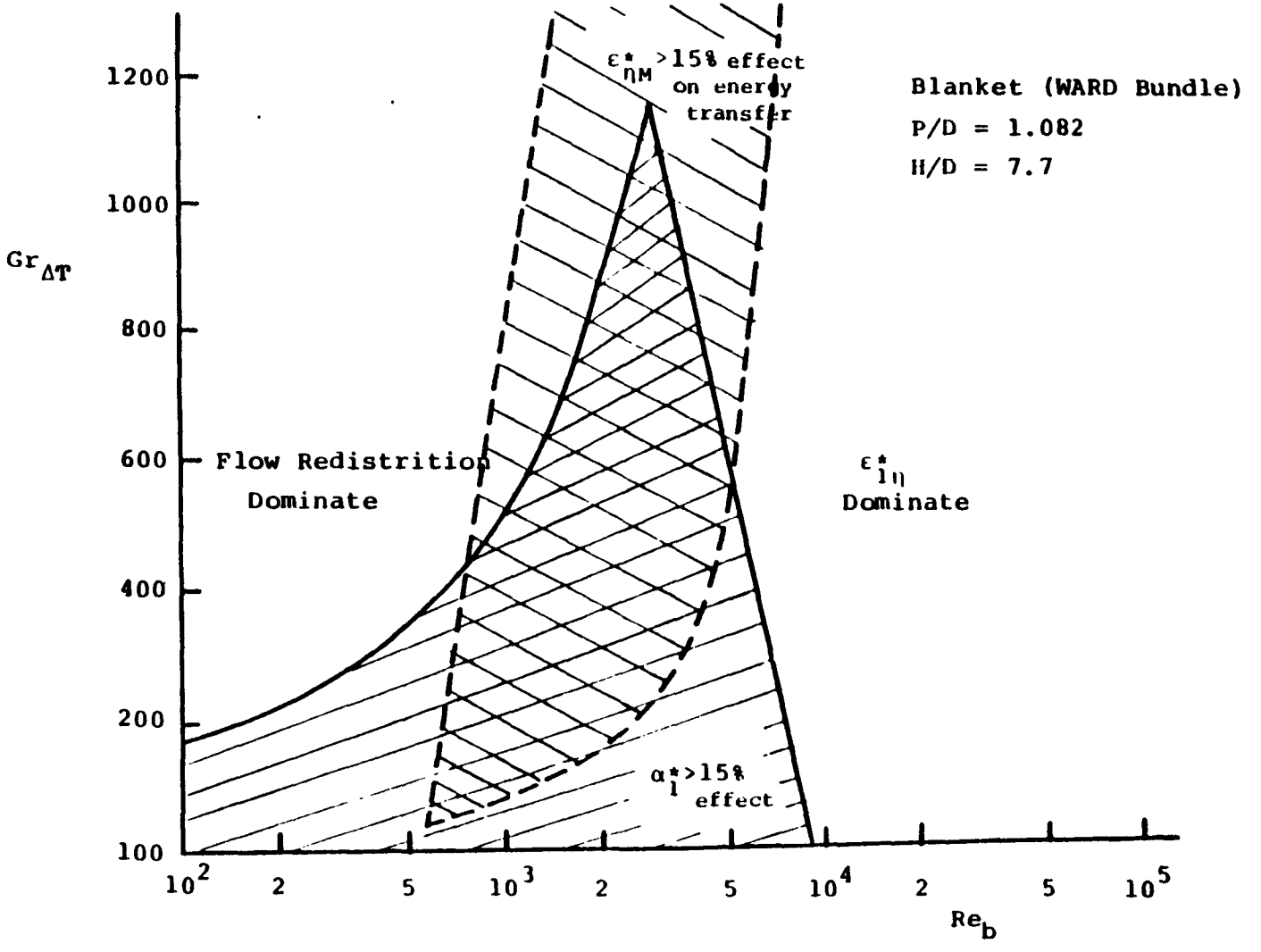

Figure 8.46 Operation Regions in which Different Energy Transfer Mechanisms Are Important for Blanket Assembly

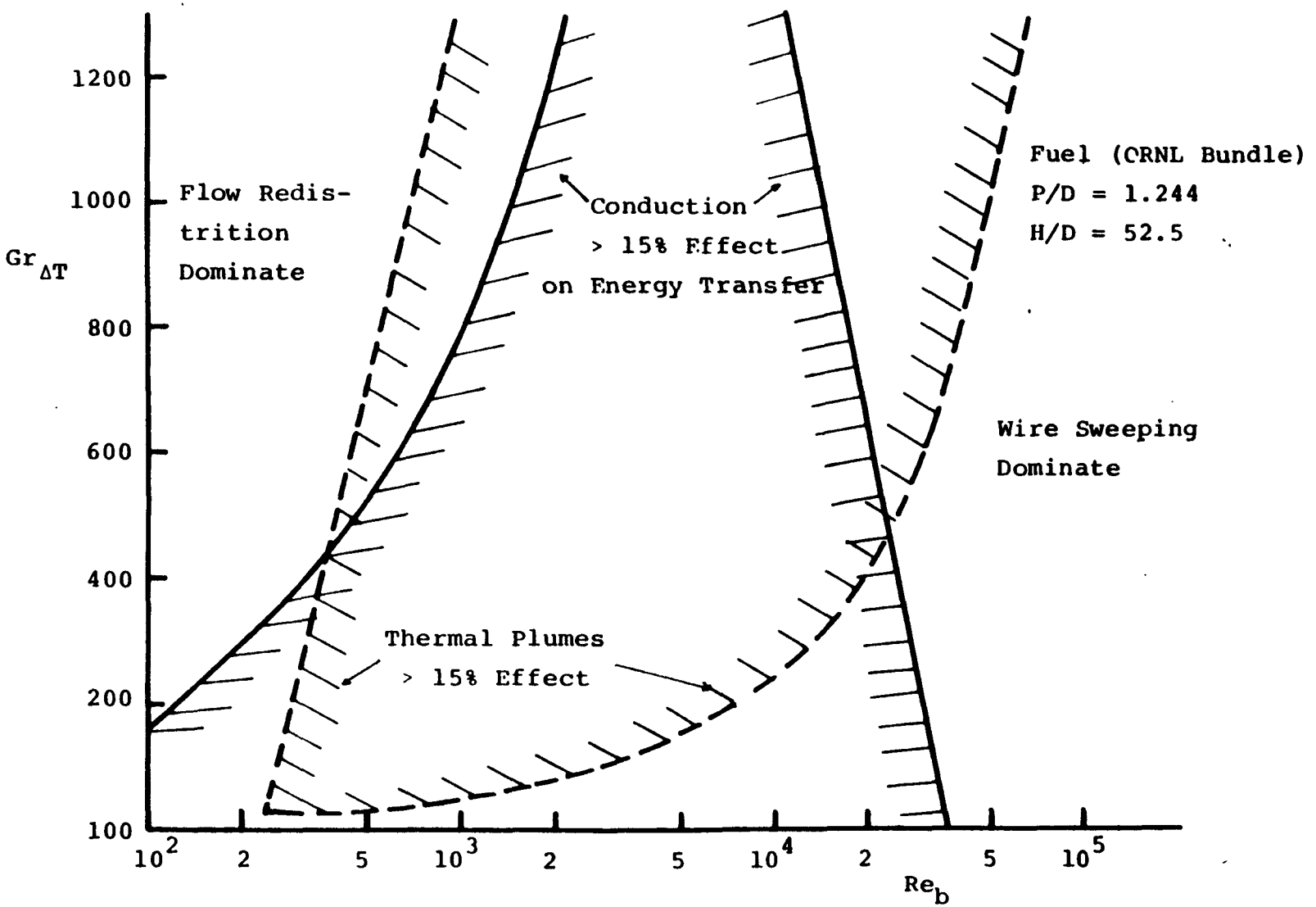

Figure 8.47 Operation Regions in which Different Energy Transfer Mechanisms Are Important for Fuel Assembly

Outside these two regions, FRD dominates the energy transfer at low Re_b operation, while $\varepsilon^*_{1\eta}$ dominates the energy transfer at high Re_b operation. This is because at high $Gr_{\Delta T}/Re_b$, all the other mechanisms are small comparing to FRD, while at low $GR_{\Delta T}/Re_b$ and high Re_b, $\varepsilon^*_{\eta M}$ is the only important mechanism. For $Gr_{\Delta T}$ lower than a particular value ($\tilde{}$100), the buoyancy effects become so small that FRD and $\varepsilon^*_{\eta M}$ are negligible. On the other hand,for $Gr_{\Delta T}$ higher than particular values (e.g., 1100 for blanket bundle) the buoyancy effects become so large that α^*_1 becomes negligible.

As seen from Figures 8.46 and 8.47, the conduction effects are significant (> 15% between Re_b = 700 to 6000, and Re_b = 600 to 2000 for typical blanket assembly and fuel assembly operations, respectively. Note that for low $Gr_{\Delta T}$ operation, conduction effect is always significant even for very low Re_b as shown in these figures. In these regions, use of the bare rod case conduction shape factor for the wire-wrapped rod bundle may require further investigation. However, the validation studies in the last two sections showed that satisfactory predictions were obtained using this conduction shape factor. Therefore, we conclude that the correlation for conduction factor proposed in Chapter 6 is applicable for predicting wire-wrapped rod bundle behavior.

Chapter 9

Summary

The products of this project have been the development of

(1) Models and Numerical tools for predicting thermal/hydraulic bundle performance

(2) Criteria and Correlations for bundle thermal/hydraulic parameters

(3) Experimental techniques for water model testing

The specific accomplishments in these areas are listed below together with the reference where explicit description can be found.

(1) Models and Numerical Tools

- Energy-IV produced and verified for predicting sodium heated bundle performance under forced and mixed convection conditions(108TR)
- The applicability of the ENERGY Model to transient analysis was demonstrated with the single bundle code TRANSENERGY-S (52TR)
- SUPERENERGY first applied the ENERGY model to multiple bundles to accomodate the effects of interassembly heat transfer (20TR); SUPERENERGY-2 extended modeling capabilities and flexability (57TR).
- A model of the CRBR secodary control assembly produced which could be coupled to SUPERENERGY(47TR)
- A two-equation turbulence model was developed and tested for

bare rod array analysis (19TR and 48TR)

- Guidelines for the use of thermo-elastic and thermo-inelastic structural analysis techniques were developed (59TR)
- The code HEATRAN for 3D analysis of local temperature and velocity fields around a single pin was developed and an approach for coupling it to a subchannel averaged code to produce a MICRO/MACRO analysis was defined (97TR and 102TR)

(2) Criteria and Correlations

- For wire wrapped assembies, criteria for the onset of mixed convection and recirculation (101TR) were developed
- For wire wrapped assemblies, flow regime maps to show regions where various energy transport mechanisms are important (108TR)
- For wire wrapped and bare rod assemblies, bundle average, and subchannel friction factor correlations, flow split correlations, transverse mixing correlations, edge swirl flow correlation and thermal plume mixing correlations (108TR)
- Thermal mixing length correlations for use in subchannel codes (58TR and 68TR)
- In isolated single channels criteria for the transition from laminar to turbulent flow and onset of flow recirculation and map for transition from forced to mixed convection (88TR)

(3) Experimental Techniques

- Refined Techniques for salt conductivity and static pressure drop measurements in LMFBR rod bundles (62TR and 77TR)
- Developed a technique for isokinetic colant extraction from subchannel to determine average subchannel axial velocity (80TR)

REFERENCES

Axford, R. A. (1964), "Multiregion Analysis of Temperature Fields and Heat Fluxes in Tube Bundles with Internal, Solid, Nuclear Heat Sources," Rep. No. LA-3167 Los Alamos Sci. Lab., Univ. California, Los Alamos, N.M. (1964), 82 pp.

Axford, R. A. (1967), "Two-Dimensional, Multiregion Analysis of Temperature Fields in Reactor Tube Bundles," Nuclear Engineering and Design, 6, (1967) 25-42.

Bartholet, T. G., et al (1976), "11:1 Scale Wire-Wrap Rod Bundle Air Flow Test, Side Subchannels," WARD-D-0129, Jan. 1976.

Bates, J. M. and Khan, E. U. (1980), "Investigation of Combined Free and Forced Convection in a 2 6 Rod Bundle During Controlled Flow Transients," AIChE Symposium Series, Heat Transfer, Orlando (1980).

Baumann, W., Cosal, V., Hoffmann, H., Moller, R. and Rust, K. (1968), "Brennelemente mit Wendelformigen Abstandshalter fur Schnelle Brutreaktoren," KfK-768 (1968). Also EURFNR-571.

Baumann, W. and Moller, R. (1969), "Experimental Study of Coolant Cross-Mixing in Multirod-Bundles," Atomkernergie, 14-56 (1969).

Biancheria, A. and Markley, R.A. (1973), "Design Analysis of the LMFBR Radial Blanket," Westinghouse Advanced Reactors Design, WARD-3045T2B-9, March 1973.

Bishop, A. A., Nelson, P. A. and McCabe, E. A. (1962), "Thermal and Hydraulic Design of the CVTR-fuel Assemblies," CVNA-115, June 1962.

Bishop, A. A. and Todreas, N. E. (1980), "Hydraulic Characteristics of Wire-Wrapped Rod Bundles," Nuclear Engineering and Design, 62, (1980) 271-293.

Bishop, A. A., Willis, J. M. and Markley, R. A. (1980), "Effects of Buoyance on Laminar Vertical Upward Flow Friction Factors in Cylindrical Tubes," Nuclear Engineering and Design, 62, (1980) 365-369.

Burns, K.J. (1980), "Thermal Hydraulic Studies of a 37-pin LMFBR Wire Wrapped Rod Bundle," S.M. Thesis, Nuclear Engineering Department, MIT, July 1980.

Carajilescov, P. and Fernandez, E. F. (1982), "Semi-Empirical Model for Friction Factors in LMFBR Wire-Wrapped Rod Bundles," 2nd Int'l Topical Meeting on Nuclear Reactor Thermal-Hydraulics, Santa Barbara, CA. (1982).

Carelli, M. D. and Willis, J. M. (1981), "The CRAB-II Computer Program and Its Verification," Presented at LMFBR Thermal-Hydraulic Information Meeting in Monterey, CA, (March 1981).

References (Continued)

Castellana, F.S., Adams, W.T. and Casterline, J.E. (1974), "Single-Phase Subchannnel Mixing in Simulated Nuclear Fuel Assembly," Nuclear Enginering and Design, Vol. 26, pp 242-249 (1974)

Chiu, T. (1979), "Fluid Mixing Studies in a Hexagonal 37-Pin Wire-Wrapped Rod Bundle," S. M. Thesis, Dept. Nuclear Engineering, MIT, (Sept. 1979).

Collingham, R. E., Thorne, W. L. and McCormack, J. D. (1971), "217-pin Wire Wrapped Bundle Coolant Mixing Test," HEDL-TME 71-146, Nov. 1971. Also NED, 24, 1973, pp 393-409.

Cushman, R. A. and McGinnis, F. D. (1969), "Experimental Breeder Reactor No. II Reactor Heat Transfer: Experience with an Operating Liquid Metal Fast Breeder Reactor," CEP Symposium Series No. 91, 65, (1969).

Davidson, C. R. (1971), "Hydraulic Tests on the 217-Rod Full-Sized Wire-Wrapped Fuel Assembly," TR-095-211-006, Atomic International Supporting Document (1971).

Deissler, R. G. and Taylor, M. T. (1957), "Analysis of Axial Turbulent Flow and Heat Transfer Through Banks of Rods or Tubes," Reactor Ht. Conference of 1956, TID-7529 (Pt. 1) Book 2, (1957) 416-461.

deStordeur, A. N. (1961), "Drag Coefficients for Fuel-Element Spacers," Nucleonics 19(6), 74-79, (June 1961).

Donovan, T. E., George, T. L. and Wheeler, C. L. (1979), COBRA-IV Wire-Wrap Data Comparisons," PNL-2938, UC-79e Feb. (1979).

Dwyer, O. E. and Berry, H. C. (1972), "Heat Transfer to Liquid Metals Flowing Turbulently and Longitudinally Through Closely-Spaced Rod Bundles, Part I," Nuclear Engineering and Design, 23, (1972) 273-294.

Ebeling-Koning, D. (1984), "Hydrodynamics of Single- an: Two-Phase Flow in Inclined Rod Arrays," Ph. D. Thesis, Nuclear Engineering Department, MIT, May, 1984.

Efthimiadis, A. (1983), "Mixed Convectiuon and Hydrodynamic Modeling of Flows in Rod Bundle," Ph. D. Thesis, Nuclear Engineering Department, MIT, May, 1984.

Eifler, W. and Nijsing, R. (1965), " Fundamental Studies of Fluid Flow and Heat Transfer in Fuel Element Geometries. Paet II. Experimental Investigation of Velocity Distribution and Flow Resistance in a Triangular Array of Parallel Rods." Report EUR 2193, European Atomic Energy Community (1965); cf. Nuclear Engineering and Design, 5, (1967) 22-42.

References (Continued)

Eifler, W. and Nijsing, R. (1967), "Experimental Investigation of Velocity Distribution and Flow Resistance in triangular Array of Parallel Rods," Nuclear Engineering and Design, 5, (1967) 22-42.

Engel, F. C. and Markley, R. A. (1978), "Buoyancy Effects on Sodium Coolant Temperature Profiles Measured in an Electrically Heated Mock-up of a 61-Rod Breeder Reactor Blanket Assembly, ASME Paper 78-WA/HT-25 (1978).

Engel, F. C., Markley, R. A. and Bishop, A. A.(1979), "Laminar, Transition, and Turbulent Parallel Flow Pressure Drop Across Wire-Wrap-Spaced Rod Bundles," Nuclear Science and Engineering, 69 (1979) 290-296.

Engel, F. C., Minushkin, B., Atkins, R. J. and Markley, R. A. (1980), "Characterization of Heat Transfer and Temperature Distributions in an Electrically Heated Model of an LMFBR Blanket Assembly," Nuclear Engineering and Design, 62, (1980) 335-347.

Engel, F. C., Markley, R. A. and Minushkin, B. (1981), "Temperature Profiles in Natural and Forced Circulation of Sodium Through a Vertical LMFBR Blanket Test Assembly," AIChE Symposium Series, Milwaukee (1981).

Engel, F. C. and Markley, R. A. (1981), "Parameter Studies of Peak Temperature Rise for LMFBR Blanket Rod Bundles," Nuclear Engineering and Design, 68, (1981) 347-357.

Engel, F. C., Markley, R. A. and Bishop, A. A. (1982), "The Effects of Radial Heat Flux Gradients and Flow Regimes on the Peak Sodium Temperature Rise in Wire-Wrapped Rod Bundles," Kiamesha Lake Meeting, NY, (Sept. 1982).

Fakori-Monazah, M. R. and Todreas, N. E. (1977), "Measurement and Analysis of Flow Wall Shear Stress in an Interior Subchannel of Triangular Array Rods," COO-2245-49TR, MIT (Aug. 1977).

Fontana, M. H. et al. (1973), "Temperature Distribution in a 19-Rod Simulated LMFBR Fuel Assembly in a Hexagonal Duct (Fuel Failure Mockup Bundle 2A)- Record of Experimental Data," ORNL-TM-4113, UC-79, Sep. 1973.

Fontana, M. H. et al (1974), "Temperature Distribution in the Duct Wall and at the Exit of a 19-Rod Simulated LMFBR Fuel Assembly (FFM Bundle 2A), Nuclear Technology, 24, (Nov. 1974).

France, D. M. and Ginsberg, T. (1973), "Evaluation of Lumped Parameter Heat Transfer Techniques for Nuclear Reactor Applications," Nuclear Science and Engineering, 51, (1973) 41-51.

References (Continued)

France, D. and Ginsberg, T. (1974), "Comparison of Analytic and Lumped Parameter Solutions for Steady-State Heat Transfer in Fuel Rod Assemblies," Progress in Heat and Mass Transfer, Vol. 7, (1974)

Fukuda (1979), private communication with T. Greene, unpublished work at ORNL, October, 1979.

Galloway, L. R. and Epstein, N. (1965), "Longitudinal Flow Between Cylinders in Square and Triangular Arrays and in a Tube with Square-Edged Entrances," AIChE Symposium Series No. 6, London (1965) 4-15.

George, T. L., Basehore, K. L. and Prather, W. A. (1980), "COBRA-WC Model and Predictions for A Fast Reactor Natural Circulation Transient," AIChE Symposium Series, Heat Transfer, Orlando (1980).

Ginsberg, T. (1972), "Forced-Flow Interchannel Mixing Model for Fuel Rod Assemblies Utilizing a Helical Wire-Wrap Spacer System," Nuclear Engineering and Design, 22, (1972) 28-42.

Ginsberg, T. and Lorentz, J. J. (1973), "Experimental Mixing Studies in Simulated Wire-Wrap Fuel Assemblies," International Meeting Reactor Heat Transfer Oct. 9-11, 1973, Karlsruhe.

Graves, A. W. (1971), "Friction Factor and Rod Bundle Entrance and Exit Loss Coefficient for 217-Rod FBR Fuel Assembly Water Test Model," TR-095-211-009, (Aug. 1971).

Greene, T. E. (1980), "Development and Evaluation of Techniques for Thermal-Hydraulic analysis of LMFBR Fuel Assemblies," M.S. Thesis, Nuclear Engineering Department, MIT, July, 1980.

Gunn, D. J. and Darling, C. W. W. (1963), "Fluid Flow and Energy Losses in Non-Circular Conduits," Transactions Institute of Chemical Engineers, (41), No. 4 (1963) 163-173.

Hines, D. P., Boyd, L. R. and Marian, V. R. (1971), "In-Core Boiling or Over Temperature Detector Development," General Electirc NEDC-13650 (1971).

Hoffmann, H. (1973), "Experimentelle Untersuchungen zur Kuhlmittelquervermichung und zum Druckabfall in Stabbundeln mit Wendelformigen Abstandshaltern," KfK-1832, (December 1973).

Hoffmann, H. and Baumgartner, E. (1975), "Experimental Investigations of the Thermodynamic Behavior of Fast Breeder Reactor Fuel Elements with Different Spacer Types," from "Fuel and Fuel Elements for Fast Reactors," International Atomic Energy Agency, Vienna, (1974).

References (Continued)

Ibragimov, M. K. et al. (1967), "Calculation of Hydraulic Resistivity Coefficients for Turbulent Fluid Flow in Channels of Non-Circular Cross Section," Atomnaya Energiya 23 (4) 300-305 (1967).

Itoh, K. (1981), Personal Communication to Professor N. E. Todreas.

Johannsen, K. (1981), "Longitudinal Flow Over Tube Bundles," NATO Advanced Study Institute on "Low Reynolds Number Forced Convection in Channel and Bundles," Ankara, Turkey, July 13-24, (1981).

Khan, E. U. (1975), "A Porous Body Model for Predicting Temperature Distribution in Wire-Wrapped Fuel Rod Assemblies," Nuclear Engineering and Design, 35 (1975) 1-12.

Khan, E. U. (198), "LMFBR In-Core Thermal-Hydraulics: The State of the Art and U.S. Research and Development Needs," PNL-3337, UC-32, April 1980.

Khan, E. U. (1982), "A Validation Study of COBRA-WC for LMFBR Steady-State and Transient Analysis," Presented in Kiamesha Lake Meeting, Sep. 1982.

Kim, S. N. (1982), "LMFBR Thermal Hydraulic Code Develpoment and Evaluation," S. M. Thesis, MIT, Nuclear Engineering Department, Oct. 1982.

Kjellstrom, B. (1971), "Transport Process in Turbulent Channel Flow," Final Report AE-RL-1344, Nykoping, Sweden (1971).

Lafay, J. and Benaut, B. (1975), "Local Pressure Measurements and Peripheral Flow Visualization in a Water 19-Rod Bundle Compound with FLICA IB Calculations: Influence of Helical Wire-Wrap Spacer System," ASME Paper 75-HT-22, (1975).

Levchenko, Y. D., Subbotin, V. I. and Ushakov, P. A. (1967), "The Distribution of Coolant Velocities and Wall Stresses in Closely Packed Rods," (transl.) Atomonaya Energiya 22, (1967) 218.

LeTourneau, B. W., Grimble, R. E. and Zerbe, J. E. (1957), "Pressure Drop for Parallel Flow Through Rod Bundles," Trans. Am. Soc. Mech. Engrs. 79, (1957), 1751-1758.

Lorenz, J. J. and Ginsberg, T. (1972), "Results and Analysis of 7-Pin Wire-Wrap Mixing Test," ANS Transactions, Vol. 15, No. 2, (Nov. 1972).

Lorenz, J. J. and Ginsbert, T. (1977), "Coolant Mixing and Subchannel Velocities in an LMFBR Fuel Assembly," Nuclear Engineering and Design, 40, (1977) 315-326.

References (Continued)

Magee, P. M. and Nilsson (1971), K. A., "Pressure Drop in Wire-Wrapped Rod Bundles," ANS Transactions, 14, No. 1, 254, (1971).

Malak, J., Hejna, J. and Schmid, J. (1975), "Pressure Losses and Heat Transfer in Non-Circular Channels with Hydraulically Smooth Walls," Int. Journal of Heat and Mass Transfer, Vol. 18, (1975) 139-149.

Markley, R. A. and Engel, F. C. (1981a), "Parameter Studies of Peak Temperature Rise for LMFBR Blanket Rod Bundles," LMFBR Core T/H Information Meeting, Monterey, CA, (March 1981).

Markley, R. A. and Engel, F. C. (1981b), "Blanket Sodium Heat Transfer Test Data and Evaluation," LMFBR Core T/H Information Meeting, Monterey, CA, (March 1981).

Markley, R. A. and Engel, F. C. (1981c), "Experimental Activities in LMFBR Core Design Thermal-Hydraulics," First IAHR Meeting on Liquid Metals Thermal-Hydraulics, MIT, Cambridge, MA, Oct. 5-6, (1981).

Markley, R. A. (1982), personal communication to S.-K. Cheng

Marten, K., Yonekawa, S. and Hoffmann, H. (1982), "Experimental Investigation on Pressure Drop in Tightly Packed Bundles with Wire Wrapped Rods," IAHR Second International Specialists Meeting on Thermal-Hydraulics in LMFBR Rod Bundles, Rome, Sept. 15-17, (1982).

Maubach, K. (1970), "Reibungsgesetze Turbulenter Stromungen," Chem. Ing. Techn. 42, 995-1004 (1970).

McAreavey, C. G. and Betts, C. (1979), "A Review of Theoretical and Experimental Studies Underlying the Thermal-Hydraulic Design of Fast Reactor Fuel Elements," Specialist Meeting on Thermodynamics of FBR Fuel Subassemblies under Nominal and Non-Nominal Operating Conditions, Karlsruhe, Feb. 5-7, (1979).

Miyaguchi, K. and Takahashi, J. (1979), "Thermal-Hydraulic Experiments with Simulated LMFBR Sub-Assemblies under Nominal and Non-Nominal Operating Conditions," Specialists Meeting on Thermodynamics of FBR Fuel Subassemblies under Nominal and Non-Nominal Operating Conditions, Karlsruhe, Feb. 5-7, (1979).

Morris, H. M., APPLIED HYDRAULICS IN ENGINEERING, The Ronald Press Company, NY (1963).

Morris, R. H., et al. (1980), "Single-Phase Sodium Tests in 61-pin Full-Length Simulated LMFBR Assembly- Record of Phase 1 Experimental Data for THOR Bundle 9," ORNL/TM-7313, (1980)

References (Continued)

Namekawa, F., Ito, A. and Mawatari, K. (1984), "Buoyancy Effects on Wire-Wrapped Rod Bundle Heat Transfer in an LMFBR Fuel Assembly," Nuclear Engineering Laboratory, Toshiba Corporation, Japan, to be plished in 1984 National Heat Transfer Conference.

Nijsing, R. and Eifler, W. (1974), "A Computational Method for the Steady State Thermohydraulic Analysis of Fuel Rod Bundles with Single Phase Cooling," Nuclear Engineering and Design, 30 (1974) 145-185.

Novendstern, E. H. (1972a), "Mixing Model for Wire Wrap Fuel Assemblies," ANS Winter Meeting, Nov. 12-17, 1972, Washington, D. C. Also ANS Transactions, 15 866 (1972).

Novendstern, E. H. (1972), "Turbulent Flow Pressure Drop Model for Fuel Rod Assemblies Utilizing a Helical Wire Wrap Spacer System," Nuclear Engineering and Design, 22 19 (1972).

Ohtake, T., Uruwashi, S. and Takahashi, K. (1976), "Velocity Measurements in the Subchannel of the Wire-Spaced Subassembly," Nuclear Technology, 30 333 (1976).

Okamoto, Y., Hishida, M. and Akino, N. (1970), "Hydraulic Performance in Rod-Bundle of Fast Reactor Fuels. Pressure Drop, Vibration and Mixing Coefficient," IAEA/SM-130/5 (1970).

Oosthuizen, R. H. (1974), "Turbulent Combined Convective Flow Over a Vertical Plane Surface," 5th International Heat Transfer Conference, Tokyo, 1974.

Panknin, W., et al. (1974), "Forced Convection Heat Treansfer in the Transition from Laminar to Turbulent Flow in Closely Spaced Circular Tube Bundles," Heat Transfer 1974, Vol. 2 pp 325-329, Scripta Book Co., Washington, D.C., 1974.

Pedersen, D. R., Pierce, R. D., Wilson, R. E. and Roop, C. J. (1974) "Crossflow Mixing in a 91-Element Bundle," ANL/RAS 74-2, (Feb. 1974).

Pedersen, D. R., Pierce, R. D., Lorentz, J. J. and Roop, C. J. (1974a), "Experimental Investigation of the Hydraulic Entrance Length and Subchannel Velocity Profiles in a 91-Element Wire-Wrapped Subassembly," ANL/RAS 74-5, (Apr. 1974).

Petrunik, K. (1968), "Turbulent Mixing Measurement for Single Phase Air, Single Phase Water, and Two Phase Air-Water Flows in Adjacent Rectangualr Subchannels," M.A. Sc. Thesis, University of Windsor, Ont. (1968).

References (Continued)

Pirelli, D. (1982), "Pressure Drop Characteristics of PEC Reactor Fuel Element," Presented at Second IAHR Specialist Meeting on LMFBR Rod Bundle Thermal-Hydraulics, Rome, Sept. 15-17, (1982).

Presser, K. H. (1967), "Warmeubergang und Druckverlust an Reaktorbrennlementen in Form langsdurchstrounter Rundstrabbundel," Jul-486-RB, KFA Julich (1967). Also, International Journal of Heat and Mass Transfer, 14 1235-1259 (1971).

Rameau, B. and Menant, B. (1984), "Sodium Thermalhydraulics under Natural and Mixed Convection in Bundle Geometry- Experimental Results and Analysis," CEA-Centre D'etudes Nucleaires de Grenoble, France, ASME Winter Annual Meeting, New Orlens, Nov. 1984.

Ramm, H., Johannsen, K. and Todreas, N. E. (1974), "Single Phase Transport within Bare-Rod Arrays at Laminar, Transition and Turbulent Flow Condition," Nuclear Engineering and Design, 30, 186-204(1974).

Ramm, H. and Johannsen, K. (1975), "Evaluation of Interchannel Heat Transport in Bare Liquid-Metal Cooled Rod Arrays of Equilateral Triangular Arrangement," ASME paper 75-HT-32 (1975).

Rehme, K. (1967), "Geometry-Dependence of the Pressure Loss in Rod Bundles with Coiled Wire Spacers and Longitudinal Flow," Ph. D. Dissertation, U. Karlsruhe, Germany, (December 1967).

Rehme, K. (1970), "Widerstandsbeitwerte von Gitterabstandshaltern fur Reaktorbrennelemente," ATKE 15 (2) 127-130 (1970).

Rehme, K. (1971), "Laminarstromung in Stabbundeln," Chemi Ingenieur Technik, 43 17 (1971).

Rehme, K. (1972a), "Pressure Drop Performance of Rod Bundles in Hexagonal Arrangements," Int. Journal of Heat and Mass Transfer, 15 2499-2517 (1972).

Rehme, K. (1973), "Pressure Drop Correlations for Fuel Element Spacers," Nucl. Tech. (17) Jan. 1973.

Rehme, K. (1972), "Simple Method of Predicting Friction Factors of Turbulent Flow in Non-Circular Channels," Int. Journal of Heat and Mass Transfer, 16 933-950 (1973).

Rehme, K. (1978a), "The Structure of Turbulent Flow Through a Wall Subchannel of a Rod Bundle," Nuclear Engineering and Design, 45 311-323 (1978).

Rehme, K. (1978b), "Turbulente Stromung in eihem Wandkanal eines Stabbundels," KfK-2617 (1978).

References (Continued)

Rehme, K. (1978c), "Geschwindigkeits-und Turbulenzverteilungen in einem Wandkanal eines Stabbundels," KfK-2637 (1978).

Rehme, K. (1980a), "Turbulent Momentum Transport in Rod Bundles," Nuclear Engineering and Design, 62 137-146 (1980).

Rehme, K. and Trippe, G. (1980), "Pressure Drop and Velocity Distribution in Rod Bundles with Spacer Grids," Nuclear Engineering and Design, 62 349-359 (1980).

Rehme, K. (1982), "Distributions of Velocity and Turbulence in Parallel Flow along an Asymmetric Rod Bundle," Nuclear Technology, 59 (Oct. 1982).

Reihman, T. C. (1969), "An Experimental Study of Pressure Drop in Wire Wrapped FFTF Fuel Assemblies," BNWL-1207, (Sept. 1969).

Reihman, T. C. (1982), "Experimental Study of Pressure Drop in Wire-Wrapped Road Bundle," Presented at 1982 AIAA/ASME Joint Fluids, Plasma, Thermophysics and Heat Transfer Conference, St. Louis, MO, June 7-11, (1982).

Rogers, J. T. and Tarasuk, W. R. (1968), "Coolant Mixing in Reactor Fuel Bundles. Part II. Forced Mixing by Flow Sweeping," R68-CAP 32, Canadian General Electric (Sept. 1968).

Rogers, J. T. and Todreas, N. E. (1968), "Coolant Interchannel Mixing in Reactor Fuel Rod Bundles Single-Phase Coolants," Heat Transfer in Rod Bundles, ASME (1968).

Rogers, J. T. and Tahir, A. E. E. (1975), "Turbulent Interchange Mixing in Rod Bundle and The Role of Secondary Flows," ASME paper 75-HT-31 (1975).

Roidt, R. M. et al. (1973), "Experimental Determination of Turbulent Exchange Coefficients in Model Reactor Rod Bundle," ASME paper 73-HT-51, Aug. 1973.

Roidt, R. M., Carelli, M. D. and Markley, R. A. (1980), "Experimental Investigations of the Hydraulic Field in Wire-Wrapped LMFBR Core Assemblies," Nuclear Engineering and Design, 62 295-321 (1980).

Rowe, D. S. and Angle, C. W. (1967), "Cross-Flow Mixing between Parallel Flow Channels During Boilng, COBRA- Computer Programm for Coolant Boiling in Rod Arrays," (Part I) BNWL-371, March 1967.

Sangster, W. A. (1968), "Calculation of Rod Bundle Pressure Loss," ASME Paper 68 WA/TH-35 (1968).

References (Continued)

Schmid, J. (1966), "Longitudinal Laminar Flow in an Array of Circular Cylinders," International Journal of Heat and Mass Transfer, Vol. 9 925-937 (1966).

Seban, R. A. and Hunsbedt, A. (1973), "Friction and Heat Transfer in the Swirl Flow of Water in an Annulus," International Journal of Heat and Mass Transfer, 16 303-310 (1973).

Sheynina, A. V. (1967), "Hydraulic Resistance of Bundles of Cores in Axial Fluid Flow," Liquid Metals, pp 210-223, Atomizdat, Moscow (1967), KfK-tr-365. Also "Resistance to Axial Flow of Fluids Past Rod Clusters, NASA TT F-522, Tr. of Liquid Metals, Atomizdat, Moscow (1967).

Simonek, J. (1966), "Prisperec K problematia prestupu tepla v proutkovem palivovem clanku," Jaderna energie 12 (7), 246-249 (1966).

Singh, K. and St Pierre C. C. (1972), "Single Phase Turbulent Mixing in Simulated Rod Bundle Geometries," Trans. CSME 1 (2) 73-80 (June 1972)

Skok, J. (1973), "Mixing of the Fluid due to Helicoidal Wires on Fuel Pins in a Triangular Array," Progress in Heat and Mass Transfer, 7 (1973).

Sparrow, E. M. and Loefler, J. R. (1959), "Longitudinal Laminar Flow Between Cylinders Arranged in Regular Array," American Institute of Chemical Engineering Journal, 5 No. 3, 1959.

Spencer, D. R. and Markley, R. A. (1980), "Friction Factor Correlation for 217-Pin Wire Wrap Spaced LMFBR Fuel Assemblies," ANS Transactions, 39 1014, 1980.

Spriggs, H. D. (1973), "Comments on Transition from Laminar to Turbulent Flow," Ind. Eng. Chem. Fundam., 12, 3, 286 (1973).

Straub, G. (1976), "Berechnung der Temperatur- und Geschwindigkeitsfelder in Parallel angestromten Brennstabbundlen Schneller natriumgekuhlter Brutreaktoren," Dissertation, IKE, TU Stuttgart 1976.

Subbotin, V. I. et al (1960), "Hydraulischer Widerstand bei durch Flussigkeiten langsumstromten Stabbundeln," Kernenergie, 4, 658-660 (1961). Cf. Atomnaya Energiya, 9, 308 (1960).

Subbotin, V. I., Gabrianovich, B. N. and Sheinina, A. V. (1972), "Hydraulic Resistance with Longitudinal Streamline Flow for Bundles of Plain and Finned Rods," Atomnaya Energiya, Vol. 33, No. 5, pp 889-892, (Nov. 1972).

References (Continued)

Sutherland, W. A. and Kays, W. M. (1965), "Heat Transfer in Parallel Rod Arrays," Report GEAP-4637 of General Electric Company, San Jose, CA (1965).

Symolon, P. D. (1982), "Mixed Convection in Vertical Rod Bundles," Ph.D. Thesis, Nuclear Engineering Department, MIT (Aug. 1982).

Symolon, P. D. (1982a) personal communication to S.-K. Cheng.

Todreas, N. E. and Turi, J. A. (1972), "Interchannel Mixing in Wire Wrapped Liquid Metal Fast Reactor Fuel Assemblies," Nucl. Tech. Vol. 13 (Jan 1972).

Todreas, N. E., (1984), 22.313 Class Notes, Nuclear Engineering Department, MIT, Jan. 1984.

Ullrich, R. (1974), "Analyse der Ansgebildeten Laminarstromung in Langsangestromten Endlichen, Hexagonalen Stabbundeln," Doktor-Ingenieur Dissertation, Inst. Kerntech., Technische Universitat Berlin, Berlin, (1974).

Wakasugi, K. and Kakehi, I. (1971), "Pressure Drop Performance of Fuel Pin Bundle with Spiral Wire Spacer," Jl. Nucl. Sci. and Tech. 8 (3) 167-172 (March 1971).

Walton, F. B. (1969), "Turbulent Mixing Measurements for Single Phase Air-Water Flows in Adjacent Triangualr Subchannels," M.A. Sc. Thesis, University of Windsor, Windsor, Ont. (1069)

Wheeler, C. L., Rowe, D. S. and Smith, J. D. (1974), "An Experimental Study of Axial and Cross Flow Velocity in a 7-Pin Wire Wrapped Bundle, BNWL-1804, (Feb. 1974).

Yang, J. W. (1976), "A Note on Turbulent-Laminar Transition for Flow in Triangular Rod Bundles," Nucl. Sci. and Eng., Vol. 62, No. 3, 579-582 (1976).

Yeung, M. R. and Wolf, L., (1980), "Evaluation of Conduction Mixing Lengths for Subchannel Analysis of Finite LMFBR Bundles," Nuclear Engineering and Design, 62 371-378 (1980).